Lateral–Torsional Buckling Response of As-built and Heat-straightened Welded Steel Girders

by

Sheldon Colby Twizell

A thesis submitted in partial fulfillment of the requirements for the degree of

Master of Science

in

Structural Engineering

Department of Civil and Environmental Engineering
University of Alberta

ABSTRACT

Lateral–torsional buckling (LTB) is a stability failure mode that occurs in unbraced segments of flexural members and is associated with simultaneous out-of-plane lateral defection and cross-section rotation. The LTB behaviour of doubly symmetric I-shaped members is generally well understood. However, there is concern that current understandings of inelastic LTB in welded steel girders may be inaccurate and not representative of the current fabrication methods employed in Canada. Moreover, recent studies (MacPhedran and Grondin 2011; Kabir and Bhowmick 2018) have indicated the current Canadian design provisions for LTB may be inaccurately estimating the inelastic LTB resistance of welded steel girders. The purpose of this study is to address these concerns and assess the LTB behaviour of modern welded steel girders through experimental and numerical means. Additionally, to assess the LTB behaviour and load-carrying performance of heat-straightened welded steel girders.

The experimental portion of this study includes the large-scale testing of four welded steel girders and five heat-straightened girders of intermediate slenderness. The test results were used to examine the LTB behaviour of welded steel girders and assess the stability response of heat-straightened girders through comparison with the as-built response. A continuum finite element model was developed and calibrated against the experimental test results and was used to simulate the experimental specimens for two loading conditions: top flange and shear centre. The adequacy of the CSA S16-19 design provisions for welded steel girders was then evaluated by comparing the code-predicted moment resistances with those of finite element analysis. The CSA S16-19 design equation is found to adequately estimate the moment resistance of modern welded steel girders; however, CSA S16-19 can overestimate the moment resistance of girders with large web width-to-thickness ratios and high initial geometric imperfection.

ACKNOWLEDGEMENTS

TABLE OF CONTENTS

LIST OF TABLES

LIST OF FIGURES

LIST OF SYMBOLS

A	=	Coefficient for moment gradient distribution in load height adjustment method of Nethercot and Rockey (1971)
A_s	=	Cross-sectional area
b	=	Flange width
B	=	Coefficient in load height adjustment method of Nethercot and Rockey (1971)
$b_{e,i}$	=	Distance from flange tip to web
c	=	Coefficient for doubly symmetric I-shapes in AISC 360-16
C_b	=	Equivalent moment factor in AISC 360-16
C_w	=	Warping torsional constant
d	=	Section depth
E	=	Elastic modulus; modulus of elasticity; Young's modulus
F	=	Longitudinal stress calculated at strain gauge locations
F_{cr}	=	Critical Stress
F_u	=	Ultimate Stress
F_y	=	Yield stress
G	=	Shear modulus
h	=	Web height
h_i	=	Distance between the top and bottom flange measured at flange tips
$h_{i,w}$	=	Distance between the top and bottom flange measured adjacent to web
h_o	=	Distance between flange centroids
I_x	=	Moment of inertia about the strong axis
I_y	=	Moment of inertia about the weak axis
J	=	St. Venant torsional constant
k_{FE}	=	Initial lateral stiffness predicted by finite element analysis
k_{Test}	=	Initial lateral stiffness of experimental specimen
L, L_b	=	Length of unbraced segment
L_p	=	Limiting laterally unbraced length for the limit state of yielding

L_r	=	Limiting laterally unbraced length for the limit state of inelastic lateral−torsional buckling
M	=	Bending moment in a member under specified load
M_a	=	Bending moment at the one-quarter point location of an unbraced segment
M_b	=	Bending moment at the mid-point location of an unbraced segment
M_B	=	Nominal moment capacity of a beam with full lateral restraint
M_c	=	Bending moment at the three-quarter point location of an unbraced segment
M_{cr}	=	Critical elastic moment of a laterally unbraced beam in EC3
M_{FE}	=	Maximum moment resistance of experimental specimen predicted by finite element analysis
$M_{FE,L/1000}$	=	Maximum moment resistance predicted by finite element analysis for maximum initial geometric imperfection
$M_{FE,SC}$	=	Maximum moment resistance for shear centre loading predicted by finite element analysis
$M_{FE,TF}$	=	Maximum moment resistance for top flange loading predicted by finite element analysis
M_{HS}	=	Maximum moment resistance of heat-straightened girder
M_{max}, M_o, M_{Test}	=	Maximum bending moment in an unbraced segment; maximum moment resistance; maximum moment resistance of original girder; maximum moment resistance of experimental specimen
M_n	=	Nominal moment resistance
M_p	=	Plastic moment resistance
M_r	=	Factored moment resistance
$M_{S16,SC}$	=	Maximum moment resistance for shear centre loading predicted by CSA S16-19
$M_{S16,TF}$	=	Maximum moment resistance for top flange loading predicted by CSA S16-19
M_u	=	Critical elastic moment of a laterally unbraced beam in CSA S16-19
M_y	=	Yield moment resistance
n	=	System constant from MacPhedran and Grondin (2011)

P	=	Applied point load
P_{HS}	=	Maximum average point load of heat-straightened girder
P_{max}	=	Maximum average point load
R	=	Torsional parameter
r_{ts}	=	Effective radius of gyration
r_y	=	Radius of gyration about the weak axis
S_x	=	Elastic section modulus about the strong axis
t	=	Flange thickness
w	=	Web thickness
W	=	Torsional parameter in load height adjustment method of Nethercot and Rockey (1971)
W_y	=	Plastic section modulus for Class 1 or 2 sections and elastic section modulus for Class 3 sections, in EC3
y	=	Distance from mid-height to the point of load application
Z_x	=	Plastic section modulus about the strong axis
α_{LT}	=	Imperfection factor
β	=	Correction factor for lateral−torsional buckling curves for rolled and welded sections in EC3
γ_{M1}	=	Resistance factor for lateral−torsional buckling in EC3
Δ_h	=	Mid-span lateral displacement
δ_{HS}	=	Compression flange sweep of heat-straightened girder
$\Delta_{HS,h}$	=	Mid-span lateral displacement of heat-straightened girder
δ_o	=	Compression flange sweep of original girder
Δ_v	=	Mid-span vertical displacement
ε_{11}	=	Logarithmic strain component local to an element in the principal 1 direction
ε_{22}	=	Logarithmic strain component local to an element in the principal 2 direction
η_f	=	Parametric high-stress-gradient region width of the flanges
η_{fe}	=	Width of the edge regions in the flanges

η_w	=	Parametric high-stress-gradient width on one edge of the web
Θ_{HS}	=	Mid-span cross-section rotation of heat-straightened girder
Θ_o	=	Mid-span cross-section rotation
λ	=	Modified beam slenderness ratio
$\bar{\lambda}_{LT}$	=	Non dimensional slenderness for lateral−torsional buckling
$\bar{\lambda}_{LT,0}$	=	Plateau length of lateral−torsional buckling curves for rolled and welded sections in EC3
σ_{cf}	=	Compressive stress of flange
σ_{cw}	=	Compressive stress of web
σ_{tf}	=	Tensile stress of flange
σ_{tw}	=	Tensile stress of web
ϕ	=	Resistance factor for lateral−torsional buckling in CSA S16-19
φ_c	=	Angle formed between the plane of the displaced compression flange and the horizontal
φ_{FE}	=	Initial cross-section twist of finite element model
φ_{LT}	=	Value to determine the reduction factor χ_{LT}
φ_t	=	Angle formed between the plane of the displaced tension flange and the horizontal
φ_{Test}	=	Initial cross-section twist of experimental specimen
χ_{LT}	=	Reduction factor for lateral−torsional buckling
ω_2	=	Equivalent moment factor in CSA S16-19
ω_2^*	=	Modified moment gradient factor to account for load height

1 INTRODUCTION

1.1 Background

The limit state of lateral–torsional buckling (LTB) is one of many considered by steel design standards when determining the flexural resistance of I-shaped members. LTB is a global instability failure mode that can occur in flexural members, within unbraced or insufficiently braced beam segments, and is characterized by simultaneous lateral deflection and twist. A flexural member is susceptible to LTB when the in-plane (major-axis) stiffness is higher than the out-of-plane (minor-axis) stiffness. Open sections, such as a wide-flange section, are consequently vulnerable to LTB failure when orientated so that bending occurs about the section's major axis and cannot fail by LTB when oriented for bending about the minor axis. Similarly, members such as square sections, which possess the same stiffness about each principal axis, will not fail by LTB, as the propensity to deflect laterally about the out-of-plane axis does not exist. Unless a member is continuously laterally braced, it may fail by LTB before achieving the full cross-sectional capacity, and the final failure pattern will be a superposition of global deflections, cross-section twist, varying extents of yielding and potentially local distortion.

The LTB response of steel beams is commonly represented as a curve of the moment resistance versus slenderness, as shown conceptually in Figure 1-1. The figure identifies the three main regions that delineate the LTB response and are characterized by distinct differences in cross-sectional yielding and slenderness. The plastic region pertains to short or stocky beams and represents a failure accompanied by full cross-sectional yielding prior to the onset of instability. Within the inelastic region, members of intermediate length fail by LTB after partial yielding of the cross-section takes place. Finally, the elastic region, consisting of long and slender beams, sees the occurrence of LTB prior to any significant yielding of the section.
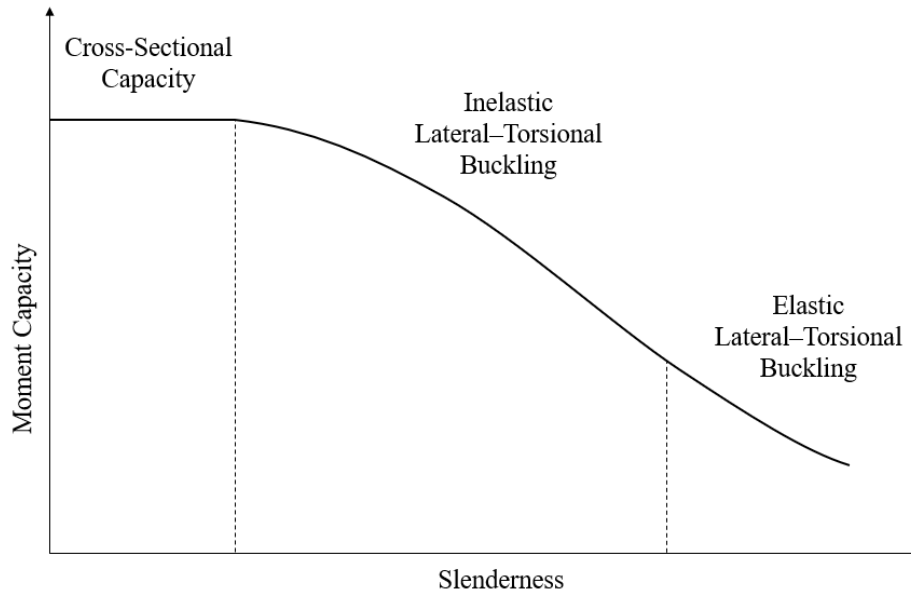
Figure 1-1: Conceptual flexural bending curve

The Canadian steel design standard CSA S16-19 (CSA 2019a) and Canadian highway bridge design standard CSA S6-19 (CSA 2019b) govern the design of steel beams. These steel beams can either be hot rolled or welded built-up sections. Hot rolled steel beams are commonly utilized for buildings and commercial construction, whereas welded plate girders are typically used in bridge construction. The primary difference between these two fabrication procedures is the resulting material properties and residual stresses, which differ based on the heating and cooling cycles experienced. As a result, the LTB responses of rolled and welded beams can differ significantly when the material yielding is most influential. Regardless of the fabrication method, Canadian provisions delineate a beam's LTB response using the upper bound cross-sectional moment capacity, lower bound elastic moment capacity and then assess the inelastic behaviour by considering the effects of yielding. For steel beams, additional limits states of shear, local buckling, vibrations, deflections, and fatigue are specified to ensure acceptable structural performance and serviceability. However, LTB is commonly a governing failure mode due to the impracticality of providing continuous lateral restraint in many projects, and especially during construction.

1.2   Statement of Research Problem

The flexural beam capacity curves prescribed by CSA S16-19 have remained relatively unchanged since 1974 and make no distinction between rolled and welded girders. However, two studies— MacPhedran and Grondin (2011) and Kabir and Bhowmick (2018)—have suggested that the current Canadian provisions for LTB may be inadequately estimating the moment resistances of welded steel girders failing by inelastic LTB. Inconsistency in the S16 prediction is theorized to arise primarily from the handling of residual stresses and geometric imperfections, which are distinct in welded steel girders, and long understood to significantly influence inelastic LTB. However, there exists a lack of modern LTB experimental test data; the test data often used to evaluate the adequacy of the Canadian design equations is from a period preceding the 1980s and is taken from tests conducted outside of North America. Assessments utilizing such test data may inappropriately reflect the behaviour of modern welded steel girders. Consequently, the performance of the Canadian design provisions is unclear. It is necessary to address these concerns and develop an improved understanding of the LTB behaviour of welded steel girders through large-scale experimental testing and numerical evaluations, given the extensive use of welded steel girders throughout Canada.

1.3   Objectives and Scope

The primary objectives of this research are to investigate and verify the performance of the CSA S16-19 design provisions for welded steel girders and to assess the LTB resistance of welded steel girders repaired by heat-straightening. The study stands to: (1) contribute a significant collection of experimental and numerical data representative of modern fabrication practices; (2) confirm the adequacy (or otherwise) of the Canadian provisions for LTB of welded steel girders, and (3) provide practical advice to practitioners of heat-straightening, concerning the influence of heat-straightening on the LTB response of flexural members. Achieving these objectives required the completion of the following tasks:

1. reviewing past and current understandings of LTB;
2. performing large-scale LTB tests;
3. analyzing the obtained moment resistances and displacements;
4. developing and applying a heat-straightening procedure;
5. performing large-scale LTB tests of heat-straightened girders;

6. analyzing the obtained moment resistances and displacements of heat-straightened girders;

7. developing a numerical model capable of predicting LTB in welded steel girders;

8. validating a numerical model against test results; and

9. evaluating the adequacy of the Canadian design provisions for LTB of welded steel girders.

The full study comprises three distinct test programs, two experimental and one numerical. The experimental test programs study the behaviour of 11 welded steel girders of intermediate slenderness and nine unique cross-sections, which are loaded to induce an LTB failure. The specimens are subject to eight equally-spaced point loads, are simply-supported, and unbraced over a 9.75 m length. Five of the 11 test specimens are repaired by heat-straightening and retested for investigation of the LTB behaviour. The numerical program includes a finite element (FE) model developed and validated upon the measured geometric properties, initial imperfections, and residual stresses obtained from the experimental program, which is then used to study the performance of the Canadian design provisions for welded steel girders.

1.4   Organization of Report

This report is organized into eight chapters. The introduction and background of LTB is presented in Chapter 1. Chapter 2 contains a review of past research studies, including the factors affecting LTB, experimental and numerical testing of welded girders, the North American and European design standards, and the practice of heat-straightening. Chapter 3 presents the experimental test programs, including specimen characteristics, test characteristics and test procedures for both the LTB and the heat-straightening investigations. The test results of the LTB and heat-straightening programs are presented and then analyzed in Chapters 4 and 5, respectively. A review of the FE model is provided in Chapter 6, covering the modelling techniques, validation and subsequent investigations into the factors influencing model behaviour. The results of a set of FE analyses for the test specimens under shear centre and top flange loading are presented in Chapter 7 and used to assess the performance of the Canadian LTB design provisions. Chapter 8 provides the key conclusions of this research study and recommendations for future work. The measured geometric imperfections of the test specimens can be found in Appendix A. Experimental load–displacement curves for the as-built and heat-straightened girders are provided in Appendix B. Appendix C contains the moment–rotation curves for calibration of the FE model.

2   LITERATURE REVIEW

2.1   Factors Affecting Lateral–Torsional Buckling

Several factors affect the stability of steel I-section members under flexural bending. As such, the majority of research focuses on the identification and assessment of these parameters. The following section serves to summarize some of the more influential parameters affecting LTB, which are pertinent to this study.

2.1.1   Initial Geometric Imperfections

Both welded steel girders and hot-rolled girders develop initial geometric imperfections in fabrication. However, welded steel girders are additionally susceptible, as localized heating and cooling during the welding procedure can induce global curvature and local cross-sectional distortion. Additionally, initial imperfections may be present in individual plates of built-up members as a result of the plate rolling process or cutting procedures. The final imperfection pattern is the superposition of the individual component imperfections and fabrication procedures. Imperfections about the cross-section's weak or longitudinal axes, such as initial lateral sweep or cross-section twist, can affect lateral stability and influence the LTB response. An imperfect beam presenting with initial lateral sweep and cross-section twist deflects out-of-plane upon load application. The presence of initial geometric imperfections in beams results in reduced lateral stiffness and strength. Figure 2-1 presents a generalized plot highlighting the effect of imperfections on the beam stability response. In comparison, a perfect beam exhibits zero lateral displacement until instability occurs at the critical load when subjected to a small disturbance. The critical load corresponds to the point of bifurcation of equilibrium, where the member is no longer stable, and out-of-plane bending and twisting initiates.
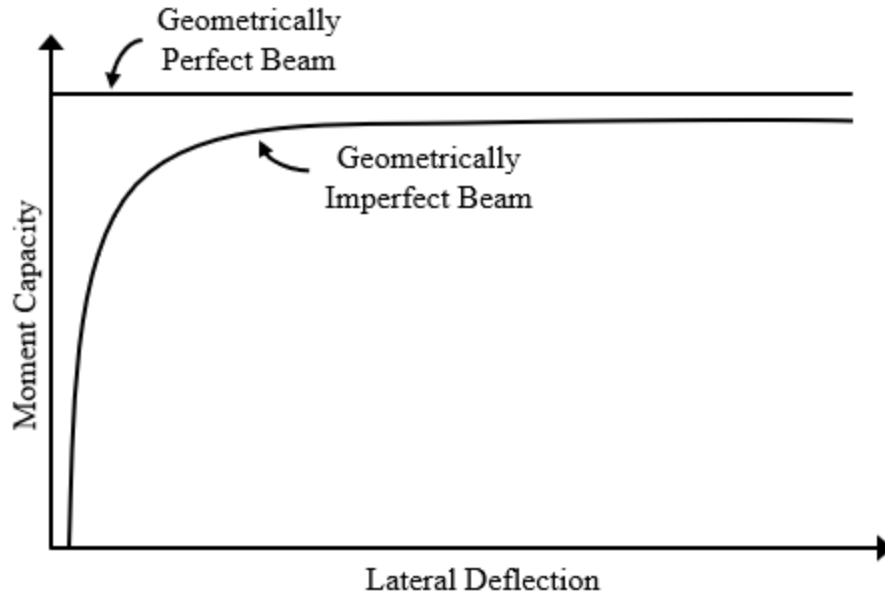
Figure 2-1: Load–deformation responses of geometrically perfect and imperfect beams

CSA S16-19 provisions account for initial geometric imperfections implicitly, meaning that there is no direct mechanism to account for imperfections during design. Instead, calibration of the beam design curves against experimental data accounts indirectly for the effect of these imperfections on member flexural capacity. This methodology differs from other steel design standards, such as the European design provisions, EC3 (CEN 2005), where an explicit imperfection factor is provided, and a distinction between welded and rolled sections is made. However, despite not being accounted for explicitly in the LTB provisions of CSA S16-19, geometric imperfections are not uncontrolled. CSA W59-18 (CSA 2018) and CSA G40.21 (CSA 2013) specify fabrication tolerances that limit both the local and global geometric imperfections of welded steel girders. Among the tolerances are limitations on the initial deviation from straightness (lateral sweep), where it is specified that welded steel girders shall not exceed 1 mm of lateral deviation per metre length, L.

As noted in Figure 2-1 for the imperfect girder, initial lateral deviations from straightness and other global geometric imperfections directly influence both the initial stiffness and overall displacement response. In numerical simulations, the definition of initial geometric imperfections is, therefore, a critical task. Generally, the effects of imperfections are captured by modelling only the initial compression flange sweep, as it is commonly considered a suitable parameter by which to capture the stiffness and displacement effects anticipated, provided the section is reasonably compact.

6

Only for girders comprising slender plate components does the presence of local imperfections become significant, and thus, they otherwise need not be modelled (Boissonnade and Somja 2012). Accordingly, most FE simulations for simplicity model the maximum allowable initial deviation from straightness specified by many steel design standards, $L/1000$, when assessing the LTB behaviour of flexural members. However, Subramanian and White (2017) suggest that FE simulations considering maximum imperfections may be unduly punishing predictions and even go so far as to suggest that the imperfections of both rolled and welded sections may be smaller than commonly assumed. Other researchers, such as Gérard et al. (2019), suggest that traditional modelling techniques utilizing only the initial compression flange sweep present a lack of adjustability, and modelling imperfections on a per plate basis may be preferred. Given this variety in modelling approaches, it can be inferred that there is a lack of consensus in the literature concerning the agreed-upon methods. Nonetheless, the inclusion of initial geometric imperfections is a critical component of the numerical simulation of LTB.

2.1.2   Residual Stresses

Residual stresses of primary interest for LTB are longitudinal stresses that develop and remain in steel members from production and fabrication and are present in both rolled and welded beams. The fabrication process, heat inputs, mechanical deformations, and cooling mechanisms dictate a beam's resulting residual stress pattern. The residual stresses develop following the same physical principles for both rolled and welded girders; however, the final distribution of residual stress differs distinctly. For a welded steel girder, highly concentrated heat and intense thermal gradients introduced during the welding procedure produce a distinct residual stress pattern from that of a rolled beam. During fabrication, the heated-affected material of a weld cools rapidly and contracts while being constrained by the adjacent (cool) materials of the girder. Consequently, as the heat-affected material contracts, large tensile stresses develop throughout the weld region, and to maintain equilibrium, compressive stresses form in the adjacent material. In an I-shape girder, the welding procedure results in a concentration of tensile stresses at the web–flange junction (the weld region) and relatively low magnitude compressive stresses along the flanges and web.

While the welding procedure and the effects of welding form the basis of a welded steel girder's residual stress distribution, the plate cutting method used to cut the flange and web plates to the desired width and depth can impact the residual stresses at the plate edge. Flame-cutting of steel

plates introduces high tensile stresses at plate edges, as a torch (commonly oxy-acetylene) introduces intense heat to cut the material (Alpsten and Tall 1970; Bjorhovde et al. 1972), while plates cut by mechanical methods, such as shear-cutting, tend to exhibit, on average, zero residual stresses near the plate edge (Nagaraja Rao et al. 1964). Similarly, other cutting methods, such as waterjet cutting or plasma-cutting, introduce distinct residual stresses to the plate edge. Figure 2-2 shows a typical welded residual stress pattern of a girder constructed of universal-mill plate and of flame-cut plate. As shown, a welded steel girder constructed of a mechanically cut plate will exhibit compressive residual stresses at the flange tips due to low initial stress levels at the plate edge. However, when fabricated using flame-cut plate, the girders exhibit narrow bands of tensile stress along the plate edge.
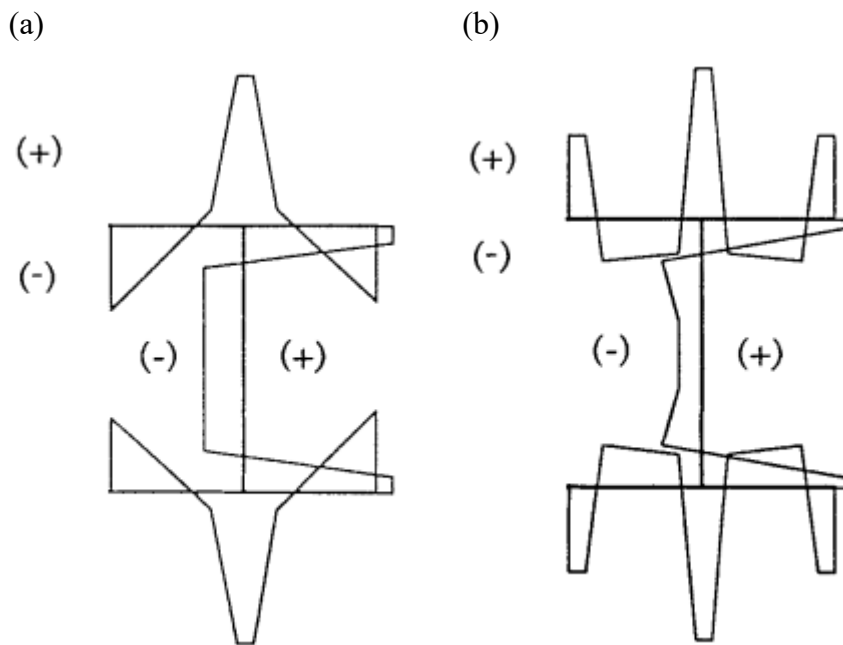
Figure 2-2: Typical residual stress patterns of welded girders constructed of (a) universal-mill plate and (b) flame-cut plate (Chernenko and Kennedy 1991)

In rolled sections, stresses are formed in a mechanically similar fashion but are instead a result of hot working during the rolling process and uneven cooling of the member. As the member cools, the portions more exposed to the surrounding environment (flange tips) cool at an accelerated pace in comparison to the locations of high thermal mass (web–flange junctions). Restraint introduced by the now-cooled flange tips imparts tensile residual stresses in the junctions as they continue to cool and contract. Equilibrium then forces the remaining material into compression. Rolled

sections are generally characterized by lower peak magnitudes of residual stress, in comparison to welded girders, and small regions of compressive stresses at the flange tips. Figure 2-3 illustrates the differences between residual stress patterns in rolled and welded girders by contrasting a representative (idealized) rolled residual stress pattern with that of a welded steel girder constructed with plates cut by a method of relatively low heat input.
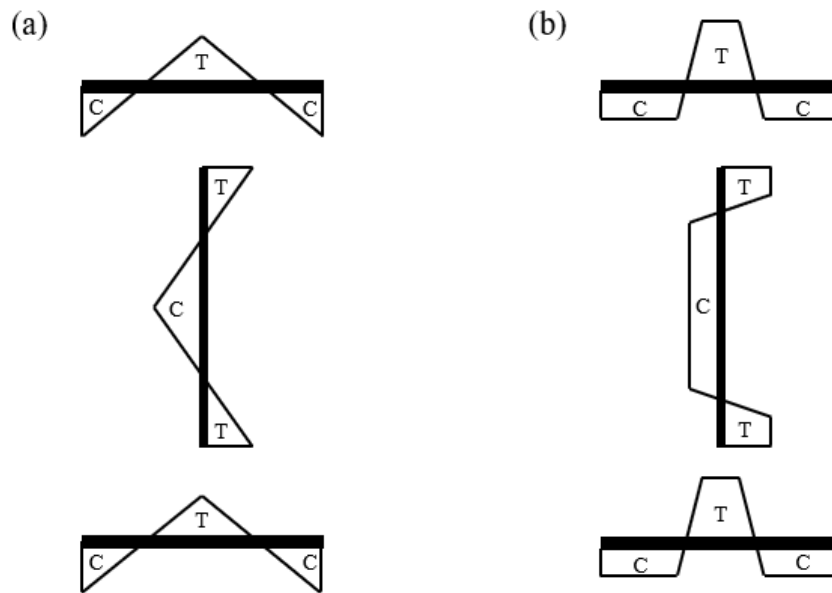
Figure 2-3: Typical residual stress patterns of (a) rolled members (Chernenko and Kennedy 1991) and (b) welded girders (Unsworth et al. 2019)

The presence and distribution of residual stresses have a significant effect on the inelastic LTB behaviour. Compressive and tensile longitudinal strains induced through loading cause areas of high residual stresses to yield and become ineffective. Therefore, the distribution of residual stress dictates the progression of yielding throughout the cross-section. Welded girders are anticipated to perform worse than an equivalent rolled section, as they typically present with higher compressive residual stresses over the cross-sections (Chernenko and Kennedy 1991). Yielding initiates under relatively small load and progresses through the tips of the compression flange, reducing the weak-axis moment of inertia and torsional properties of the section, thus lowering the buckling capacity. However, built-up members constructed with flame cut plates can perform better than equivalent milled or shear cut plates due to the introduction of high tensile stresses along the plate edges (Alpsten and Tall, 1970, Bjorhovde et al. 1972). As residual stresses are highly dependent on cutting and fabrication methods, assessing their effect on inelastic LTB is

complex; it requires an analysis of the progression of yielding and the calculation of the corresponding gradual reductions in stiffness and torsional properties.

2.1.3 Load Height

When a beam is loaded transversely, the elevation of the load point with respect to its shear centre has a significant effect on LTB behaviour. The LTB moment resistance may either be amplified or reduced, and this phenomenon is called the load height effect. When a section deflects laterally and rotates about its longitudinal axis, as a result of either LTB or initial geometric imperfections, the point of load application may no longer pass through the shear centre of the beam. The effect results in an applied torque about the member's longitudinal axis. If the point of load application is above the shear centre, a destabilizing torque develops, and below the shear centre, a restoring torque, as shown in Figure 2-4. Steel design standards commonly assume shear centre loading when assessing the LTB resistance, but this loading condition is rarely the case in practice. Furthermore, when a beam is loaded at the top flange, the load delivery mechanism commonly imposes some lateral restraint to the beam, which can reduce or mitigate the destabilizing effect of the load height, further complicating an assessment of the moment resistance. Nevertheless, methodologies do exist for assessing the load height effect in steel beams, as specified in CSA S16-19 or in the literature.
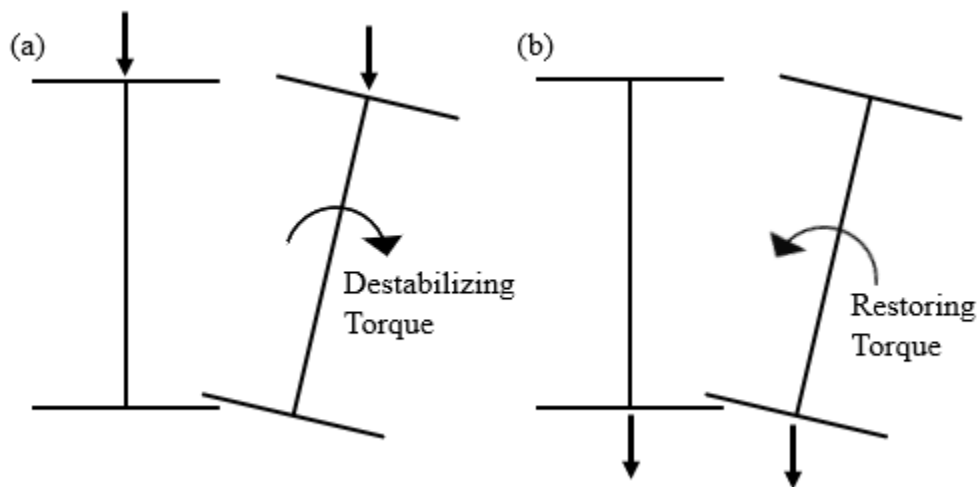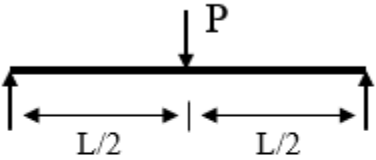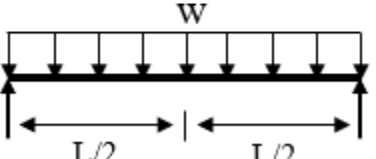
Figure 2-4: Depiction of the load height inducing (a) destabilizing torque and (b) restoring torque

Nethercot and Rockey (1971) proposed an overall coefficient method to account for the load height effect, where a modifier, ω_2^*, is applied to adjust the critical elastic moment, M_u, and accounts for the effects of top flange, bottom flange and shear centre loading. The researchers proposed the coefficients A and B, which are determined for cases of concentrated and distributed transverse loading of simply-supported beams. As the method applies only for a finite set of girder configurations and does not consider loading at any elevation, it can often be inapplicable in design. Nevertheless, the method is summarized in Table 2-1, Equation 2-1 and Equation 2-2, where A represents a coefficient analogous to the equivalent moment factor, ω_2, and the parameter B, which is a function of the torsional parameter, W, accounts directly for the load height effect. In Equation 2-2, E is the elastic modulus of steel, G is the shear modulus, I_y is the moment of inertia about the weak axis, J is the St. Venant torsional constant, and C_w is the warping torsional constant.

Table 2-1: Load height adjustment coefficients by Nethercot and Rockey (1971)

Loading	A	B
	1.35	$1 - 0.180W^2 + 0.649W$
	1.12	$1 - 0.154W^2 + 0.535W$

$$\omega_2^* = AB, \text{ for bottom flange loading}$$
$$\omega_2^* = A, \text{ for shear centre loading} \qquad (2\text{-}1)$$
$$\omega_2^* = A/B, \text{ for top flange loading}$$

$$W = \frac{\pi}{L}\sqrt{\frac{EC_w}{GJ}} \qquad (2\text{-}2)$$

Ziemian (2010) presents Equation 2-3, which is based on the work of Nethercot and Rockey (1971) but developed and extended by Helwig et al. (1997):

$$\omega_2^* = \omega_2 \left(1.4^{\frac{2y}{h_0}} \right)$$ (2-3)

in which ω_2 is the equivalent moment factor, h_o is the distance between flange centroids, and y accounts for the load position that is positive for loading below the mid-height of the cross-section and negative for loading above. Helwig et al. (1997) found a constant factor of 1.4 to be a close approximation of the parameter B, defined by Nethercot and Rockey (1971), and extended their method to account for loading at any elevation within the cross-section height. Both the method of Nethercot and Rockey (1971) and Helwig et al. (1997) are proven to accurately and conservatively estimate the load effect; however, the estimations begin to break down when considering stocky sections and increasing end fixity (Wong et al. 2015).

Wong et al. (2015) investigated the load height effect and proposed an effective length method that consistently provides conservative results for various load cases and over a range of the torsional parameter. The torsional parameter, R, discussed by Wong et al. (2015), can be calculated as shown in Equation 2-4 and is analogous to the parameter W, used in the method by Nethercot and Rockey (1971). In this method, a designer can retrieve an effective length factor from a set of design curves based on the loading and torsional parameter of their beam, as shown in Figure 2-5.

$$R = L \sqrt{\frac{GJ}{EC_{\mathrm{w}}}}$$ (2-4)

CSA S16-19 adopted a simplified but conservative version of the method proposed by Wong et al. (2015) for doubly symmetric I-sections. For cases of top-flange loading, CSA S16-19 recommends using a moment gradient coefficient, ω_2, of 1.0, together with an effective length of 1.2L, where L is the unbraced length of the girder, for simply-supported members and 1.4L for all other cases of flexural end restraint when determining the elastic critical moment, M_u. However, a designer is given the option to assess the load height effect by more sophisticated and potentially less conservative methods from the literature.
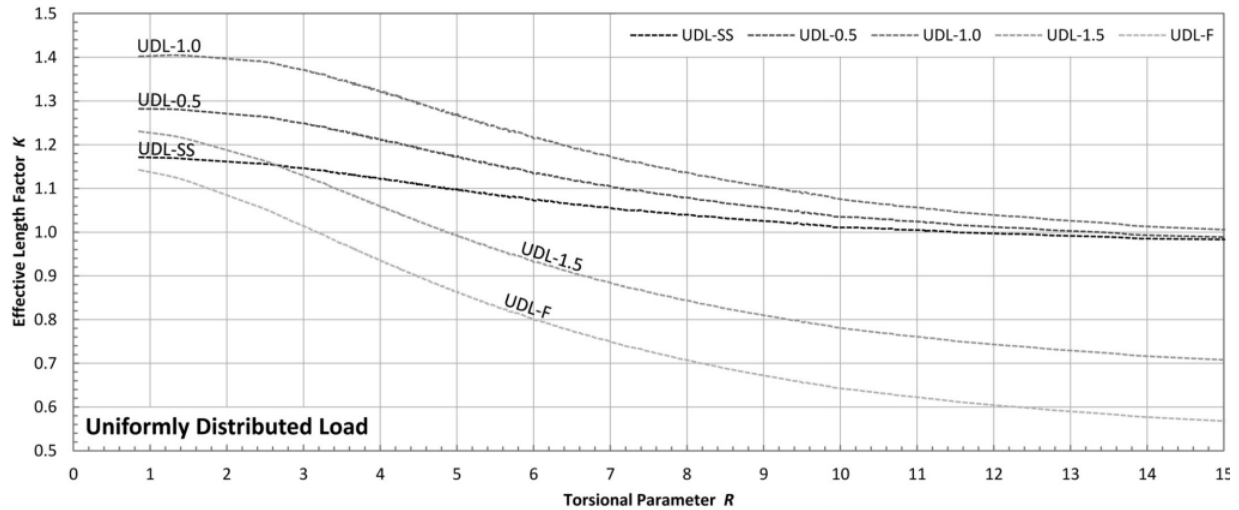
Figure 2-5: Effective length method of Wong et al. (2015) for uniformly distributed load

2.2   Lateral–Torsional Buckling Resistance of Welded Steel Girders

This section serves to summarize the extent of LTB research on welded girders to date. The literature reviews focus on the results and conclusions drawn from the experimental and numerical assessment of welded girders; however, in most cases, the studies in question analyzed rolled sections as well. The literature presented here covers some experimental testing fundamental to the Canadian design provisions, followed by several FE investigations assessing the influential parameters of LTB. The research is presented in chronological order and is organized by author.

2.2.1   Dibley (1969)

Dibley (1969) sought to verify and extend the prevailing design theories for laterally unsupported beams following the introduction of new high-strength steels into the British Standard. The study consisted of 30 experimental tests of rolled beams, with five unique geometries and a range of slenderness, where elastic, inelastic and plastic LTB failures were expected. The test program did not include welded girders; however, Baker and Kennedy (1984) used the test data to calibrate the resistance factors for laterally unsupported beams currently used in CSA S16-19. Since there is no distinction made in CSA S16-19 between rolled and welded girders, Dibley's (1969) test data is indirectly related to the design of welded steel girders in Canada.

The tested specimens were simply-supported, restrained against cross-section twist at the end conditions, but free to warp. Dibley (1969) tested the beams under four-point bending, developing

a uniform moment in the centre unbraced segment. The vertical, lateral and longitudinal displacements, as well as the in- and out-of-plane rotations, were recorded. Cross-section measurements of the flange thickness, flange width, and section depth were taken at four positions along the girder length and averaged, while the web thickness was recorded at both ends of the member and averaged. The initial deviations from straightness were captured by extension of a string-line between the beam ends and measuring the offset, and the residual stresses were collected by sectioning.

The magnitude and distribution of residual stresses in the sections were found to be similar to those of conventional steel grades, suggesting the effect of residual stresses may be less severe for higher grades of steel. Dibley (1969) concluded that the British specification's predictions matched closely with the achieved test capacities; however, he also noted that sections carrying partially plastic bending moments achieved higher buckling resistances than the anticipated design capacities. The findings of Dibley (1969), in the context of the present research, are less important than his contribution of experimental test data, including test moment resistances, initial geometric imperfections and residual stresses.

2.2.2   Fukumoto (1976)

Fukumoto (1976) completed an experimental investigation into the behaviour of high-strength, welded steel beams to assess the performance of the prevailing LTB design theory. The experimental program included 36 welded specimens, with 21 of those specimens being SM 50 grade steel, and 15 being HT 80 quenched and tempered steel. Of the 21 SM 50 specimens, nine were annealed, and of the 15 HT 80 specimens, three were annealed. The researcher does not detail the annealing process; however, it is stated that the annealing conditions were designed purposefully to relieve the welding residual stress. The end conditions consisted of torsional and flexural pin supports. The girders were subjected to two load configurations, a uniform bending moment and a moment gradient with an end-moment ratio of 0.5. Initial geometric imperfections were measured, and maximum values of $L/620$ and $L/435$ were reported for the initial compression flange sweep and initial tension flange sweep, respectively. Residual stresses were not measured. Instead, a comparison of the annealed result with the non-modified specimens illustrated the residual stresses' effects. Fukumoto (1976) found that by taking the ratio of annealed capacities to as-built capacities of the test specimens, on average, there was an increase in the moment

resistances of the annealed girders of 11% and 6% for SM 50 and HT 80 steel, respectively. Fukumoto (1976) concluded that welded girders are adversely affected by the welded residual stress patterns, and the influence of these patterns decreases with increasing yield strength.

2.2.3   *Fukumoto and Itoh (1981)*

A test program by Fukumoto and Itoh (1981) consisted of 34, 5 m-long welded steel girders fabricated using flame cut plates. The test specimens were cut into three sections for testing: a 1.8 m length (D series), a 2.6 m length (E series), and a stub section used to measure residual stresses. Test specimens were simply supported with end torsional restraint and unrestricted warping. A concentrated transverse load was applied at the mid-span through Lehigh-type gravitational load simulators (Yarimci et al. 1967). The cross-sectional dimensions and geometric properties were measured and reported as their mean-plus-standard-deviation. Similarly, the initial geometric imperfections and residual stresses were measured, where the mean magnitudes of initial geometric imperfections were reported, and the average residual stress patterns were plotted.

The coefficients of variation of initial out-of-straightness measured about the major and minor axes are 1.808 and 0.922, respectively; in comparison, for rolled sections tested by Fukumoto et al. (1980), the coefficients of variation are 1.84 and 0.66, respectively, which indicates that an increased scatter of minor-axis initial geometric imperfections is present in welded girders. The measured residual stresses feature peak values of tensile stress reaching near the yield stress at the web–flange junction and small compressive stresses present at the flange tips, as shown in Figure 2-6. A nondimensional residual stress parameter was defined by the researcher, which represents the average compressive residual stress normalized by the yield stress. The coefficients of variation of this parameter for the series D and E welded girders were reported as 0.120 and 0.466, respectively, while the counterpart rolled girders report coefficients of variation of 0.066 and 0.241. Higher compressive stresses and larger variations in compressive residual stresses are noted of welded beams.
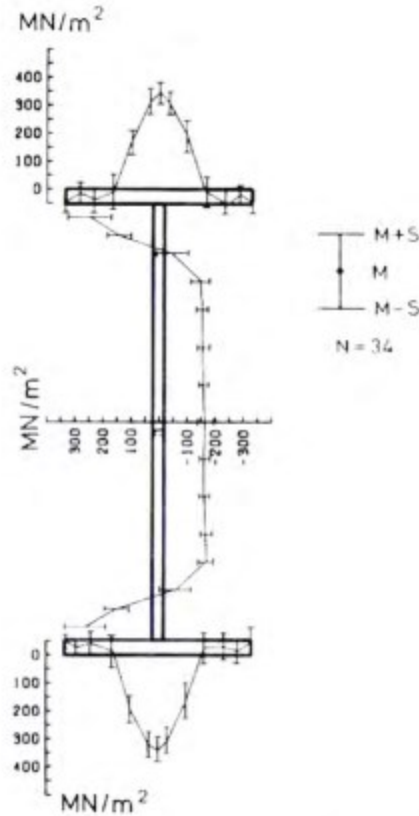
Figure 2-6: Mean residual stresses measured by Fukumoto and Itoh (1981)

To assess the influence of imperfections on the variation of strength, the researchers plotted the test capacities normalized by the plastic moment against parameters representing residual stresses and initial out-of-straightness, as shown in Figure 2-7. A statistical analysis was conducted to assess the effects of the defined residual stress parameter on the ultimate strength of the series E welded girders and the counterpart rolled girders of Fukumoto et al. (1980). Little correlation between the residual stress parameter and the normalized moment resistance was reported for both series. However, the mean residual stress parameter of the welded girders was reported 1.82 times larger than that of the rolled girders and is suggested to contribute to the observed lower mean normalized moment resistance reported for the series E welded girders. In a similar statistical analysis of the initial out-of-straightness and the normalized moment resistance, a reduction of the normalized moment resistance was observed in the welded girders, with the mean value of initial out-of-straightness being 4.38 times larger in welded girders than rolled; however, little correlation was found. Low correlation implies the relationship between the imperfections and the normalized moment resistance is unclear; it does not mean these parameters are uninfluential.
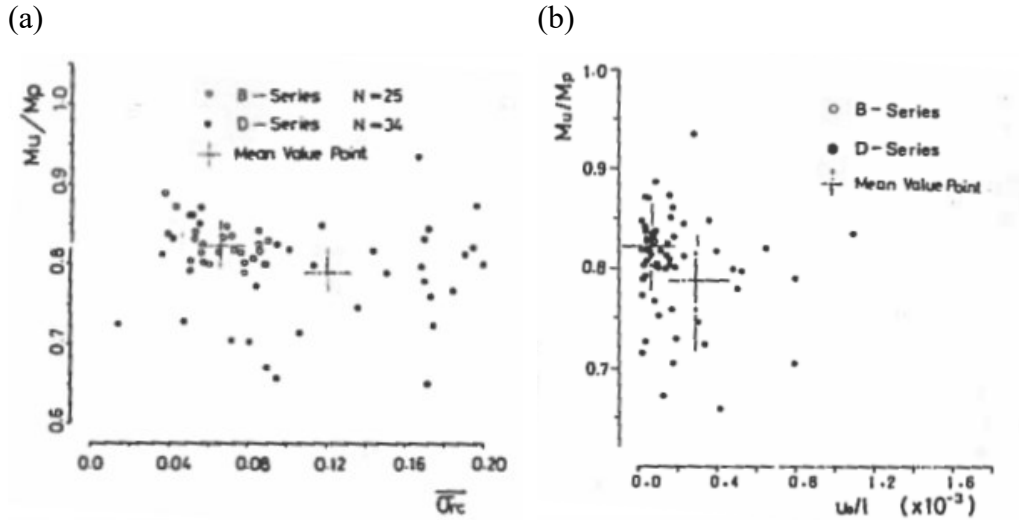
Figure 2-7: Test results of Fukumoto and Itoh (1981) plotted against (a) residual stress parameter and (b) initial out-of-straightness parameter

2.2.4 MacPhedran and Grondin (2011)

MacPhedran and Grondin (2011) examined the history of the LTB design equation specified in CSA S16-09 (CSA 2009), noting that the equation has remained relatively unchanged since 1974 and makes no distinction between welded and rolled girders. However, upon examination of test data from Greiner and Kaim (2001), the authors observed significant scatter and lower buckling capacities in the welded girders than in their counterpart, rolled sections. MacPhedran and Grondin (2011) proposed Equation 2-4, a unified equation that allows for a distinction between welded and rolled sections, to replace the three-part beam curve specified by CSA S16-09. The proposed equation uses a modified slenderness concept and is analogous to the column buckling equation of CSA S16-09.

$$M_n \; = \; M_B(1 + \lambda^{2n})^{-1/n} \text{ , where } \lambda = \sqrt{M_B/M_u} \qquad (2\text{-}4)$$

Where λ is a modified slenderness ratio, and M_B is the moment capacity of a section with full lateral restraint. M_B is set equal to the plastic moment, M_p, for Class 1 and 2 sections, or the yield moment, M_y, for Class 3 sections. The modifying parameter "n" is calibrated to account for variations of flexural strength due to imperfections and addresses the differences in moment capacities observed in the literature between welded and rolled sections.

17

The test data of Greiner and Kaim (2001) was used to calibrate the modifying parameter "*n*" for both rolled and welded girders. A data set totalling 215 tests, with 144 rolled shapes and 71 welded sections, was used. Upon analysis, the researchers found values of $n = 3.1$ and $n = 1.9$ for rolled and welded sections, respectively, to minimize the coefficient of variation between the proposed equation's predictions and the test data. Figure 2-8 plots the proposed equation using $n = 1.9$ and the CSA S16-01 (CSA 2001) beam design curve against the test data of the welded sections. It should be noted that there are no differences between the LTB equations of S16-01 and S16-09.
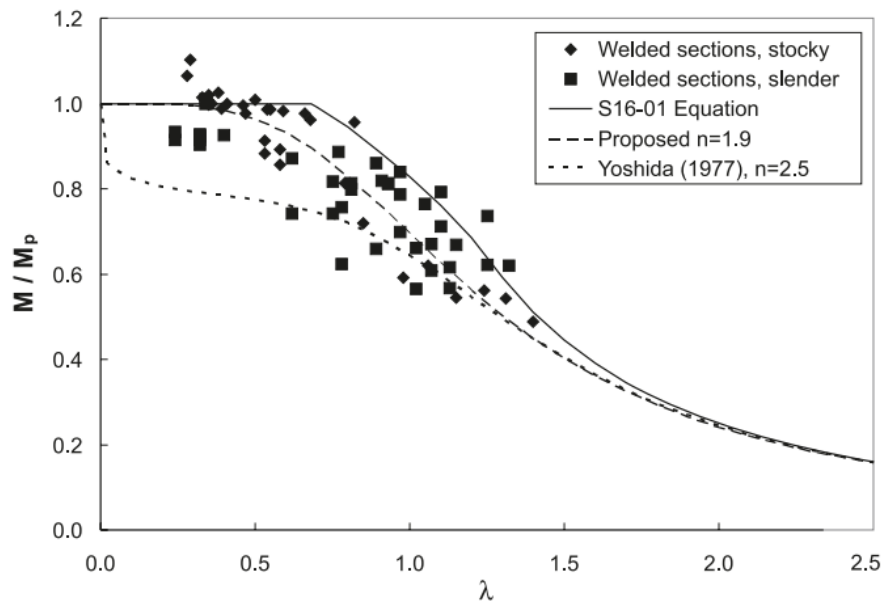
Figure 2-8 Comparison of welded test data to moment resistance predictions by CSA S16-01 and equation proposed by MacPhedran and Grondin (2011)

As shown in Figure 2-8, a significant scatter of test data is observed. Furthermore, it was found that CSA S16-01 over-predicts the flexural capacity of the welded sections in almost all cases. MacPhedran and Grondin (2011) performed a reliability analysis of the proposed equation considering Class 1 and 2 rolled and welded sections and a range of slenderness ratios up to $\lambda = 2.5$. For a resistance factor of 0.9, minimum reliability indices of 2.63 and 2.7 are obtained when using $n = 3.1$ and $n = 1.9$ for rolled and welded shapes, respectively. In comparison, analysis of the existing beam strength curve found reliability indices of 3.0 for rolled sections and 1.6 for welded sections when using a resistance factor of 0.9. Assuming that the target reliability index is 3.0, this study suggests that the CSA S16 provisions accurately and reliably predict the capacities of rolled sections but are over-predicting those of welded girders.

2.2.5   Subramanian and White (2017)

Subramanian and White (2017) observed that many numerical studies utilizing typical residual stress patterns and geometric imperfection modelling techniques tend to predict lower LTB capacities than equivalent experimental test results. Furthermore, the researchers note that the unified provisions of AISC 360-10 (AISC 2010) have been found to over-predict experimental test results. This "disconnect" between experimental tests and numerical simulations was a concern of the researchers due to the increasing reliance and general prevalence of numerical simulations in modern LTB studies. In an investigation of this disconnect, the authors manipulated the residual stress patterns and imperfections of an FE model in order to observe the sensitivity of predictions and achieve a good agreement between the FE predictions and experimental data.

The study features six tests that failed in the LTB mode under uniform bending. The data set contains four tests of rolled sections and two tests of welded girders. To simulate the experiments, the authors developed a FE model consisting of shell elements, an idealized tri-linear material model, with simple end supports in flexure and unrestricted warping. The residual stresses and initial geometric imperfections were varied to examine the accuracy of the FE model in estimating the experimental moment resistances. Two residual stress patterns were considered: Best-Fit Prawel (Kim 2010) and a pattern from Galambos and Ketter (1959). The former residual stress pattern is representative of lightweight welded sections, and the latter is a classical representation of a rolled member; regardless, both patterns are applied to the entire data set. The initial geometric imperfections considered ranged between $L/1000$ and $L/8000$, representing a range of geometric imperfection between the maximum allowable (by dimensional tolerances) and, effectively, zero imperfection. Results indicate that FE simulation utilizing half magnitudes of the two residual stress patterns and $L/2000$ geometric imperfections correlates well with the experimental data. The researchers suggest that these imperfections are an excellent choice for future FE studies regarding LTB.

A second sensitivity analysis was conducted, considering two rolled and welded sections but assessed under an expanded pool of residual stress patterns for the same range of imperfections. Additionally, flange tilt and web out-of-flatness imperfections are defined in the models for the welded girders. The load configuration and boundary conditions remain the same. The additional residual stress patterns also vary in magnitude and are assigned at one-quarter, one-half and full

amplitudes. The results of the second sensitivity analysis are presented in Figure 2-9. The figures highlight that the strength predictions are most sensitive to residual stresses and initial geometric imperfections within the inelastic regime. FE predictions utilizing the full magnitude Best-Fit Prawel pattern and $L/1000$ geometric imperfections resulted in capacities up to 28% lower than AISC Specification for Structural Steel Buildings ANSI/AISC 360-10 (AISC 2010) resistances. Observed are negligible differences in moment resistance between $L/4000$ and $L/8000$, however, the FEA predictions for these magnitudes of geometric imperfection are significantly higher than those for $L/2000$ and $L/1000$.

(a)   (b)
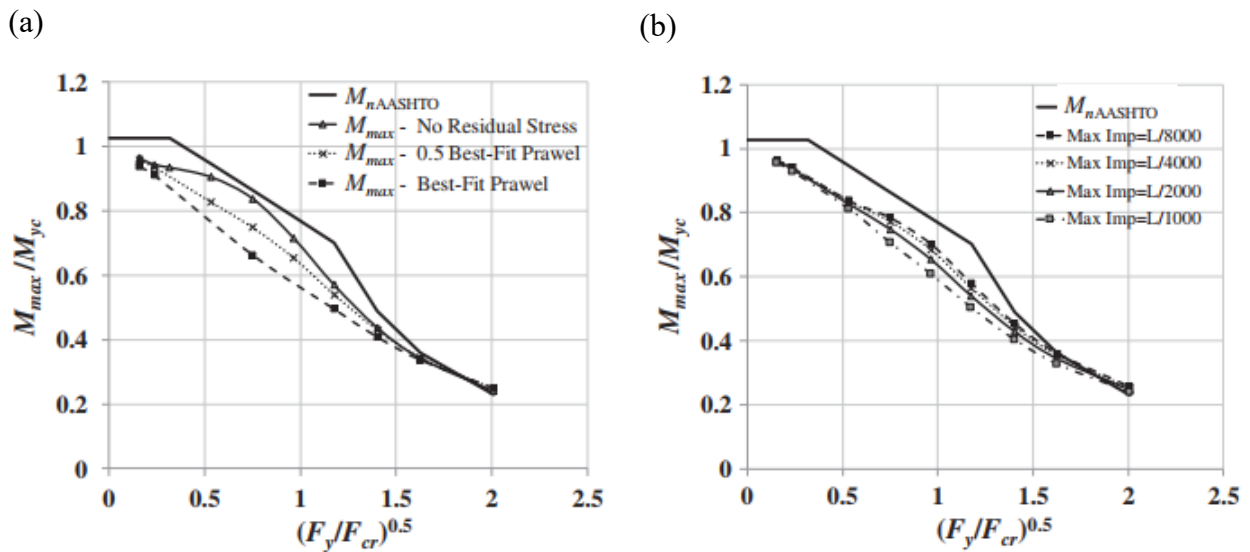
Figure 2-9: Lateral–torsional buckling curves for the variation of (a) Best-Fit Prawel residual stress pattern magnitude and (b) initial lateral sweep (Subramanian and White 2017)

The authors conclude, for welded girders, that using a maximum flange sweep of $L/2000$, one half the AWS (2010a) tolerances for flange tilt and web out-of-flatness, and one-half the Best-Fit Prawel residual stress pattern can achieve an appropriate prediction of the beam flexural resistance that is consistent with experimental test results. Furthermore, it is noted that combinations of residual stresses and initial geometric imperfections more severe than these produce numerical results not consistent with experimental test data. The proposed magnitudes of residual stress and initial geometric imperfections are additionally consistent with magnitudes often measured experimentally, which are typically less than the fabrication tolerances.

2.2.6   Kabir and Bhowmick (2018)

Kabir and Bhowmick's (2018) study was motivated by MacPhedran and Grondin's (2011) observation that the CSA S16-09 provisions may overestimate the flexural capacity of welded steel girders. An extensive FE study was performed, which included 416 girders, considering various cross-sections, member lengths, moment gradients, and load height. The prediction of flexural capacities by the Canadian steel design standard was assessed in comparison to the finite element analysis (FEA) results, as well as in comparison to the moment resistances obtained from the AISC 360-16 (AISC 2016) and Eurocode 3 (CEN 2005) provisions, as well as the equation proposed by MacPhedran and Grondin (2011).

A FE model is constructed and initially validated against the test results by Dibley (1969) and then by Fukumoto et al. (1980), Fukumoto and Itoh (1981) and Dux and Kitipornchai (1983). The FE model features shell elements, in-plane simple end supports, unrestricted warping, and additional constraints imposed on the web elements, based on the work of Dong and Sause (2009), to avoid localized web distortions at the beam ends. A mill plate residual stress pattern measured at Lehigh University and complied by Chernenko and Kennedy (1991) is applied. The initial geometric imperfections are superimposed and scaled to $L/1000$. Validation of the model found a mean test-to-predicted ratio of 1.037 with a coefficient of variation of 0.0485.

The researchers simulated ten unique geometries of varying lengths to achieve a distribution of slenderness suitable to capture plastic, inelastic and elastic responses. Section depths ranged between 700 mm to 1800 mm and did not include Class 3 sections. The FEA strength predictions are normalized by the plastic moment and plotted against a modified slenderness ratio, $\lambda = \sqrt{M_p/M_u}$, where M_u is the elastic LTB moment and M_p the plastic moment. Figure 2-10 shows the FEA results under uniform bending, plotted in comparison to the test results and code predictions. Observed are over-predictions of beam flexural capacity by CSA S16-14 throughout the entire inelastic range and a worst-case over-prediction of 37%. However, the FEA predictions of the response within the elastic range match the predictions of CSA S16-14 closely. In comparison, the Eurocode performs quite well over the entire inelastic region, while the proposed equation by MacPhedran and Grondin (2011) over-predicts the inelastic capacities but performs better in comparison to the CSA S16-14 prediction.
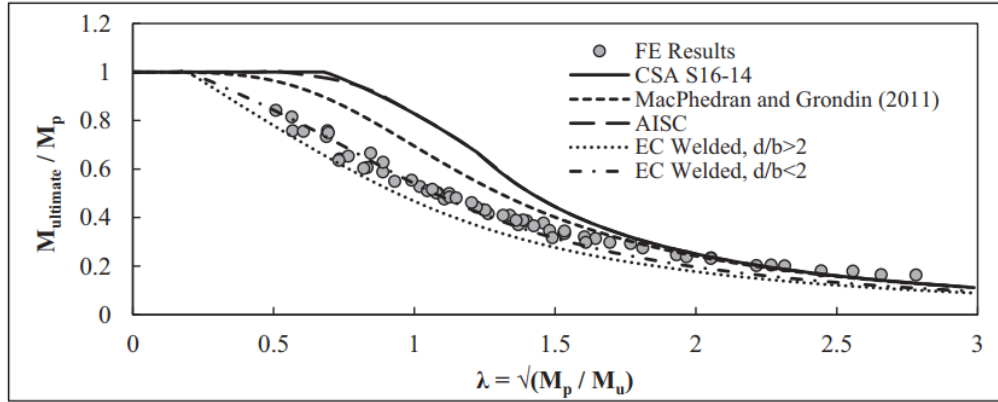
Figure 2-10: Finite element analysis results for a uniform moment by Kabir and Bhowmick (2018)

For cases of linear moment gradients, the study showed that CSA S16-14 suitably predicts the beam flexural capacity in the elastic range; however, the LTB capacity of beams in the inelastic range is significantly over-predicted by CSA S16-14. Under transverse loads, CSA S16-14 predicts reasonably well when the load is applied at the shear centre; however, the flexural capacity is over-predicted when the load is applied on the top flange with a maximum over-prediction of 17% and 33% for concentrated and distributed loading, respectively. As the cases of distributed transverse load are relevant to this study, Figure 2-11 and Figure 2-12 are provided and contain the results of the model predictions for a uniformly distributed load at the shear centre and top flange, respectively. Observed is a scatter of the FEA results in the inelastic region at either load height and over-predictions of the numerical results by CSA S16-14. The EC3 predictions are quite conservative and under-predict the FEA results in almost all cases, with the exception of a few girders with top-flange loading buckling in the inelastic region. Finally, MacPhedran and Grondin's (2011) proposed equation is slightly conservative for cases of uniformly distributed load; however, it performs better in comparison to CSA S16-14 within the inelastic region and for cases of top flange loading.
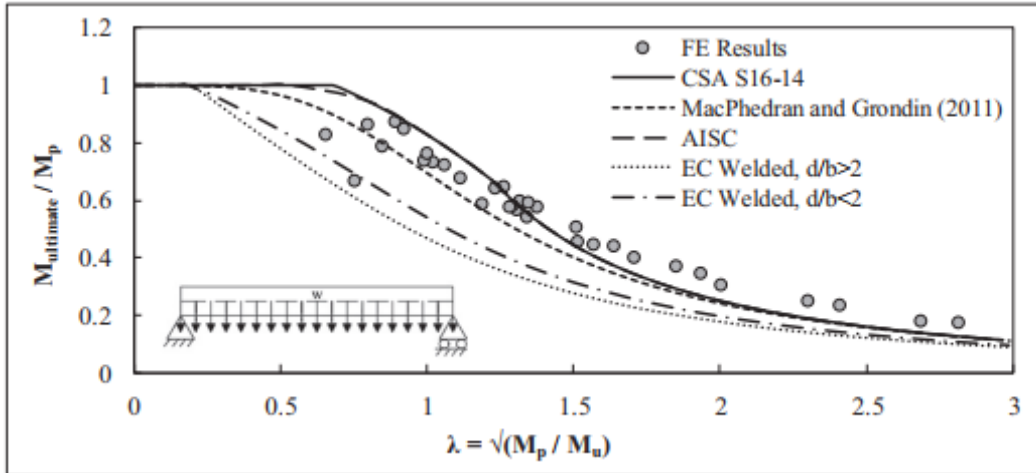
Figure 2-11: Finite element analysis results for a uniformly distributed load applied at the shear centre (Kabir and Bhowmick 2018)
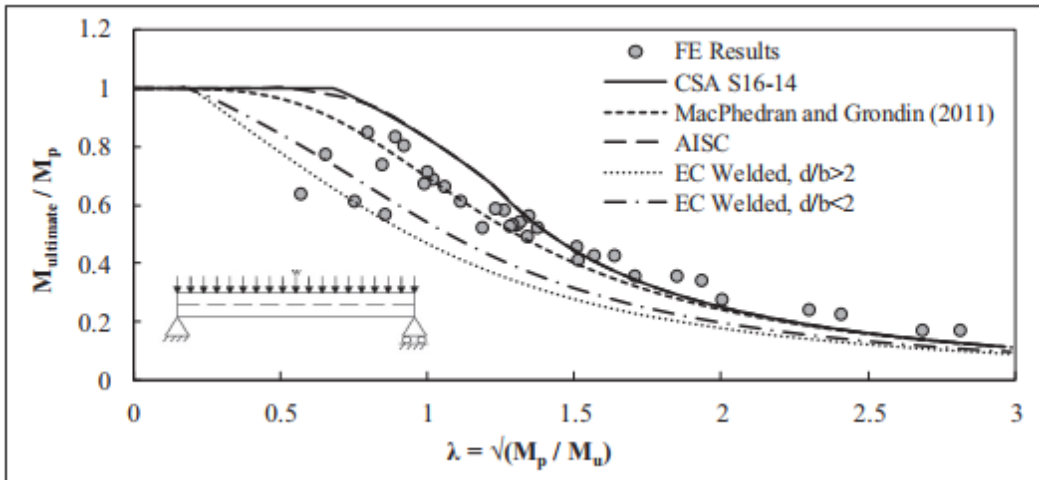
Figure 2-12: Finite element analysis results for a uniformly distributed load applied at the top flange (Kabir and Bhowmick 2018)

2.3   Review of Design Standards for Prediction of Flexural Resistance

The following is a review of three steel design standards and their provisions to determine the flexural resistance of doubly symmetric I-sections. CSA S16-19 is presented first, with the understanding that the assessment of its performance is the primary objective of this study. The Canadian highway bridge design standard, CSA S6-19, specifies identical LTB provisions and is not reviewed here; however, in general, discussion or findings regarding CSA S16-19 apply to CSA S6-19. AISC 360-16 and EC3 provisions are then presented.

2.3.1 CSA S16-19

The Canadian steel design standard prescribes a three-part strength curve to obtain the flexural resistance of doubly symmetric Class 1, 2 and 3 sections. The calculated resistance is a function of the elastic LTB capacity, plastic moment capacity, and slenderness. If the compression flange of the beam is laterally supported along its full-length, the section is expected to fail in the plastic range, and the moment resistances for a Class 1 or 2 section can be determined using Equation 2-5.

$$M_r = \phi M_p = \phi F_y Z_x \tag{2-5}$$

M_r is the factored moment resistance, ϕ is the resistance factor, F_y is the nominal yield stress of the material, and Z_x is the plastic section modulus about the strong axis. However, if full lateral restraint is not provided, LTB will govern the design either in the elastic or inelastic range. The critical elastic LTB moment, M_u is calculated as follows:

$$M_u = \frac{\omega_2 \pi}{L} \sqrt{E I_y G J + \left(\frac{\pi E}{L}\right)^2 I_y C_w} \tag{2-6}$$

where ω_2 is the equivalent moment factor, which is a function of the applied moment gradient and can be determined as follows:

$$\omega_2 = \frac{4 M_{max}}{\sqrt{M_{max}^2 + M_a^2 + M_b^2 + M_c^2}} < 2.5 \tag{2-7}$$

M_{max} is the maximum factored bending moment magnitude in the unbraced segment, M_a, M_b, and M_c are the factored bending moments at the one-quarter point, mid-point and three-quarter point locations of the unbraced segment, respectively. The factored moment resistance of the member is computed using Equations 2-8 and 2-9 depending on whether the member is governed by elastic or inelastic LTB:

If $M_u > 0.67 M_p$, the member fails in inelastic LTB:

$$M_r = 1.15 \phi M_p \left[1 - \frac{0.28 M_p}{M_u}\right] \leq \phi M_p \tag{2-8}$$

Otherwise, if $M_u < 0.67 M_p$, the elastic LTB mode controls the moment capacity of the beam:

$$M_r = \phi M_u \tag{2-9}$$

For Class 3 sections, the plastic moment capacity, M_p, is replaced in Equations 2-5 and 2-8 by the elastic moment capacity, M_y, as well as when assessing whether the member is governed by elastic or inelastic LTB, where M_y is determined as the product of the material yield stress, F_y, and the strong-axis elastic section modulus, S_x.

2.3.2 AISC 360-16

The design of doubly symmetric compact sections given in Section F2 of AISC 360-16 is presented here. Compact sections consist of plate elements that meet the limiting width-to-thickness ratio λ_p and are functionally equivalent to the Class 1 and 2 sections of CSA S16-19. AISC 360 prescribes similar LTB provisions to those of CSA S16 but differ slightly in the formulation. A three-part beam curve defines the behaviour of doubly symmetric I-shaped members; however, it is delineated by limiting plastic and elastic unbraced lengths, as opposed to strength. The nominal flexural strength, M_n, is determined as follows:

$$M_n = M_p = F_y Z_x, \quad \text{when } L_b < L_p \tag{2-10}$$

$$M_n = C_b \left[M_p - (M_p - 0.7 F_y S_x) \left(\frac{L_b - L_r}{L_r - L_p} \right) \right], \quad \text{when } L_p < L_b < L_r \tag{2-11}$$

$$M_n = F_{cr} S_x, \quad \text{when } L_b > L_r \tag{2-12}$$

L_b is the length between the lateral bracing points of the compression flange. L_p is the limiting laterally unbraced length for the limit state of yielding. L_r is the limiting laterally unbraced length for the limit state of inelastic LTB and marks the transition from inelastic LTB to elastic LTB. When $L_b < L_p$, LTB does not apply, and the section develops its full cross-sectional moment capacity, M_p. When $L_p < L_b < L_r$, inelastic LTB governs the beam's flexural strength, and when $L_b > L_r$, the section fails by elastic LTB. The limiting unbraced lengths are calculated as follows:

$$L_p = 1.76 r_y \sqrt{\frac{E}{F_y}} \tag{2-13}$$

$$L_{\mathrm{r}} = 1.95 r_{\mathrm{ts}} \frac{E}{0.7F_{\mathrm{y}}} \sqrt{\frac{Jc}{S_{\mathrm{x}}h_{\mathrm{o}}} + \sqrt{\left(\frac{Jc}{S_{\mathrm{x}}h_{\mathrm{o}}}\right)^2 + 6.76\left(\frac{0.7F_{\mathrm{y}}}{E}\right)^2}} \qquad (2\text{-}14)$$

in which r_{y} is the radius of gyration about the y-axis, r_{ts} is the effective radius of gyration, J is the torsional constant, h_{o} is the distance between flange centroids, and for doubly symmetric sections, the coefficient c is taken as 1.0. F_{cr} represents the elastic buckling stress, and can be determined as follows:

$$F_{\mathrm{cr}} = \frac{C_{\mathrm{b}}\pi^2 E}{\left(\frac{L_{\mathrm{b}}}{r_{\mathrm{ts}}}\right)^2} \sqrt{1 + 0.078 \frac{Jc}{S_{\mathrm{x}}h_{\mathrm{o}}}\left(\frac{L_{\mathrm{b}}}{r_{\mathrm{ts}}}\right)^2} \qquad (2\text{-}15)$$

where C_{b} is the LTB modification factor for non-uniform bending moments, analogous to ω_2 of CSA S16:

$$C_b = \frac{12.5 M_{\max}}{2.5 M_{\max} + 3 M_{\mathrm{a}} + 4 M_{\mathrm{b}} + 3 M_{\mathrm{c}}} \qquad (2\text{-}16)$$

2.3.3   European Steel Design Standard EC3

The Eurocode 3 (EC3) provisions differ from those of the Canadian and American standards. Rather than the three-part buckling curves of the North American standards, EC3 is based on the Perry-Robertson equation and specifies multiple strength curves depending on the fabrication method and cross-sectional geometry (MacPhedran and Grondin 2011). The design of rolled or equivalent welded I-shaped members differs from the provisions for non-specific cross-sections in EC3. Presented here are the provisions of EC3 that are pertinent to the design of welded girders. For members without continuous lateral restraint in the compression flange, the design buckling resistance can be determined using Equation 2-17.

$$M_{\mathrm{b,Rd}} = \chi_{\mathrm{LT}} W_{\mathrm{y}} \frac{f_{\mathrm{y}}}{\gamma_{\mathrm{M1}}} \qquad (2\text{-}17)$$

26

where W_y is the appropriate section modulus depending on the section class, γ_{M1} is a limit states factor equal to 1.0 and χ_{LT} is the reduction factor for LTB, which is a function of slenderness and imperfections and is calculated as follows:

$$\chi_{LT} = \frac{1}{\varphi_{LT} + \sqrt{\varphi_{LT}^2 - \beta\bar{\lambda}_{LT}^2}}, \; \chi_{LT} \leq 1.0 \tag{2-18}$$

$$\varphi_{LT} = 0.5\left[1 + \alpha_{LT}(\bar{\lambda}_{LT} - \bar{\lambda}_{LT,0}) + \beta\bar{\lambda}_{LT}^2\right] \tag{2-19}$$

$$\bar{\lambda}_{LT} = \sqrt{\frac{W_y F_y}{M_{cr}}} \tag{2-20}$$

φ_{LT} is a value used to calculate χ_{LT}, $\bar{\lambda}_{LT}$ is the nondimensional slenderness for LTB, $\bar{\lambda}_{LT,0}$ is the plateau length of the LTB curves for rolled and welded sections, and β is a correction factor. For welded sections, a maximum value of $\bar{\lambda}_{LT,0} = 0.4$ and a minimum value of $\beta = 0.75$ are recommended. For the general design case, these factors are 0.2 and 1.0, respectively. The imperfection factor, α_{LT}, is explicitly defined in the standard by imposing a distinction in flexural strength between welded and rolled sections, as well as for section aspect ratios (d/b), where d is the section depth and b is the flange width. Tables 2-2 and 2-3 summarize the specifications for selecting the appropriate buckling curve and the imperfection factor, respectively.

Table 2-2: Selection of lateral−torsional buckling curves in EC3

Cross-Section	Limits	Buckling Curve
Rolled I-sections	d/b < 2	b
	d/b > 2	c
Welded I-sections	d/b < 2	c
	d/b > 2	d

Table 2-3: Imperfection factors for lateral−torsional buckling curves in EC3

Buckling Curve	a	b	c	d
Imperfection Factor α_{LT}	0.21	0.34	0.49	0.76

The elastic critical moment for LTB, M_{cr}, is not explicitly given in EC3. Instead, designers are free to determine M_{cr} by an appropriate method of the designer's choice. However, the designer must take into account the actual loading conditions, real moment distribution and lateral restraint.

2.4 Heat-straightening Techniques

Heat-straightening is a method of correcting curvature and local distortions of steel members resulting from various loading events, impacts or fabrication. Damages incurred during construction or collision events with bridge girders are examples of common motivations for the specification of a heat-straightening repair. Heat-straightening differs from heat curving, or other hot working techniques, as the latter is typically performed in controlled environments and on undamaged members, whereas, heat-straightening typically occurs in the field, on damaged members that present with significant yielding and plastic deformations. It is a process of controlled, sequential heating, typically in a specific pattern. Until recently, the scholarship of heat-straightening focused primarily on qualitative assessments and investigations of fieldwork. The practice is rarely specified by structural engineers and widely considered a skill of practitioners rather than a science. However, more focused research has culminated in many quantitative assessments investigating the factors affecting heat-straightening, including temperature effects, residual stresses and material properties.

2.4.1 Fundamental Concepts in Application of Heat-straightening

Heat-straightening utilizes thermal expansion and contraction rather than mechanical loading to impart desired deformations or curvatures. Straightening works by controlling and targeting favourable deformations by the skilled manipulation of material upsetting and plastic flow that occur as a result of thermal expansion and contraction. Figure 2-13 schematically depicts this upsetting effect and a resulting change in the geometric configuration. This simplified case demonstrates the basic principles of heat-straightening. Through many controlled cycles, the bar

may be shortened significantly. However, in a practical case, the damage will be complex and require a targeted heat straightening procedure to achieve the desired geometric configuration.
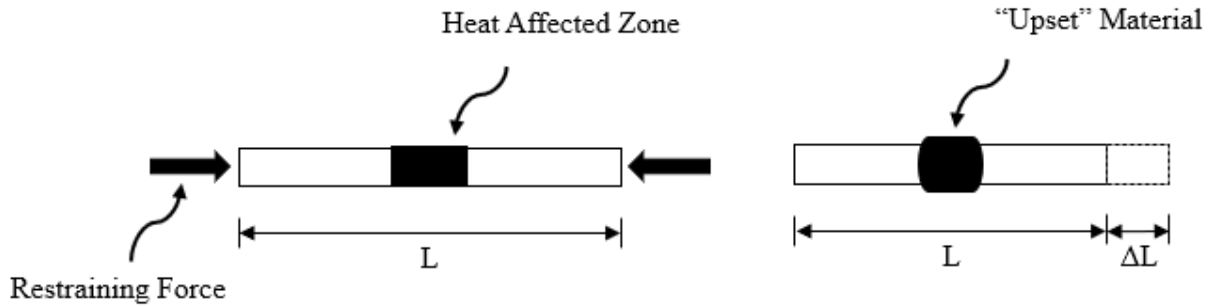
Figure 2-13: Schematic depiction of material shortening under heat application and removal

The development of an adequate heat sequence requires the identification of damage, selection of an appropriate heating pattern, the specification of temperature controls, the application of external load and cooling requirements. Common damage types include strong- and weak-axis flexural yielding, torsional yielding, and local distortions. Fundamental heating patterns include Vee heats, line heats, edge heats and spot heats, with the Vee heat being most commonly utilized (FHWA 2008). The fundamental patterns are associated with the correction of specific damage types. For example, Vee heats are specified to repair strong- and weak-axis flexural yielding observed in I-shaped members or plates, whereas local distortions require targeted spot heating. Care is taken by the engineer when developing a heat-straightening procedure to ensure an appropriate heating pattern or sequence of patterns is selected to address complicated damages. Figures 2-14 and 2-15, respectively, depict strong-axis damage of an I-shaped beam and associated heating patterns that would be specified to address the damage.

Figure 2-14: Flexural yielding at the mid-span of a beam under strong-axis bending
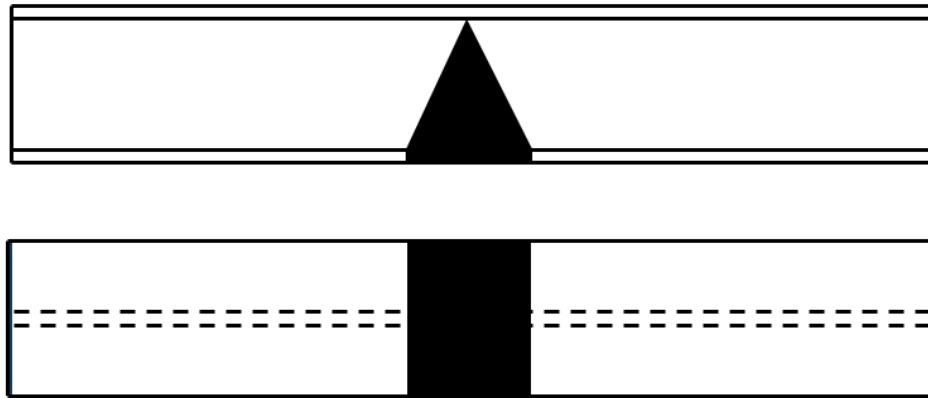
Figure 2-15: Schematic depiction of a typical heating pattern specified for repair of strong-axis damage

A Vee heat is used to correct undesirable curvatures, primarily through contraction of the longitudinal fibres during cooling. As the Vee cools, the open end sees longitudinal contractions at a distance from the neutral axis. The differential contraction of fibres through the depth of the Vee imparts a curvature into the member. In repair, the practitioner would apply the heating pattern such that the induced curvature opposes the existing damage. In Figure 2-15, closure of the Vee would impart an upwards curvature within the member upon cooling, opposing the damages shown by Figure 2-14. In this instance, a strip heat is applied simultaneously to the flange adjoining the open end of the Vee to relax the restraining effect imposed by the flange material. Figure 2-16 depicts the stages of movement expected during a Vee heat. The specimen will initially upset due to the expansion of fibres above the neutral axis and then move downwards due to the expansion of the fibres below the neutral axis. Finally, as the material cools, the fibres contract to a greater degree than the expansion due to heating, which results in a net contraction, and uplift of the specimen.
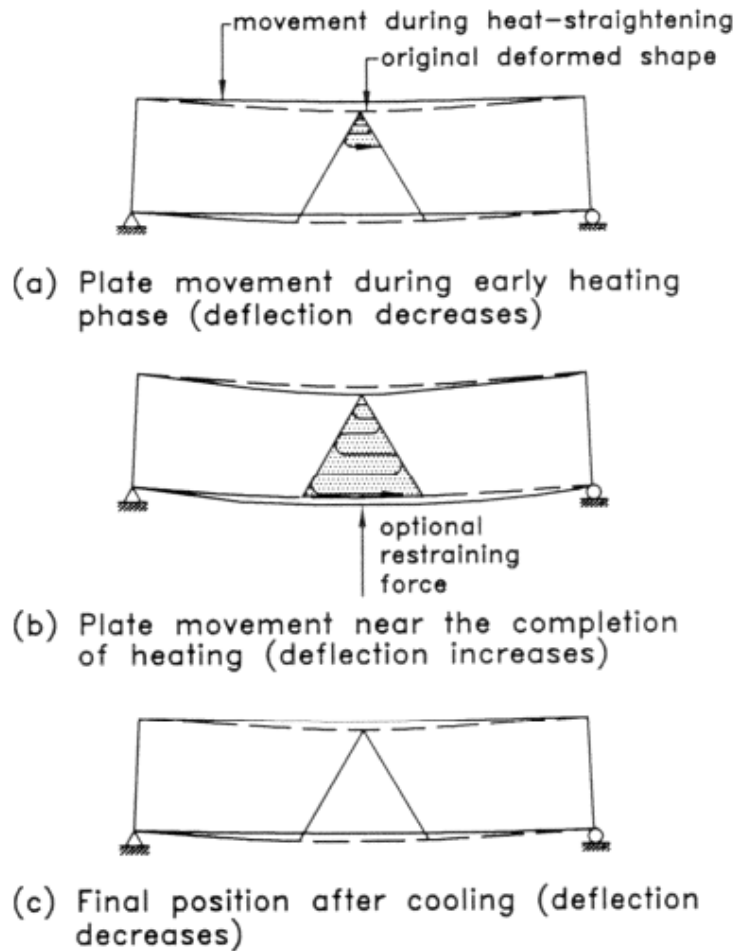
Figure 2-16: Stages of movement during a Vee heat (FHWA 2008)

A major concern when performing the procedure is temperature control, as improper heating of the material will introduce undesirable material effects and residual stresses. The speed, intensity, type of flame and torch size will all affect the practitioner's ability to maintain a specified temperature. The upper limit of heat noted by Avent et al. (2000) is 700°C and represents the lower phase transition temperature of high-strength steels. Temperatures above this alter the molecular structure, compromise behaviour, reduce ductility, and increase sensitivity to brittle fracture. Similarly, rapid cooling of the material may introduce brittle behaviours, and so it is best practice to allow a specimen to cool to at most 315°C before accelerating the cooling process (FHWA 2008)

External restraining forces may be applied to assist in the straightening process and may be critical in attaining the desired movement in as few cycles as possible. Often this is achieved through the specification of external jacking forces prior to heating of the specimen. However, the jacking

force must be calculated and the jacks properly gauged to ensure that the specimen is not over-stressed. Otherwise, under significant strain, the specimen may yield under elevated temperatures, over-correct, or even fracture (FHWA 2008). If yielding occurs, the process strays towards what is commonly called hot-working and not heat-straightening. Heat-straightening relies on the plastic material flow of thermal expansion and contraction to induce movement and not movement resulting from the material's yielding. Thus, engineers specifying external restraining forces in their heat sequence should perform a thorough structural analysis of the limiting force to avoid yielding.

2.4.2   Roeder (1986)

Structural engineers rarely specify heat-straightening, despite being economical, due to a fundamental lack of understanding. To address this, Roeder (1986) investigated the commonly accepted heat-straightening methods experimentally as a means to identify influential parameters, which led to a practical set of guidelines. The experimental program totalled 80 specimens, split into two series: 68 individual steel plates in series A and 12 wide-flange sections in series B. The steel plates of the first series are subjected to varied heating techniques, geometry and applied loading to identify how each of these techniques influenced the specimen's movement. Series B specimens serve to assess the extension of the techniques from plates to composite members and identify the influence adjacent cross-sectional components, such as the web of an I-shape member, have on the specimen's movement. Of the 12 series B specimens, six are subject to service levels of axial compression.

Experienced technicians performed the heat-straightening procedure using oxy-acetylene torches. The steel temperatures were measured by indicating crayons, thermocouples and non-contact thermometers. An equally spaced grid of steel pins was affixed to the heat-affected area, whereby the pin's local movements provided a measure of the specimen's deformation. The operator's technique and methods of applying heat to the specimens were recorded. The study concluded that small differences in style between operators, such as the operators preferred torch height and travel speed, can be attributed to small variances in the test data. The practitioners used visual cues to judge temperatures; among operators, misjudgments of +/- 40ºC were observed.

The results of the series A experiments indicated that a relationship exists between the temperature and the magnitude of permanent (plastic) deformation exhibited by the specimens. Plastic deformations were not observed for temperatures lower than 315ºC, and above 315ºC, the plastic deformations of the specimens were observed to increase steadily with increasing temperature. During heating, the specimens were observed to displace opposite to the final displacement direction initially. After cooling, thermal contraction shortened the member, bringing the specimen to its final deformed configuration. When subjected to bending during a heating cycle, the measured plastic deformations increased, specifically under bending, which produced flexural compression within the heat-affected zone. Quenching of the steel and manipulations of the cooling rate were found to increase the measured plastic deformations, between 20% to 80%, depending on the time delay to quenching from when the desired steel temperatures were achieved and the quantity of heat removed. Variations of the heat-affected zone's geometry, such as variations of the Vee depth or angle, resulted in increased plastic deformations, albeit with diminishing returns. Finally, the researchers observed significant, undesirable, out-of-plane deformations for large Vee's encompassing nearly the full section depth and wide angles.

Vee heats were applied to the flanges of series B specimens. This heating pattern is commonly used to repair flexural damages associated with LTB or to repair lateral deviations from straightness. When compared to similarly-dimensioned series A plates, the flanges of the wide-flange members exhibited reduced plastic deformations. The restraint imposed by the unheated web and opposite flange reduced the development of plastic deformations by 25% to 30%. Six of the series B specimens were axially loaded between 40% to 80% of the allowable service load and heated. These columns showed no indications of local buckling, and the researchers suggest that heat-straightening can be performed on members at service loads. Columns loaded with relatively high axial loads (80% of the service load) exhibited more plastic deformation than columns loaded with relatively low axial loads (50% of the service load). Secondary moments arising from P-Δ effects are observed to reduce the plastic deformations of the specimens. A reduced stiffness due to the P-Δ effects led to increased initial deflections opposite to the direction of the final displacements (direction of contraction), reducing the difference between the specimen's final and initial geometric configuration. The researchers suggested that given the influence of P-Δ on the plastic deformations, applying a lateral load to the specimens to resist the initial (opposing) deformations would significantly increase the plastic deformations.

Overall, the results of the study suggest that temperature, the heating pattern, and the geometry of the heat-affected zone are the most influential parameters. In practice, the researchers suggest using small Vee angles for larger depths to reduce the potential for developing out-of-plane distortions. The temperature should be carefully controlled with anticipation of variance by practitioners. Furthermore, the heat should be applied consistently, such that the through-thickness thermal gradient is minimized and the in-plane thermal gradient is maximized. A through-thickness thermal gradient promotes out-of-plane distortion of the plate, which is undesirable. Applied compressive stress by in-plane bending can increase efficiency and reduce the number of heating cycles required to achieve the desired movement. Members under service loads may be repaired by heat-straightening, but the effects of performing heat-straightening under service loads are not fully understood.

2.4.3   *Avent et al. (2000)*

Avent et al. (2000) reported the results of a study in which structural members were damaged and wholly repaired to clarify the effect of heat-straightening on material properties. The specimens were heated and repaired cyclically. Experiments include the testing of undamaged plates, damaged plates, and wide-flange members damaged about their minor axis. The results of tensile, Charpy V-notch, and Rockwell hardness tests are reported, indicating that the material properties, including yield stress, tensile strength, modulus of elasticity, and percent elongation (ductility), were subject to change during heat-straightening. However, the magnitude varies per number of cycles, type of damage, and type of specimen.

Tensile tests indicate increases in the yield stress within the heat-affected zone and significant increases near the apex of the Vees. Cycles of repair and damage directly influence the tensile response. Considering cycles of 2 or fewer, wide-flange members show increases in yield strength ranging between 9% and 21%, with an average increase of 13%. The percent elongation decreases on average by a third, and the modulus of elasticity is reduced by 8% to 23%. For cycles of 4 or more, more substantial increases in yield strength are reported in the heated areas, accompanied by considerable reductions in elongation and the modulus of elasticity. The researchers suggest limiting heat cycles to 2, where only modest changes in material properties are observed, to avoid developing the brittle behaviours associated with a large number of cycles. It is additionally noted that the extent of damage before the repair will not influence the resulting material properties.

Members exhibiting damages with strains exceeding 100 times the yield strain, a metric which signifies extensive damage, were successfully repaired and reported similar changes in ductility and the modulus of elasticity as lightly damaged specimens.

2.4.4   Avent et al. (2001)

The residual stress effects of heat-straightening are addressed by Avent et al. (2001). Residual stresses are formed and localized to the heat-affected zones of straightened members in a manner analogous to the residual stress development during production and fabrication. By extension, the resulting residual stresses may affect the performance of repaired members in a manner analogous to the differences between rolled and welded sections. The residual stress development is reported in steel plates, angles, channels, and rolled wide-flange sections for varying heating patterns, geometries, cycles and types of damage. Furthermore, some specimens are repaired and damaged several times. The residual stresses are measured by the method of sectioning and are taken at the centre of damage.

Residual stresses measured from plates subject to variations of Vee geometries indicate that the depth and angle of the Vee have little influence on the resulting residual stress pattern. When subject to multiple heat cycles, it was found that repeated heat cycles tended to result in lower magnitudes of residual stress. The testing of I-shaped members included a single unheated specimen, eight undamaged specimens, four specimens bent about their weak-axis, and a single specimen bent about its strong-axis. The undamaged but heated specimens exhibited larger magnitudes of residual stress than the damaged specimens, for the same heating patterns and Vee geometry. Peak values of residual stress at, or near, the material's yield stress was measured in both damaged and undamaged members. Variations of the heat-affected zone's geometry minimally influenced the resulting residual stress pattern of the I-shaped members. The resulting residual stresses showed little sensitivity to the magnitude of external bending utilized in repair.

Distinct residual stress patterns develop between cases of strong- and weak-axis damage. Figure 2-17 presents the residual stress measurements for cases of (a) strong-axis damage and (b) weak-axis damage. The two damage types utilize inverse heating patterns. Strong-axis damage requires Vee heats applied about the web and strip heats in the flanges, whereas weak-axis damage requires the opposite. In the case of strong-axis damage, compressive stresses approaching the

yield stress developed in the flange, with tensile residual stresses developing through the web. For weak-axis damage, tensile stresses nearing the yield stress developed in the flanges, and compressive stresses developed within the web. Multiple cycles of heating appeared to have a negligible effect on residual stress development. However, small differences in the residual stress magnitude are observed among cycles of 2, 4 and 8.
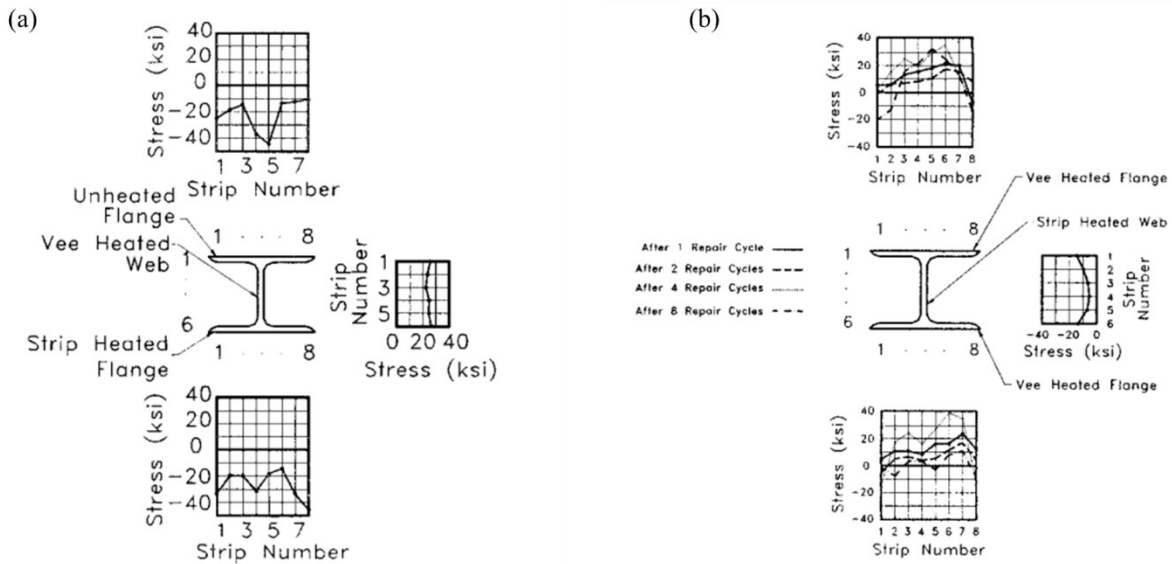
Figure 2-17: Measured residual stresses after repair of (a) strong-axis damage and (b) weak-axis damage (Avent et al. 2001)

This study concluded that the residual stresses of heat-straightened I-shaped members can approach the yield stress of the material. Instances of large compressive stresses developing in the flange tips of a member may influence the buckling behaviour, similar to the differences in bucking behaviour observed between rolled and welded sections. If a designer evaluates the buckling resistance of a heat-straightened member by North American standards, no moment capacity reduction would be assumed. However, if the Eurocode methodology is applied, a difference between capacities due to residual stresses can be applied. The authors suggest consideration of assessment under lower buckling curves.

2.4.5 Review of Design Standards

Specifications for heat-straightening procedures are limited in steel design standards; however, welding codes provide general rules and limitations. In Canada, CSA W59-18, the standard governing welded steel construction, specifies methods of heat-straightening for the repair of

distorted steel elements provided the maximum temperature, as measured by approved methods, does not exceed 590ºC for quenched and tempered steels or 650ºC for all other steels. However, the extent to which the member can carry the loads at the elevated temperature shall be assessed. A stress analysis shall be conducted and include all stresses induced through restraint while heating, as well as consider all in-situ service loads. The development of a straightening procedure is unspecified, and the practice of heat-straightening is subject to the judgment of the supervising engineer.

Heat-straightening specifications in American standards are slightly more extensive, with provisions found in the structural steel welding code AWS D1.1 (AWS 2020), bridge welding code AWS D1.5 (AWS 2015), and the guide for strengthening and repairing existing structures, AWS D1.7 (AWS 2010b). However, the American provisions are largely the same as the Canadian provisions. Temperatures must be limited to 600ºC, the member should be substantially free from stress, and the extent to which the member can carry the load at an elevated temperature shall be determined. AWS D1.1 discusses the metallurgical effects of heat-straightening and provides references to standard heat-straightening practices, while AWS D1.7 provides extra guidance regarding quality control of the heat-straightening procedure, specifying requirements to identify cracking, to ensure the member is free to contract, limiting tensile stresses from developing during heating, and prohibiting rapid cooling above 320ºC.

2.5   Summary

Formal LTB research dates to the 1960s, and since then, studies investigating the influence of slenderness, load configurations, imperfections and residual stresses have been extensive. The experimental studies presented in this report summarize a large extent of the testing conducted on welded steel girders, specifically. The general conclusions of the experimental testing indicate that welded steel girders exhibit reduced moment resistances in comparison to their rolled counterparts, which is attributed to differences in initial geometric imperfection and residual stress. FE studies suggest that the LTB provisions of CSA S16-19 for welded steel girders may be inadequate, particularly when estimating the inelastic LTB capacity. However, these FE studies tend to employ severe assumptions regarding the initial geometric imperfections and residual stresses, of which there is a fundamental lack of recent experimental data. The current understandings of the initial geometric imperfections and residual stresses of modern welded steel girders are insufficient.

Without further experimental testing and FE studies, the performance of the CSA S16-19 provisions for LTB of welded steel girders will remain unclear.

Studies concerning the effects of heat-straightening on the stability performance of repaired members are few. Early historical research consists primarily of qualitative and observational studies investigating the application of heat-straightening techniques and the specimen's behaviour. Moreover, these investigations examine the effect of heat-straightening mainly on individual steel plates, rather than other common cross-sections, such as angles, channels, or I-shapes. The majority of recent studies cover quantitative assessments of material properties and residual stresses on a variety of common cross-sections. These studies report a reduction of the percent elongation, a reduction of modulus of elasticity, the introduction of additional residual stresses, and in some instances, brittle behaviours. However, the load–deformation response and LTB performance of members after heat-straightening and repair are typically not assessed experimentally. Experimental testing of this nature may bring clarity to this topic and indicate the efficacy of heat-straightening for structural members.

3 EXPERIMENTAL PROGRAMS

3.1 Lateral–Torsional Buckling Experiments

This section provides a summary of the primary components of the LTB test program, including the test matrix, experimental test set-up and test procedure. Note that a focus is placed on the specimens tested in this MSc project. Additional information regarding the design constraints, specimen selection, and development of the test matrix can be found in Ji et al. (2019).

3.1.1 Experimental Specimens

3.1.1.1 Test Matrix

An investigation into the geometric parameters affecting LTB was conducted by Ji et al. (2019), which included the section depth, flange width, web thickness and flange thickness. A range of cross-sectional dimensions, totalling 4000 combinations, was created. Observations suggested the flange width to be the most influential geometric parameter on the LTB capacity, and the web thickness, the least influential. However, the investigation neglected the effects of local slenderness, assuming all geometries can achieve their plastic moment capacity. As a result, the influence of the web thickness on LTB may have been neglected.

A few constraints are examined to reduce the possible geometries, which included laboratory limitations and the desire to observe only inelastic LTB. A modified distributed load was selected for the experiments and simulated through the application of equally-spaced point loads along the unbraced length. The maximum allowable load for the loading apparatus is 360 kN, which imposed a strict upper limit for test specimen selection. All members should fail by inelastic LTB before exceeding the laboratory capacity; thus, the pool of 4000 combinations was reduced to 143 geometries. From this, the final specimens are selected to include an adequate representation of potential aspect ratios, section classes, global slenderness ratios, and torsional parameters.

The final test matrix is presented in Table 3-1, totalling nine unique cross-sections and 11 distinct specimens. The dimensions, b, d, h, t and w, are the flange width, section depth, web height, flange thickness and web thickness, respectively. The parameter A_s is the cross-sectional area, I_y is the weak-axis moment of inertia, J is the St. Venant torsional constant, C_w is the warping torsional constant, and L/r_y is the global slenderness ratio with respect to the weak axis. Fabrication of the girders was completed locally by Supreme Group, and the plate material was donated by SSAB.

The test specimens are designed to span an unbraced length of 9.75 m (32 ft) between supports but are fabricated 10.4 m (34 ft) in length. For ease of alignment and configuration of the boundary conditions, a 0.305 m (2 ft) overhang is provided at either end. An alphanumeric labelling system was created by Ji et al. (2019), which is also used throughout this report. The labelling system contains information on the cross-section dimensions, class and plate cutting method. The naming convention is 'G' (for girder) followed by the first digit of section depth in mm – flange width in mm – flange thickness in mm – section class – cutting method ('p' for plasma and 'f' for oxy flame).

To illustrate the range of inelastic behaviour, Figure 3-1 plots the relationship between the normalized moment resistance for shear centre loading and the global slenderness ratio, where the definitions of inelasticity prescribed by CSA S16-19 are used to denote the transition between elastic and inelastic LTB. In accordance with this standard, inelastic LTB occurs when $1.0 > M/M_p > 0.67$ for Class 1/2 sections and between $1.0 > M/M_p > 0.67$ for Class 3 sections. As shown in Figure 3-1, all specimens are expected to fail by inelastic LTB and are selected such that the distribution of slenderness covers the entire inelastic region.
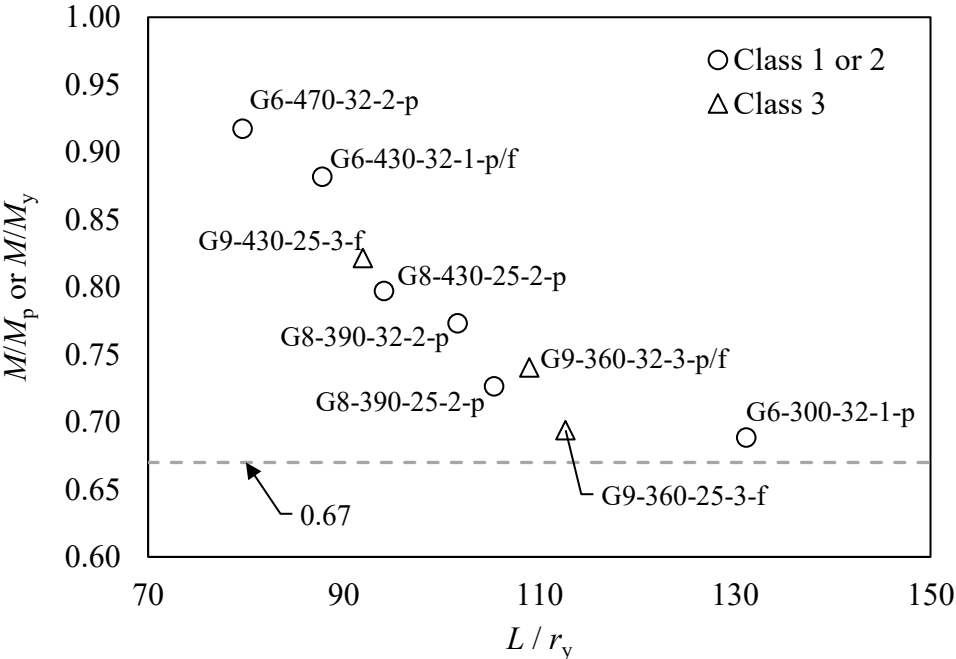
Figure 3-1: Nominal moment resistance vs. global slenderness ratio (adapted from Ji et al. 2019)

Table 3-1: Test specimen matrix

Specimen ID	Class	d (mm)	b (mm)	t (mm)	w (mm)	A_s (mm²)	I_y (x10⁶ mm⁴)	J (x10³ mm⁴)	C_w (x10⁹ mm⁶)	d/b	b/t	h/w	L/r_y
G6-470-32-2-p	2	600	470	31.8	12.7	36659	549	10417	44351	1.28	7.4	42.2	79.7
G6-430-32-1-p	1	600	430	31.8	12.7	34119	421	9563	33964	1.40	6.8	42.2	87.8
G6-430-32-1-f	1												
G6-300-32-1-p	1	600	300	31.8	12.7	25864	143	6789	11534	2.00	4.7	42.2	131.2
G8-430-25-2-p	2	800	430	25.4	12.7	31359	337	5227	50487	1.86	8.5	59.0	94.1
G8-390-32-2-p	2	800	390	31.8	12.7	34119	314	8846	46316	2.05	6.1	58.0	101.7
G8-390-25-2-p	2	800	390	25.4	12.7	29327	251	4790	37668	2.05	7.7	59.0	105.4
G9-360-32-3-p*	3	900	360	31.8	9.53	30828	247	7932	46530	2.5	5.7	87.8	109.0
G9-360-32-3-f*	3												
G9-360-25-3-f*	3	900	360	25.4	9.53	26377	198	4185	37770	2.50	7.1	89.2	112.7
G9-430-25-3-f*	3	900	430	25.4	9.53	29933	337	4950	64365	2.09	8.5	89.2	92.0

* Denotes the specimens tested in this research project.

3.1.1.2 Cross-section Measurements

Cross-sectional dimensions are measured before testing for the assessment of the as-built design condition. For the G6 and G8 series of girders, measurements are collected at five equally-spaced points along the girder length, whereas for the G9 series, measurements are collected at nine equally-spaced points. The increase in collection frequency is not for the LTB program; instead, the G9 series of specimens are to be heat-straightened, as described in Section 3.2, and more data points along the member length were desired for comparisons among the as-built, damaged and repaired conditions. Nonetheless, per station, each geometric dimension is measured at least twice and averaged to reduce the influence of human error. Figure 3-2 depicts the cross-sectional measurements collected and the location of measurement. The primary plate dimensions, flange width and section depth, are found by measuring tape, whereas calliper and ultrasonic measurements record plate thicknesses for the flange and web, respectively. The remaining dimensions noted on the figure are measured using a Fluke 414D distancing-measuring device.
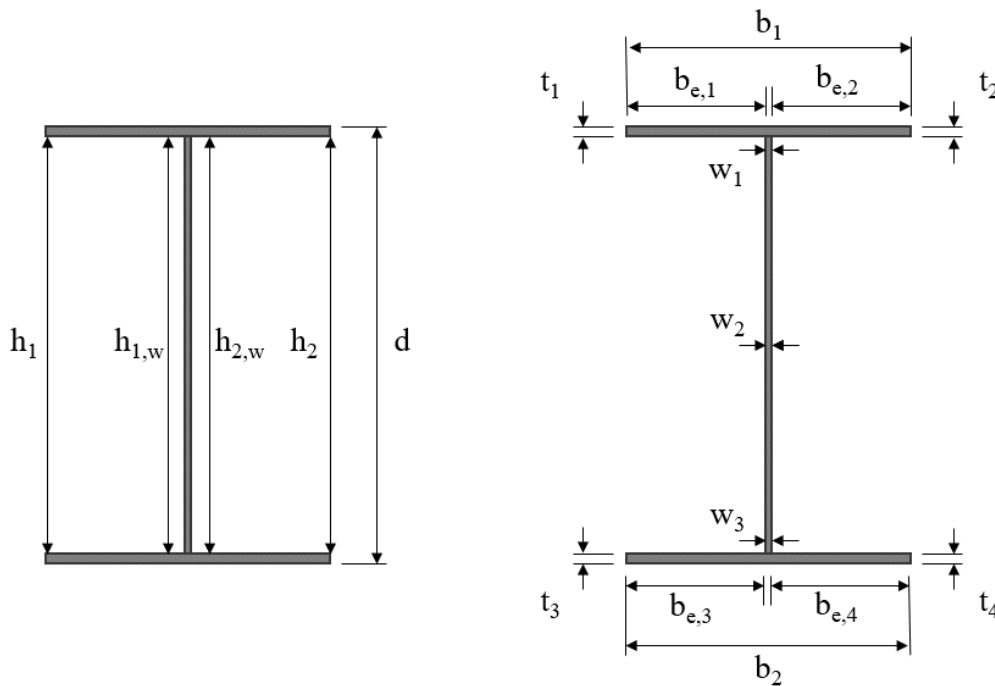
Figure 3-2: Cross-sectional measurements and locations

The dimensions h_i and $h_{i,w}$, are measures of the distance between flanges at the flange tips and adjacent to the web, respectively. The dimensions $b_{e,i}$ are measures of the distance from the flange tip to the web surface, and the remaining measurements, b, d, t and w are the flange width, section

depth, flange thickness and web thickness, respectively, where the subscript, i, denotes the respective measurement locations, as indicated in Figure 3-2. A summary of the as-built cross-sectional measurements is given in Table 3-2.

Analysis of the $b_{e,i}$ dimension indicates that the positioning of the web is relatively centred about the flange and consistent for all series of girders, showing misalignments of no greater than 4 mm. The difference of the dimensions h_i and $h_{i,w}$ (h_i–$h_{i,w}$) measures the offset of the flange tip from a line normal to the plane of the web and is indictive of flange warpage (tilt or curling). A positive value of h_i–$h_{i,w}$ indicates that the tip of one half of the flange is inclined upwards from the elevation of the web−flange junction, and a negative value implies a downwards inclination. To be considered a flange tilt, h_1−$h_{1,w}$ and h_2−$h_{2,w}$, which represent the offset of the east and west halves of the flange, respectively, should be approximately equal and opposite, meaning the flange plate is rotated from horizontal about the web−flange junction. Otherwise, any magnitude of h_1−$h_{1,w}$ and h_2−$h_{2,w}$ indicate a curl of one half of the flange, where positive values of h_1−$h_{1,w}$ and h_2−$h_{2,w}$ indicate an upwards curl, and negative values indicate a downwards curl.

Examining h_i–$h_{i,w}$, in Table 3-2 shows some degree of flange warpage in all specimens. Most girders exhibit a form of flange curl, whereby one half of the flange curls downward, and the opposing half-flange remains relatively horizontal. G8-390-32-2-p and G8-390-25-2-p are the only girders to exhibit a slight flange tilt. In general, the measured vertical offset (h_i–$h_{i,w}$) between the elevation of the flange tips and the web−flange junction ranged between 0 to 7 mm, with a mean offset of -3 mm. G6-30-32-1-p is the only girder to exceed the fabrication tolerance of CSA W59-18, where the flange warpage is limited to the greater of $b/100$ and 6 mm, of which the latter always governed.

For members fabricated with a 32 mm-thick flange plate, there exists a discrepancy between the nominal and as-built plate widths of up to 10 mm. The reasoning for the discrepancy is reported by Ji et al. (2019), where it is assumed that the desired gap between flange plates cut from the 32 mm source plate was unachievable, and therefore the pieces were purposefully cut narrower in fabrication. The remaining cross-sectional dimensions match closely to the nominal values. However, the web thickness of the G9 series of girders is, on average, 0.35 mm larger. While this is minimal, it represents a 3% error between the nominal and as-built dimensions and affects the web classification, as discussed in Section 3.1.1.7.

Table 3-2: As-built cross-sectional measurements

Specimen ID	d (mm)	b (mm)	t (mm)	w (mm)	$b_{e,1}$ (mm)	$b_{e,2}$ (mm)	$b_{e,3}$ (mm)	$b_{e,4}$ (mm)	h_1 (mm)	$h_{1,w}$ (mm)	h_2 (mm)	$h_{2,w}$ (mm)	h_1-$h_{1,w}$ (mm)	h_2-$h_{2,w}$ (mm)
G6-470-32-2-p	599	461	31.9	12.9	226	226	224	226	533	536	534	536	-3	-2
G6-430-32-1-p	599	422	32.1	12.9	206	204	207	208	538	537	530	537	+1	-7
G6-430-32-1-f	597	422	32.2	13.1	203	205	205	204	534	535	529	535	-1	-6
G6-300-32-1-p	599	291	31.8	13.0	139	140	139	140	536	537	533	537	0	-4
G8-430-25-2-p	799	429	25.1	12.8	210	209	211	208	743	749	746	749	-6	-3
G8-390-32-2-p	800	382	32.1	12.9	187	188	187	189	729	735	738	735	-6	+3
G8-390-25-2-p	801	390	25.1	12.9	188	189	189	189	743	749	751	749	-6	+2
G9-360-32-3-p*	898	353	31.6	9.9	173	171	172	171	833	835	834	835	-2	-1
G9-360-32-3-f*	900	351	31.7	9.9	170	172	173	169	837	836	830	836	+1	-5
G9-360-25-3-f*	900	359	24.9	9.9	176	177	176	176	845	849	848	849	-4	-1
G9-430-25-3-f*	902	429	25.1	9.8	209	210	208	209	848	849	844	849	-1	-5

* Denotes the specimens tested in this research project.

3.1.1.3 Global Geometric Measurements

Measurements of the initial lateral sweep, camber and cross-section twist are collected at five equally-spaced points along the span length, L, for the G6 and G8 series, and at nine points for the G9 series. The span length, L, is measured with a Fluke 414D distance-measuring laser and is taken as the centre-to-centre distance between the girder's end stiffeners, which, in turn, are centred on the end supports, as described in Section 3.1.2.2. Upon receipt of the girders, the initial lateral sweep and camber of both the top and bottom flanges are measured, as the specimens bear upon pedestal supports, resting on the laboratory floor, whereas the initial twists are measured after the specimen has been suspended and aligned within the test frame. The sign convention of the global geometric measurements is as follows: upwards in-plane deviations from straightness (camber), eastward out-of-plane deviations from straightness (lateral sweep), and cross-section twists that translate the top flange eastward are positive. The cardinal directions are indicative of the orientation of the girder within the structure's lab and are used to describe the direction of the global geometric imperfections.

The global measurements collected by Ji et al. (2019) for the G6 and G8 series, and the G9 series of the present study, are provided in Table 3-3. Reported are the maximum measured values of the initial lateral sweep, camber, and cross-section twist along the span length, without regard for the location; however, the maximum values often occurred approximately at mid-span. For a look at the typical distribution of the measured geometric imperfections, reference Figure 3-3, Figure 3-4 and Figure 3-5, which contain plots of the distribution of initial lateral sweep, camber and cross-section twist of G9-360-32-3-p along the girder length.

Table 3-3: Measured global measurements

| Specimen ID | L | Sweep | | Camber | | Twist |
| | | Top Flange | Bottom Flange | Top Flange | Bottom Flange | |
	(mm)	(mm)	(mm)	(mm)	(mm)	(°)
G6-470-32-2-p	9752	+1.5	+1.5	-1.0	-1.4	+0.4
G6-430-32-1-p	9751	-2.0	-2.5	-9.8	+7.5	+0.6
G6-430-32-1-f	9761	-3.0	-1.0	-6.3	+2.3	-0.3
G6-300-32-1-p	9755	+3.0	2.5	-1.8	+4.1	+0.4
G8-430-25-2-p	9749	+7.0	-3.5	-2.9	-1.8	+1.3
G8-390-32-2-p	9760	-1.0	-11.0	-7.3	-4.8	-1.1
G8-390-25-2-p	9751	-1.0	-6.0	-4.3	-3.0	-0.2
G9-360-32-3-p	9754	-9.0	-0.5	+3.5	+2.0	-0.8
G9-360-32-3-f	9770	-5.5	-4.5	-1.3	-2.5	+0.3
G9-360-25-3-f	9767	-3.0	-2.0	-1.5	-2.5	-0.2
G9-430-25-3-f	9764	-2.0	+2.5	-1.5	-1.3	-0.4

The initial lateral sweep has been measured by stretching a string line along the girder length, which was aligned to pass through the member ends at the centerline of the flange. The girder ends are used as the point of reference, and any deviation between the flange position and the string line represents the girder's initial lateral sweep. For the G9 series, the measured initial lateral deviations ranged between L/4900 to L/1100 in the top flange and L/19500 to L/2200 in the bottom flange. The average values of the initial top and bottom flange sweep for the G9 specimens are L/2800 and L/7600, respectively. In comparison, the mean initial top and bottom flange sweeps recorded for the G6 and G8 series were L/5500 and L/4200, respectively, indicating the G9 series exhibited larger magnitudes of initial top flange sweep and a reduction in the magnitude of the initial bottom flange sweep. None of the G9 girders exceeded the dimensional tolerances of CSA W59-18, which allows a maximum deviation from straightness of L/1000. However, G9-360-32-3-p came close, with a measured initial top flange sweep of L/1100. As LTB behaviour is sensitive to the initial top flange sweep (Subramanian and White 2017), the increased magnitude of initial top flange sweep in G9 specimens is expected to influence their LTB response.
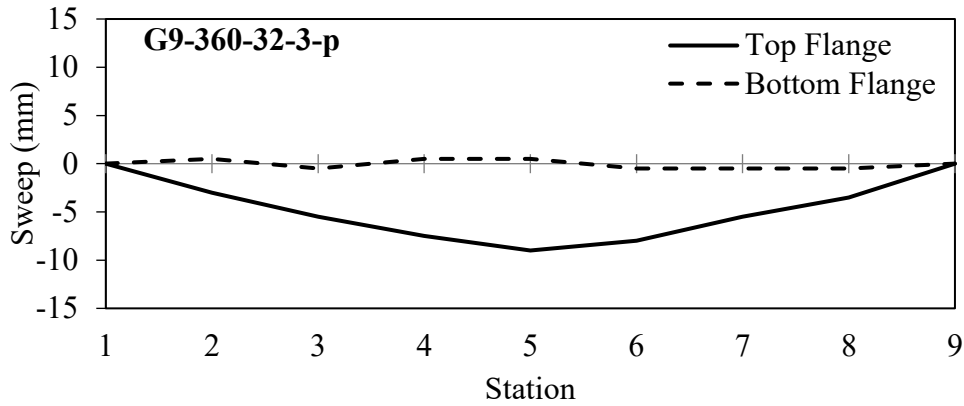
Figure 3-3: Measured initial lateral sweep of G9-360-32-3-p

A Fluke 180LG line laser level was used to measure the camber. The laser is self-levelling and capable of providing a horizontal reference line, by which the vertical distance between the flange and reference can be determined. Since the laboratory floor is not necessarily horizontal, the slope between the endpoints of the specimen is first calculated and any deviation from this slope represents the specimen's camber. At a given station, the camber can be calculated as the difference between the reference distance and the line parallel to the laboratory floor. For all specimens, the camber ranged between $L/9800$ to $L/1000$ measured to the top flange and between $L/7800$ to $L/2100$ measured to the bottom flange. The mean top and bottom flange cambers are $L/4800$ and $L/4200$, respectively. It should be noted that the specimens are specified with zero camber. However, as the camber never exceeds $L/1000$, the girders are within tolerance as prescribed in CSA W59-18 and deemed satisfactory.
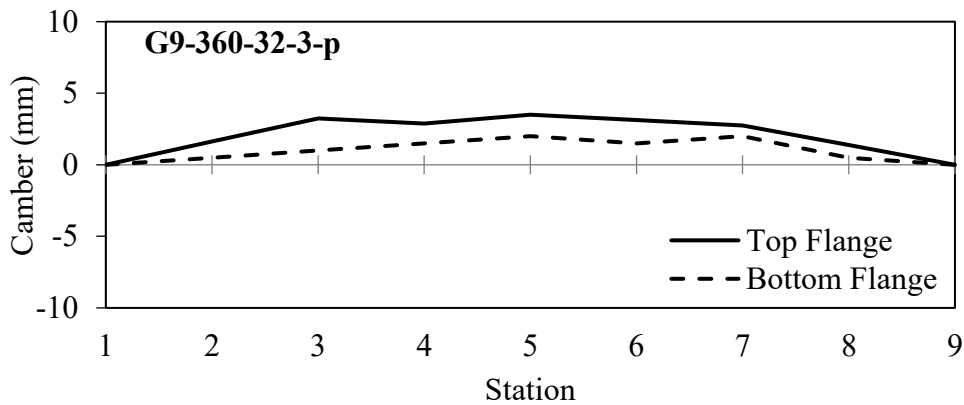
Figure 3-4: Measured camber of G9-360-32-3-p

CSA W59-18 does not specify a tolerance on initial cross-section twist; nevertheless, an initial cross-section twist can influence the LTB behaviour. A Mitutoyo Pro 360 digital protractor is used to record the twists at the mid-height of the girders. For a perfectly vertical web, the digital protractor reads zero degrees and any deviation from there, in either direction, corresponds to the specimens' initial cross-section twist. Before the cross-section twist measurements are taken, the girder is suspended in the test set-up and aligned vertically at the boundary conditions. During alignment, the boundary conditions are manipulated such that the verticality of the cross-section at the beam ends is ensured, and measurements are taken in reference to the vertical end conditions. The average cross-section twist measured for the G9 series was 0.39º, and the average cross-section twist reported for G6 and G8 series was 0.60º. The G9 series exhibits a reduced mean cross-section twist; however, both the largest (0.75º) and smallest (0.2º) magnitudes of cross-section twist in the entire experimental program are measured for the girders, G9-360-32-3-p and G9-360-25-3-f, respectively, suggesting that the deeper series of specimens may be susceptible to a larger variance of cross-section twist.
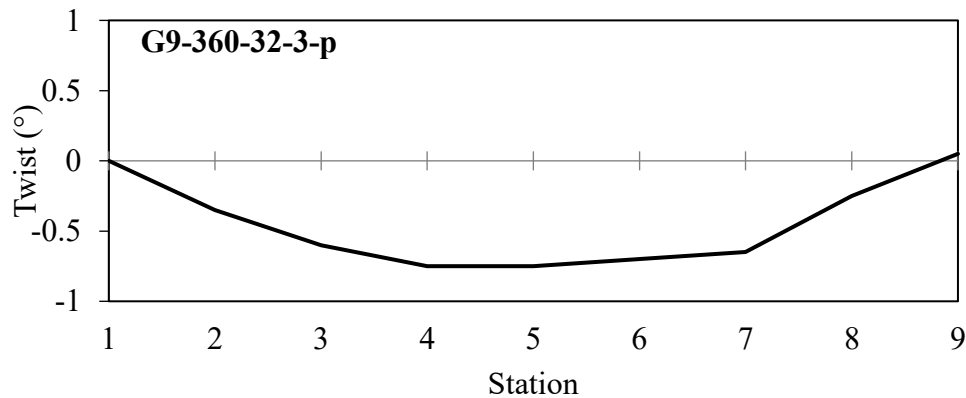
Figure 3-5: Measured initial cross-section twist of G9-360-32-3-p

3.1.1.4 Cutting Method

Discussions with Supreme Group engineers indicated that their typical fabrication process includes both flame cutting and plasma cutting techniques, where plasma cutting is often employed for building-type applications and flame-cutting reserved for bridge girder construction. However, it is known that plate cutting methods introduce distinct residual stress patterns and influence the LTB response. Flame cutting methods tend to introduce high tensile stresses at the plate edges (Alpsten and Tall 1970, Bjorhovde et al. 1972), whereas plasma cutting techniques tend to produce

much lower residual stresses at the plate edges (Unsworth et al. 2019). To analyze the effects of the cutting methods on the LTB response, specimens of the G6 and G8 series of girders are fabricated from plasma-cut plates, while the G9 series, which are more representative of bridge-type girders, use flame-cut plates. Two geometries, G6-430-32-1 and G9-360-32-3, are fabricated twice, where the only difference is between plate cutting methods, in order to assess the effect of plate cutting while eliminating the influences of geometric properties.

3.1.1.5 Material Properties

In this study, the tensile properties of the 9.53 mm web plates of the G9 girders are experimentally determined and reported. The 12.7 mm, 25.4 mm, and 31.8 mm plates' material properties, which were determined by Ji et al. (2019), and are also reported for completeness. The yield stress, yield strain, modulus of elasticity and ultimate stress are assessed per the specifications of ASTM A370-19 (ASTM International 2019). Dog-bone specimens are cut from ancillary lengths of 3.05 m (10 ft) girders fabricated alongside the LTB test specimens and using the same procedures for destructive material testing. The entire 3.05 m length is not required for material testing. So, the ancillary girders are flame-cut into three distinct segments with a 1.3 m length reserved for tension coupon testing. The web and flange plates are separated, and the coupon locations are marked.

The tensile coupons are waterjet cut, orientated in the longitudinal direction of the girder, and dimensioned as per the specifications of ASTM A370-19. For the 9.53 mm, 12.7 mm and 25.4 mm plates, sheet-type coupons are specified, with a gauge length of 50 mm, and for the 31.8 mm plates, 200 mm gauge length, plate-type specimens are used, as required by the standard. Two coupons are cut from the separated flange and web plates until a total of four unique tensile coupons were collected per plate thickness, except for the 9.53 mm specimens where a total of three coupons are taken from the web of one of the G9 series of girders. The coupons are strained under a uniaxial loading frame at a rate of 0.2 mm/min until the onset of strain hardening, then increased to a rate of 3 to 4 mm/min until failure. Three static points are taken within the yield plateau for assessment of the mean static yield stress, and a final static point is taken at the approximate ultimate stress to obtain the static ultimate stress. Finally, the modulus of elasticity is calculated as the slope of the stress–strain response between zero stress and the proportional limit. A summary of the material properties is given in Table 3-4.

Table 3-4: Summary of material properties

Plate Thickness (mm)	Yield Stress (MPa)	Ultimate Stress (MPa)	Youngs Modulus (MPa)
9.53	357	440	204,550
12.7	364	450	203,673
25.4	355	442	202,368
31.8	347	–	201,263

The ultimate stress of the 31.8 mm thick plate is not reported due to the uniaxial load frame's limitations on grip strength; therefore, these coupons were only tested to yield. There was an error in waterjet cutting of the 9.53 mm specimens, where the received gauge width is 10.25 mm on average as opposed to the anticipated gauge width of 12.7 mm, specified by ATSM A370-19. As the width was uniform within the test region, tensile testing of the 9.53 mm coupons was carried out despite their non-compliance with the standard. However, the tensile test results are verified in comparison to the results of other sheet-type specimens. Figure 3-6 shows the stress–strain response of three coupons: a 25.4 mm flange coupon of G8-430-25-2-p, a 12.7 mm web coupon of G6-300-25-3-f, and one of the 9.53 mm coupons in question from G9-430-25-3-f. No observable or concerning difference in response is found, and the results are accepted despite the non-compliance.
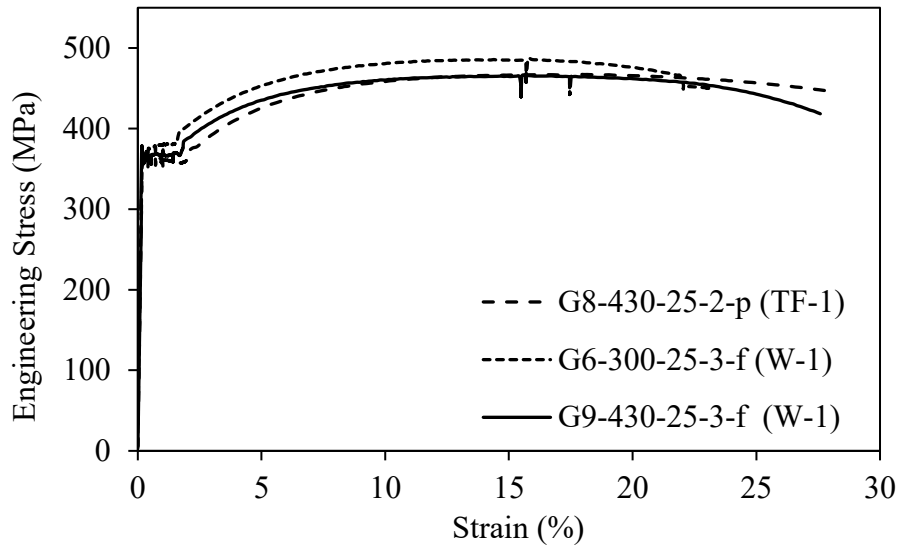
Figure 3-6: Typical stress–strain response of 9.53 mm, 12.7 mm and 25.4 mm plates

3.1.1.6 Residual Stresses

Residual stresses significantly influence the inelastic LTB response of welded girders. For this reason, their measurement is a primary component of the research. The residual stress measurements were carried out in the companion study by Unsworth et al. (2019), where the residual stresses of the specimens G6-430-32-1-p, G6-430-32-1-f, G6-300-32-1-p and G8-430-25-2-p are investigated by sectioning (Pekoz et al. 1981). Much like the measurement of tensile material properties, the residual stresses of the LTB specimens are not measured directly, but are instead assessed from the testing of the ancillary 3.05 m (10 ft) girders, first discussed in the preceding section. Testing ancillary girders for the residual stresses differs from some LTB studies (Dibley 1969, Fukumoto 1981), where the material properties and residual stresses are measured directly from sections cut from the as-built specimens. However, it was elected to fabricate secondary girders with consistent batch materials, geometries and welding procedures to avoid large as-built specimen lengths and unnecessary flame cutting in the lab.

A 400 mm portion of the 3.05 m section is flame cut and removed from the center of the ancillary girders, then cut by a mechanical band saw to the specified minimum length of 150 mm. A series of 30 mm strips are located, marked and measured, about the test segment for separation and assessment of the released strain energy. The residual stresses are then calculated as a function of the released strains and elastic moduli. Strain measurements are taken of both faces of the sectioned

flange pieces and reported as exterior and interior measurements. For the web, the strain measurements are taken only on one side of the plates. The measured residual stresses for specimens G6-430-32-1-p and G6-430-32-1-f are shown in Figure 3-7 and Figure 3-8, respectively. Note that these two specimens differ only by the cutting method, and therefore also exhibit the influence that the cutting method had on the residual stresses.

As shown in Figure 3-7 and Figure 3-8, peak tensile stresses are measured at the web–flange junction, with compressive stresses measured throughout the web and flange plates of either girder. However, a mean tensile stress of 10 MPa is measured at the flange tips of the flame-cut specimen and, a mean compressive stress of 16 MPa is measured at the flange tips of the plasma-cut specimen. A difference in residual stresses at the flange tips is expected and is attributed to the cutting method. However, in either case, the residual stresses measured at the flange tips are significantly smaller than those measured by previous researchers for welded girders (Nagaraja Rao et al. 1964; Alpsten and Tall 1970; Bjorhovde et al. 1972; Fukumoto and Itoh 1981). Unsworth et al. (2019) note that their use of 30 mm wide strips during sectioning likely resulted in an underestimation of the highly localized tensile residual stresses at the flange tips for the flame cut flanges, based on the observed stress gradients in the region. Similarly, the same concept can be extended to the residual stresses measured of the plasma-cut specimen; highly localized but small tensile stresses may not be reflected in the mean compressive stress measured.
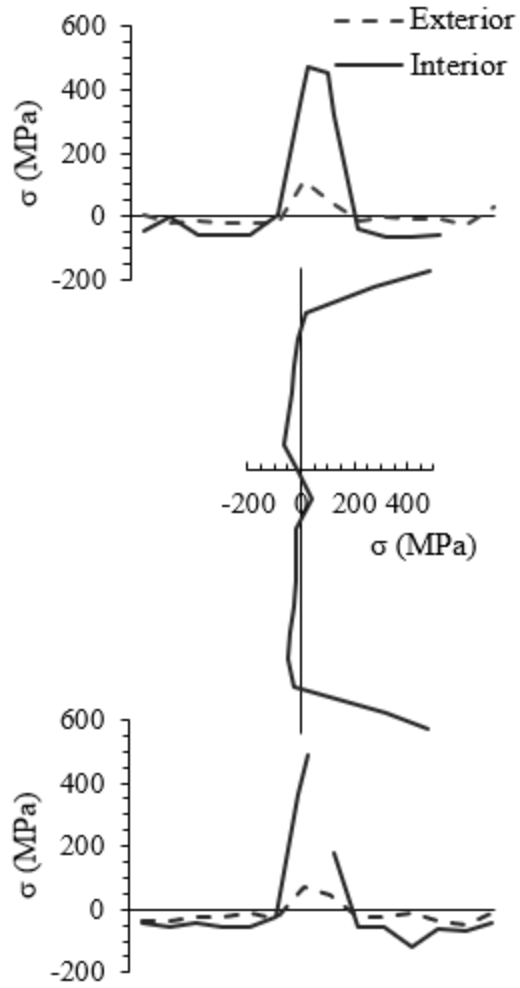
Figure 3-7: Residual stress distribution for G6-430-32-1-p (Unsworth et al. 2019)
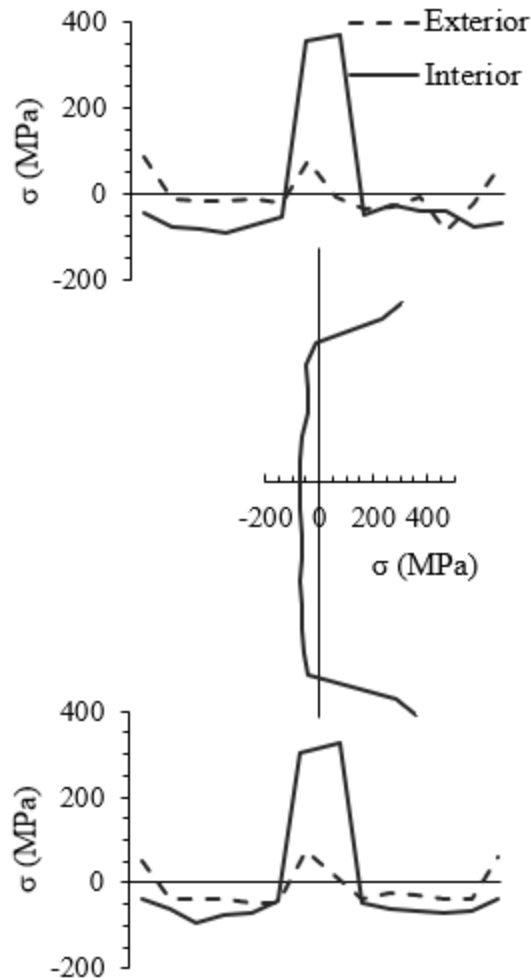
Figure 3-8: Residual stress distribution for G6-430-32-1-f (Unsworth et al. 2019)

3.1.1.7 Section Class

The test matrix of this study includes specimens that were nominally designed Class 1, 2 and 3, as per the provisions of CSA S16-19 for elements in flexure. The inclusion of Class 3 girders was deemed important during the initial development of the experimental program, as Class 3 cross-sections are extensively used in bridge construction. Furthermore, welded steel girders often fall under Class 3 designations due to the use of slender webs. Therefore, the G6 and G8 series were designed to consist of Class 1 or 2 cross-sections, whereas the G9 series was designed to be Class 3. In addition, the test matrix was also developed to consider a range of local web and flange slenderness, despite CSA S16-19's only concern being the overall section class. Therefore, some girders may have Class 1 flanges with Class 2 webs, and so on, but it should be noted that only the

G9 series exhibit Class 3 webs. The nominal flange and web local slenderness ratios have been plotted in Figure 3-9 to show the range of local slenderness considered in this study. The grey dotted lines represent the local slenderness limits specified by CSA S16-19 to delineate Class 1, 2 and 3 plates and are calculated using the nominal anticipated yield stress, $F_y = 385$ MPa.
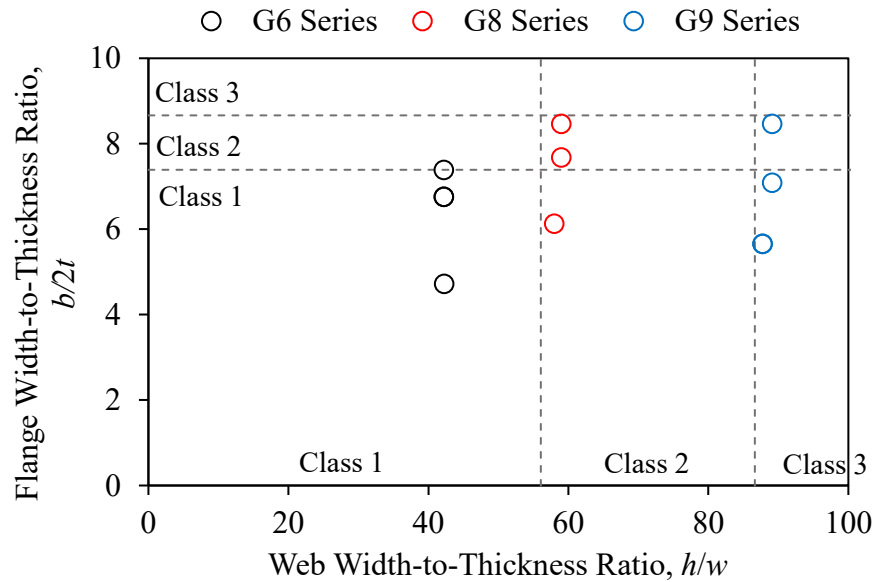
Figure 3-9: Anticipated section classes

Figure 3-10 shows the as-built range of local slenderness based on the measured dimensions and material properties, reported in Sections 3.1.1.2 and 3.1.1.5. The intention of the study was to investigate the behaviour of sections with Class 3 webs by examining the test results of the G9 series. However, as received, the G9 specimens are considered Class 2 by CSA S16-19 provisions. Nonetheless, local buckling is a nuanced phenomenon. Despite specific section class boundaries imposed by CSA S16-19 provisions, it is expected that the behaviours associated with Class 3 sections may still be observed, as Figure 3-10 indicates that the G9 series of girders approach the Class 3 width-to-thickness limits. Analysis of the test results will, therefore, need to consider the effects of local web slenderness.
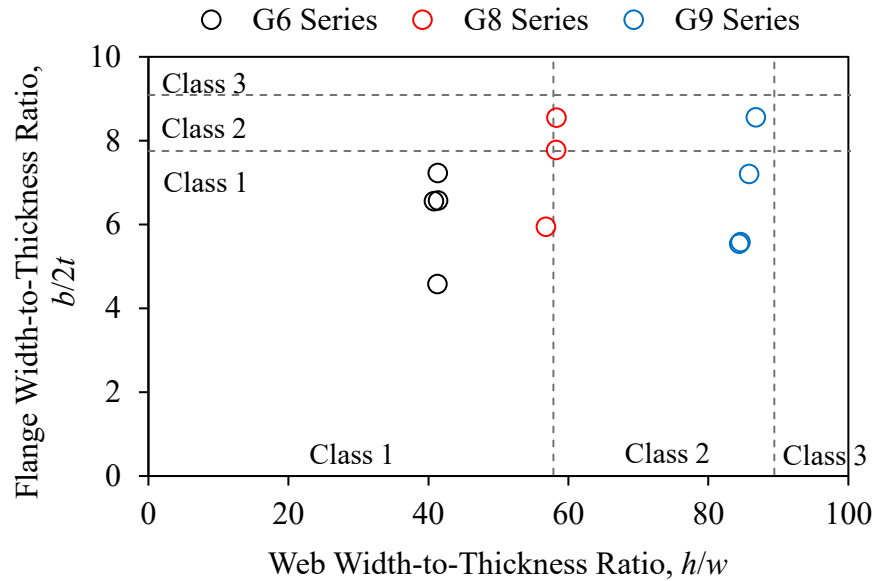
Figure 3-10: As-built section classes

3.1.2 Test Characteristics

3.1.2.1 Loading

The test specimens are subject to an approximated distributed load, where eight equally-spaced point loads are applied to the girders at 1.22 m (4 ft) intervals along the girder length, as shown in Figure 3-11. A set of gravity load mechanisms are designed to apply a series of point loads through the top flange of the specimens; the mechanism consists of three distinct components: (1) gravity load simulators, (2) hydraulic actuators and (3) load collars. The design and detailing of these components are described by Ji et al. (2019). Nevertheless, the assembly and functionality of each component are reviewed herein.
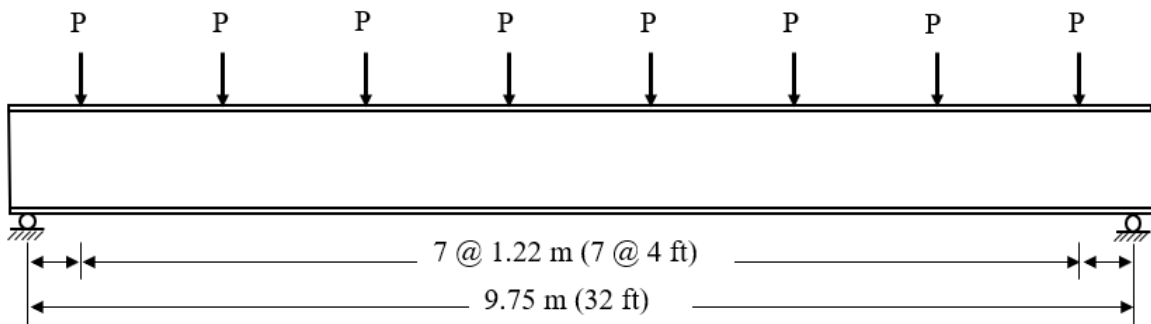
Figure 3-11: Load configuration of the lateral–torsional buckling tests

It is undesirable to introduce lateral restraint at the point of load application when evaluating LTB behaviour. Thus, gravity load simulators (GLS) are used at all load points. The GLS is a pin-jointed mechanism capable of freely displacing laterally from its equilibrium position, while providing a mounting location for hydraulic actuators and maintaining an approximately vertical load orientation (Yarimci et al. 1967). The GLS system ensures the loading apparatus itself does not influence the unpredictable nature of LTB, as the mechanism can effectively track buckling as it occurs and accommodates up to 400 mm of lateral displacement in either direction. The hydraulic actuators used to deliver the load are rated to 385 kN of force in retraction, feature a 150 mm stroke, and operate dependently through a single manifold. A GLS and actuator are shown in Figure 3-12.
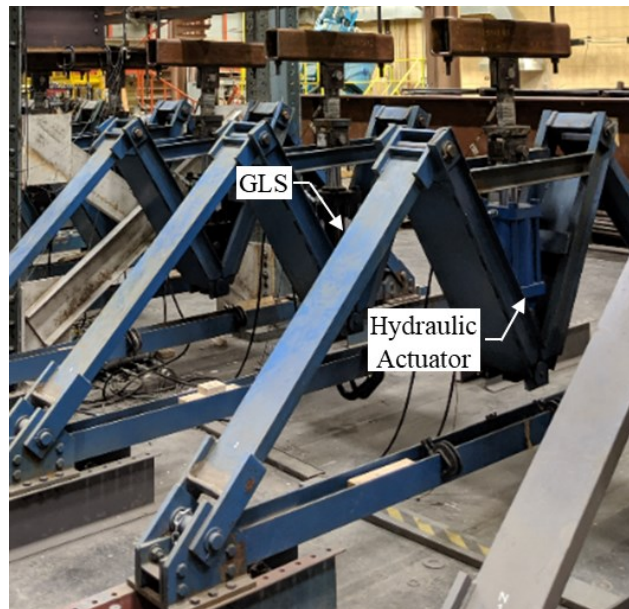
Figure 3-12: Gravity load simulator and hydraulic actuator

The load collars shown in Figure 3-13 are designed to translate the pulling force of the hydraulic actuators through to the top flange of the specimens. The load collar assembly consists of two HSS sections, two threaded rods, a yoke and a tension rod. The load is translated from the actuators through the tension rod and threaded rods and directed downwards onto the specimen's top flange through a spherical bearing bolted to the top HSS. Each component is designed to remain elastic during loading to ensure the load collar assembly remains square, while the hemispherical bearing accommodates the cross-section rotation. The load collar assembly is shown in Figure 3-13 when

a specimen was undergoing LTB. Note that the load collars remain square and pivot about the spherical bearing as intended.
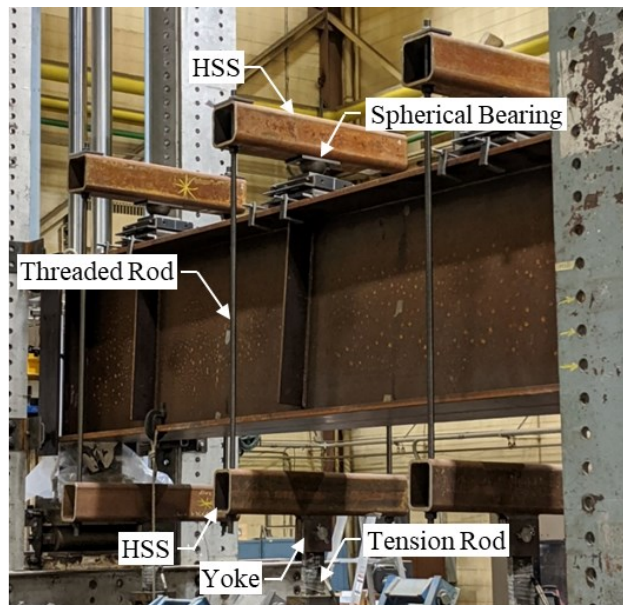
Figure 3-13: Load collar assembly during buckling

Rollers are mounted to the top flange of the girders, as shown in Figure 3-14. The rollers accommodate the longitudinal displacement of specimens. If not for the rollers, as the girder displaces longitudinally, the spherical bearing would move with the girder as it bears upon the top flange and bend the load collar assembly. Adjustable tabs secure the roller assembly to the specimens' top flange, preventing slippage between the roller and flange surface at large degrees of cross-section rotation during LTB. A plate of sacrificial steel was placed between the spherical bearing and the roller surface to limit the surface damages resulting from the large concentrated loads. As a result, the spherical bearing (the point of load application) sits 178 mm above the top flange of the girders, and therefore any assessment of the LTB behaviour will require analysis of the load height effect.
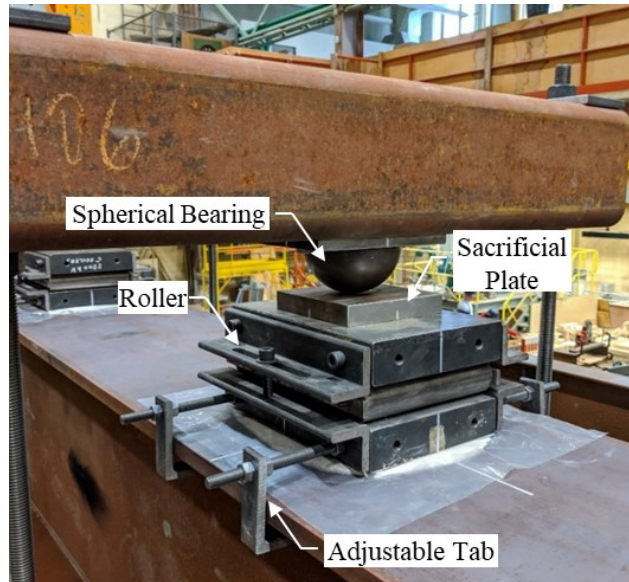
Figure 3-14: Roller/bearing assembly

3.1.2.2 End Conditions

A set of simple supports are provided at the specimen ends, where the girders are free to displace longitudinally but prevented from displacing vertically or laterally. Longitudinal displacement is released at both ends, which is necessary for the initial alignment of the test specimens within the test-frame and accommodates the tightening of the inherent slack throughout the system prior to load application. Rotationally, the member is free to displace in and out-of-plane, where only the rotation about the longitudinal axis (cross-section rotation) is restricted at each end.

As shown in Figure 3-15, the specimens rest upon a roller, load cell and knife-edge at each end support. This configuration allows for both longitudinal displacements and in-plane rotations, as the girder is free to pivot about the knife-edge and displace via the roller. Two vertical steel plates bear against the flange tips of the specimens to restrain cross-section twist and lateral displacement, where four rollers welded to threaded rods brace the steel plate against the flange tips of the girder without restricting longitudinal movement of the flange. The threaded rods are adjusted until a snug fit is observed, pinning the plates to the flange tips, and in this manner, the lateral restraint system can accommodate variable flanges widths. Furthermore, the cylindrical rollers of the lateral braces allow the specimen to rotate out-of-plane at the supports while imposing no external warping restraint.
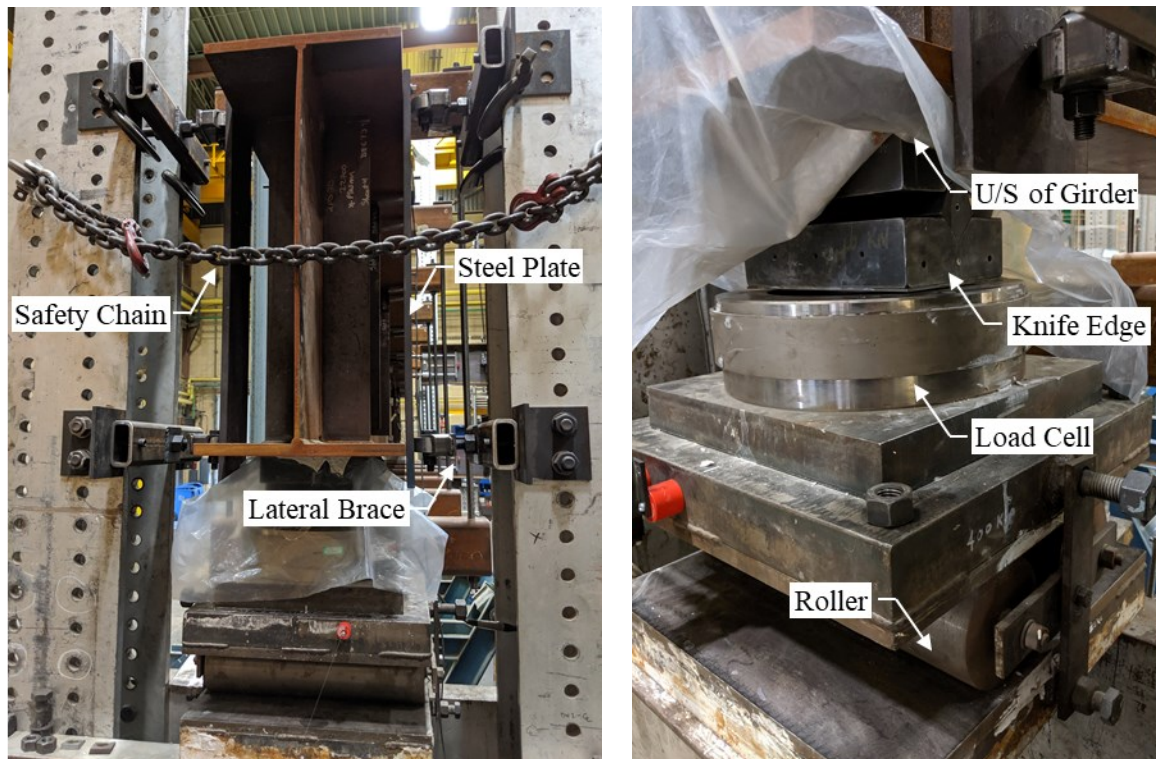
Figure 3-15: End support conditions

3.1.2.3 Instrumentation

A series of cable transducers, clinometers, linear variable displacement transducers, strain gauges and load cells were located about the test specimens, either at the ends or at mid-span, to capture the specimen displacements, strains, and the applied loads. The test girders are oriented in the N-S direction of the structures lab, and the cardinal directions are used to describe the two respective ends of the specimen. Longitudinal displacements are captured at the north and south ends of the girder by cable transducers attached to the end support rollers. Mid-span lateral displacements are measured at the top and bottom flange of the girders by Miller-West Gliders, as shown in Figure 3-16 and Figure 3-17. The Miller-West Gliders permit a direct and continuous measurement of the lateral component of flange displacements through 190 mm of vertical displacement without the need for adjustments during the test. They feature a spring-loaded bar that rests against the flange tip of the specimen and is set to slide along a horizontal track. Depending on the direction of buckling, the bar is either extended by force of a spring or retracted by movement of the girder. A cable transducer measures the movement of the bar, recording positive lateral displacement for extension and negative for retraction, to a maximum of 135 mm in either direction. The glider can

only move in the lateral plane; therefore, vertical displacement is not measured. However, the girder is free to slide downward against the bar as it displaces laterally.
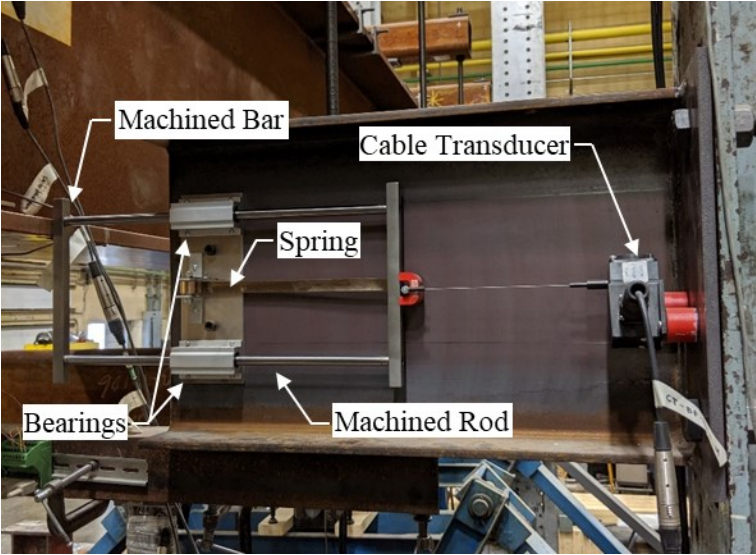
Figure 3-16: Miller-West Glider

Figure 3-17: Miller-West Gliders showing differential flange displacements during buckling

The vertical displacement of the girder is measured at mid-span by a linear variable displacement transducer (LVDT) mounted to the underside of the specimen at the bottom flange and centred about the web. The in-plane rotation is tracked by two clinometers mounted to the girder's top flange located directly above the web at the north and south ends. Out-of-plane rotations about the girder's longitudinal axis are captured at mid-span by a set of three clinometers, with one mounted to each flange and one at mid-height of the web. All instrumentation was calibrated upon first use, reviewed and recalibrated if the need was identified before each test.

Strainsert load cells with a 2200 kN capacity are mounted at the girder ends and incorporated into the end support for measurement of the total reaction forces developed throughout the test. Load cells fabricated from biaxial strain gauges are mounted to the tension rod of each GLS/load collar, as shown in Figure 3-18 and track the force exerted per actuator. Redundancy in force measurement is used as a quality control measure, where agreement should be observed throughout testing between the reaction forces and the total load of the GLS load cells. All load cells were calibrated prior to the initial tests using a uniaxial load frame and are not recalibrated throughout testing if the agreement between sources is observed.
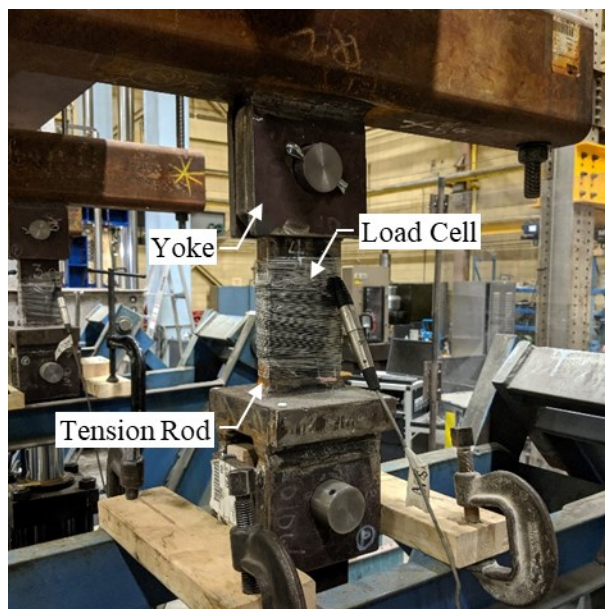
Figure 3-18: Tension rod load cell at gravity load simulator

Strain gauges are mounted to the girders' top and bottom flanges at mid-span to assess the extent of yielding exhibited during LTB. Three strain gauges are installed per flange, 10 mm from the

flange tips and at the web–flange junction. Yielding is expected to occur first at these gauge locations for the bottom flange of the girder. However, the straining of the compression flange is more complicated and preferably would be tracked by Digital Image Correlation (DIC) technologies. The G6 and G8 series of tests utilized DIC technologies to track the top flange strains; however, for the testing of the G9 series, the DIC was not available. Instead, an approximate distribution of strain is estimated in this project using the strain gauges. If the yield strain is not exceeded at the three locations where the strain gauges are installed, it is assumed that the girders failed in elastic LTB.

3.1.2.4 Test Procedure and Assembly

Upon delivery, the cross-sectional measurements and global imperfections are measured and recorded as per Sections 3.1.1.2 and 3.1.1.3. At this stage, the girder is marked for alignment within the test set-up. The location of load points and reaction points are identified about the specimen and marked with crosshairs. The girders are lifted by crane into the test set-up, and initially aligned about the bearing stiffeners, ensuring the centres of the knife edges in the end supports align with the marked locations at either end of the girder. A layer of plaster is used between the knife-edge and the girder bottom flange to ensure the girder sits flat at the boundary conditions. The side plates of the lateral restraint system are lifted into place, and the threaded rods are adjusted until the girder is secured. The threaded rods are additionally utilized to align the girder ends laterally in the test-frame and to ensure verticality of the cross-section at the support.

Once the end supports are set, attention turns to the installation and alignment of the load collars. The rollers of the load collars are lifted into place by crane and aligned on the top flange about the marked crosshairs. A layer of plaster is placed upon the flange surface, the roller is lowered into position, displacing the plaster until the roller settles, and a flat, flush surface is ensured. The GLS's are moved into their equilibrium positions, aligning the bottom HSS of the load collars horizontally. The top section of the load collars, which consists of an HSS member, spherical bearing and threaded tension rods, is flown into position about the girder and lowered until the tension rods can be threaded through the bottom HSS. The distance between flange tips and the load collar is measured at installation, and the spherical bearing is then centred about the roller to ensure the assembly is geometrically square.

Before testing, the measurements of the initial cross-section twist are taken, and the instrumentation is installed. Cable transducers, LVDTs and clinometers are verified, rollers are released, stabilizing blocks at the knife edges are removed, and the instrumentation is zeroed. A dry run is performed, loading the specimen up to 10% of the anticipated buckling load to observe the physical behaviour and ensure the test specimens, the overall assembly, and instrumentation behave as expected. The operator controls the load rate during the test, maintaining a rate between 0.5 to 1.0 kN/s until the load–displacement response begins to plateau. At this stage, the load rate is slowly reduced as the specimen gradually continues to pick up load and deform laterally, until the applied load is no longer resisted and the specimen deflects freely. The load is then held constant, as the post-buckling response is recorded so long as maximum limits of lateral displacement or cross-section rotation are not observed. The hydraulic pressure of the actuators is released when nearing either 80 mm of lateral displacement or 9º of top flange rotation or once the applied load has dropped by approximately 10% of the maximum load, ending the test.

3.2   Heat-straightening Experiments

The heat-straightening experimental program intends to provide qualitative and practical insight into the stability response and load-carrying capacity performance of members repaired through heat-straightening. Heat-straightening was performed on two specimens tested in the first phase of this project, G8-390-32-2-p and G8-390-25-2-p, and on the entire G9 series. This test program was carried out in collaboration with Supreme Group by developing the heat sequence following the requirements specified by CSA W59-18 and AWS D1.1. The practitioners' intuition and knowledge have been relied upon to produce results representative of how the procedure may be conducted in the field. At the practitioners' advice, slight alterations to the straightening procedure, such as cycling the girders a third time or utilizing an external load, were carried out in order to meet dimensional tolerances. Depending on the extent of damage and the specimens' behaviour during the procedure, no two members in this study saw identical heat-sequences. However, the general procedure described herein has been followed.

3.2.1 Specimen Characteristics

3.2.1.1 Test Matrix

Heat-straightening is a common practice of steel fabricators and is often used to repair damaged structural steel members, or correct members found not to be within dimensional tolerance. However, the load-carrying performance of a heat-straightened member is not often studied. Thus, an experimental program has been developed, where damaged welded steel girders are heat-straightened to satisfy dimensional tolerances and retested for LTB. To qualify for heat-straightening, the specimens of the LTB test program had to exhibit permanent (plastic) damages following LTB that exceeded global or cross-sectional dimensional tolerances specified by CSA W59-18. Additionally, the magnitude of global or cross-sectional imperfection had to differ considerably from the as-built condition. "Repair" then, a term used throughout this research, is the alteration of a specimen's geometric properties such that the specimen's geometric condition is returned from an out-of-specification state into tolerance. Of all the global and cross-sectional geometric imperfections, the lateral deviation from straightness increased most significantly following the LTB failures and is the criterion that dictated a need for repair. The following girders exhibited lateral deviations from straightness exceeding the dimensional tolerance of $L/1000$ and thus, form the heat-straightening programs test matrix: G8-390-32-2-p, G8-390-25-2-p, G9-360-32-3-p, G9-360-25-3-f, and G9-430-25-3-f.

3.2.1.2 Cross-section Measurements

The cross-sectional dimensions of the specimens to be heat-straightened are measured following the methods discussed in Section 3.1.1.2 for both the damaged and repaired states. Dimensions such as the plate thickness, flange width, and section depth remain constant regardless of the condition and, therefore, are not remeasured. However, there is potential to observe cross-sectional distortion following LTB or resulting from the localized heating of the repair. For this reason, the dimensions h_i and $h_{i,w}$ are re-evaluated at nine equally-spaced stations along the girder length. The difference of these parameters, $h_i - h_{i,w}$, is a measure of flange warpage (as discussed in Section 3.1.1.2), and therefore, a change in $h_i - h_{i,w}$ between the as-built, damaged and repaired states may indicate the development of cross-section distortion. Table 3-5 contains the average magnitudes of $h_i - h_{i,w}$ measured. Comparing the values of $h_i - h_{i,w}$ reveals that the measured flange warpage differs negligibly from the as-built condition after LTB and heat-straightening. In fact, the

parameters $h_1-h_{w,1}$ and $h_2-h_{w,2}$ differ by no more than 2 mm among the three states considered, and most of the changes are likely within the range of measurement error. Given this observation, it can be stated that the girder cross-sections did not permanently (plastically) distort, either as a result of LTB or heat-straightening.

Table 3-5: Flange warpage measurements of the as-built, damaged and the repaired states

Specimen ID	As-built		Damaged		Repaired	
	$h_1-h_{1,w}$ (mm)	$h_2-h_{2,w}$ (mm)	$h_1-h_{1,w}$ (mm)	$h_2-h_{2,w}$ (mm)	$h_1-h_{1,w}$ (mm)	$h_2-h_{2,w}$ (mm)
G8-390-32-2-p	-6	3	-6	3	-5	3
G8-390-25-2-p	-6	2	-6	2	-4	2
G9-360-32-3-p	-2	-1	-2	-2	-2	-1
G9-360-25-3-f	-4	-1	-4	-1	-4	0
G9-430-25-3-f	-1	-5	-1	-5	-1	-6

3.2.1.3 Global Geometric Measurements

Global measurements are collected as per the methods described in Section 3.1.1.3, where the specimens' lateral sweeps, cambers and cross-section twists are measured in the damaged state and after repair. Table 3-6 and Table 3-7 summarize the girders' global geometric measurements when damaged and after heat-straightening, respectively. The cross-section twist was not measured in the damaged state and is therefore not included in Table 3-7. Otherwise, the maximum measured geometric imperfections are provided, following the sign convention described in Section 3.1.1.3.

Table 3-6: Global geometric imperfections of damaged specimens

| Specimen ID | L | Sweep | | Camber | |
| | | Top Flange | Bottom Flange | Top Flange | Bottom Flange |
	(mm)	(mm)	(mm)	(mm)	(mm)
G8-390-32-2-p	9760	-31.0	-19.0	-11.5	-12.5
G8-390-25-2-p	9751	-13.0	-2.0	-5.0	-9.0
G9-360-32-3-p	9754	-20.0	-1.5	1.3	2.1
G9-360-25-3-f	9767	10.0	1.5	-4.0	-3.4
G9-430-25-3-f	9764	15.0	2.5	-3.8	-3.8

The lateral sweep of the damaged specimens ranged between $L/1000$ to $L/310$ in the top flange and between $L/6500$ to $L/500$ in the bottom flange. The mean top and bottom flange sweeps of the damaged specimens are $L/700$ and $L/4500$, respectively. Every damaged specimen exhibited a lateral deviation of the top flange exceeding the dimensional tolerances of CSA W59-18. In contrast, the bottom flange of the damaged specimens generally did not sweep more than $L/1000$, except for G8-390-32-2-p, which swept 19 mm westwards. The mean values of the top and bottom flange camber are $L/3100$ and $L/2400$, respectively, and when compared to the mean as-built top and bottom flange cambers of $L/4700$ and $L/4400$, an increase of nearly double the mean magnitude is observed. However, like the observations for the bottom flange sweep, the camber of the damaged specimens fell within tolerance ($L/1000$), with the exception of G8-390-32-2-p.

Table 3-7: Global geometric imperfections of repaired specimens

| Specimen ID | L | Sweep | | Camber | | Twist |
| | | Top Flange | Bottom Flange | Top Flange | Bottom Flange | |
	(mm)	(mm)	(mm)	(mm)	(mm)	(°)
G8-390-32-2-p	9760	-11.0	-5.0	-11.5	-12.5	+0.0
G8-390-25-2-p	9751	+2.5	-1.0	-14.0	-13.3	+0.3
G9-360-32-3-p	9754	-6.0	+2.5	+0.4	+1.1	-0.6
G9-360-25-3-f	9767	-3.3	-1.0	-5.0	-6.0	+0.3
G9-430-25-3-f	9764	+5.0	-2.5	-5.5	-4.0	+0.6

After repair, the specimens' top and bottom flange sweeps ranged from L/890 to L/3900 and from L/2000 to L/9800, respectively. The mean value of the top flange sweep is L/2300 and L/5900 in the bottom flange. G8-390-32-2-p is the only specimen not brought within tolerance by heat-straightening, due to limitations on the number of allowable heat cycles. As mentioned in Chapter 2, Avent et al. (2000) suggest limiting the number of heat cycles to 2 or fewer in order to minimize the effects of heat-straightening on material properties; for cycles of 4 or more, the loss of ductility and stiffness becomes significant. Therefore, a decision was made to cease the correction of G8-390-32-2-p following the third cycle of heating regardless of the final geometric configuration. All other specimens are brought within tolerance, seeing an average reduction in the lateral sweep of 10 mm. In some cases, the top flange sweep is corrected to magnitudes smaller than was initially received, where a top flange sweep of L/1600 is measured for G9-360-32-3-p after heat-straightening, but when received, was L/1100.

As the heat-straightening procedure was specifically developed to target the weak-axis damage of the girders, which arose from LTB failure, and manifested as lateral deviations from straightness, a minimal change in the camber between the damaged and repaired conditions should be observed. However, specimen G8-390-25-2-p saw a significant increase in the camber between the damaged and repaired states where the top flange and bottom flange cambers increased by 9 mm and 4.5 mm, respectively. The camber increase is primarily the result of a line heat applied to the top flange of this particular specimen. G8-390-25-2-p was the first specimen heat-straightened, and an

attempt was made to remove a downwards flange curl that was present in the as-built and damaged states, in addition to the out-of-tolerance lateral sweep. No other specimens underwent this procedure, but the methods utilized are detailed in Section 3.2.2.2. All other specimens, which are only heated to repair the lateral sweep, exhibited negligible—1 mm to 2 mm—differences in camber after repair.

Cross-section twist was always measured immediately prior to testing with the specimen mounted in the testing apparatus, as described previously, and therefore was only recorded after heat-straightening (repaired). A mean cross-section twist of 0.34º can be compared to the mean cross-section twist of the as-built specimens, 0.52º. A reduction in cross-section twist is observed and expected, as the cross-section twist is related to the relative sweep of the two flanges. As the top flange lateral sweep is brought into tolerance, the relative sweep between the two flanges is reduced, and the cross-section twist is indirectly corrected. In general, the heat-straightening procedure appears to have significantly altered the lateral sweep of the girders with minimal unintended secondary effects.

3.2.1.4 Material Properties and Residual Stresses

The mechanical properties and residual stresses of the heat-straightened material are not explicitly assessed in this study. Consequently, their influence on the LTB response is unknown. Nevertheless, the parameters of heat-straightening, which are known to influence the mechanical properties and residual stresses, such as the temperature, number of heat cycles, and geometry of the heat-affected zone, are controlled and meet the requirements of CSA W59-18 to minimize any influence on the LTB response. The resulting analyses of the LTB response (Chapter 5) are limited to qualitative assessments of the change in LTB behaviours from the original LTB tests or an analysis of the LTB response's sensitivity to geometry changes.

3.2.2   Test Characteristics

3.2.2.1 Heating Patterns

All specimens of the heat-straightening experimental program required correction of the lateral sweep and are subject to the heating pattern described herein. Vee heats are applied in the correction of the weak-axis damage where controlled use of the pattern allows for the introduction of favourable curvatures (opposing the damage) and minimal cross-section distortion. Vee heats

are applied only to the flanges that exhibit an out-of-tolerance lateral sweep, as shown schematically in Figure 3-19. For some specimens (e.g., G8-390-32-2-p), tolerances are exceeded in both flanges, requiring each flange to be cycled and heated independently. Traditionally, both flanges would be heated simultaneously, and a strip heat would be applied to the webs at each Vee location to relax any restraining forces imposed by the web. However, attaining and maintaining the desired temperatures over large areas at each location was not possible in the laboratory setting.

As shown in Figure 3-19, the Vee heats are distributed longitudinally, 0.6 m (2 ft) on center near the mid-span and 1.2 m (4 ft) on center approaching the supports. A variable spacing is implemented to address the concentration of lateral sweep at mid-span, while still distributing the heat-affected zones along the girder length to repair the global deviation. Partial-depth Vees are specified due to equipment limitations and restrictions on heat output. A typical rule of thumb for Vee geometry is to limit the Vee opening between one-third and one-half the Vee depth, and no larger than 254 mm (FHWA 2008), to minimize accidental out-of-plane distortions of the flange. A geometry following these rules corresponds to Vee angles of approximately 20-30º. However, in this study, the depth and opening are kept equal, resulting in a Vee angle of 54º, with primary dimensions (i.e., depth or opening) ranging between 180 mm and 215 mm. Analysis of the flange warpage in Section 3.2.1.2 revealed that the flange and cross-section did not distort during heat-straightening, justifying the use of Vee angles of 54º.
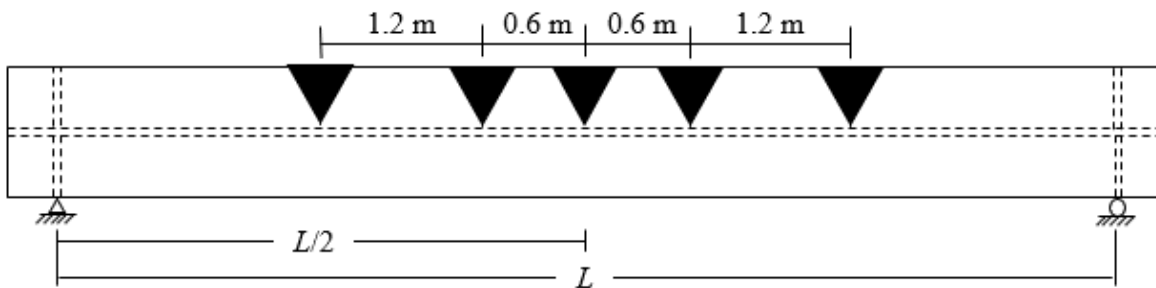
Figure 3-19: Vee heating pattern (intermediate stiffeners not shown)

G8-390-25-2-p was the first specimen repaired, and when assessing the geometry in the damaged condition, the east half of the flange was observed to curl about the flange–web junction and exhibit a maximum downwards offset from the horizontal of 8 mm. The dimensional tolerances of CSA W59-18 limit flange warpage to the greater of $b/100$ and 6 mm, where 6 mm governs for the range of flange widths considered in this study. Therefore, a decision was made to repair the flange

warpage, and through consultation with Supreme Group engineers, a heating procedure was developed. A single line heat is specified to pass along the girder length at the top flange–web junction, as shown in Figure 3-20. A line heat located at the centre of a plate will bend or curl the plate about that line, and in this case it is used to pull the downwards curling east half of the flange upwards by thermal contraction. However, the line heat did not lead to an effective repair of the flange warpage along the girder length. Additionally, as reported in Section 3.2.1.2, the parameters $h_i - h_{i,w}$ (which represent flange warpage) changed negligibly after the initial LTB failure and therefore are not considered damage. For these reasons, no further flange warpage repairs were attempted.
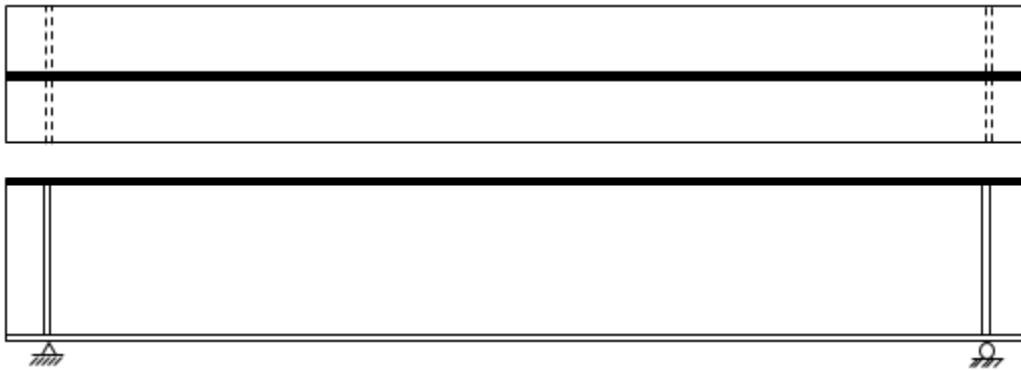
Figure 3-20: Line heating pattern for G8-390-25-2-p (intermediate stiffeners not shown)

3.2.2.2 Straightening Procedures

In preparation for the Vee heat procedure, the specimens are supported about their weak axis, sweeping upwards. Pedestal supports are located at the girder ends, directly adjacent to the bearing stiffeners, supporting the web of the girder. The Vee heats are located and marked as described in Section 3.2.2.1, by white paint pen, on the out-of-tolerance flanges. A total external dead load of 12 kN (2.68 kip) is applied before heating and is centred around the mid-span of the specimens, bearing on the flange tips, as shown in Figure 3-21. The external load is introduced to assist in straightening and reduce the number of cycles required by increasing the amount of movement per cycle of the procedure. CSA W59-18 specifies the use of external loading for this purpose, provided that the external load does not induce yielding of the specimens at the elevated temperature. The specimen with the lowest out-of-plane moment capacity (G9-360-25-3-f) limits the allowable external load, where the maximum allowable load is 84 kN considering the reduced

yield strengths prescribed for the anticipated maximum temperature by Annex K of CSA S16-19. Beyond this load level, flexural yielding would occur.
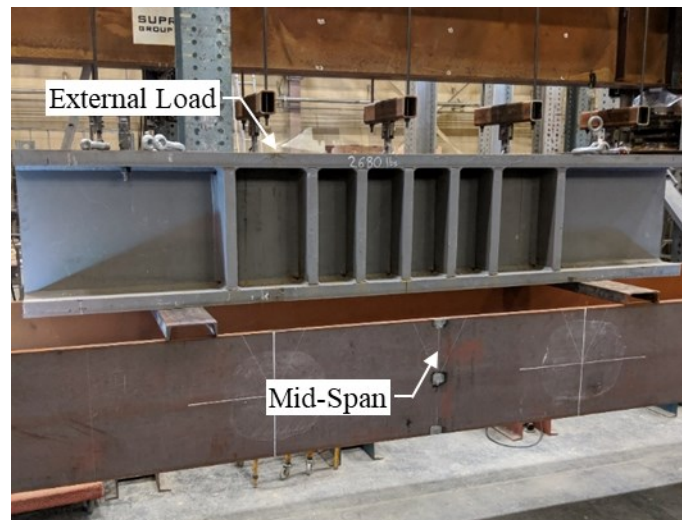
Figure 3-21: External load applied during heat-straightening

Two oxyacetylene torches with Rosebud 15A tips are utilized and operated by two heat-straightening practitioners from Supreme Group. Heating is started at the Vee's closest to the ends and progressively moved inwards towards mid-span as each location reaches the desired temperature of at least 600ºC. A Fluke 56 noncontact infrared thermometer rated to 800ºC is used to record temperatures throughout the process. Temperatures are taken a few seconds after removal of the heat source to eliminate the influence of the torch on the readings and record only the metal temperature. The practitioners heated the Vee's in a snaking pattern, varying the direction of travel between the Vee's closed and open ends until the desired temperatures are achieved. No specimen was permitted to exceed 650ºC, where the maximum temperature recorded was 645ºC, and on average, the minimum and maximum temperatures ranged between 592ºC and 640ºC. Temperatures in this range were indicated by the attainment of a cherry-red colour over the entire heated area, as shown in Figure 3-22.

Figure 3-22: Vee heat on the damaged specimen at the desired temperature

The Vee heat procedure is cycled until the lateral sweep of the specimens is brought within tolerance, where one full cycle includes the heating of the Vee's to the desired temperature and the ambient cooling of the specimen until at most 315ºC. Measurements of the girder's elevation above the laboratory floor are taken before heating, at the maximum temperature, and after cooling, per cycle. The difference in elevation to the girder's flange between cycles represents the specimen's lateral movement. A girder must move at least the difference between the measured lateral sweep and L/1000 mm to be brought within tolerance. For instance, the damaged G9-360-32-3-p specimen initially presented with a 20 mm lateral sweep at the mid-span, which is approximately 10 mm out-of-tolerance. Before the first cycle of heating, the distance measured between the floor and the girder's flange was 768 mm, and after cooling the distance was 762 mm, totalling 6 mm of lateral movement. The specimen must move an additional 4 mm to meet the L/1000 mm tolerance. An acceptable elevation following a cycle of the Vee heat procedure would range between 738 mm to 757 mm. G9-360-32-3-p was therefore cycled a second time, and the entire procedure repeated. The lateral sweep correction for all specimens is approached in this manner, where the measured elevation of the flange dictates the need for additional movement through more cycles. All specimens were allowed to cool ambiently at room temperature, and the elevation measurements are taken below 80ºC.

In some instances, the generalized Vee heating procedure, as outlined above, is slightly modified during a repair. However, consistency between specimens is maintained by controlling Vee

geometries, Vee locations, and the practitioner's approach to heating the material. The modifications include performing more than two cycles of heating, removing the external load, or heating only three of the five Vee heat locations. As mentioned earlier, G8-390-32-2-p and G9-360-32-3-p remained out-of-tolerance following the second heat. A decision was made to cycle these specimens a third and final time, accepting the final geometric conditions, regardless of tolerances, to avoid significant effects on the material properties. Some girders had minimal imperfections and did not require the application of an external load—specifically G9-360-25-3-f, which required only 1 mm of movement to meet tolerance. In some instances, often for the second and third cycles of heating, a reduced number of Vee's were heated, either concentrating the localized heat to the three-interior Vee's or the two exterior Vee's and the middle Vee.

A line heat is applied to G8-390-25-2-p to correct a downward curl of the east half of the flange, as shown in Figure 3-23. In this procedure, G8-390-25-2-p is oriented vertically and supported at either end by pedestal supports located at the bearing stiffeners. Two oxyacetylene torches apply the line heat starting from the mid-span and moving outwards along the web−flange junction towards the end supports. Temperatures are recorded trailing the torch tip to ensure the steel does not exceed 650ºC. Each torch progresses at a rate capable of sustaining a cherry-red colouring of the steel for the entire length of the girder. Jacking forces are applied to the underside of the east half of the flange to assist in bending this portion of the flange upwards, about the web–flange junction. The west half of the flange is initially relatively plane and not curling. Therefore, the west half of the flange is braced at discrete points along the girder length to prevent the rigid body rotation of the entire flange about the web–flange junction and encourage only the bending of the east half of the flange about the line heat.

The distance between the top and bottom flange is measured at stations along the girder length between cycles of this procedure, where any height difference represents the vertical movement of the flange. The line heat procedure was cycled twice, at which point the vertical movement of the east of the flange was found to be inconsistent along the girder length. At the mid-span, the measured downwards offset of this portion of the flange was reduced to 1 mm from 8 mm. However, along the girder length, the measured downwards offset varied +/- 3.5 mm, with a maximum downwards offset of 6 mm at the girder's north end. No further flange warpage procedures were attempted.

Figure 3-23: Line heat procedure performed on G8-390-25-2-p

4 LATERAL–TORSIONAL BUCKLING EXPERIMENTS: RESULTS

This chapter presents the results of the lateral–torsional buckling (LTB) experimental program, as described in Chapter 3. The test results serve to strengthen understandings of the LTB response of welded girders, assess the influential parameters on LTB, and expand the repository of available experimental test data for use in future research. The capacities and displacements of the G9 series of test specimens are first presented. The results are then used to evaluate the effect of influential parameters, including the geometry, initial geometric imperfections, residual stresses, and cutting method. It should be noted that the experimental data collected and presented by Ji et al. (2019) is included in the analyses of the results, where prudent, to assess the LTB response over the full range of geometries.

4.1 Flexural Capacity

The girders were loaded, as described in Section 3.1.2.1, until the load–deformation response approached a plateau, and buckling initiated. No evidence of local buckling, shear buckling, or other failure modes was visually observed following the experiments. Table 4-1 contains the maximum concentrated transverse load applied at each of the eight points and the respective bending moment sustained by the G9 girders before buckling, alongside the normalized moment resistances. The maximum load, P_{max}, represents the maximum average magnitude of a point load applied to the specimens and is calculated by averaging the eight GLS load cell readings when the total load reached its maximum. The maximum bending moment, M_{max}, is determined at the mid-span, through equilibrium, and is based on the individual maximum GLS load cell readings. The moments induced due to the specimen's self-weight and the load collars are also included in M_{max}. The M_{max} values were normalized by the plastic moment, M_{p}, which is calculated using the measured geometric properties and the measured static yield stresses of both the flange and web plates.

Table 4-1: Maximum applied loads and lateral–torsional buckling moments

Specimen ID	Maximum Load P_{max} (kN)	Maximum Moment M_{max} (kN-m)	M_{max}/M_p
G9-360-32-3-p	185	1852	0.47
G9-360-32-3-f	201	2002	0.50
G9-360-25-3-f	164	1645	0.48
G9-430-25-3-f	242	2408	0.60

4.1.1   Influence of Material Inelasticity

Figure 4-1 is a plot of the normalized moment resistances against the global slenderness ratios, L/r_y. The grey dashed line delineates the limit of elastic lateral–torsional buckling as defined by the CSA S16-19 provisions. For specimens with a normalized moment of 0.67 or higher, CSA S16-19 considers the failure inelastic, and when lower than 0.67, elastic. As indicated in Figure 4-1, the moment resistances range between 0.47 and 0.85, with 7 of the 11 total specimens falling below the elastic limit. It should be noted that all the specimens were initially designed to fail inelastically, with normalized moments ranging between 0.69 and 0.92, as shown in Figure 3-1 of Section 3.1.1.1. However, it was found that a considerable difference exists between the attained moment resistances and the anticipated moment resistances, as most specimen's moment resistances are significantly less than the anticipated values. The G9 series, which were nominally designed as Class 3 but received as Class 2, as noted in Section 3.1.1.7, exhibited particularly low moment resistances as compared to the respective nominal design capacities reported in Section 3.1.1.1. It is theorized that the load height effect considerably reduced the moment resistances, as the specimens are loaded 178 mm above the top flange of the girders during the tests, as was noted in Section 3.1.2.1. Nonetheless, the classification of the LTB failure (elastic vs. inelastic) requires an analysis of the stresses at the onset buckling as the CSA S16-19 LTB provisions may not accurately predict inelastic buckling in all cases, and particularly for those that are close to the limit.
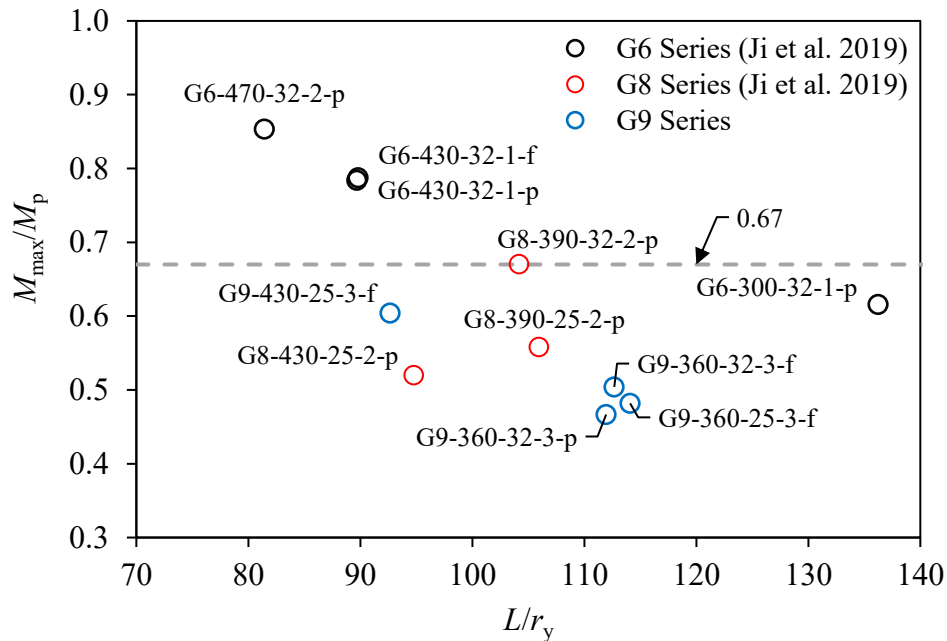
Figure 4-1: Moment resistance vs. global slenderness ratio

Inelastic LTB is characterized by the presence of cross-sectional yielding at the onset of lateral instability. If the net stress, that is, the algebraic sum of the residual stresses and those induced through flexure of the compression flange, equals or exceeds the yield stress at the onset of buckling, the section failed in the inelastic range (Nethercot 1974). Yeilding at the web–flange junction of the tension flange may precede yielding in the compression flange, but as yielding of the tension flange does not compromise lateral stability, it is not considered a criterion to determine material inelasticity during LTB. To assess if yielding occurred and to determine if the test specimens failed inelastically, two sets of three strain gauges installed at the mid-span of the girders, as described in Section 3.1.2.3, were used. The net stress is determined at each gauge location by the addition of the anticipated residual stresses and the stresses calculated from the strain gauge data at buckling. Inelastic LTB has occurred if the calculated net stress exceeds the static yield stress (as measured experimentally).

The anticipated residual stresses are based on the residual stress model proposed by Unsworth et al. (2019) and shown in Figure 4-2. For each girder geometry, the residual stress distribution is assessed, and the anticipated residual stresses present at the strain gauge locations are extracted.

The Unsworth et al. (2019) residual stress model was developed using the sectioning data of the ancillary girders that were fabricated alongside the LTB specimens, as described in Section 3.1.1.6. Ideally, the residual stresses utilized in this flange stress analysis would be based on experimental data rather than a residual stress model. However, sectioning of the test specimens was only completed for G6-430-32-1-p, G6-430-32-1-f, G6-300-32-1-p and G8-430-25-2-p, and no residual stress data is available for the G9 series. Despite this, it is expected that the proposed model offers a close approximation of the probable residual stresses. The factors σ_{tf} and σ_{tw} are the flange and web's peak tensile stresses, respectively, and are equal to the materials' yield stresses. The compressive stresses of the flanges and web, σ_{cf} and σ_{cw}, respectively, are calculated through the equilibrium of the section. The parameter η_f is the parametric high-stress-gradient region width of the flanges, η_{fe} is the width of the edge regions in the flanges and η_w is the parametric high-stress-gradient width on one edge of the web.
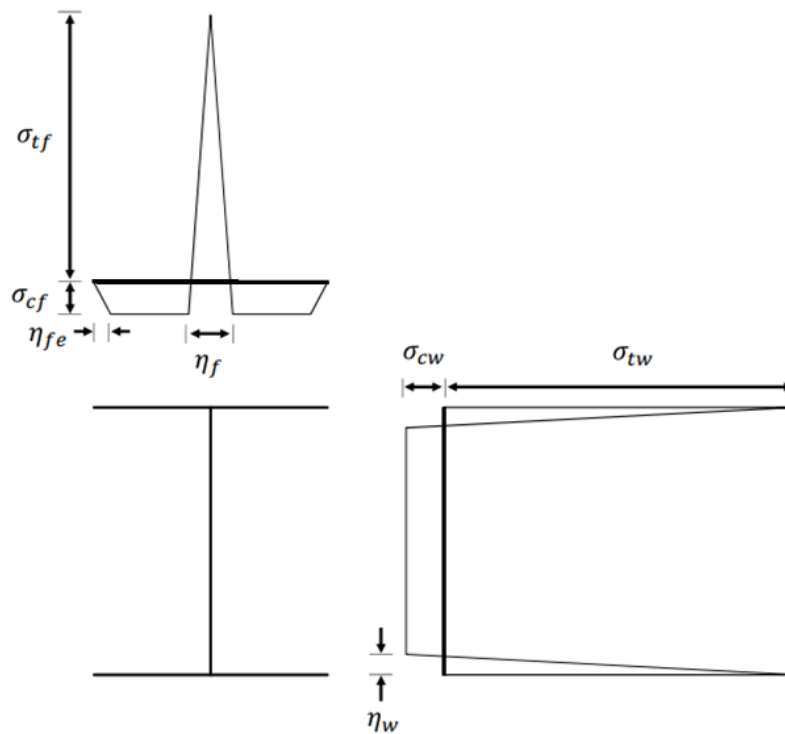
Figure 4-2: Residual stress model proposed by Unsworth et al. (2019)

Strains recorded at the onset of the buckling in each specimen are obtained and multiplied by the measured elastic modulus to determine the stresses developed at the gauge locations. This approach is simplistic and assumes the material remains elastic, and the stress state is uniaxial. If

the material has not yielded, the stresses obtained are considered valid, as the through-thickness and transverse stresses are expected to be negligible; however, the stress may be slightly overestimated if the material becomes inelastic. Despite this simplification, the stresses are approximated sufficiently to confirm whether yielding has occurred. The calculated net stresses should be mindfully interpreted because, while the strain gauges are placed where the theoretical maximum strains are anticipated, this may not be the actual location of maximum strain. Thus, if yielding is not identified at these locations, a definitive statement concerning the type of LTB failure cannot be made, but if yielding of the compression flange is observed, it can be inferred that the specimens failed inelastically. Furthermore, as the strain gauges are located only at the flange tips and the web–flange junction, no conclusive comment can be made on the extent of yielding in the cross-section. The flange stress analysis results for the G9 series are given in Table 4-2, and contained within are the normalized net stresses, F/F_y, determined as described above, for the compression flange at the west and east flange tips, as well as the web–flange junction.

Table 4-2: Stress analysis of the compression flange for the G9 series

Specimen ID	Normalized Net Longitudinal Stress (F/F_y)		
	West Flange Tip	Web–Flange Junction	East Flange Tip
G9-360-32-3-p	0.06	0.51	**-1.06**
G9-360-32-3-f	**-1.00**	0.51	-0.17
G9-360-25-3-f	-0.74	0.49	-0.36
G9-430-25-3-f	**-1.11**	0.37	-0.27

A ratio of F/F_y exceeding +/- 1.0 (bold typeface in the table) indicates material yielding in flexure at the onset of buckling, where positive and negative values of F/F_y denote tensile and compressive stresses, respectively. Flexural yielding is observed in three of the four specimens at the flange tips; only G9-360-25-3-f remained essentially elastic. G9-360-32-3-p and G9-430-25-3-f were found to exceed the yield stress, which suggests that these specimens yielded well before buckling and failed by inelastic LTB. The stress in the west flange tip of G9-360-32-3-f matches exactly the yield stress of the material at buckling, so this girder appears to lie on the boundary between inelastic and elastic LTB. However, the failure of G9-360-32-3-f may be considered inelastic.

Since the strains are only measured at three locations, it is unlikely that the maximum strain was observed.

It should be noted that G9-360-32-3-p exhibited the lowest $M_{\mathrm{max}}/M_{\mathrm{p}}$ value of 0.45 (see Section 4.1.1) and, despite this, the specimen is one of the three in the G9 series to yield. As per CSA S16-19 provisions, G9-360-32-3-p would be expected to undergo elastic LTB but instead, failed in inelastic LTB. Additionally, specimens with $M_{\mathrm{max}}/M_{\mathrm{p}}$ ratios greater than 0.67, which would be expected to undergo inelastic LTB, may instead fail by elastic LTB, as suggested by Ji et al. (2019), where G6-430-32-1-f, which exhibited a $M_{\mathrm{max}}/M_{\mathrm{p}}$ ratio of 0.79, was found to lie on the boundary of inelastic and elastic LTB. These observed inconsistencies suggest that the CSA S16-19 criterion, $M_{\mathrm{max}}/M_{\mathrm{p}} > 0.67$, is not an accurate parameter for predicting inelastic LTB. However, due to the limitations associated with the strain data and the reliance on a residual stress model to conduct the flange stress analysis, the preceding statements should be considered approximate.

4.1.3 Influence of Cross-section Torsional Properties

Within a depth series, the section depth and certain other cross-sectional dimensions remain relatively consistent. Additionally, the effects of individual cross-sectional dimensions are hard to isolate when assessing the LTB response. However, the torsional parameter, R (see Equation 2-4) represents the effects of the torsional stiffness, is known to affect the LTB resistance, and encapsulates the specimens' geometric properties. Figure 4-3 plots the torsional parameter against the ratio $M_{\mathrm{max}}/M_{\mathrm{u}}$ to review the influence of the cross-section's torsional properties on the LTB resistance. M_{u} is the cricitcal elastic moment for shear centre loading specified by CSA S16-19 and is calculated using the measured geometric and material properties of the specimens. Figure 4-3 contains the G6 and G8 series data, as published by Ji et al. (2019), and the G9 series (of this study) differentiated by black, red, and blue markers, respectively.

The G6 series shows a linearly increasing relationship between the parameter $M_{\mathrm{max}}/M_{\mathrm{u}}$ and the torsional parameter R, as shown in Figure 4-3. The G8 series exhibits an unclear relationship with $M_{\mathrm{max}}/M_{\mathrm{u}}$; however, $M_{\mathrm{max}}/M_{\mathrm{u}}$ for the G8 series does increase with increasing magnitudes of the torsional parameter R. In contrast, no clear relationship is observed for the G9 series. The relationships noted in Figure 4-3 suggest that the sensitivity of $M_{\mathrm{max}}/M_{\mathrm{u}}$ to the torsional parameter

R decreases with the class of the cross-section (local slenderness). Furthermore, based on the G9 series results, girders approaching the Class 3 limit, and Class 3 girders themselves, may be altogether insensitive to *R*.
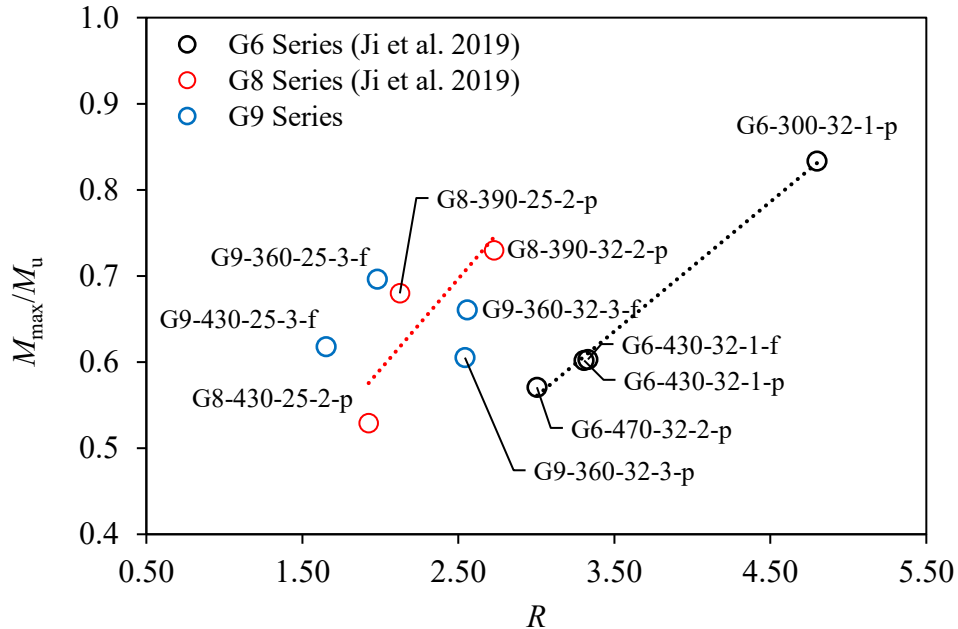
Figure 4-3: Moment resistance vs. torsional parameter

4.1.4   *Influence of Geometric Imperfections*

The relationship between initial geometric imperfection and moment resistance is examined in Figure 4-4 and Figure 4-5, where the normalized moment resistance is plotted against the maximum measured initial compression flange sweep and initial cross-section twist, respectively. Camber is assumed not to influence the LTB response significantly, as it should not contribute to the lateral displacement of the girder and trigger LTB. Similarly, the initial bottom flange sweep is expected to minimally impact the LTB response, as it is in tension and does not significantly contribute to the initiation of LTB. On the x-axis of Figure 4-4 is the measured initial compression flange sweep normalized by the maximum allowable imperfection of *L*/1000. No such limit is specified for initial cross-section twist, and therefore the actual magnitude of the initial cross-section twist is considered in Figure 4-6. Some girders do not buckle in the direction following their initial geometric imperfections; such girders are denoted by a cross through the plotted marker.
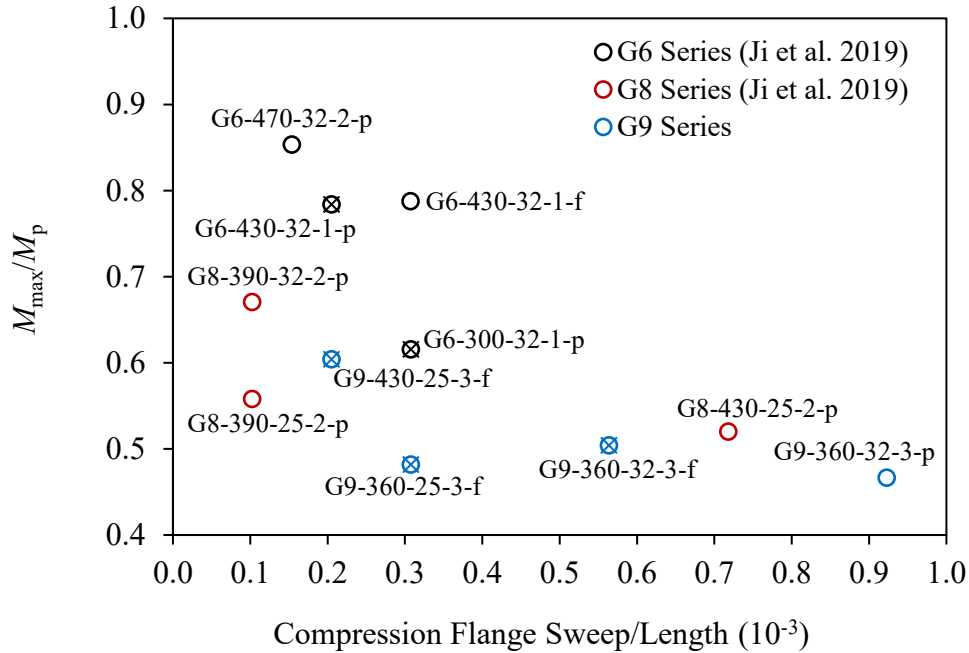
Figure 4-4: Moment resistance vs. initial compression flange sweep

As shown in Figure 4-4, as normalized initial compression flange sweeps increase and approach a ratio of 1.0 on the horizontal axis, the moment resistances tend to reduce. Furthermore, there is a tendency towards lower M_{max}/M_p ratios with increasing initial compression flange sweep when isolating the results based on depth series. It appears that the girders with relatively large initial compression flanges sweep (greater than 0.55 times $L/1000$), which buckle in the direction of this imperfection, are more likely to exhibit lower moment resistances than those girders with an initial compression flange sweep less than 0.35 times $L/1000$. For girders that buckle in the direction opposite to their initial compression flange sweep, it is expected that these specimens would exhibit higher moment resistances than otherwise; however, this is not necessarily reflected in Figure 4-4. Examining Figure 4-5 reveals no relationship between the magnitude of the initial cross-section twist and moment resistance. Specimens with large initial cross-section twists do not appear to be more likely to exhibit lower moment resistances.
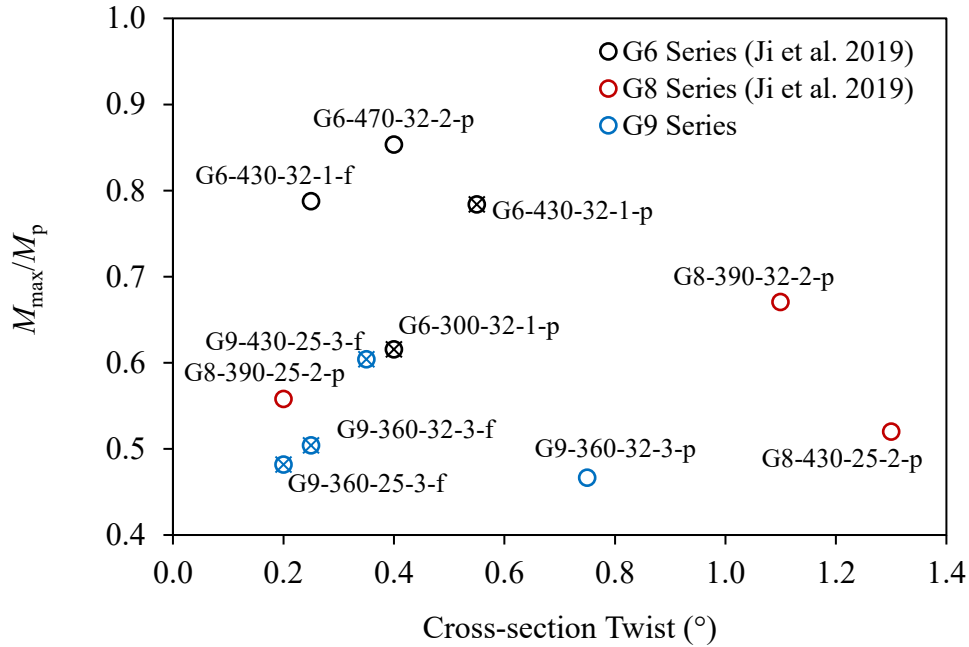
Figure 4-5: Moment resistance vs. initial cross-section twist

4.1.5   Influence of Cutting Method and Residual Stresses

The effects of flame-cutting and plasma-cutting on the LTB response of welded girders are examined through a comparison of the moment resistances of the specimen pairs G6-430-32-1-p, G6-430-32-1-f, and G9-360-32-3-p, G9-360-32-3-f. The pairs differ only by the plate cutting method; all geometric properties are nominally identical, and the remaining fabrication procedures remain unchanged. The response of the former pair (the G6 pair) has been discussed by Ji et al. (2019). The moment resistances of the G6 pair differed negligibly (0.4%), suggesting there is little-to-no discernable difference between the two cutting methods and their influence on the LTB response (Ji et al. 2019). However, the latter pair (the G9 pair), experimentally tested in this study, exhibit a significant difference in the moment resistance, where the LTB capacity of G9-360-32-3-p is 7.5% lower than that of its flame-cut counterpart, G9-360-32-3-f. Thus, the residual stresses and geometric properties are assessed to determine if it is the cutting method, or otherwise, contributing to the appreciable difference in moment resistance of the G9 pair.

The pairs' nominal geometric properties are identical, but the specimens are fabricated with different cross-sectional dimensions and initial geometric imperfections. The measured cross-sectional dimensions reported in Table 3-2 of Chapter 3 are examined to find no considerable

difference between the cross-sectional geometries of a girder pair. However, the global geometric measurements differ considerably and may influence the LTB response. Therefore, the initial compression flange sweep and cross-section twist of the specimens have been summarized in Table 4-3 for comparison with the moment resistances, $M_{\max}$.

Table 4-3: Comparison of initial compression flange sweep and cross-section twist with the moment resistance for identical girders with different cutting methods

Specimen ID	Lateral Sweep (mm)	Cross-section Twist (°)	$M_{\max}$ (kN-m)	Percent Difference in Moment Capacity
G6-430-32-1-p	-2.0	0.55	2349	
				0.42%
G6-430-32-1-f	-3.0	-0.25	2359	
G9-360-32-3-p	-9.0	-0.75	1852	
				7.50%
G9-360-32-3-f	-5.5	0.25	2002	

Table 4-3 shows the average initial compression flange sweep of the G9 pair to be nearly three times larger than the average of the G6 pair. Furthermore, the magnitude of initial compression flange sweep in G9-360-32-3-p is 3.5 mm larger than G9-360-32-3-f and relative to the sweeps present in the G6 pair, a 3.5 mm difference is significant. G9-360-32-3-p also exhibits a relatively large magnitude of initial cross-section twist, and this cross-section twist corresponds to a rotation of the cross-section such that girder's top flange is displaced as a result of the initial cross-section twist in the direction of the measured lateral sweep. These geometric imperfections may combine and contribute to the lower moment resistance exhibited by G9-360-32-3-p. In contrast, the maximum initial compression flange sweep and cross-section twist of G9-360-32-3-f oppose each other. Moreover, G9-360-32-3-f buckles in the opposite direction of its initial compression flange sweep, but in the direction of its initial cross-section twist, which may favourably influence the moment resistance. It is likely that the large and detrimental combination of initial geometric imperfection in G9-360-32-3-p contributed to the observed difference in moment resistance as opposed to the cutting method. However, the influence of residual stresses should be addressed.

Residual stresses resulting from flame-cutting are expected to increase the LTB capacity (Cherenko and Kennedy 1991), as welded steel girders constructed with flame-cut plates typically

present with high tensile stresses along the plate edges (Alpsten and Tall, 1970, Bjorhovde et al. 1972). These tensile stresses delay the progression of yielding in the compression flange and, consequently, delay minor-axis stiffness deterioration. When plasma-cutting is used, compressive residual stresses, or very limited tensile stresses, are measured at the flange tips (Unsworth et al. 2020), yielding develops within the compressive region at the flange tips, and buckling occurs at a lower moment than would be expected of a flame-cut specimen. Table 4-3 shows that the flame-cut specimens, G6-430-32-1-f and G9-360-32-3-f, exhibited higher moment resistances than the plasma-cut girders, aligning with these expectations. However, the negligible difference in the moment resistance of the G6 pair (0.4%) suggests that the difference between cutting methods and the resulting residual stresses on the moment resistance is not pronounced. It is theorized that this may be attributed to the width of this tensile region along the flange edge, as in flame-cut plates this width may be quite narrow in some cases (Unsworth et al. 2020) and may not always have a significant influence on the LTB moment resistance.

4.2   Displacement Response

The vertical, lateral and longitudinal displacements, as well as the cross-section rotations of each specimen, were tracked either at the girder mid-span or the reaction points, as outlined in Section 3.1.2.3. The sign convention used for displacement data is similar to that used when discussing the global imperfections in Section 3.1.1.3. Upwards in-plane vertical displacement, eastward out-of-plane lateral displacement, outwards longitudinal displacement (i.e., axial extension) and cross-section rotations by which the top flange translates eastwards are assigned positive values in this study. Table 4-4 and Table 4-5 give the displacement of each specimen at "buckling" and "ultimate", where buckling is defined as the highest bending moment achieved, and ultimate refers to the maximum lateral displacement or maximum cross-section rotation observed immediately before unloading. It should be noted that ultimate displacements cannot be compared directly, as the unloading point was not consistent among specimens.

Table 4-4: Displacements and rotations at buckling

Specimen ID	Vertical Displacement	Lateral Displacement		Cross-section Rotation			Longitudinal Displacement	
		Top Flange	Bottom Flange	Top Flange	Web	Bottom Flange	North	South
	(mm)	(mm)	(mm)	(°)	(°)	(°)	(mm)	(mm)
G9-360-32-3-p	-25.2	-55.1	+4.3	-3.3	-4.2	-2.9	-0.4	+6.7
G9-360-32-3-f	-26.5	+37.6	-5.3	+2.9	+3.0	+1.8	-0.1	-6.0
G9-360-25-3-f	-24.9	+16.8	-3.8	+2.0	+1.4	+0.7	+5.6	+0.3
G9-430-25-3-f	-32.4	+32.7	-7.3	+2.9	+2.6	+1.7	+4.4	+3.2

Table 4-5: Displacements and rotations at ultimate

Specimen ID	Vertical Displacement	Lateral Displacement		Cross-section Rotation			Longitudinal Displacement	
		Top Flange	Bottom Flange	Top Flange	Web	Bottom Flange	North	South
	(mm)	(mm)	(mm)	(°)	(°)	(°)	(mm)	(mm)
G9-360-32-3-p	-25.7	-80.2	+5.6	-4.9	-6.1	-4.1	-0.5	+6.7
G9-360-32-3-f	-27.0	+74.2	-7.7	+5.2	+5.8	+3.6	+0.02	-6.0
G9-360-25-3-f	-25.6	+85.6	-13.1	+7.6	+6.7	+4.6	+5.5	-0.1
G9-430-25-3-f	-31.9	+80.9	-13.2	+6.2	+6.5	+4.5	+4.1	+2.9

4.2.1 Displacement Response Observations

The in-plane vertical displacement of the G9 girders is accompanied by moderate out-of-plane displacement from the onset of loading until the buckling load was achieved; beyond this point, the specimen suddenly destabilized, resulting in significant lateral displacement of the top flange and twisting of the cross-section. The specimens did not always buckle in the direction of their initial compression flange sweep or the angle that follows the initial cross-section twist, as noted in Section 4.1.4. Two specimens (G9-360-32-3-f and G9-360-25-3-f) are unique, as the specimens began buckling in one direction; however, prior to reaching the peak moment resistance, the direction of lateral displacement abruptly changed, and the specimens ultimately failed opposite the direction of their initial lateral displacement.

Symmetrical longitudinal displacement about the girders centreline was anticipated due to the roller–roller end conditions. However, only one end of the girders tended to displace, while the opposite end exhibited nearly zero displacement. G9-430-25-3-f was the only specimen to displace outwards from the centerline of the girder, at both ends. In all cases, the longitudinal displacements developed steadily from the onset of loading until the peak moment was achieved and remained effectively constant from buckling to ultimate.

The tension flange of the specimens displaced laterally between 4 mm to 13 mm, and always in the direction opposite to that of the compression flange. In contrast, the compression flange displaced laterally between 17 mm and 55 mm at buckling to a maximum of 86 mm at ultimate. The magnitude of lateral displacement exceeded the amount of vertical displacement at buckling, with the exception of G9-360-25-3-f. Compared to the data reported by Ji et al. (2019) for G6 and G8 series, the specimens of the G9 series showed a tendency towards increased lateral displacement at buckling, which can be attributed to the increased section depths (i.e., relatively lower lateral stiffness) subject to similar magnitudes of rotation.

Clinometers recorded the top flange, web and bottom flange rotation about the specimen's longitudinal axis throughout the test. At buckling, the three clinometers varied on average +/- 0.8° and differed at most by 1.3°. The variation of rotation between the top, bottom and mid-section elements increased at ultimate, differing on average by +/- 1.5° and at most by 3.0°. The maximum 3.0° difference in rotation observed is the difference between the top and bottom flange of G9-

360-25-3-f. Such a difference between the two flanges suggests that the cross-section of G9-360-25-3-f may have distorted during LTB. Furthermore, the average difference of flange rotation of 1.5° suggests that the entire G9 series may have been susceptible to cross-sectional distortion. In contrast, the G6 and G8 series experienced negligible differences in cross-section rotation (Ji et al. 2019). This observation is further investigated in Section 4.2.3.

4.2.2   Load–Displacement Response

The load–displacement plots of the G9 series are provided in Figures 4-6 to 4-9 to show the LTB response of the specimens and to accompany the observations concerning the displacement response made in Section 4.2.1. The applied loads, P, on the vertical axis of these figures equate to the average of the eight concentrated loads applied to the specimens. The mid-span lateral displacement, Δ_h, and vertical displacement, Δ_v, are measured at the compression flange and the bottom web–flange junction, respectively. The sign convention used to distinguish the direction of translation has not been incorporated in the figures; regardless of the buckling direction, the specimens' translations have been plotted as a positive quantity for visual clarity. However, G9-360-32-3-f and G9-360-25-3-f still show a negative quantity on the horizontal axis, which indicates the development of lateral displacements initially in the direction opposing that of the direction in which the specimens ultimately buckled, as noted in Section 4.2.1. The specimens' load–displacement responses differ primarily by the magnitude of displacement developed prior to buckling, the initial stiffness, and the buckling loads. Numerous parameters may affect the load–displacement responses, including distortion and initial geometric imperfections, which are investigated in Section 4.2.3 and Section 4.2.4, respectively.
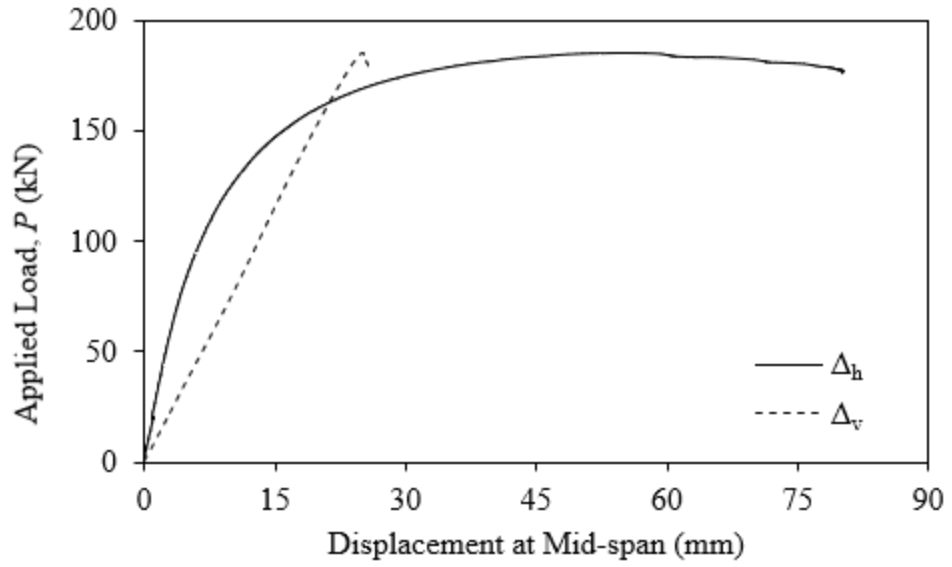
Figure 4-6: Load–displacement response of G9-360-32-3-p
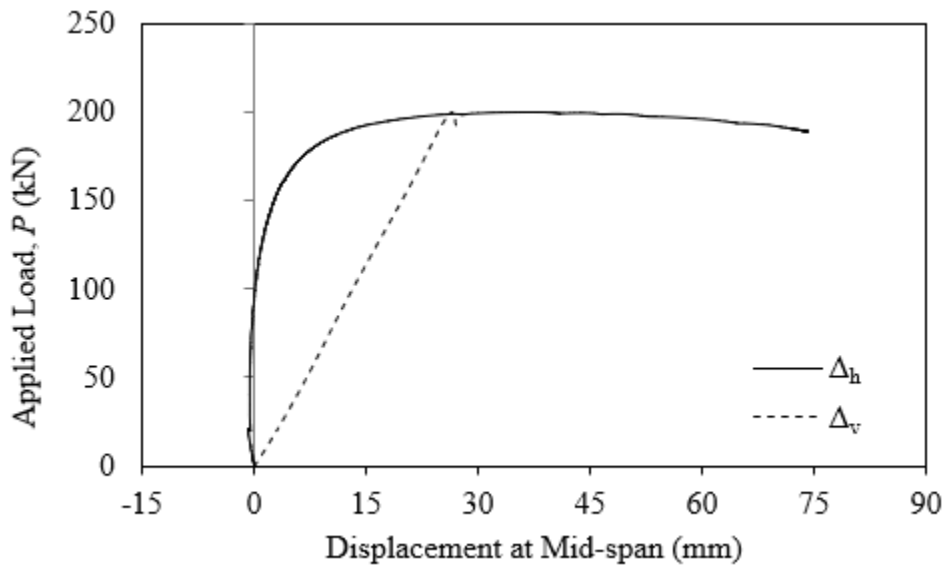
Figure 4-7: Load–displacement response of G9-360-32-3-f
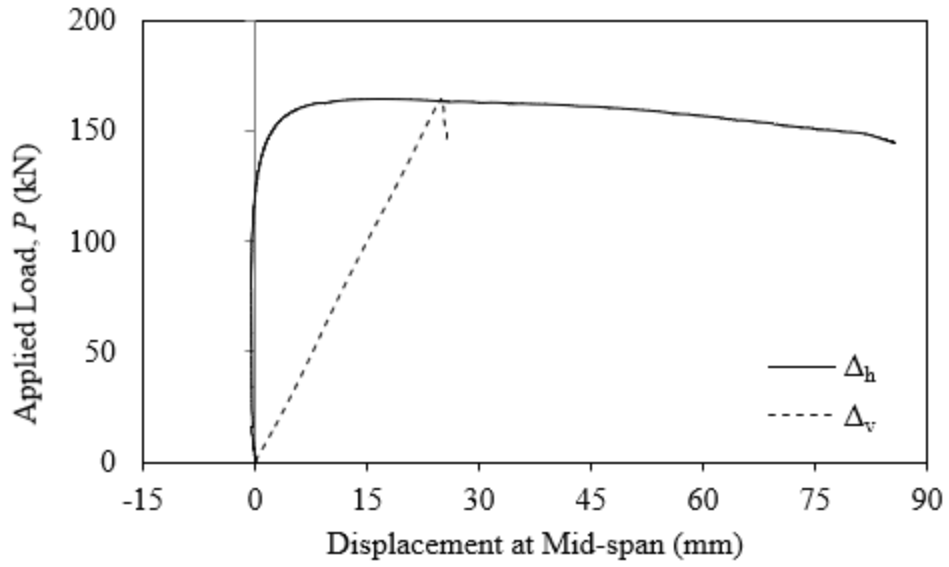
Figure 4-8: Load–displacement response of G9-360-25-3-f
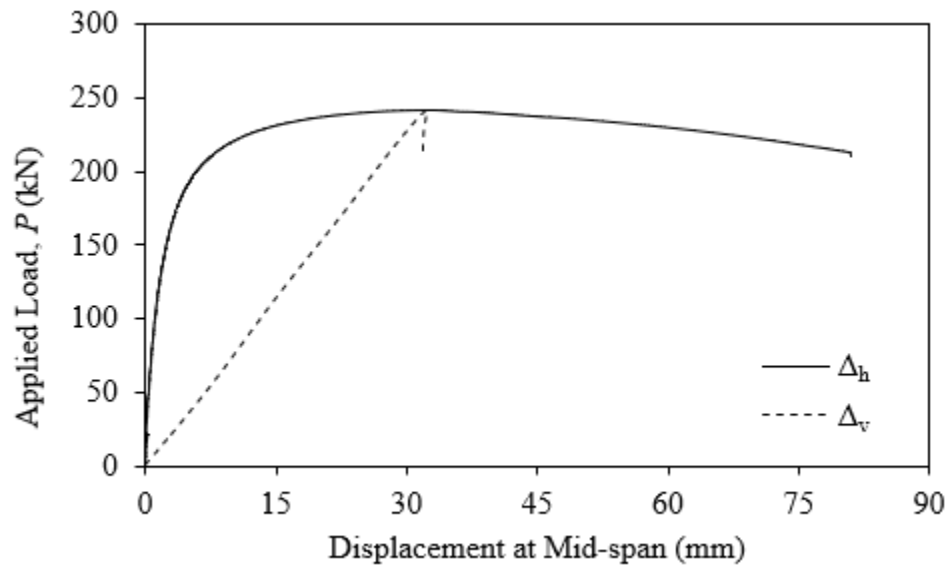
Figure 4-9: Load–displacement response of G9-430-25-3-f

4.2.3   Distortional Buckling

Lateral–distortional buckling (LDB), or distortional buckling, is a failure mechanism of flexural members characterized by simultaneous lateral deflection, cross-section rotation and cross-section distortion at the onset of instability (Bradford 1992). In a traditional LTB response, a girder displaces laterally and rotates as a rigid body, but girders with slender webs or rigid flanges relative to the webs can also distort when buckling, as depicted in Figure 4-10 where φ_c and φ_t are the angles formed between the planes of the displaced compression and tension flanges, respectively, and the horizontal. The presence of web distortion signifies a failure by distortional buckling; often, the criterion used to identify web distortion is the observation of a difference in the magnitude of rotation experienced by the top and bottom flanges. When the web of a flexural member distorts, as shown in Figure 4-10b, the overall cross-section rotations are less than expected in a rigid failure, and the flanges plus the adjacent portions of the web displace laterally, acting as semi-independent beams. In this manner, the effective St. Venant torsional stiffness is reduced, and a lower moment resistance than that of an LTB failure is observed (White and Jung 2007).
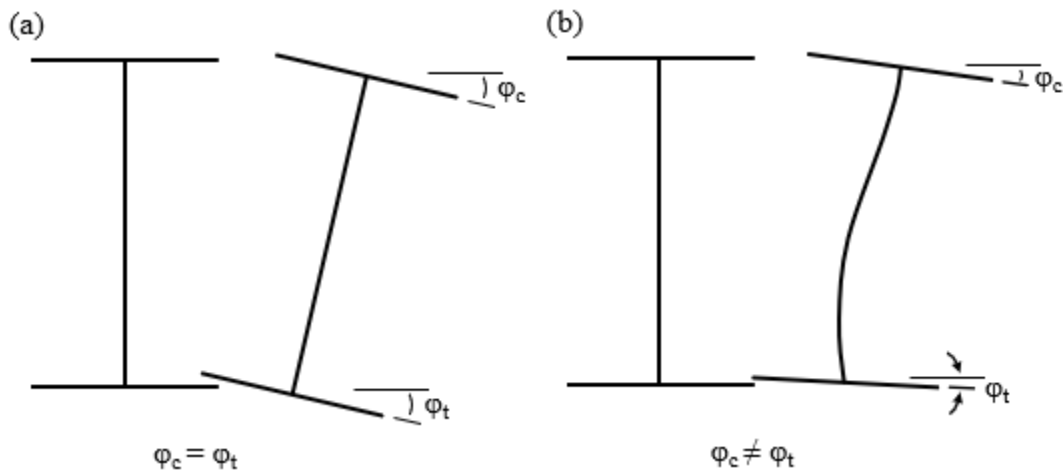
Figure 4-10: Schematic depiction of (a) lateral–torsional buckling and (b) lateral–distortional buckling

Although beams made of cold-formed steel have been the subject of a large number of studies where they undergo distortional buckling, limited experimental data is available exploring the effect of distortional buckling on the moment resistance of girders made of hot-rolled structural steel. Research in this area has primarily been conducted through numerical analyses and focused

on the response of doubly-symmetric rolled I-shapes. However, it is known that the reduction in strength due to web distortion can be significant and most severe in girders with relatively stocky flanges (small ratios of b/t) and flexible webs (large ratios of h/w). White and Jung (2007) reported the results obtained from numerical simulations for girders with $h/w = 90$ and $b/t = 15$, comparable to the G9 girders having $h/w = 86$ and $b/t = 11$ to 17, where a 1 to 9% reduction of the anticipated elastic buckling load is observed and is attributed to web distortion. However, the girders most severely affected by distortion in White and Jung's (2007) study have relatively large ratios of flange thickness to web thickness ($t/w > 6$) and are not comparable in this respect to the G9 series. Therefore, it is anticipated that any reduction potentially experienced by the G9 girders would fall towards the lower end of the losses reported by White and Jung (2007), provided that distortional buckling is verified to have occurred.

Summarized in Table 4-6 are the cross-section rotations for the entire test matrix. Of the top flange, bottom flange and web rotations, the largest rotations are observed in the web, with the top flange rotating at similar but smaller magnitudes. The G6 and G8 series exhibit negligible differences in cross-section rotations at buckling; however, the G9 series are found to have, on average, a 1.0° difference in rotation between the top and bottom flanges, suggesting that the distortion started at or shortly preceding buckling. At ultimate, all three series exhibit a difference in top and bottom flange rotation, where the two rotations differ on average by 1.0°, 1.4°, and 1.8° for the G6, G8 and G9 series, respectively. The maximum difference in cross-section rotation is observed in G9-360-25-3-f, where the bottom flange has rotated 3° less than the top flange. A 3° difference in rotation corresponds to approximately 40% of the overall top flange rotation measured at the ultimate displacement and suggests that the amount of distortion G9-360-25-3-f experienced was appreciable and the girder likely failed by LDB.

Table 4-6: Summary of cross-section rotation at buckling and ultimate

Specimen ID	Buckling			Ultimate		
	Top Flange (°)	Web (°)	Bottom Flange (°)	Top Flange (°)	Web (°)	Bottom Flange (°)
G6-470-32-2-p	+1.4	+1.5	+1.2	+7.0	+7.5	+6.1
G6-430-32-1-p	+2.0	+1.9	+1.4	+8.5	+9.0	+7.2
G6-430-32-1-f	+0.9	+1.0	+0.8	+7.3	+7.6	+6.2
G6-300-32-1-p	-0.8	-0.7	-0.6	-7.1	-7.4	-6.5
G8-430-25-2-p	+3.1	+3.2	+2.8	+7.2	+7.2	+6.2
G8-390-32-2-p	-1.2	-1.2	-0.9	-9.7	-9.5	-7.5
G8-390-25-2-p	-1.9	-2	-1.7	-6.7	-6.8	-5.8
G9-360-32-3-p	-3.3	-4.2	-2.9	-4.9	-6.1	-4.1
G9-360-32-3-f	+2.9	+3.0	+1.8	+5.2	+5.8	+3.6
G9-360-25-3-f	+2.0	+1.4	+0.7	+7.6	+6.7	+4.6
G9-430-25-3-f	+2.9	+2.6	+1.7	+6.2	+6.5	+4.5

No cross-section distortion was observed through a visual examination of the buckled specimens. For repair and retesting as part of the heat-straightening experimental program, comprehensive data on the cross-sectional state exists, as presented in Section 3.2.1.2, which were used to verify the occurrence of distortion. Cross-sectional distortion could manifest as flange tilt or warpage, as a distortion of the web could alter the orientation of the flanges from horizontal. However, it was concluded in Section 3.2.1.2 that specimens did exhibit permanent cross-section distortion as a result of LTB. A lack of permanent deformations suggests that the distortion measured during the experiments was insignificant, or the specimens failed elastically. As reported in Section 4.1.2, a stress analysis of the G9 series revealed three of the four girders yielded before buckling and failed inelastically. Of these, only the flange tips yield at buckling, and while the exact amount of yielding is unknown due to a limited number of strain gauges, it is not unlikely that the web, excluding the

regions immediately around the web−flange junction, distorted when buckling but did not yield and did not result in permanent distortion.

All observations of the test data for the G9 girders indicate that distortion likely occurred simultaneously with buckling. An appreciable difference in top and bottom flange rotation is present at buckling, and it is inferred that the G9 series failed by lateral–distortional buckling; however, the specimens did not exhibit permanent or visual distortion. This failure mode's influence on the buckling response, and M_{max}, is not quantified, but it can be anticipated that the experimental moment resistances are lower than the theoretical LTB moment resistance.

4.2.4   *Effect of Initial Geometric Imperfections on Displacement*

LTB is known to be sensitive to the distribution and magnitude of initial geometric imperfections. In particular, the geometric imperfections of initial lateral sweep and initial cross-section twist are anticipated to influence the magnitude of lateral movement (displacement and rotation) at buckling and are, therefore, compared in Table 4-7. The lateral displacements and cross-section rotations are measured at the specimen's mid-span, while the geometric imperfections are maximum values regardless of the location but often occurring at mid-span. The sign convention first reported in Section 3.1.1.3 is used and applies to both properties (displacement and imperfection).

Table 4-7 shows G9-360-32-3-p, which exhibits the largest initial geometric imperfections of those studied, to exhibit the greatest lateral displacement and cross-section rotation at buckling. G9-360-32-3-p has also buckled in the direction corresponding to the direction of these imperfections. In contrast, G9-360-25-3-f has buckled in the direction opposing both its initial top flange sweep and cross-section twist and exhibits the least lateral displacement and cross-section rotation at buckling. These observations suggest that more displacement and a lower initial stiffness may be expected of a girder that buckles in the direction corresponding to the direction of their initial compression flange sweep or initial cross-section twist. Furthermore, if a girder displaces in the direction opposite to that of its initial imperfection, less displacement and a stiffener response may be expected.

In Table 4-7, G9-360-32-3-f is shown to exhibit opposing initial top flange sweep and cross-section twist values and also exhibited a change in the direction of lateral displacement during the test. G9-360-32-3-f ultimately failed following the direction of the initial cross-section twist and not the initial top flange sweep, despite exhibiting relatively a relatively large initial top flange sweep of 5.5 mm. While the relative influence of initial compression flange sweep or initial cross-section twist on the LTB response is unclear, this observation suggests that initial cross-section twists can appreciably influence LTB and the displacements at buckling.

Examining the initial bottom flange sweeps in Table 4-7 reaffirms that the bottom flange sweep is likely an uninfluential parameter. The specimens with appreciable initial bottom flange sweep do not necessarily exhibit increased lateral translations or cross-section rotation at buckling, nor do the specimens with minimal initial bottom flange sweep report less displacement.

Table 4-7: Comparison of lateral displacement and cross-section rotation at buckling with initial lateral sweep and cross-section twist

Specimen ID	Lateral Displacement		Cross-section Rotation			Initial Lateral Sweep		Initial Cross-section Twist
	Top Flange	Bottom Flange	Top Flange	Web	Bottom Flange	Top Flange	Bottom Flange	
	(mm)	(mm)	(°)	(°)	(°)	(mm)	(mm)	(°)
G9-360-32-3-p	-55.1	+4.3	-3.3	-4.2	-2.9	-9.0	-0.5	-0.75
G9-360-32-3-f	+37.6	-5.3	+2.9	+3.0	+1.8	-5.5	-4.5	+0.25
G9-360-25-3-f	+16.8	-3.8	+2.0	+1.4	+0.7	-3.0	-2.0	-0.20
G9-430-25-3-f	+32.7	-7.3	+2.9	+2.6	+1.7	-2.0	2.5	-0.35

5 HEAT-STRAIGHTENING EXPERIMENTS: RESULTS

This chapter presents the results and analysis of the heat-straightening experimental test program. The test program aims to evaluate the LTB response of heat-straightened welded steel girders, provide practitioners with insight into the performance of heat-straightened flexural members, and produce a new experimental database on such girders. The subsequent analysis focuses on the changes in the LTB response with respect to the behaviour reported in Chapter 4 for the original test specimens. Comparison with the original test results serves to identify the influential parameters of the heat-straightening process that affected the LTB performance and evaluate the efficacy of heat-straightening welded steel girders. Chapter 5 is organized around the two primary aspects of LTB: the strength and displacement responses. Each aspect is discussed independently, where the relevant data is initially presented and then studied for sensitivity to the parameters of the heat-straightening procedure and geometry.

5.1 Flexural Capacity

The heat-straightened girders were retested following the same procedures as for the original specimens, outlined in Chapter 3. The test capacities of the heat-straightened specimens are summarized in Table 5-1. The maximum average (of eight) point load (P_{max}) and maximum moment (M_{max}) are collected as was described in Section 4.1.1, and herein are designated as P_{HS} and M_{HS}, for distinction from the original LTB test results. Similarly, the plastic moments, M_p, used to normalize the test moment capacities have been calculated as reported in Section 4.1. Observations of the specimens during testing showed the typical signs of LTB failure: deflecting primarily in-plane, with some out-of-plane movement typical of imperfect girders, until lateral instability occurred. Additionally, all the heat-straightened girders have buckled in the direction of their measured initial geometric imperfections. The specimens were visually observed at the peak load, and after testing, for signs of other failure modes such as local buckling and web crippling to find only the signs of LTB.

Table 5-1: Maximum applied loads and lateral–torsional buckling moments

Specimen ID	Maximum Load P_{HS} (kN)	Maximum Moment M_{HS} (kN-m)	M_{HS}/M_p
G8-390-32-2-p	206	2049	0.52
G8-390-25-2-p	163	1633	0.49
G9-360-32-3-p	199	1989	0.50
G9-360-25-3-f	153	1534	0.45
G9-430-25-3-f	214	2134	0.54

5.1.1 Evaluation of Moment Resistance

The achievable moment resistance of a specimen repaired through heat-straightening is affected by the geometric conditions after repair and potential changes to the material properties. It is desired that the repaired specimens should perform at or near the original performance, and if there is degradation, the girders should still nominally resist the factored design forces. Therefore, the moment resistances pre- and post-repair are compared in Table 5-2 to assess the efficacy of heat-straightening on specimens for re-use as structural elements. Note that M_{max}, which denotes the moment resistance of the original specimens, is replaced by M_o herein and referred to in the text as the original moment resistance.

Table 5-2: Comparison of original and heat-straightened moment resistances

Specimen ID	Original Moment, M_o (kN-m)	Heat-Straightened Moment, M_{HS} (kN-m)	M_{HS}/M_o
G8-390-32-2-p	2619	2049	0.78
G8-390-25-2-p	1869	1633	0.87
G9-360-32-3-p	1852	1989	1.07
G9-360-25-3-f	1645	1534	0.93
G9-430-25-3-f	2408	2134	0.89

The data presented in Table 5-2 indicates there has been an overall degradation of the moment resistances of the heat-straightened specimens, and, on average, the moment resistances are 9% lower than those of the original LTB tests. At the most extreme, the loss in flexural strength is significant, where G8-390-32-2-p exhibited a 22% reduction in the moment resistance. For engineers specifying the application of heat-straightening, a reduction of this magnitude is concerning, as the specimen in question would likely not perform satisfactorily under the original design loads. However, as shown for G9-360-32-3-p, the moment resistance of the heat-straightened girder has increased by 7%, suggesting that a lower moment resistance is not an inherent characteristic of heat-straightening. Furthermore, some girders that have lower moment resistances exhibit less significant losses (-7% to -11%). The factors that influenced the moment resistance and how they can be controlled are discussed in the subsequent sections.

5.1.2   Influence of Heat-straightening

A generalized heat-straightening procedure was developed under the guidance and advice of heat-straightening practitioners from Supreme Group, as described in Section 3.2.2.2, to repair the LTB program's failed test specimens. Some parameters of the heat-straightening procedure, such as the maximum temperature, number of heat cycles performed, and Vee geometry, can influence the material's mechanical properties, and consequently, may influence the LTB response. As these parameters vary per application of the heat-straightening procedure, they have been summarized in Table 5-3 for comparison with the percent difference in moment resistance.

The maximum measured temperature, irrespective of the heat cycle and the Vee heat it corresponds to, is provided in Table 5-3. It is assumed that only the maximum temperature is of concern, as it should not exceed the lower phase transition temperature of the material. As shown, the provisions of CSA W59-18 concerning the maximum steel temperature are satisfied, and no girder exceeds 650°C. However, it should be noted that the maximum temperature of G8-390-32-2-p and G8-390-32-2-p are not reported, as the temperature measuring device available at the time of these tests was rated to 250°C. When heat-straightening G8-390-32-2-p and G8-390-32-2-p, a cherry-red colouring of the steel (as shown in Figure 3-22), was relied upon to denote the attainment of the desired temperature. Following this method, temperatures can range +/-100°C of the target (Roeder 1986), and as a result, the lower phase transition temperature could have been reached or exceeded in portions of the heated areas of G8-390-32-2-p and G8-390-32-2-p, but this is unlikely.

Comparing the maximum temperatures with the percent change in moment resistance, the specimen that experienced the overall lowest temperatures (G9-360-32-3-p) is the only girder to exhibit an increased moment resistance after repair, which is notable. However, there is an overall lack of temperature data and many interrelated parameters that may affect the moment resistance, making it difficult to comment on a relationship between the temperature and the loss of flexural strength.

The number of cycles performed to straighten the girders is shown in Table 5-3. As noted in Chapter 3, G8-390-32-2-p and G9-360-32-3-p were cycled a third time in an attempt to meet dimensional tolerances. Examining the percent change in moment resistance of these two girders reveals that a third heat cycle did not particularly influence the moment resistance. In fact, these girders exhibit opposing changes in the moment resistance, where G8-390-32-2-p exhibited the single largest reduction in moment resistance, and G9-360-32-3-p is the only girder to exhibit an increased moment resistance after repair. Given this observation, if the heat-straightening procedure has influenced the material's mechanical properties, it is unlikely to be related to the number of heat cycles. Furthermore, a strength gain despite the third cycle of heat suggests the material effects due to this parameter may be less influential than anticipated.

The Vee width, depth, angle and surface area are provided in Table 5-3. It should be noted that G8-390-32-2-p and G8-390-25-2-p were the first two specimens repaired, and at this time, the research intent was to follow the practitioner's judgment entirely, leaving them to mark the Vee geometries and mimic field conditions. As a result, the Vee geometries of these specimens varied slightly at each location for these girders. Therefore, the average Vee dimensions of G8-390-32-2-p are reported. However, the Vee dimensions of G8-390-25-2-p were not captured during the procedure and are not reported. For all other test specimens, the Vees were marked to the heat sequence specification (see Section 3.2.2.1)

As shown in Table 5-3, the Vee angle varies negligibly over the test matrix. The Vee dimensions only differ by 35 mm among the straightened girders, as the flange widths vary by only 70 mm. There is an increase in the overall heated surface area as the flange widths increase, which is ultimately the primary geometric difference. No relationship is found between the Vee dimensions and the changes in the girders' moment resistances. The specimens with larger Vees, including G8-390-32-2-p, G8-390-25-2-p and G9-430-25-3-f, do exhibit larger reductions in moment

capacity. However, the specimen with the largest overall Vee geometry, that is, G9-430-25-3-f, experienced less degradation than G8-390-32-2-p and G8-390-25-2-p. Furthermore, G9-360-32-3-p and G9-360-25-3-f, despite having the smallest Vee geometries, increased and decreased in moment resistance, respectively. This observed variability for relatively consistent Vee geometries suggests that the Vee geometries do not contribute significantly to the observed reductions in moment resistance and are relatively uninfluential.

As the available temperature data indicates that the lower phase transition temperature (700°C) has not been exceeded, the mechanical properties of the material should remain relatively unaffected, and the material unaltered. Similarly, the adverse mechanical property effects noted by Avent et al. (2000) for multiple cycles of heat-straightening appear not to have influenced the girders of this test program, nor has the Vee geometry and the area of heated material been shown influential. Therefore, it is reasonable to assume that any material and mechanical properties changes were minimal and do not significantly contribute to the losses of flexural strength observed. However, the conclusions drawn concerning the presumed minimal influence of heat-straightening on the mechanical properties of the material are qualitative in nature.

Table 5-3: Comparison of influential parameters of the heat-straightening procedure with percent change in moment capacity

Specimen ID	Max Temperature (°C)	Number of Cycles	Width (mm)	Depth (mm)	Vee Angle (°)	Heated Area (mm^2)	Percent Change in Moment Capacity
G8-390-32-2-p	-	3	195	200	52	19500	-21.8%
G8-390-25-2-p	-	2	-	-	-	-	-12.6%
G9-360-32-3-p	633	3	180	180	53	16200	7.4%
G9-360-25-3-f	645	2	180	180	53	16200	-6.8%
G9-430-25-3-f	643	2	215	215	53	23113	-11.4%

A comparison of the moment resistances with respect to the global slenderness ratio is presented in Figure 5-1. Both the heat-straightened and original girder' test capacities are normalized by the plastic moment, determined from measured parameters, and plotted against the global slenderness ratio (L/r_y). Figure 5-1 indicates that the loss of flexural capacity exhibited by the heat-straightened girders (see Section 5.1.1) is related to the ratio M/M_p for the initial test. Comparing between the original and heat-straightened moment resistances (grey zone vs. red zone in Figure 5-1) indicates that the upper bound of the moment resistances ($M/M_p = 0.67$) has dropped significantly to $M/M_p = 0.54$, while the lower bound of the moment resistances remained virtually unchanged, dropping from 0.47 to 0.45. In other words, the flexural response of specimens that exhibited larger original ratios of M/M_p has degraded more severely than specimens with lower original ratios of M/M_p ($M/M_p < 0.49$). This observation suggests that inelastic LTB and plasticity may influence the repair's efficacy.
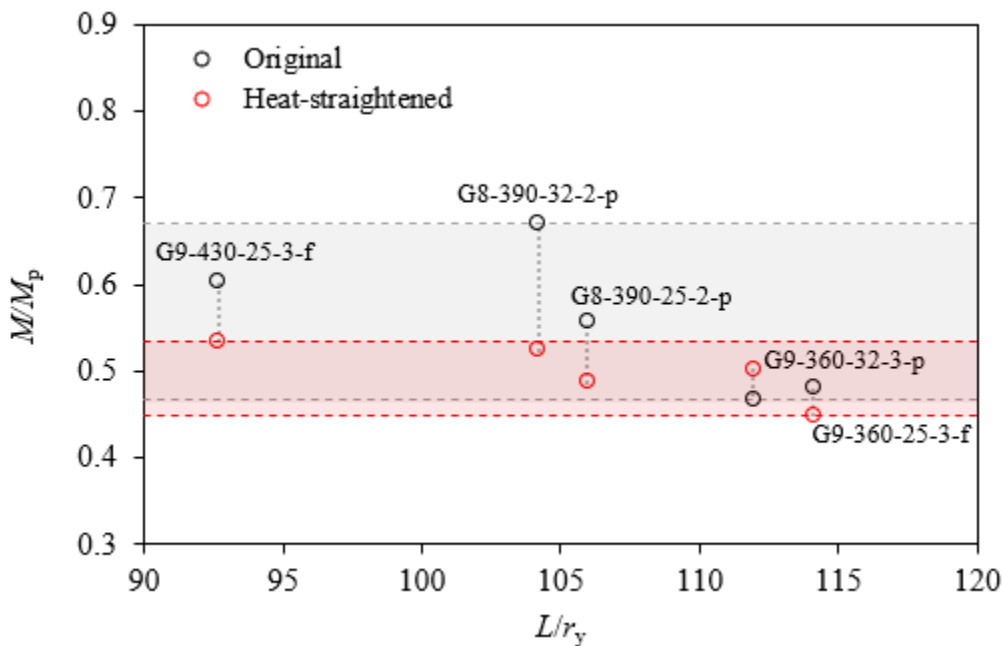

Figure 5-1: Original and heat-straightened moment resistances vs. global slenderness ratio

An increase in the amount of yielded material resulting from the original tests may lead to more extensive damage and less successful repair in terms of correcting the geometry or the need for a more aggressive application of the heat-straightening procedure. However, examining the cross-sectional and global geometric measurements of the damaged specimens (see Sections 3.2.1.2 and 3.2.1.3) reveals that this is not necessarily the case. G9-360-32-3-p exhibits the second largest

compression flange sweep (damage) of 20 mm, the lowest original ratio of M/M_p, and has exhibited an increase in moment resistance after repair. Furthermore, Table 5-3 revealed that G9-360-32-3-p is one of two girders to be cycled a third time, which qualifies as a "more aggressive" heat-straightening, but has not degraded. It is unclear why the degradation of the moment resistance is associated with inelastic LTB and higher original ratios of M/M_p, but it may be related to the specimens' geometric condition after heat-straightening and the magnitude of geometric imperfection present in the repaired state and is investigated in Section 5.1.3.

5.1.3 Influence of Change in Geometric Imperfections

Repair, as defined in Chapter 3, is the correction of out-of-tolerance geometric properties. The magnitude of remaining imperfections, while meeting tolerance criteria, may still be significant and differ from the original state. Since the initial compression flange sweep was found to be an influential parameter on the LTB response, the relationship between the change in compression flange sweep of the original and heat-straightened states of each girder and the change in moment resistance is investigated here. Initial cross-section twist and camber are neglected for the following analysis, as the camber of the specimens is expected to influence the LTB response negligibly, and the initial cross-section twist is captured indirectly due to its relationship with the sweep of the two flanges. Table 5-4 contains a summary of the initial compression flange sweep for comparison with the percent change in the moment resistance. Note that, herein, the initial compression flange sweep is denoted as δ_o and δ_{HS} when referring to the as-built (original) and heat-straightened states, respectively.

Table 5-4: Comparison of as-built and repaired initial compression flange sweep with percent change in moment capacity

Specimen ID	As-Built Sweep, δ_o (mm)	Repaired Sweep, δ_{HS} (mm)	Percent Change in Moment Capacity
G8-390-32-2-p	-1.0	-11.0	-21.8%
G8-390-25-2-p	-1.0	+2.5	-12.6%
G9-360-32-3-p	-9.0	-6.0	+7.4%
G9-360-25-3-f	-3.0	-3.3	-6.8%
G9-430-25-3-f	-2.0	+5.0	-11.4%

As shown in Table 5-4, most girders exhibit greater initial compression flange sweep after heat-straightening than was measured in their original condition. An increase of the initial compression flange sweep after heat-straightening appears to be associated with a loss of flexural capacity. The only girder corrected to a magnitude of initial compression flange sweep less than in the as-built condition is G9-360-32-3-p, which is also the only specimen to exhibit an increased moment resistance after repair. These observations suggest that the LTB response of a heat-straightened girder is heavily influenced by the change in geometry and the geometric imperfections after heat-straightening. Figure 5-2 shows the ratio M_{HS}/M_o against δ_{HS}/δ_o and provides an indication of the LTB performance of the heat-straightened girders relative to their original condition. Note that $\delta_{HS}/\delta_o = 1.0$ or less on the x-axis represents a girder that has met or improved from the original level of initial lateral deviation; however, as the absolute value of this ratio is provided, it does not differentiate between a change in the direction of the lateral deviation.
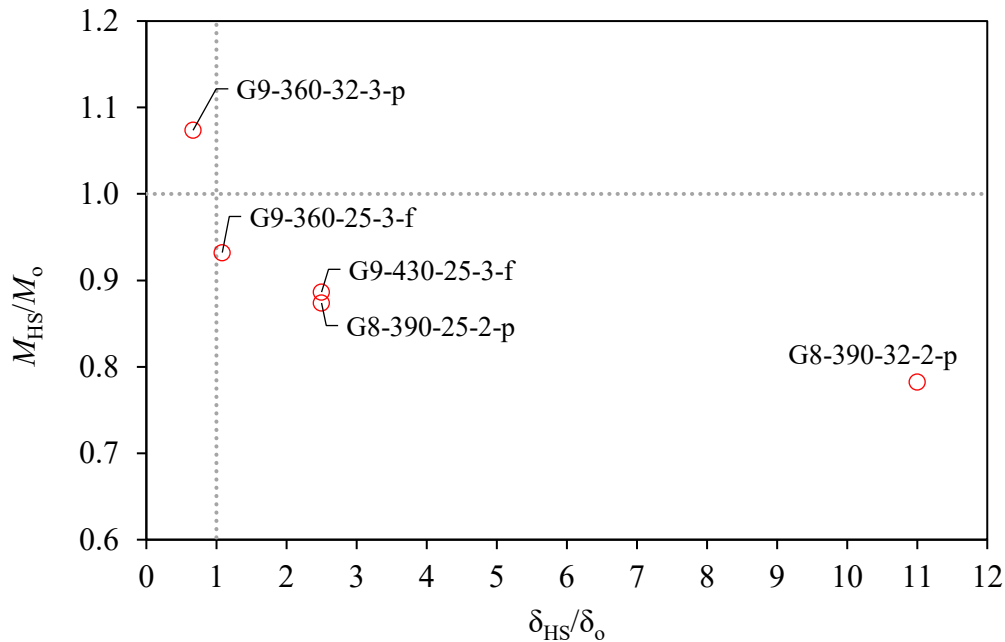

Figure 5-2: Change in moment resistance vs. change in initial compression flange sweep

As shown in Figure 5-2, when the magnitude of δ_{HS}/δ_o increases, the specimens degrade and exhibit lower moment resistances. In the most extreme, a specimen with 11 times the original initial lateral deviation reported a 22% loss in moment capacity, and for smaller differences in initial deviation, girders sweeping 2.5 times the original conditions showed a 13% loss in their

moment capacity. The flexural strength losses appear to plateau at large magnitudes of δ_{HS}/δ_o. However, for relatively small values of δ_{HS}/δ_o, the moment resistance appears quite sensitive, dropping from +7% to -7% as a result of relatively small changes in δ_{HS}/δ_o. As δ_{HS}/δ_o only indicates the change from original geometric conditions, it does not consider the actual magnitude of imperfections. A large change of already significant imperfection levels may exhibit a similar ratio of δ_{HS}/δ_o to that of a girder with small magnitudes of imperfection and little overall change. Therefore, similar magnitudes of δ_{HS}/δ_o can potentially correspond to large differences in M_{HS}/M_o.

The relationship between δ_{HS}/δ_o and M_{HS}/M_o indicates that a change in the flexural capacity of a heat-straightened girder is directly related to the magnitude of initial geometric imperfection. Moreover, the observed losses of moment resistance do not suggest the heat-straightened girders perform poorly; instead, the losses are associated with a greater magnitude of initial geometric imperfection. Additionally, minimizing the ratio δ_{HS}/δ_o can ensure that a heat-straightened girder's attainable moment resistance does not differ significantly from the as-built response. A specimen may perform better after a repair if the magnitude of imperfection is less than that originally measured.

5.2   Displacement Response

As the girder displacements are a critical component of LTB, the specimen's displacements at buckling and ultimate are provided in Table 5-5 and Table 5-6. The girder displacements are measured following an identical procedure to that of the original tests, and the sign convention remains the same. Additionally, as mentioned in Section 5.1, all the heat-straightened girders have buckled in the direction of their measured compression flange sweep and cross-section twist (see Table 3-7 for those geometric imperfections).

Table 5-5: Displacements of heat-straightened girders at buckling

Specimen ID	Vertical Displacement	Lateral Displacement		Cross-section Rotation			Longitudinal Displacement	
		Top Flange	Bottom Flange	Top Flange	Web	Bottom Flange	North	South
	(mm)	(mm)	(mm)	(°)	(°)	(°)	(mm)	(mm)
G8-390-32-2-p	-32.3	-75.6	+9.8	-6.7	-6.5	-5.2	+1.5	+4.3
G8-390-25-2-p	-27.2	+42.2	-4.7	+3.4	+3.4	+3.1	+1.9	+2.9
G9-360-32-3-p	-26.1	-62.8	+5.1	-4.0	-4.8	-3.3	-0.3	+6.4
G9-360-25-3-f	-22.7	-24.4	+1.4	-1.1	-1.9	-1.6	+1.1	+3.8
G9-430-25-3-f	-28.6	+59.2	-14.2	+6.0	+5.0	+3.1	+5.0	+1.7

Table 5-6: Displacements of heat-straightened girders at ultimate

Specimen ID	Vertical Displacement	Lateral Displacement		Cross-section Rotation			Longitudinal Displacement	
		Top Flange	Bottom Flange	Top Flange	Web	Bottom Flange	North	South
	(mm)	(mm)	(mm)	(°)	(°)	(°)	(mm)	(mm)
G8-390-32-2-p	-32.7	-84.8	+9.9	-7.3	-7.3	-5.8	+1.4	+4.4
G8-390-25-2-p	-28.3	+80.1	-8.5	+6.4	+6.5	+5.9	+1.5	+2.9
G9-360-32-3-p	-26.4	-82.0	+6.0	-5.2	-6.3	-4.3	-0.3	+6.4
G9-360-25-3-f	-24.5	-94.6	+9.6	-6.6	-7.3	-5.5	+0.9	+3.9
G9-430-25-3-f	-29.8	+86.3	-17.3	+7.7	+7.2	+4.7	+4.9	+1.7

5.2.1 Evaluation of Displacement Response

The ratios of the girder displacements at buckling from the heat-straightened tests to those of the original tests are compared in Table 5-7. Where $\Delta_{HS,h}$ is the mid-span lateral displacement for the heat-straightened girders, Δ_h is the mid-span lateral displacement for the original girders, Θ_{HS} is the mid-span cross-section rotation for the heat-straightened girders, and Θ is the mid-span cross-section rotation for the original girders. Only the lateral displacements and cross-section rotations are included in the comparison, as the vertical and longitudinal displacements are less relevant to the analysis of the LTB behaviour. Table 5-7 shows the general amplification of lateral displacement and cross-section rotation exhibited by the heat-straightened specimens at buckling, as evidenced by ratios greater than 1.0. The ultimate displacements are not considered, as the start of unloading (ultimate) varied per girder depending on the stopping criteria and are therefore relatively arbitrary and cannot be directly compared.

Table 5-7: Comparison of the lateral displacement and cross-section rotation at buckling

Specimen ID	$\Delta_{HS,h}/\Delta_h$		Θ_{HS}/Θ_o		
	Top Flange	Bottom Flange	Top Flange	Web	Bottom Flange
G8-390-32-2-p	7.1	2.1	5.5	5.5	5.7
G8-390-25-2-p	1.9	1.1	1.8	1.7	1.8
G9-360-32-3-p	1.1	1.2	1.2	1.2	1.2
G9-360-25-3-f	1.5	0.4	0.5	1.4	2.3
G9-430-25-3-f	1.8	1.9	2.0	1.9	1.8

As shown in Table 5-7, the deformation of all specimens at buckling increased after heat-straightening and repair, except the bottom flange lateral displacement and top flange rotation of G9-360-25-3-f. The lateral displacements of the heat-straightened specimens are 1.1 to 7.1 times greater than those recorded in the original tests and, on average, are 2.2 times larger than the original displacements. The cross-section rotations of the heat-straightened specimens on average are 2.4 times larger than those of the original tests, and the top flange, bottom flange and web rotations of the specimens typically increased by similar amounts, except for G9-360-25-3-f. A

consistent increase of rotation observed in each component of the cross-section does not indicate distortion, and heat-straightening appears not to have exacerbated the distortion observed in Section 4.2.3. G8-390-32-2-p is the only specimen not to meet the dimensional tolerances of CSA W59-18 after heat-straightening. When excluding G8-390-32-2-p from the data set, the observed increases in the lateral displacement and cross-section rotation range between 0.5 to 2.3 times the ones obtained from original tests, showing 50% larger displacements on average. The range of increased displacements for the specimens that satisfy dimensional tolerances is relatively small compared to those noted for the entire test matrix.

5.2.2   Influence of Change in Geometric Imperfections

A change in the magnitude of geometric imperfections for a given member is anticipated to manifest as a change in the exhibited displacements at buckling. To assess the relationship between the change in imperfections and the displacement response, $\Delta_{HS,h}/\Delta_h$ is plotted against δ_{HS}/δ_o in Figure 5-3. Only the compression flange lateral displacement and sweep are considered in this analysis, as the compression flange's behaviour is critical to the LTB response.
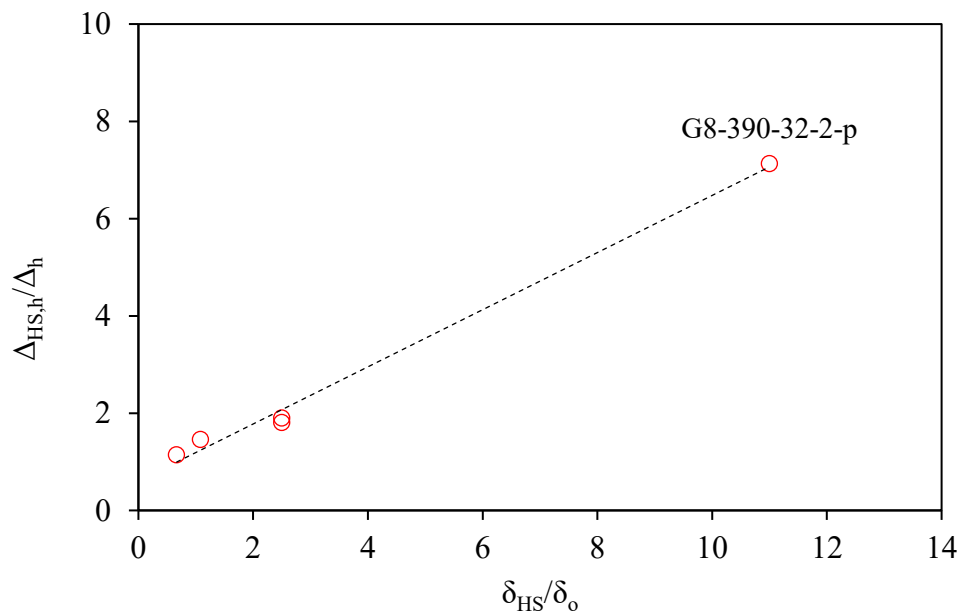

Figure 5-3: Change in compression flange lateral displacement ($\Delta_{HS,h}/\Delta_h$) vs. change in initial compression flange sweep (δ_{HS}/δ_o)

As shown in Figure 5-3, a linear relationship between $\Delta_{HS,h}/\Delta_h$ and δ_{HS}/δ_o is obtained, which suggests that the observed changes in girder displacements (Section 5.2.1) are directly related to a change in compression flange sweep. Moreover, the heat-straightening procedure appears not to compromise a girder's initial lateral stiffness or significantly increase displacements at buckling, provided that dimensional tolerances are satisfied. While it is acknowledged that the as-built geometry and global geometric measurements are not measured in practice, the relationship observed in Figure 5-3 suggests that minimizing δ_{HS}/δ_o can lead to a displacement response that differs negligibly from the as-built response.

5.3   Load–Displacement Response

The load−displacement plots for G8-390-32-2-p and G9-360-32-3-p are provided in Figure 5-4 and Figure 5-5. The load in these figures equates to the average point load, P, delivered at each of the eight GLS locations, as described in Section 3.1.2.1. The vertical and lateral load–displacement responses are plotted, denoted by the subscripts v and h, respectively, for the original and heat-straightened girders. The lateral displacement is measured on the girders' compression flange, at the flange tip, and the vertical displacement is measured at the girder's underside, at the web–flange junction. G8-390-32-2-p is specifically assessed, as it stands out from the rest of the girders, exhibiting seven times more top flange displacement and five times the amount of cross-section rotation, at buckling, than those of its original LTB test. The response of G9-360-32-3-p is presented to contrast G8-390-32-2-p, as this girder reported the least change in displacement and is the only specimen to exhibit an increase in the moment resistance after heat-straightening. The load–displacement responses of the remaining specimens of the heat-straightening program are provided in Appendix B.
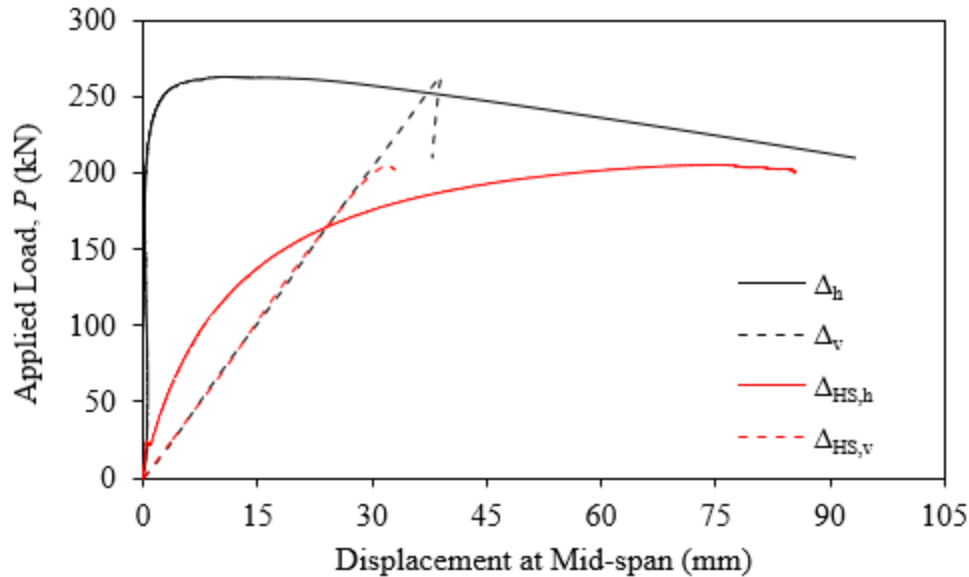
Figure 5-4: Load–displacement responses of G8-390-32-2-p: original vs. heat-straightened

As shown in Figure 5-4, the lateral stiffness of G8-390-32-2-p after heat-straightening degraded significantly from the original tests. The original girder initially displaced in-plane with negligible lateral displacement until approximately $P = 260$ kN, at which point the girder destabilized and rapidly displaced out-of-plane. The original specimen did not start deflecting laterally until approximately 75% of the buckling load had been achieved and displayed a relatively high initial stiffness. A small lateral deviation of 1 mm was initially measured for this specimen, explaining the very stiff initial response and rapid destabilization. When retested, the heat-straightened girder immediately began displacing laterally, at significantly lower load levels. This behaviour is typical of imperfect beams with large geometric imperfections, as was the case of this specimen, which exhibited 11 mm of initial lateral deviation after the heat-straightening procedure. Furthermore, the girder's in-plane response was virtually unaffected, suggesting that the girder's out-of-plane imperfections heavily influenced the LTB behaviour and did not impact the in-plane behaviour.
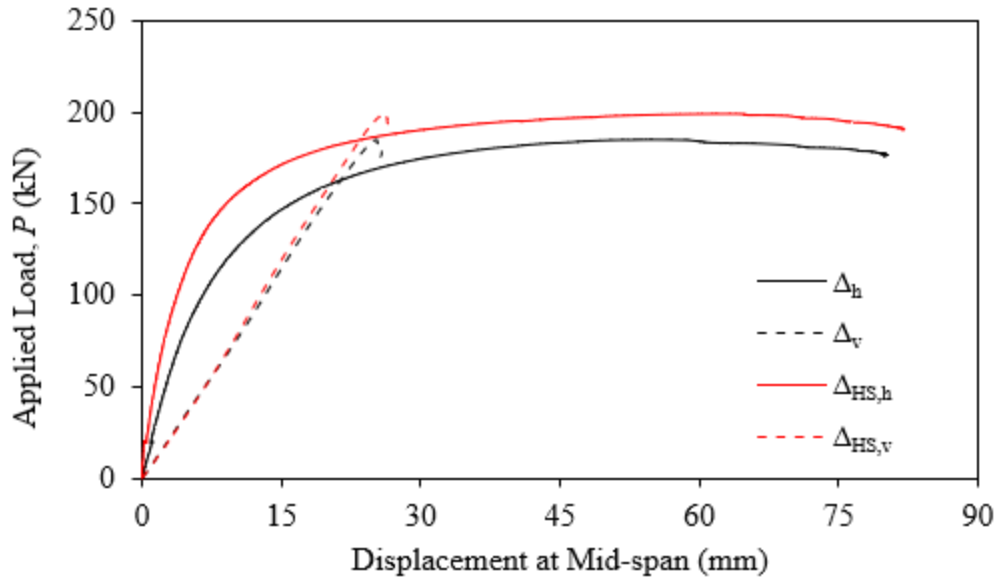
Figure 5-5: Load–displacement responses of G9-360-32-3-p: original vs. heat-straightened

The load–deformation plot of G9-360-32-3-p indicates an increase in the lateral stiffness and buckling load after heat-straightening, as shown in Figure 5-5. The lateral load–displacement curves of the original and heat-straightened cases differ minimally relative to G8-390-32-2-p. There was an increase in the initial stiffness and buckling load after heat-straightening; however, the overall behaviour, including the transition to instability and the post-buckling response, remains nearly the same. A probable reason for the similarities stems from a relatively smaller difference in the magnitude of initial lateral deviations. The compression flange of G9-360-32-3 originally swept laterally 9 mm, and after the repair, 6 mm. As 6 mm of lateral deviation is still significant relative to the allowable tolerance of $L/1000$, in both conditions, G9-360-32-3 exhibits a relatively significant amount of lateral displacement prior to buckling, low initial stiffness, and gradual destabilization. The observed increase in the lateral stiffness and the 7.4% higher moment resistance may be attributed to the improved geometry and 3 mm reduction of the initial lateral sweep. Observations of the load–displacement plots suggest that the LTB response of a heat-straightened girder can remain functionally the same, provided the magnitude of initial geometric imperfections differs minimally from the original state.

115

5.4 Design Recommendations

It must be acknowledged that the mechanical properties of the material can be affected, and residual stresses will develop when heat-straightening, both of which may also influence the stability response of the girders studied. However, the sensitivity of the LTB response of heat-straightened girders to small changes in the geometric condition stands out, and a clear relationship between the geometric condition and LTB response after the repair has been established. The heat-straightening procedure appears not to compromise the moment resistance, initial lateral stiffness or LTB behaviour of a flexural member. Changes observed in the load–displacement response between the as-built and heat-straightened specimens are attributed to changes in initial geometric imperfection. Practitioners need not be concerned that heat-straightening will compromise the LTB response, provided the specimens meet dimensional tolerances. This advice is given under the assumption that all specifications and best practice requirements of heat-straightening guidelines and prevailing literature are met to ensure the heating procedure has not significantly affected the mechanical properties of the material.

6 FINITE ELEMENT MODEL

The test specimens of the LTB experimental program are modelled in the general-purpose finite element (FE) program ABAQUS (Dassault Systèmes 2016a) and validated against the experimental test data described in Chapter 4. The FE model developed in this study is capable of reproducing inelastic LTB of welded girders taking into account material nonlinearity, residual stresses and initial geometric imperfections. In particular, the boundary conditions and load configurations are modelled to mimic the experimental test set-up. The development of the FE model is first described, followed by the validation against experimental results. Finally, the sensitivity of the model to initial imperfections, load height effects, and distortion are evaluated.

6.1 Modelling Assumptions and Technique

Several parameters are defined in the creation of the FE model, including material model properties, element type, mesh size, geometric properties, initial geometric imperfections, residual stresses, boundary conditions, analysis procedures and load application methods.

6.1.1 Elements and Mesh

The FE model of the test girders is shown in Figure 6-1. A 4-node, reduced integration shell element (S4R) is selected from the ABAQUS element library, which can reproduce the large deformations and rotations expected when a girder yields and buckles in the LTB mode. The S4R element is considered a robust finite element that can efficiently capture large inelastic strains and features reduced integration for an enhanced computational time. When using reduced integration elements, hourglass modes can occur, where the element deforms, but zero strain is calculated at the corresponding integration point, resulting in an element with zero stiffness (Dassault Systèmes 2016b). If hour glassing propagates in the mesh, it can lead to a more flexible structure and increased deformations. However, such negative effects are limited to relatively coarse meshes under large distortions. Therefore, a fine mesh size of 20 mm by 20 mm is selected in this study, which is not expected to have hourglass modes. Depending on the girder, 16 to 24 elements are defined across the flange width, and 28 to 44 elements are assigned over the web depth. This mesh density is relatively high compared to previous numerical simulations (Subramanian and White 2017) and is calibrated against the experimental test results produced in this study and those from Ji et al. (2019), as presented in Section 6.2.1.

The roller assembly, shown in Figure 3-14, is modelled and assigned to bear upon the top flange to simulate the experimental program's load delivery mechanism. The three-dimensional (3D) solid element, C3D8R, with a mesh density of 20 mm, is selected to simulate the roller assembly. A 3D solid element is required to simulate the area by which the rollers bore upon the top flange and the load height. Further discussion of the techniques employed to model the roller assembly and an investigation into the interaction between the top flange and the roller assembly is provided in Section 6.1.7.
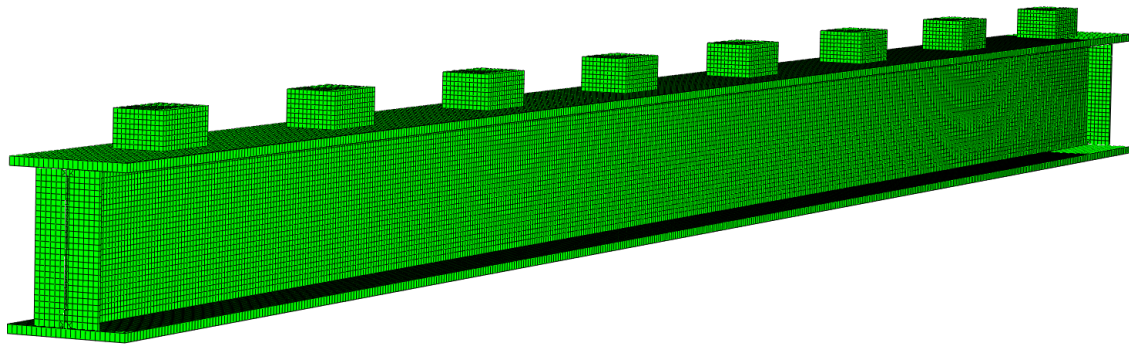
Figure 6-1: Finite element model of test girders

6.1.2 Material Properties

A tri-linear material definition is assigned within the FE model, per plate thickness, based on the tension coupon tests performed, as described in Section 3.1.1.5. The nonlinear strain hardening region of steel has been approximated linearly between the yield stress of the material, F_y, and the ultimate stress, F_u. It should be noted that if the nonlinear strain hardening region of the stress–strain response were modelled, increased member capacities could be expected. However, a linear approximation was deemed satisfactory for the present study's needs, as it is anticipated that the strains induced during LTB will not significantly exceed the yield strain and illicit significant strain hardening effects. This assumption is based on the observations made in Section 4.1.1, where the flange stress analysis of the G9 series revealed that only the tips of the compression flange yield at buckling and do not strain enough to exhibit significant strain hardening effects. The modulus of elasticity, E, and static yield stress, F_y, assigned to the FE model are those presented in Table 3-4. A Poisson's ratio of 0.3 is assumed. Figure 6-2 shows the tri-linear true stress–strain relationship of a 25.4 mm plate, which is assigned in ABAQUS.
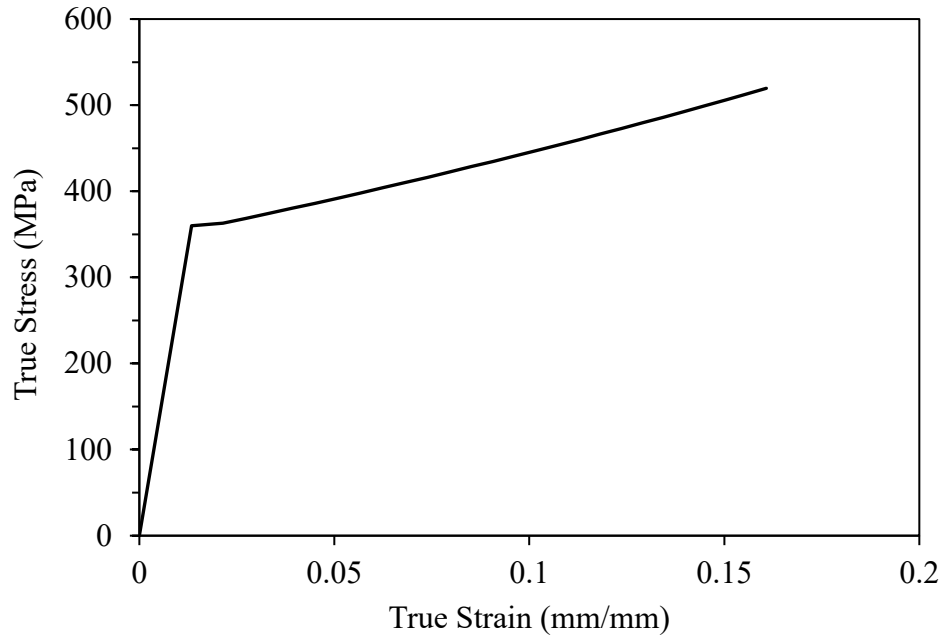
Figure 6-2: Tri-linear true stress–strain relationship of the 25.4 mm-thick plate

6.1.3   Boundary Conditions

In the experimental test set-up, the end conditions consisted of simple-supports, and a set of lateral braces used to restrict the cross-section rotation, but not rotation in- and out-of-plane, or warping, as described in Section 3.1.2.2. The boundary conditions of the FE model are defined to replicate the conditions of the experimental test set-up. The end conditions of the test set-up are simulated through the restriction of the translational degrees-of-freedom (DOF) and the coupling of the rotational DOFs over the web and flange nodes at the girder ends. Figure 6-3 shows the coordinate system used in ABAQUS. In this coordinate system, movement in the directions of axes 1, 2, and 3 are defined by the translational DOFs, U_1, U_2 and U_3, respectively, and rotations about the respective axes are defined as UR_1, UR_2 and UR_3.
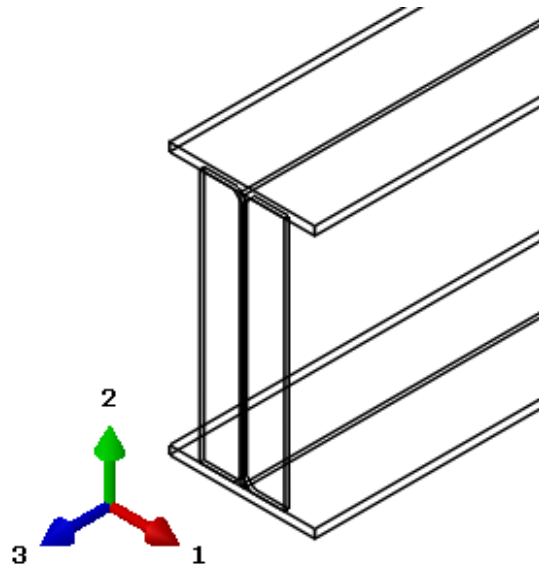
Figure 6-3: Finite element model coordinate system

The test set-up end conditions are simulated through the controlled restriction of the DOFs at the girder ends and by two multi-point kinematic coupling (MPC) constraints. The end conditions of the FE model are shown in Figure 6-4. The translational DOFs U_1 and U_3 of the node coinciding with the bottom web–flange junction are restricted to prevent lateral and longitudinal movement. However, the longitudinal displacement (U_3) is restricted only at one end of the girder to ensure the stability of the model during the analysis and simulate traditional pin–roller conditions instead of the roller–roller conditions of the test set-up. A restriction of the vertical displacement ($U_2 = 0$) is assigned to every node of the bottom flange to simulate the experimental end conditions and how the girders bear upon a knife-edge under the bottom flange (see Figure 3-15).

Multi-point kinematic coupling constraints are defined across the web and top flange to prevent the cross-section rotation (UR_3) and allow in- and out-of-plane rotations, as well as warping. MPC constraints restrain the DOFs of the multiple nodes to the rigid body motion of a reference, or "Master", node. In these constraints, the DOFs U_1, U_2, UR_1, UR_2, and UR_3 of the girders web and top flange are coupled to the master nodes at the top and bottom web–flange junctions. U_3 is not included in the MPC constraints to allow warping. The master node located in the bottom web–flange junction has the cross-section rotation restricted ($UR_3 = 0$), and therefore, as all the remaining nodes of the flange and web are coupled to the bottom web–flange junction, the web and top flange cannot rotate about the longitudinal axis. UR_1 and UR_2 for the bottom web–flange

junction node are left unrestricted, as free in- and out-of-plane rotations are desired. However, UR_1 and UR_2 are included in the MPC constraints to ensure the web and top flange nodes rotate as a rigid body.
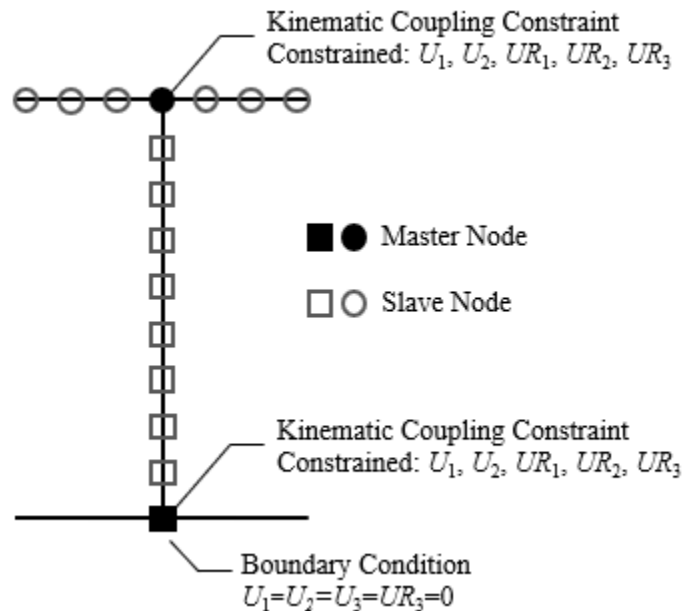

Figure 6-4: Pinned end boundary conditions of the finite element model

6.1.4 Analysis Method

A linear perturbation buckling analysis (eigenvalue buckling analysis) and a nonlinear modified Riks analysis are defined to simulate LTB. The buckling analysis is utilized to estimate the buckled shape and assign initial geometric imperfections. A Riks analysis is selected to solve the nonlinear buckling problem while tracking the post-buckling behaviour of the test girder after significant stiffness degradation has occurred. ABAQUS employs a modified Riks analysis to solve the nonlinear problem based on the arc-length method (Powel and Simons 1981; Ramm 1981; Crisfield 1981), where a load proportionality factor is introduced to the set of governing equilibrium equations and solved iteratively. The method is capable of tracking displacements well into the post-buckling response and is not affected by load shedding, softening of the structure or a snap-back of the load–displacement response. The Riks analysis uses a modified version of the traditional Newton–Raphson method for solving nonlinear problems, as shown in Figure 6-5. The

solution point, A^2, is found by moving an increment size (based on the load proportionality factor) along the tangent (A^0 to A^1) and searching for equilibrium in a plane orthogonal to the tangent.
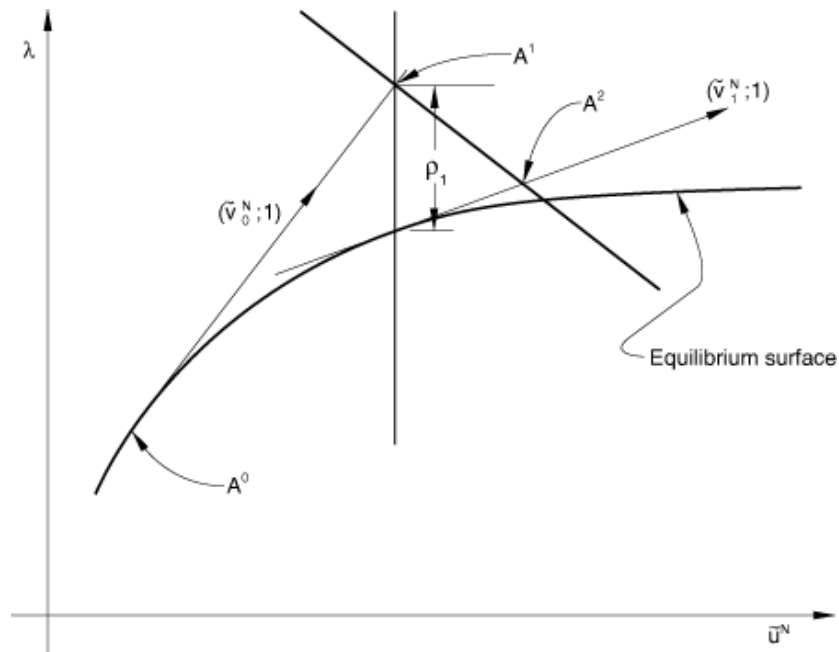

Figure 6-5: Modified Riks algorithm employed in ABAQUS (Dassault Systèmes 2016b)

6.1.5 *Initial Geometric Imperfections*

The first eigenmode of the structure is obtained through a linear eigen-buckling analysis, and the initial geometric imperfections are distributed following this imperfect shape after being scaled to an appropriate magnitude. The magnitude of initial geometric imperfection considered in numerical studies of LTB (Kabir and Bhowmick 2018) is commonly based on dimensional tolerances for lateral deviation from straightness specified by the governing steel design and material standards. In Canada, this corresponds to $L/1000$, where L is the length of the girder. However, in this research, the maximum measured initial compression flange sweep, as reported in Table 3-3, is applied. The application of the initial geometric imperfections is handled by ABAQUS as follows: (1) the first positive buckling mode is determined; (2) the nodal displacements of the buckled shape are normalized by the maximum displacement to obtain unit displacements; (3) the unit displacements are scaled by the desired scaling factor (i.e., the maximum measured compression flange sweep) and applied to each node of the girder. It should be noted that when using an eigenvalue analysis to assign geometric imperfections in the FE model, camber is neglected, and initial cross-section twists are indirectly assigned.

6.1.6 Residual Stresses

The residual stress model (Unsworth et al. 2019) introduced in Chapter 4 is used in the FE model, as it is anticipated to provide a close approximation of the actual residual stresses and facilitate an accurate estimation of the experimental LTB response. The parameters that delineate the residual stress pattern, shown in Figure 4-2, have been calculated per specimen of the test matrix and are summarized in Table 6-1. σ_{tf} and σ_{tw} are the yield stresses of the flange and web, respectively (at the web−flange junction), σ_{cf} is the compressive stress of the flange, σ_{cw} is the compressive stress of the web, η_f is the parametric high-stress-gradient region width in the flanges, η_{fe} is the width of the edge regions in the flanges, and η_w is the parametric high-stress-gradient width at one edge of the web. The distribution of the residual stresses formed by these parameters has then been used to calculate the anticipated magnitude of residual stress at each element across the flange and web.

Table 6-1: Parameters of Unsworth et al. (2019) residual stress model

Specimen ID	σ_{tf} (MPa)	σ_{tw} (MPa)	σ_{cf} (MPa)	σ_{cw} (MPa)	η_f (mm)	η_{fe} (mm)	η_w (mm)
G6-470-32-2-p	347	364	-41	-41	90.4	32.9	47.3
G6-430-32-1-p	347	364	-43	-43	88.1	30.1	47.2
G6-430-32-1-f	347	364	-43	-43	87.8	30.1	46.9
G6-300-32-1-p	347	364	-52	-52	77.8	20.8	47.5
G8-430-25-2-p	355	364	-44	-44	101.4	30.6	56.3
G8-390-32-2-p	347	364	-49	-49	107.1	27.3	60.5
G8-390-25-2-p	355	364	-46	-46	98.6	27.8	56.3
G9-360-32-3-p	347	357	-45	-45	87.4	25.2	52.2
G9-360-32-3-f	347	357	-45	-45	87.1	25.1	52.1
G9-360-25-3-f	355	357	-51	-51	101.7	25.7	62.6
G9-430-25-3-f	355	357	-47	-47	106.9	30.7	62.4

When defining residual stresses in ABAQUS, there is only a discrete number of elements in the model, and each element across the width or depth of the specimen can be assigned a unique initial condition (stress in this case). Thus, the average value of the proposed residual stresses within the

width of each element is taken and applied in the model. If the mesh is not discretized sufficiently, peaks and significant rates of change can be lost, introducing unintended forces that influence the LTB response. As inelastic LTB is especially sensitive to residual stresses, it is essential to ensure the discretized residual stresses defined in the FE model are accurate. To verify the pattern used in the simulation, the discretized residual stresses of G6-300-32-1-p are compared with the residual stresses measured by Unsworth et al. (2019) and the residual stresses calculated from the Unsworth et al. (2019) residual pattern, as shown in Figure 6-6 and Figure 6-7 for the flanges and web respectively.
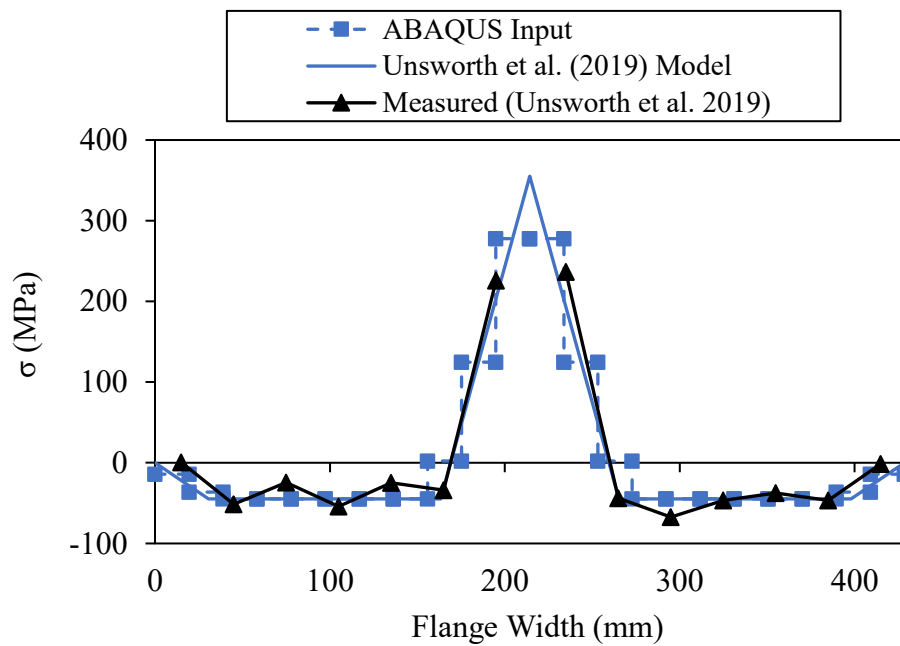
Figure 6-6: Comparison of the residual stress patterns for the flange of G6-300-32-1-p
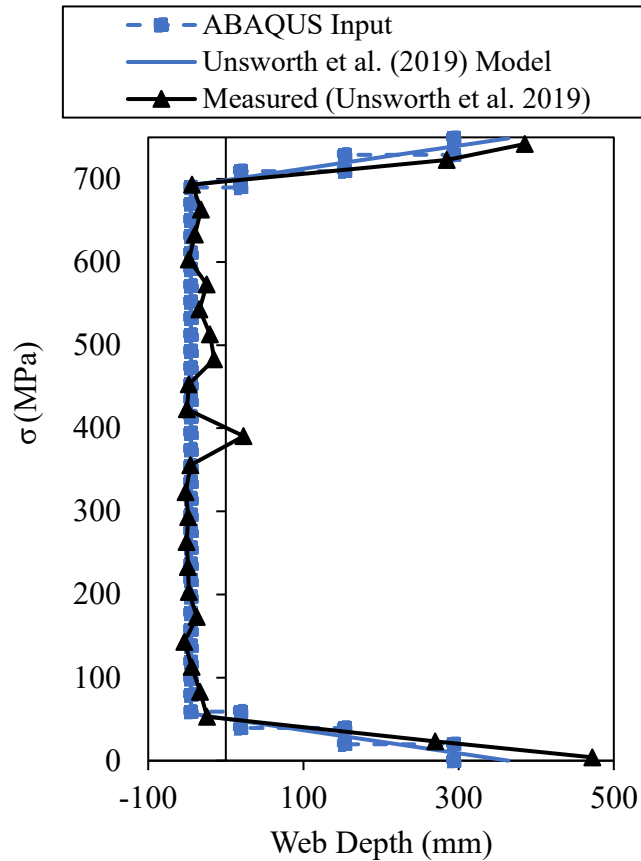
Figure 6-7: Comparison of the residual stress patterns for the web of G6-300-32-1-p

Figure 6-6 and Figure 6-7 show that the residual stress pattern proposed by Unsworth et al. (2019) correlates well with the measured residual stresses and eliminates the natural variance of the experimental data. The effects of discretization are shown when comparing the ABAQUS input with the Unsworth et al. (2019) model and the measured residual stress, where only 80% of the tensile peak is captured and defined in the FE model. However, as the extreme tensile stress, which is not captured when discretizing the residual stress pattern, is concentrated over a finite area, the average residual stress coming from the discretization over a broader region of the flange is likely to induce a similar magnitude of longitudinal force to that of the exact tensile stress. Thus, the discretized residual stresses assigned in the FE model are anticipated to elicit a similar response to that of a continuous residual stress pattern, suggesting that the application of residual stresses in this manner is suitable to estimate the LTB response.

6.1.7   Load Application

The analysis method chosen (Riks) is a load-controlled procedure, which requires an arbitrary load to be applied to the girders at the start of the analysis, which is then amplified on successive steps. The load magnitude is handled by ABAQUS as part of the Riks analysis and is, therefore, not a critical parameter of the FE model. However, the elevation of the load is varied in this research and is applied in three ways; (1) above the top flange, (2) at the top surface of the top flange, and (3) at the shear centre. The latter two methods are considered for direct assessment of the CSA S16-19 design provisions for LTB, whereas the former is studied for simulation of the experimental specimens and validation of the FE model.

As discussed in Section 3.1.2.1, the elevation of the load during testing resides 178 mm above the top flange of the test specimens. Therefore, the moment resistances, M_{max}, reported in Section 4.1 have been reduced from the anticipated top flange and shear centre moment resistances due to the load height effect. Helwig et al. (1997), Nethercot and Rockey (1971), and Wong et al. (2015) provide methods to assess the moment resistance of girders loaded above the shear centre, but are only applicable when loading within a domain between the mid-height of the section and the top or bottom flanges. Therefore, to emulate the experimental program and estimate the moment resistances of the test girders, the roller assembly (see Figure 3-14) has been explicitly simulated in the FE model, as shown in Figure 6-8.
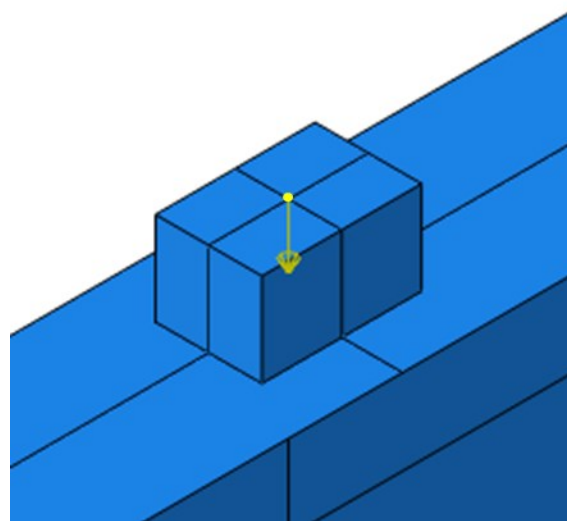
Figure 6-8: Load application above the top flange

The rollers are modelled as solid elements, as discussed in Section 6.1.1 and constrained to the top flange through surface tie constraints. A surface tie constraint in ABAQUS connects the DOFs of the nodes of two surfaces together such that there is no relative motion between the two surfaces. As a result, the surface tie constraints may indirectly inhibit material strains under the roller and influence the LTB response. The influence of the surface tie constraints is explored in Section 6.2.2. Nevertheless, each roller is modelled 300 mm × 200 mm × 178 mm based on the roller's measured dimensions, including the thickness of sacrificial steel placed between the spherical bearing and the roller surface (see Figure 3-14). The rollers are centred about the web–flange junction with a point load applied at the centre of each roller, as shown in Figure 6-8.

Figure 6-9a and 6-9b depict the approach taken to simulate top flange loading and shear center loading, respectively. A series of concentrated loads are applied to a small set of nodes in the top flange and web at each of the eight load locations along the girder length. It is desired to distribute the concentrated loads over an area sufficient in size to avoid stress concentrations, which may lead to local yielding or local crippling at the point of load application. The concentrated loads on the top flange are applied to a 3×3 element set, centred about the flange width, and for loading at the shear centre, a set of five nodes is selected at mid-height of the web.

(a)   (b)
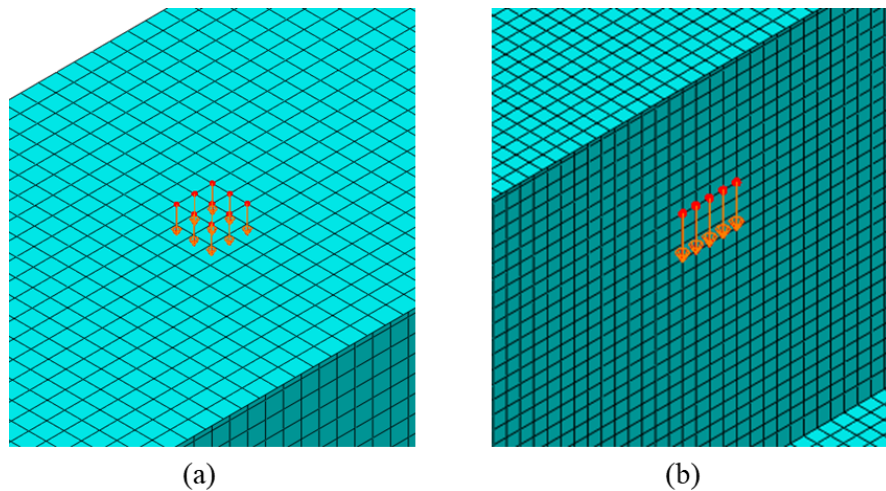
Figure 6-9: Load application for (a) top flange loading and (b) shear centre loading

6.2   Validation of Finite Element Model

The FE model is validated against the data of the LTB experimental program. The FE model's performance and some of the influential parameters, including the assumptions made when modelling the roller assembly and initial geometric imperfections, are then investigated. For all comparisons in this section, above top flange loading is used, while the calibrated model, with shear centre and top flange loading, is used in Chapter 7 to assess the LTB design provisions of CSA S16-19 for welded steel girders.

6.2.1   Validation against Experimental Test Data

The moment–rotation curves of G6-430-32-1-p, G8-390-25-2-p and G9-360-25-3-f, obtained from the LTB experiments and the finite element analyses (FEA), are shown in Figure 6-10. Plotted on the horizontal axis of Figure 6-10 are the cross-section rotations recorded by the mid-web clinometer, as reported in Section 3.1.2.3 and the FEA rotations, UR_3, of a node located at the mid-web of the girder's mid-span. The remaining moment–rotation comparisons for the girders of this study are provided in Appendix C. The FEA moment resistances, M_{FE}, are summarized in Table 6-2 and are compared with the experimental moment resistances, M_{Test} (referred to as M_{max} in Chapter 4).
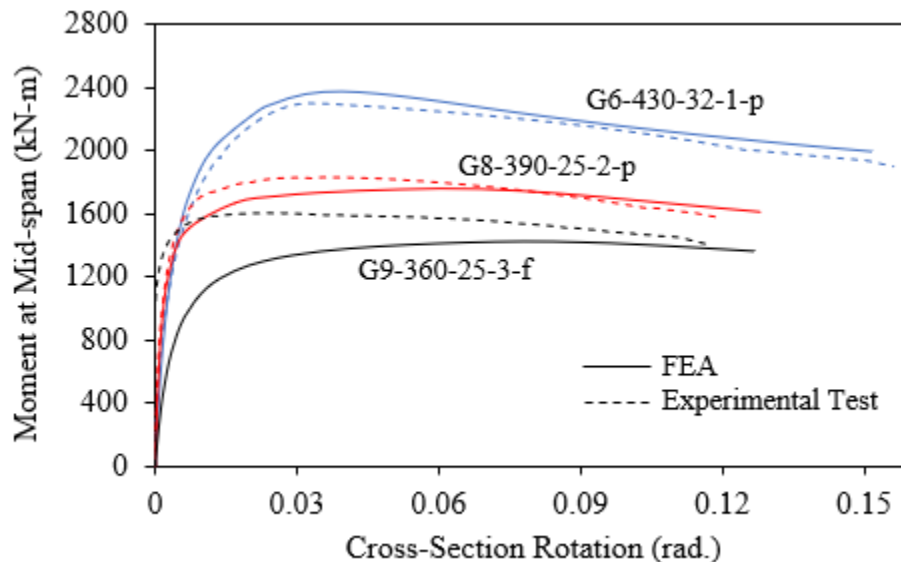
Figure 6-10: Moment–rotation responses of G6-430-32-1-p, G8-390-25-2-p and G9-360-25-3-f

Table 6-2: Maximum experimental and finite element analysis moment resistances

Specimen ID	Experimental Moment, M_{Test} (kN-m)	Finite Element Analysis, M_{FE} (kN-m)	M_{Test}/M_{FE}	Percent Difference of Moment Resistance
G6-470-32-2-p	2756	2786	0.99	+1.1
G6-430-32-1-p	2349	2373	0.99	+1.0
G6-430-32-1-f	2359	2312	1.02	-2.0
G6-300-32-1-p	1327	1377	0.96	+3.6
G8-430-25-2-p	1877	1907	0.98	+1.5
G8-390-32-2-p	2619	2324	1.13	-12.7
G8-390-25-2-p	1869	1765	1.06	-5.9
G9-360-32-3-p	1852	1743	1.06	-6.3
G9-360-32-3-f	2002	1816	1.10	-10.3
G9-360-25-3-f	1645	1423	1.16	-15.6
G9-430-25-3-f	2408	2237	1.08	-7.6

As shown in Figure 6-10, the FEA estimates the experimental moment–rotation response suitably for G6-430-32-1-p, G8-390-25-2-p. However, the initial stiffness of G9-360-25-3-f is estimated to be much lower than that of experimentally obtained initial stiffness. G6-430-32-1-f, G6-300-32-1-p and G9-360-32-3-f (see Appendix C) also exhibit a similarly softer estimation of the initial stiffness by the FEA. Comparing the experimental moment resistances with the FEA moment resistances in Table 6-2 reveals experimental moment resistances of the G6 series are predicted well and within 1% on average. There is a tendency for the FEA to under-predict the experimental moment resistances as the depth series increases, where the average percent difference in moment resistance between the experiments and FEA are -5% and -9%, in the G8 and G9 series, respectively. FEA can underestimate the experimental moment resistance by as much as 16% (G9-360-25-3-f). However, the experimental moment resistances are estimated by FEA within 5% on average, which is deemed suitable for this study. The factors influencing the FE model's behaviour are investigated in the subsequent sections.

6.2.2 Influence of Load Application Assumption

Due to the above top flange loading conditions, described in Section 6.1.7, there is concern that the surface tie constraints, which "fuse" the top flange and bottom roller surfaces together, negatively affect the FEA results. To investigate this concern, the logarithmic strain components, ε_{11} and ε_{22}, at a node included as one of the surface tie constraints, and an unconstrained node of the top flange, have been extracted and plotted against the lateral displacement, in Figure 6-11. The logarithmic strain components ε_{11} and ε_{22} are the principal strains local to the shell elements of the top flange. Logarithmic strain is one (of many) strain measures available in ABAQUS for nonlinear analyses and is specific to large–strain shells. Plotted on the horizontal axis is the mid-span lateral displacement of the compression flange tip.
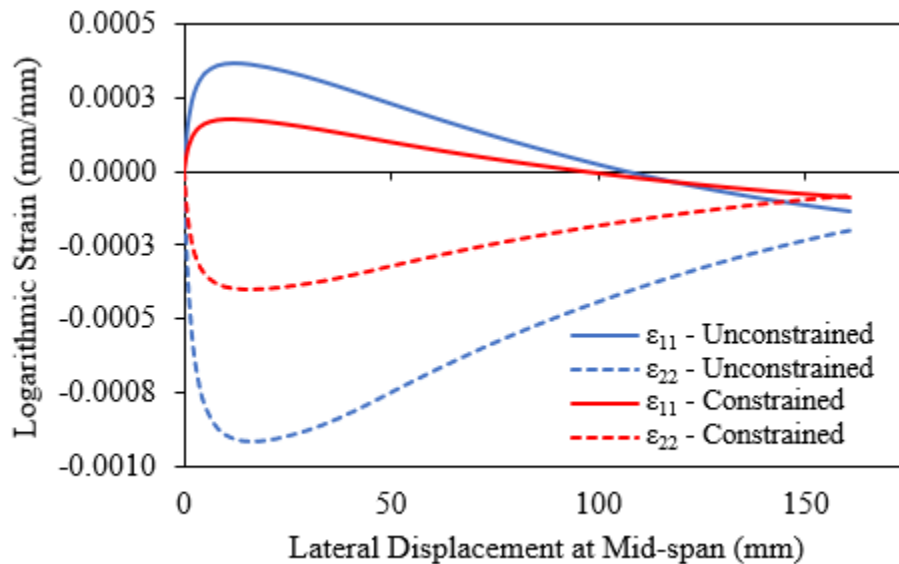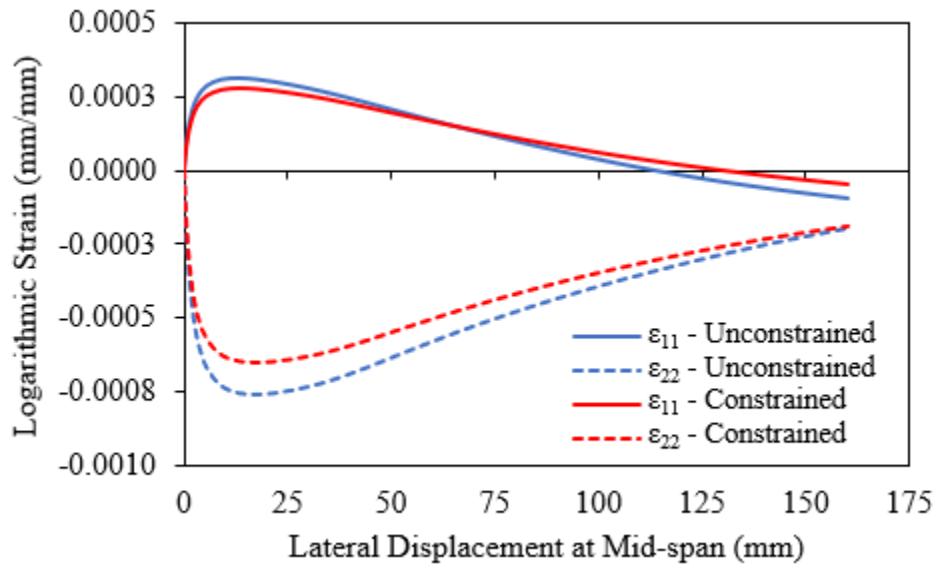

Figure 6-11: Logarithmic strain components, ε_{11} and ε_{22}, of G9-430-25-3-f vs. top flange lateral displacement with an isotropic material assigned to the "roller"

Figure 6-11 shows that the constrained nodes are inhibited from straining freely under flexure, as anticipated. When comparing the strain components ε_{11} and ε_{22} of the constrained nodes to those of the unconstrained nodes, the constrained nodes exhibit significantly (approximately 50%) less strain at the same magnitudes of lateral displacement. The "roller" material properties are, therefore, manipulated in the FE model to mitigate the rollers' influence on the top flange strains. A linear elastic orthotropic material is assigned to the "roller" to provide flexibility in the plane of the constrained surface and a vertical rigidity to apply the point loads. When defining the

orthotropic material, it was found that the longitudinal and lateral stiffnesses can only be reduced to $1/10^{th}$ of the stiffness in the vertical direction before numerical convergence issues occur. Thus, the orthotropic material definition includes a modulus of elasticity of $E = 200$ GPa in the vertical direction and $E = 20$ GPa in the lateral and longitudinal directions. This allows the roller to deform laterally and longitudinally more readily than if the stiffness of steel ($E = 200$ GPa) was defined in these directions and, consequently, allows the top flange to deform more realistically. However, this is simply a numerical technique employed to simulate the desired response; it does not truly remove the influence of the "roller" and release the DOFs of the top flange. The logarithmic strain components ε_{11} and ε_{22} of the same constrained and unconstrained node, with the orthotopic material defined, are plotted in Figure 6-12 to assess the efficacy of this modelling approach.

Figure 6-12: Logarithmic strain components ε_{11} and ε_{22} of G9-430-25-3-f vs. top flange lateral displacement, with an orthotropic material assigned to the "roller"

Figure 6-12 shows the difference in strain exhibited by a constrained and unconstrained node is reduced from the differences in strain observed in Figure 6-11. This finding suggests that the modified material properties have allowed the constrained surface to strain more realistically; however, the influence of the surface tie constraint is not eliminated. Table 6-3 compares the FEA moment resistances obtained from the FE model with an isotropic material of $E = 200$ GPa defined, and the FE model with the aforementioned orthotropic material defined.

Table 6-3: Test-to-predicted ratios of moment resistance with an isotropic material vs. an orthotropic material assigned to the roller

Specimen ID	Test-to-predicted Ratio	
	Isotropic	Orthotropic
G6-470-32-2-p	0.99	0.99
G6-430-32-1-p	0.97	0.99
G6-430-32-1-f	1.00	1.02
G6-300-32-1-p	0.92	0.96
G8-430-25-2-p	0.96	0.98
G8-390-32-2-p	1.09	1.13
G8-390-25-2-p	1.03	1.06
G9-360-32-3-p	1.03	1.06
G9-360-32-3-f	1.06	1.10
G9-360-25-3-f	1.12	1.16
G9-430-25-3-f	1.05	1.08

As shown in Table 6-3, the orthotropic material definition reduces the FEA moment resistances from those obtained using an isotropic material and increases the test-to-predicted ratios. On average, the FEA moment resistances with the orthotropic material defined were 3% lower than those of the isotropic model. The isotropic "roller" tied to the top flange of the beam inhibits deformation of the top flange nodes, thus increasing girders stiffness, and in turn, the moment resistance. Removal or relaxation (e.g., defining a flexible orthotopic material) of the tie constraints encourages deformation and decreases the moment resistance. These findings suggest that the FEA is somewhat sensitive to manipulations of the tie constraints when predicting the moment resistance. However, the material modification to provide flexibility in the plane of the constrained surface is likely sufficient to eliminate any adverse effects of the tie constraints. The relaxation of 90% of the restraining stiffness resulted in a 3% average reduction of the moment resistance, which suggests that the complete removal of the restraining effects, or an exact simulation of a roller, would negligibly affect the FEA results.

6.2.3 Influence of Initial Geometric Imperfections

The magnitude of the initial compression flange sweep measured in the LTB experimental program is used to scale the initial geometric imperfections in the model, as described in Section 6.1.5. This modelling technique has been utilized in past studies (Subramanian and White 2017; Kabir and Bhowmick 2018) and is considered suitable to reproduce the LTB response of imperfect girders. The method does not account for local geometric imperfections, such as web out-of-flatness, flange tilt, or some global geometric imperfections such as camber, so an investigation into the suitability of the proposed imperfection modelling technique is conducted here. First, a sensitivity analysis is performed, analyzing the changes in the FEA moment–rotation response per incremental changes of the initial compression flange sweep. A second analysis is then conducted, investigating the efficacy of the eigenmode technique for modelling initial geometric imperfections with a focus on initial cross-section twist.

The initial compression flange sweep of the specimens has been recorded by measuring tape in the laboratory and is assumed to introduce +/- 1 mm measurement errors. The FEA moment–rotation responses of G8-390-25-2-p are plotted in Figure 6-13 for various initial compression flange sweeps ranging between +/- 1 mm, with an increment of 0.5 mm, to evaluate the sensitivity of the FEA results to the anticipated measurement errors. In this analysis, the geometric imperfections are assigned using the eigenmode technique as described in Section 6.1.5, and only the scaling factor is adjusted from the measured initial compression flange sweep. The solid black line of Figure 6-13 represents the model response with the measured imperfection amplitude assigned, and the blue and red dashed lines represent the model responses with an incremental increase and decrease of the imperfection amplitude, respectively. Note that the measured initial compression flange sweep of G8-390-25-2-p is 1.0 mm, and therefore, the curve for 0 mm is not provided in Figure 6-13, as the FEA cannot evaluate LTB with zero initial geometric imperfection defined.
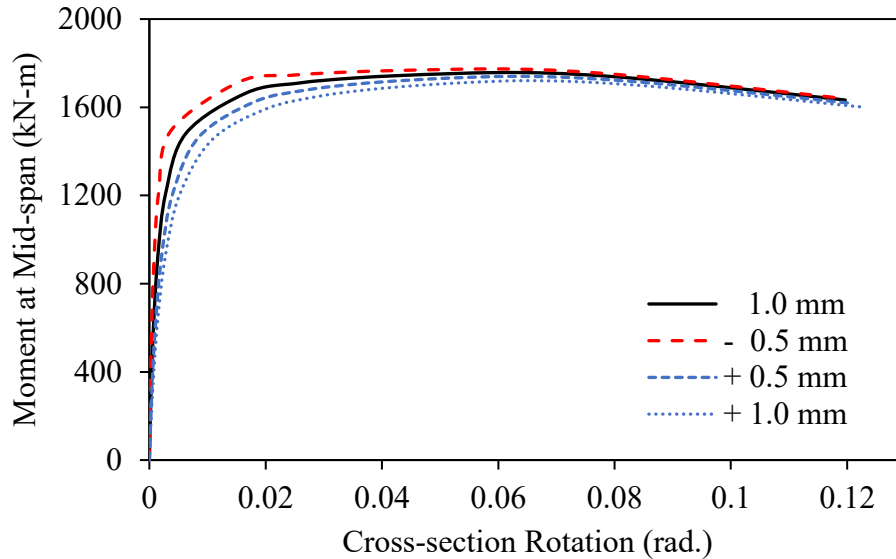
Figure 6-13: Sensitivity of G8-390-25-2-p finite element analysis to initial geometric imperfection

As shown in Figure 6-13, both the initial stiffness and moment resistances decrease with increasing magnitudes of initial compression flange sweep. The peak moment varied between +/- 2%, overall, and per 0.5 mm increment of initial compression flange sweep, the average percent change in the moment resistance is 1%. The same sensitivity analysis has been performed for G8-430-25-2-p and G9-360-25-3-f, although the moment–rotation plots are not shown. Like G8-390-25-2-p, the initial stiffness and moment resistance of G8-430-25-2-p and G9-360-25-3-f exhibit sensitivity to variations of the initial compression flange sweep, where the peak moment resistances of G8-430-25-2-p and G9-360-25-3-f varied between +/- 1% and +/- 2%, respectively. Given that the FEA moment resistances vary at most by 2% when simulating the probable measurement error, the FEA is expected to adequately estimate the moment resistance of a welded girder, even if the measured initial geometric imperfection distribution is not exactly reflected in the FE model. This finding is important to consider, given the fact that the eigenmode technique for defining initial geometric imperfections in the FE model only accounts for the amplitude of measured geometric imperfections and not the actual distribution, unless the actual distribution follows the deformed shape of the first eigenmode.

Initial cross-section twists have been indirectly assigned to the FE models when applying the eigenmode technique, which may not be representative of the measured geometry of the test specimens. Therefore, the initial cross-section twist present in the FE model has been determined by calculating the angle formed between the deformed web and the vertical plane. The test-to-predicted ratio of maximum moment, M_{Test}/M_{FE}, and the test-to-predicted ratio of initial stiffness are plotted against the ratio of measured initial cross-section twist to FE cross-section twist, $\varphi_{Test}/\varphi_{FE}$, as shown in Figure 6-14 and Figure 6-15, respectively. In these figures, the FEA moment resistance, M_{FE}, is the same moment resistance reported in Section 6.2.1. k_{Test} and k_{FE} are calculated by taking the secant of the moment–rotation response between zero moment and approximately 40% of the peak moment for the experimental and FEA data, respectively. G8-390-32-2-p has not been plotted, as the magnitude of the initial cross-section twist in the FE model approaches zero, which causes the ratio $\Theta_{Test}/\Theta_{FE}$ to approach infinity and distort the figure.
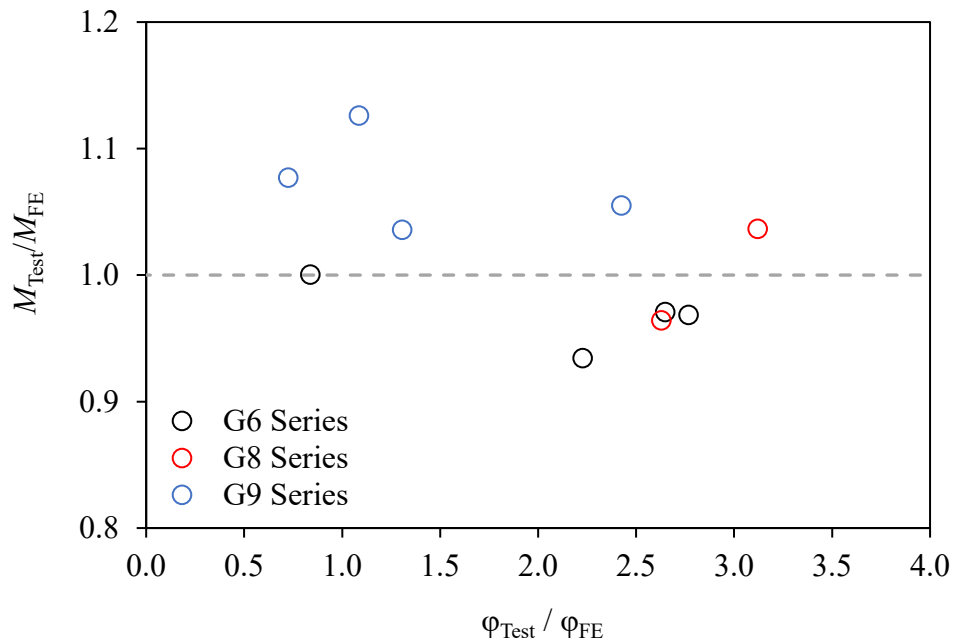
Figure 6-14: Test-to-predicted ratio of moment resistance vs. ratio of initial cross-section twist
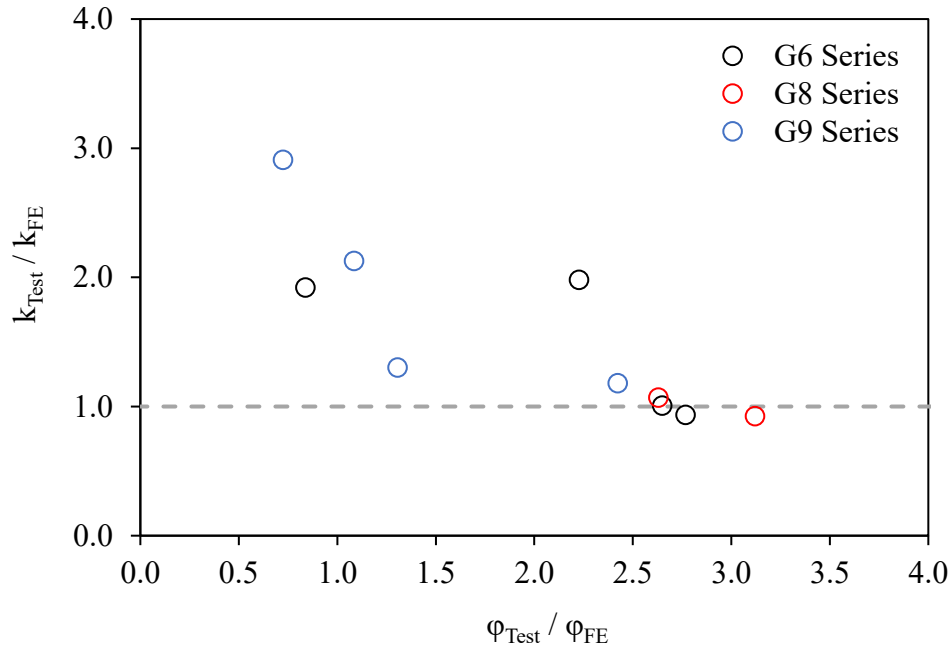
Figure 6-15: Test-to-predicted ratio of initial stiffness vs. ratio of initial cross-section twist

As shown in Figure 6-14, the magnitude of the initial cross-section twist implicit in the FE model does not appear to significantly influence the flexural strength predictions. However, as shown in Figure 6-15, the magnitude of initial cross-section twist does appear to affect the initial stiffness. The test-to-predicted ratio of initial stiffness decreases as the ratio of initial cross-section twist increases, meaning that the FEA predicts lower stiffness for higher magnitudes of initial cross-section twist. Despite this, the use of the eigenmode technique to define the initial geometric imperfections, based on the amplitude of the measured initial compression flange sweep alone, appears suitable for estimating the experimental moment resistances.

6.2.4 Influence of Distortion

When simulating the G8 and G9 series of girders, the FEA exhibited signs of web distortion. As lateral–distortional buckling (LDB) was confirmed to have occurred in the G9 series (see Section 4.2.3), it is anticipated that the FEA may be simulating web distortion or lateral–distortional buckling (LDB) to occur in the G9, and potentially the G8 series. In Chapter 4, the measured rotations of the top flange, web and bottom flange were examined to identify web distortion and the occurrence of LDB. Here, the nodal coordinates of the cross-section at mid-span are examined to confirm if the LDB is predicted by FEA, where the presence of web distortions at the peak

moment resistance signifies LDB. Figure 6-16 shows the cross-sections of G6-470-32-2-p and G9-430-25-3 at the start of the analysis, the peak moment resistance, and in the post-buckling region.
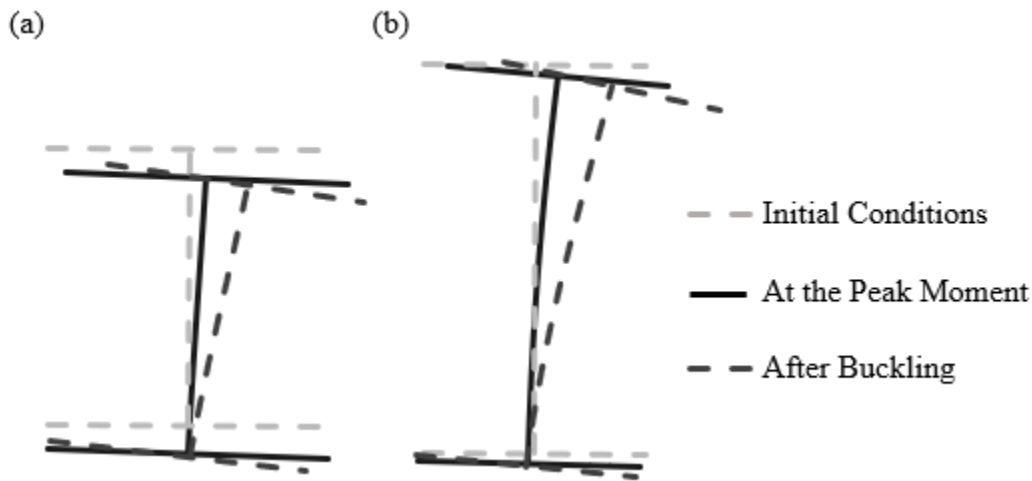
Figure 6-16: Deformed shape of the cross-section for (a) G6-470-32-2-p and (b) G9-430-25-3-f

As shown in Figure 6-16, G6-470-32-2-p exhibits only lateral translation and cross-section rotation when the peak moment resistance is achieved, with no apparent distortion of the web or flange. A similar response is observed in the post-buckling range. In contrast, G9-430-25-3-f exhibits non-rigid body rotation and distortion of the web in conjunction with lateral translation and cross-section rotation at the peak moment. Furthermore, the distortion exhibited by G9-430-25-3-f worsens after buckling. A review of the specimens in the G8 series (not shown) reveals the G8 series also exhibit web distortion at the peak moment; however, less distortion is observed for the G8 series than is shown in Figure 6-16 for G9-430-25-3-f. The presence of web distortion prior to attaining the peak moment resistance confirms that the FEA predicts LDB failure for the G8 and G9 series.

Since LDB is confirmed to occur both experimentally and numerically, the test-to-predicted ratios of moment resistance (M_{Test}/M_{FE}) have been plotted in Figure 6-17 against the local web slenderness ratio, h/w. The horizontal grey dashed line in Figure 6-17 delineates a test-to-predicted ratio of 1.0. Any test-to-predicted ratio above this threshold signifies an under-prediction of the experimental moment resistance by FEA.
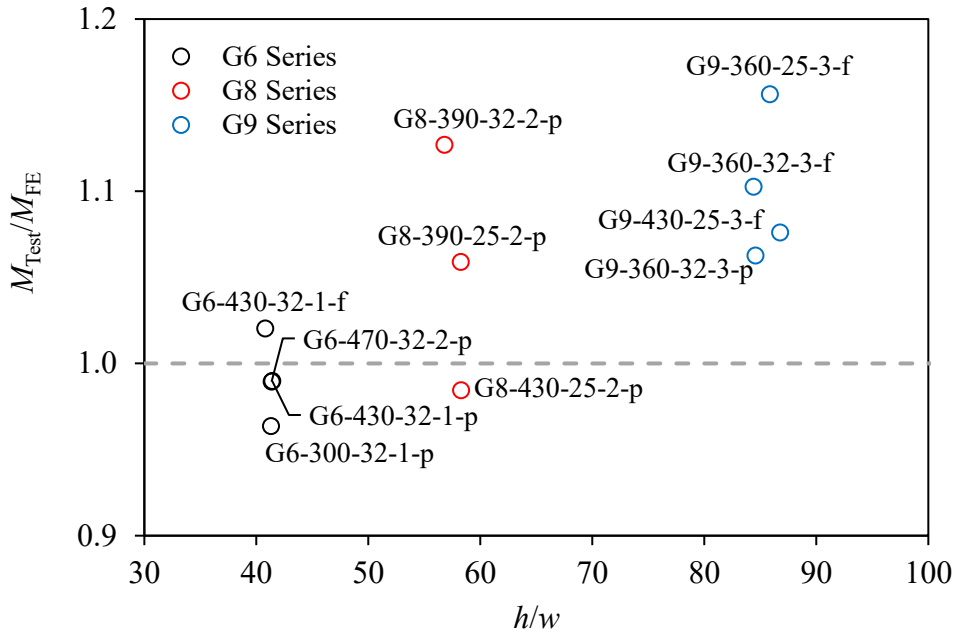
Figure 6-17: Test-to-predicted ratios of moment resistance vs. local web slenderness ratio

As shown in Figure 6-17, the test-to-predicted ratios of moment resistance increase with the local web slenderness. Moreover, the FEA predictions worsen per depth series. The FEA adequately predicts the moment resistances of the G6 series (where no distortion is simulated), under-predicts most of the G8 series, and under-predicts the entire G9 series. Given these observations and noting that LDB is predicted by FEA to occur for the G8 series and was not observed experimentally, it is inferred that the FEA is predicting more distortion than was present in the experiments. Consequently, the influence of LDB on the FEA may contribute to the high test-to-predicted ratios observed in the G8 and G9 series. However, as web distortion is only one of the many factors that influence the FEA moment resistances, including local geometric imperfection, residual stresses, boundary conditions, and expected numerical error, the exact influence of LDB on the test-to-predicted ratios of moment resistance is unclear.

6.2.5   Influence of Web Stiffeners

In flexural members with slender webs, bearing and transverse stiffeners can be designed to prevent a failure of the web, either at the girder ends to resist the support reactions (bearing stiffeners) or in regions of high shear (transverse stiffeners). In design, bearing and transverse stiffeners may be considered unrelated to flexural limit states such as LTB and only a requirement of bearing and shear limit states, respectively. For this reason, when modelling the test specimens to estimate the LTB response, the bearing and transverse stiffeners were initially assumed to be uninfluential and were not modelled. However, transverse stiffeners can mitigate the effects of LDB on the moment resistance of flexural members by reinforcing the web against distortion (White and Jung 2007).

The test girders were all designed with bearing stiffeners located at the end supports. However, the G9 series required transverse stiffeners 0.61 m (2 ft) and 1.8 m (6 ft) from the end supports, except for G9-360-25-3-f, where only one set of transverse shear stiffeners was required, 0.61 m (2 ft) from each end support. Both the bearing and transverse stiffeners are nominally 12.7 mm (0.5 in) thick, 125 mm wide and span either the height of the web or 795 mm, respectively. The bearing and transverse stiffeners, as simulated in the FE model, are shown in Figure 6-18.
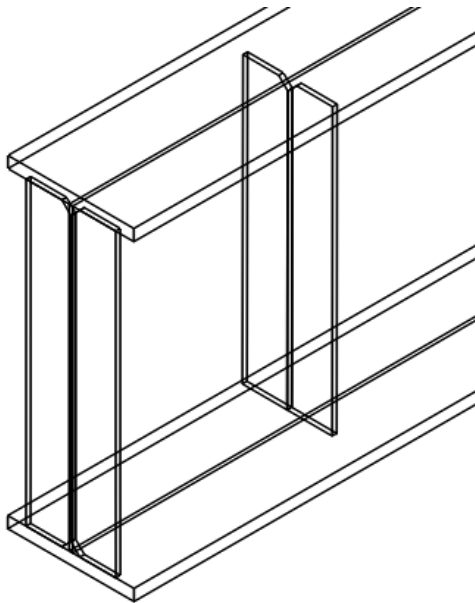
Figure 6-18: Bearing and transverse stiffeners simulated at end of test specimen

The as-built dimensions of the bearing and transverse stiffeners were used in the simulation with the tri-linear material definition described in Section 6.1.2. S4R shell elements are utilized, with a mesh density of 20 mm, except at the stiffener's interior corner, where a triangular element is assigned to accommodate the coping specified for the web–flange weld. The stiffeners have been "fused" to the girders, utilizing tie constraints, in a manner similar to what was done when modelling the rollers (see Sections 6.1.7 and 6.2.2). Since the web and flange nodes constrained to the bearing stiffeners are the same nodes that form the boundary conditions, there is concern that the bearing stiffeners may indirectly influence the boundary conditions, and this is therefore investigated. Nevertheless, the test-to-predicted ratios of moment resistance with and without bearing and transverse stiffeners are compared in Table 6-4.

Table 6-4: Test-to-predicted ratios of moment resistance, with and without stiffeners

Specimen ID	Test-to-predicted Ratio	
	Without Stiffeners	With Stiffeners
G6-470-32-2-p	1.00	0.99
G6-430-32-1-p	1.00	0.99
G6-430-32-1-f	1.03	1.02
G6-300-32-1-p	0.98	0.96
G8-430-25-2-p	1.01	0.98
G8-390-32-2-p	1.16	1.13
G8-390-25-2-p	1.10	1.06
G9-360-32-3-p	1.14	1.06
G9-360-32-3-f	1.19	1.10
G9-360-25-3-f	1.23	1.16
G9-430-25-3-f	1.21	1.08
Average	1.10	1.05

As shown in Table 6-4, the average test-to-predicted ratio of moment resistance for the entire test matrix decreased from 1.10 to 1.05, with the addition of stiffeners to the FE model. The test-to-predicted ratios of the G6 series modelled with shear stiffeners differ negligibly from the FEA without, where the average test-to-predicted ratio of the G6 series is 0.99 and 1.0, respectively. Both the G8 and G9 series exhibit an overall decrease of the test-to-predicted ratios of moment resistance, with the addition of stiffeners to the FE model. The moment resistances of the G9 series change the most from the FEA without shear stiffeners, as the average test-to-predicted ratio of the G9 series decreased from 1.19 to 1.10, and in the most extreme case, the moment resistance of G9-430-25-3-f is 13% larger than that of the moment resistance without stiffeners. The small change in the test-to-predicted ratio, observed in the G6 series for the FEA with and without stiffeners, suggests that the addition of bearing stiffeners to the FE model does not influence the boundary conditions, which was initially a concern. However, the transverse stiffeners are observed to significantly alter the moment prediction in the G9 series.

The FEA estimation of the experimental LTB response has appreciably improved, as the average test-to-predicted ratio of moment resistance decreased from 1.1 to 1.05. Transverse shear stiffeners are observed to increase the FEA moment resistances of girders with slender webs ($h/w > 80$) by as much as 13%, and this increase may be attributed to the stiffeners' ability to mitigate web distortion. Therefore, it is recommended that transverse stiffeners be explicitly modelled as required by steel design provisions for future FEA studies of LTB, as neglecting them can significantly affect the flexural response when the girder is sensitive to LDB.

7   FINITE ELEMENT ANALYSIS: RESULTS

In this chapter, the results of two sets of finite element analyses (FEA) are presented: (1) shear centre loading; and (2) top flange loading. The results are then used to evaluate the adequacy of the CSA S16-19 (CSA 2019a) design requirements for LTB of welded steel girders. In addition, the CSA S16-19 LTB provisions are compared to the LTB provisions of AISC 360-16 (AISC 2016) and EC3 (CEN 2005), the design equation proposed by MacPhedran and Grondin (2011), and the top flange loading methods of Wong et al. (2015), Helwig et al. (1997) and Nethercot and Rockey (1971). The FEA results used herein represent the anticipated moment resistances of the welded steel girders and are used in place of the experimental test results of Chapter 4, as direct comparisons between the experiments and CSA S16-19 cannot be made due to the point of load application residing above the top flange. In the finite element (FE) models, only the point of load application differs from the experimental program; otherwise, the measured geometric properties, material properties and residual stresses resemble those described in Chapter 6. Additionally, the transverse and bearing stiffeners of the test specimens are explicitly modelled.

7.1   Shear Centre Loading

The results obtained from the FEA of the test girders where the point loads are applied at the shear centre are compared to the moment resistances of CSA S16-19, AISC 360-16 and EC3, as well as the equation proposed by MacPhedran and Grondin (2011). The equation proposed by MacPhedran and Grondin (2011) is included in the comparative assessment because the results of numerical simulations performed by Kabir and Bhowmick (2018), which were validated by the test data available at the time, show that this equation can suitably predict the moment resistances of welded steel girders. Finally, the influence of geometric imperfections on the performance of the CSA S16-19 LTB provisions is examined.

7.1.1   Evaluation of CSA S16-19 Design Equation

The maximum moment resistances for shear centre loading, obtained from the FE model, $M_{FE,SC}$, are compared to the design predictions by CSA S16-19 in Table 7-1. In this table, the percent difference of moment resistance is provided. A negative percent difference indicates that the S16 design equation underestimates the anticipated moment resistance, and a positive percent difference indicates an overestimation by S16. The CSA S16-19 moment resistance, $M_{S16,SC}$ is

unfactored (nominal) and calculated using the measured cross-sectional properties and static yield stress, with an equivalent moment factor $\omega_2 = 1.13$.

Table 7-1: Comparison of CSA S16-19 moment resistances with finite element analysis moment resistances

Specimen ID	CSA S16-19, $M_{S16,SC}$ (kN-m)	Finite Element Analysis, $M_{FE,SC}$ (kN-m)	Percent Difference (%)
G6-470-32-2-p	3018	2996	+0.7
G6-430-32-1-p	2705	2753	-1.7
G6-430-32-1-f	2706	2715	-0.3
G6-300-32-1-p	1539	1745	-11.8
G8-430-25-2-p	2968	2679	+10.8
G8-390-32-2-p	3123	3265	-4.3
G8-390-25-2-p	2538	2617	-3.0
G9-360-32-3-p	2907	2353	+23.6
G9-360-32-3-f	2892	2475	+16.9
G9-360-25-3-f	2338	2104	+11.1
G9-430-25-3-f	3272	3115	+5.0

Table 7-1 shows that $M_{S16,SC}$ and $M_{FE,SC}$ align closely for specimens of the G6 and G8 series, where $M_{S16,SC}$ differs 1-5% from $M_{FE,SC}$, except for two specimens, G6-300-32-1-p and G8-430-25-2-p. G8-430-25-2-p is the only girder within the G6 and G8 series, where S16 is significantly unconservative when predicting the FEA moment resistance. The most significant discrepancies between $M_{S16,SC}$ and $M_{FE,SC}$ occur within the G9 series, where the FEA moment resistances are consistently overestimated, with a maximum overestimation of 24%. Nevertheless, overall, S16 predicts the FEA moment resistances within 4% on average. Figure 7-1 plots the moment resistances obtained from the FEA and those predicted by S16, normalized by the respective plastic moment, M_p, against the global slenderness ratio, L/r_y.
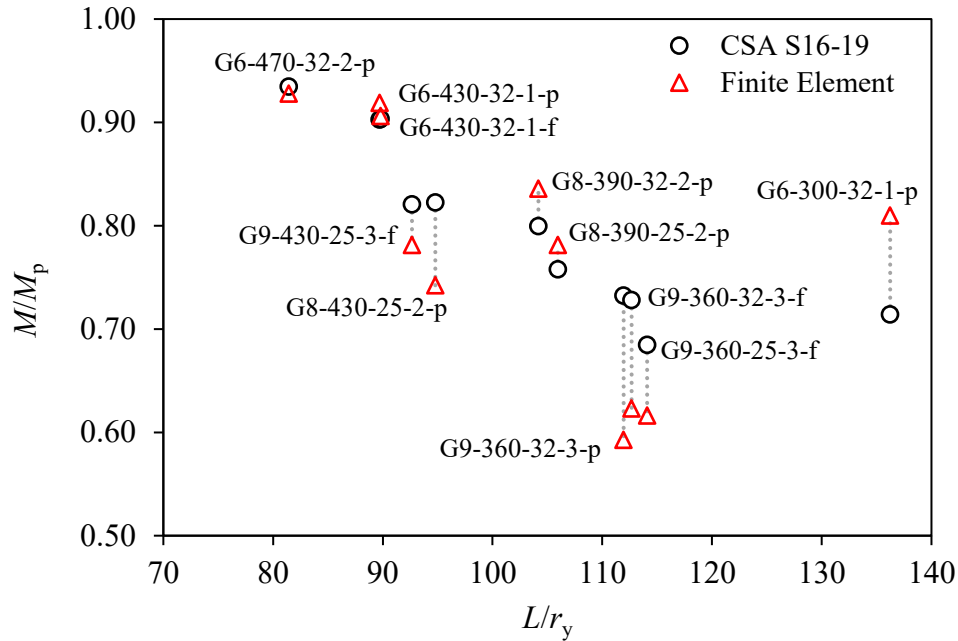
Figure 7-1: Comparison of moment resistances by CSA S16-19 and finite element analysis vs. global slenderness ratios

Figure 7-1 shows that the girders with low slenderness ratios ($L/r_y < 90$) and moment resistances approaching their plastic capacity are closely approximated by S16. For increasing global slenderness ratios, the agreement between S16 and the FEA lessens; however, the FEA moment resistances are predicted relatively well, and within 5% over a range of slenderness ratio between 90 and 110, except for G8-430-25-2-p. Both under- and over-estimations (see G6-300-32-1-p) of the moment resistances by S16 are observed for $L/r_y > 90$; however, most often, S16 is unconservative for this range of global slenderness ratios. Inconsistency of LTB moment resistances within the range $90 < L/r_y < 120$ is anticipated and was a motivating principle for this research. However, not shown in Figure 7-1 is the local web slenderness ratio, which increases with the depth series. Examining the G9 series in Figure 7-1 and Table 7-1 shows S16 to underestimate the moment resistances of these girders consistently, suggesting that the S16 design equation may specifically underperform when estimating the inelastic LTB resistance of welded steel girders with web width-to-thickness ratios approaching the Class 3 limit (G9 series).

7.1.2 Evaluation of AISC 360-16, EC3, and MacPhedran and Grondin (2011)

The LTB design equations of AISC 360-16, EC3, and the equation proposed by MacPhedran and Grondin (2011) are compared to $M_{FE,SC}$. The adequacy of these provisions relative to CSA S16-19 is then discussed. Figure 7-2 contains a plot of the normalized moment resistances per specimen of the test matrix, and Table 7-2 summarizes the percent differences of moment resistance. Note that the moment resistances predicted by each of the specified design equations are unfactored (nominal) and calculated using the measured cross-sectional properties, static yield stresses and an equivalent moment factor prescribed by the respective design method for a uniformly distributed load. The equation proposed by MacPhedran and Grondin (2011) utilizes the equivalent moment factor in CSA S16-19.
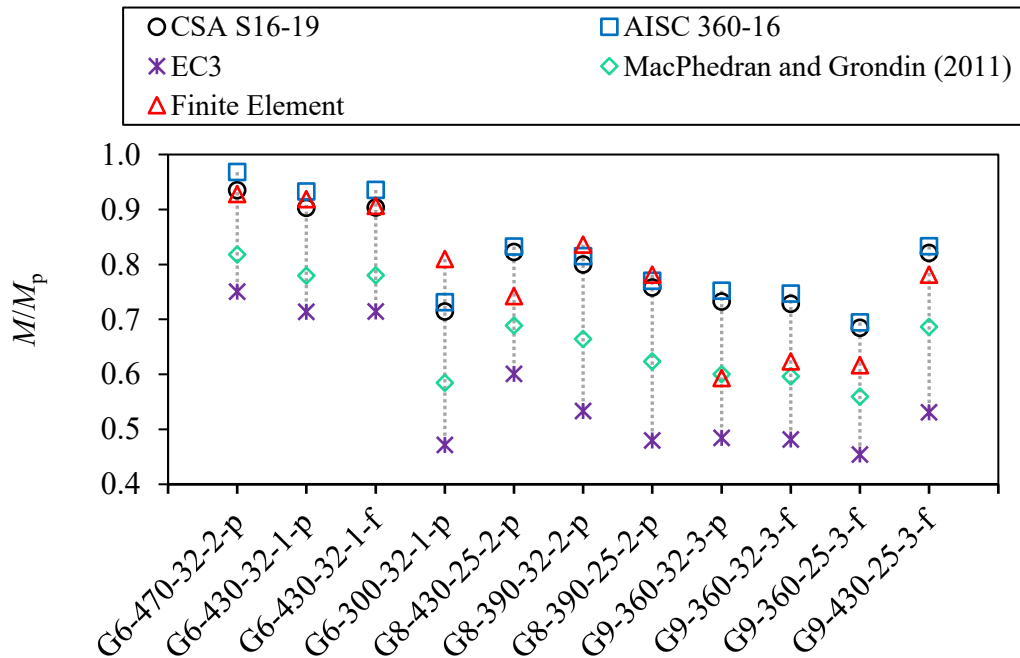
Figure 7-2: Normalized moment resistances by CSA S16-19, AISC 360-16, EC3, MacPhedran and Grondin (2011), and finite element analysis

The LTB design provisions of AISC 360-16 for doubly symmetric I-sections are functionally similar to those of CSA S16-19 and differ only in the formulation. For instance, AISC 360-16 differentiates inelastic LTB and elastic LTB by a limiting unbraced length, whereas CSA S16-19 uses a fraction of the plastic moment to set the boundary between elastic and inelastic LTB. Thus, negligible differences are anticipated between the two standards in the prediction of the LTB

resistance of welded steel girders. The comparisons, as shown in Figure 7-2 and Table 7-2, indicate that the moment resistances predicted by AISC 360-16 are close to those predicted by CSA S16-19, with an average percent difference of +6.7% and +4.3% between the FEA results and those predicted by AISC 360-16 and CSA S16-19, respectively. Similar to CSA S16-19, AISC 360-16 predicts the moment resistance of girders with lower slenderness ratios (i.e., G6 and G8 series) suitably, within 2-5%, but overestimates the capacity of the G9 series considerably (up to 27%).

The moment resistances predicted by EC3 are significantly lower than those of CSA S16-19, AISC 360-16 or MacPhedran and Grondin (2011) and are, on average, 27% lower than the FEA moment resistance. The moment resistances of all series predicted by the EC3 design equation are lower than the moment resistances obtained from the FEA. This observed response can be attributed to the EC3 design methodology, which sets multiple buckling curves to account for initial geometric imperfections explicitly, and more importantly, the buckling curves are delineated by the fabrication method (rolled or welded) and the girder aspect ratio ($2 \leq d/b$ or $d/b > 2$). As the specimens in this study are welded and have aspect ratios ranging between 1.3 and 2.5, the LTB capacities are obtained using buckling curves associated with the largest reduction factors (curves c and d), resulting in relatively low design strengths and the observed conservatism.

The proposed equation by MacPhedran and Grondin (2011) is consistently conservative, with the exception of G9-360-32-2-p, and predicts the moment resistances of the G6, G8 and G9 series, on average, by −13%. However, the equation proposed by MacPhedran and Grondin (2011) can be overly conservative in the G6 and G8 series as it estimates the moment resistances, on average, within −16% and −17%, respectively. For the G9 series, the equation by MacPhedran and Grondin (2011) provides a close and conservative estimation of the moment resistance with an average percent difference of -6%.

Table 7-2: Comparison of the moment resistances by CSA S16-19, AISC 360-16, EC3, and
MacPhedran and Gondin (2011) with finite element analysis moment resistances

Specimen ID	Finite Element Analysis, $M_{FE,SC}$ (kN-m)	Percent Difference in Moment Capacity (%)			
		CSA S16-19	AISC 360-16	EC3	MacPhedran and Grondin (2011)
G6-470-32-2-p	2996	+0.7	+4.3	-19.2	-11.9
G6-430-32-1-p	2753	-1.7	+1.5	-22.3	-15.2
G6-430-32-1-f	2715	-0.3	+3.2	-21.2	-13.9
G6-300-32-1-p	1745	-11.8	-9.7	-41.8	-27.9
G8-430-25-2-p	2679	+10.8	+12.1	-19.1	-7.3
G8-390-32-2-p	3265	-4.3	-2.5	-36.2	-20.5
G8-390-25-2-p	2617	-3.0	-1.5	-38.7	-20.2
G9-360-32-3-p	2353	+23.6	+26.9	-18.4	+1.2
G9-360-32-3-f	2475	+16.9	+19.9	-22.8	-4.3
G9-360-25-3-f	2104	+11.1	+12.7	-26.3	-9.2
G9-430-25-3-f	3115	+5.0	+6.6	-32.1	-12.1
Average		+4.3	+6.7	-27.1	-12.8
Standard Deviation		10.37	10.56	8.58	8.14

7.1.3   Influence of Initial Geometric Imperfections

The ratio $M_{S16,SC}/M_{FE,SC}$ is plotted against the measured initial compression flange sweep, normalized by $L/1000$, as shown in Figure 7-3. The ratio $M_{S16,SC}/M_{FE,SC}$ on the vertical axis is an indicator of the performance of the CSA S16-19 LTB design equation, where the ratio $M_{S16,SC}/M_{FE,SC} = 1.0$ implies that CSA S16-19 accurately predicts the moment resistance. Values of $M_{S16,SC}/M_{FE,SC}$ higher or lower than 1.0 represent unconservative or conservative predictions of the flexural strength, respectively.
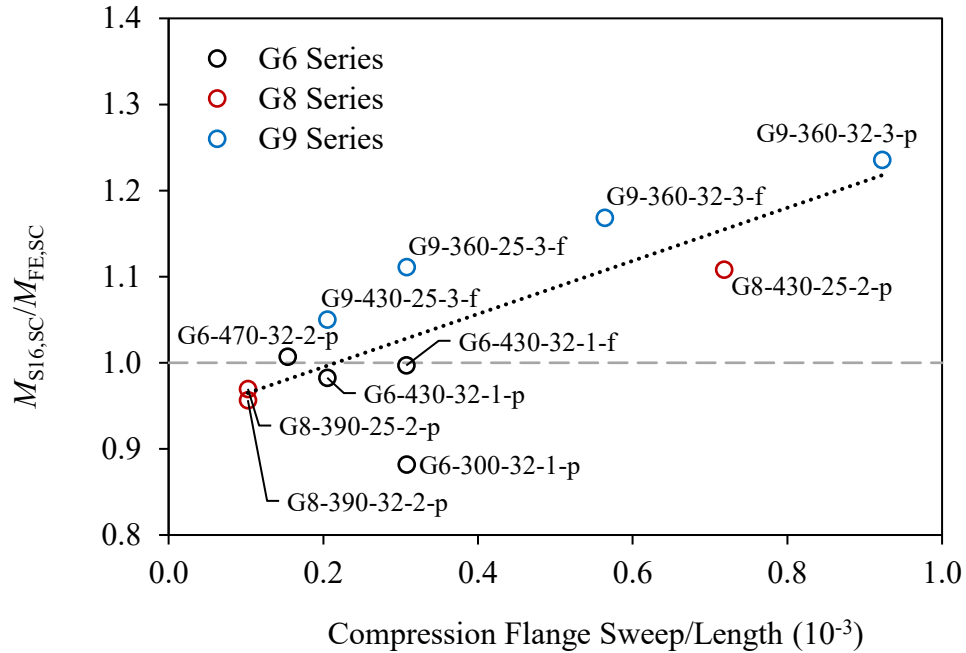
Figure 7-3: CSA S16-19 moment resistances vs. initial compression flange sweep

A relationship between $M_{S16,SC}/M_{FE,SC}$ and the magnitude of initial compression flange sweep is observed in Figure 7-3 and shows the moment resistance predictions by S16 to become increasingly unconservative with increasing initial compression flange sweep. A majority of the girders (8 of 11) exhibit initial compression flange sweeps less than 0.35 times $L/1000$, and of these girders, S16 estimates the moment resistance within 1% on average. However, for specimens with initial compression flange sweeps exceeding 0.35 times $L/1000$, the S16 prediction can be as much as 24% greater than the anticipated moment resistance. To further examine the performance of the S16 design equation considering a maximum amplitude of geometric imperfection, the FE model is modified and assigned a magnitude of initial geometric imperfection scaled to $L/1000$. The results of the modified FEA analysis are presented in Table 7-3 as $M_{FE,L/1000}$ and compared to $M_{S16,SC}$.

Table 7-3: Comparison of CSA S16-19 moment resistances with finite element analysis moment resistances with an amplified initial sweep

Specimen ID	CSA S16-19, $M_{S16,SC}$ (kN-m)	Finite Element Analysis, $M_{FE,L/1000}$ (kN-m)	Percent Difference (%)
G6-470-32-2-p	3018	2763	+9.2
G6-430-32-1-p	2705	2480	+9.1
G6-430-32-1-f	2706	2496	+8.4
G6-300-32-1-p	1539	1569	-1.9
G8-430-25-2-p	2968	2568	+15.6
G8-390-32-2-p	3123	2691	+16.1
G8-390-25-2-p	2538	2173	+16.8
G9-360-32-3-p	2907	2328	+24.9
G9-360-32-3-f	2892	2318	+24.7
G9-360-25-3-f	2338	1885	+24.0
G9-430-25-3-f	3272	2671	+22.5

Table 7-3 indicates that S16 overestimates the moment resistances of the specimens (with the exception of G6-300-32-1-p) on average by 15% when the maximum allowable initial geometric imperfection (L/1000) is assigned in the FE model. Given this observation, and considering the relationship observed in Figure 7-3, it is inferred that the S16 design equation can adequately estimate the moment resistances of welded steel girders, although the moment resistance predictions for girders with an initial geometric imperfection amplitude of L/1000 tend to be unconservative.

7.2 Top Flange Loading

The FE model is modified to develop a loading condition where the point loads are applied at the top flange. All other parameters remain unchanged, and the measured initial compression flange sweep is assigned. The moment resistances obtained from the FEA are compared to those predicted by the CSA S16-19 design equation adjusted for top flange loading. Load height adjustment factors

are back-calculated using the moment resistances of the shear centre and top flange loading models and are compared to those proposed by Wong et al. (2015), Helwig et al. (1997), and Nethercot and Rockey (1971). Finally, the adjusted moment resistances by CSA S16-19 are compared to those by Wong et al. (2015), Helwig et al. (1997) and Nethercot and Rockey (1971) to evaluate the adequacy of the code requirements.

7.2.1 Evaluation of CSA S16-19 Top Flange Loading Provisions

The CSA S16-19 approach to account for top flange loading is a simplified adoption of effective length methods published in the literature (Wong et al. 2015). The standard specifies, in lieu of a more accurate analysis, to take $\omega_2 = 1.0$, with an unbraced length of $1.2L$ for simply-supported members or $1.4L$ for all other end restraint conditions. To assess the adequacy of these provisions, the maximum moment resistances for top flange loading, obtained from the FEA, $M_{FE,TF}$, are compared to the S16 moment resistances for top flange loading, $M_{S16,TF}$, in Table 7-4. The percent differences in moment resistance are also provided, where a negative percent difference represents an under-prediction by S16, and a positive percent difference represents an over-prediction by S16.

Table 7-4: Comparison of CSA S16-19 moment resistances with finite element analysis moment resistance for top flange loading

Specimen ID	CSA S16-19, $M_{S16,TF}$ (kN-m)	Finite Element Analysis, $M_{FE,TF}$ (kN-m)	Percent Difference (%)
G6-470-32-2-p	2684	2923	-8.2
G6-430-32-1-p	2358	2556	-7.7
G6-430-32-1-f	2361	2693	-12.3
G6-300-32-1-p	1118	1470	-23.9
G8-430-25-2-p	2306	2138	+7.9
G8-390-32-2-p	2402	2566	-6.4
G8-390-25-2-p	1801	1984	-9.2
G9-360-32-3-p	2032	1863	+9.1
G9-360-32-3-f	2015	1946	+3.6
G9-360-25-3-f	1536	1594	-3.6
G9-430-25-3-f	2502	2521	-0.8

Table 7-4 shows that the top flange moment resistance predictions by S16 align well with the moment resistances obtained from the FEA, with the exception of G6-300-32-1-p. S16 conservatively estimates the moment resistances within 4.7% on average, and when compared to observations made in Section 7.1.1 regarding the performance of S16 for shear centre loading, the top flange loading design provisions exhibit less variability and a slightly lower standard deviation (10.3 vs. 9.5). The most significant discrepancies between $M_{S16,TF}$ and $M_{FE,TF}$ occur in the G6 series, where S16 consistently underestimates the moment resistance. Per girder series, the average percent difference in moment resistance increases and are -13.0%, -2.6% and +2.1% for the G6, G8, and G9 series, respectively. Figure 7-4 plots the normalized FEA and S16 moment resistances (both for top flange loading) against the global slenderness ratio L/r_y.
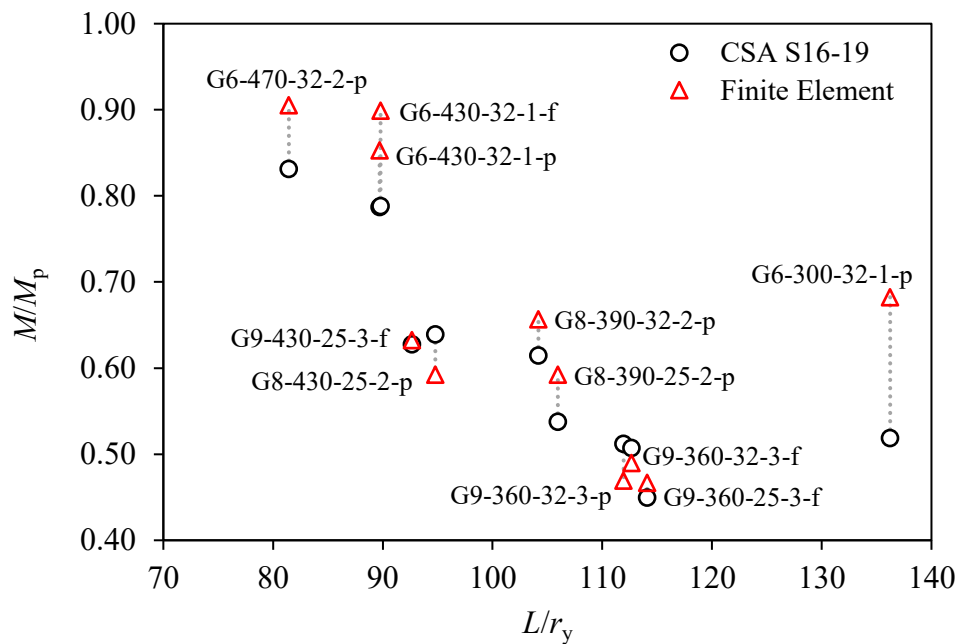
Figure 7-4: Comparison of moment resistances by CSA S16-19 and finite element analysis vs. global slenderness ratio for top flange loading

Figure 7-4 shows that the agreement between the adjusted S16 moment resistances and those predicted by FEA improves as the global slenderness ratio increases, with the exception of G6-300-32-1-p. This response contrasts the relationship observed in Figure 7-1 for shear centre loading. The conservatism of S16's top flange loading provisions diminishes as the web slenderness ratio increases; however, S16 does not become highly unconservative in the G9 series (i.e., with higher web slenderness ratios), contrasting the unconservative estimations observed for

shear centre loading in Section 7.1.1. In general, S16 performs adequately when girders are loaded at their top flange and is conservative on average for the range of global and local slenderness ratios studied. The conservatism of the standard's top flange loading provisions may be attributed to the simplified effective length approach employed and is not unexpected, as Wong et al. (2015) found the S16 method to be consistently conservative over a diverse set of girder geometries and end restraint conditions.

7.2.2 Load Height Adjustment Factors

For the specimens tested in this study, the load height adjustment factors are back-calculated using the shear centre and top flange loading models. The values are then compared to those proposed by Nethercot and Rockey (1971), Helwig et al. (1997) and Wong et al. (2015). Nethercot and Rockey (1971) proposed the ω_2^* factor to adjust the critical elastic moment, M_u, for simply supported girders subject to distributed transverse loading:

$$\omega_2^* = 1.12 \left[1 - 0.154 \left(\frac{\pi}{L} \sqrt{\frac{EC_w}{GJ}} \right)^2 + 0.535 \left(\frac{\pi}{L} \sqrt{\frac{EC_w}{GJ}} \right) \right]^{-1} \tag{7-1}$$

in which E and G are the elastic and shear moduli of the material, L is the unbraced length, J is the St. Venant torsional constant, and C_w is the warping torsional constant.

Helwig et al. (1997) modified the ω_2^* factor as given in Eq. 7-2, by simplifying and expanding the method by Nethercot and Rockey (1971) to be applicable for transverse loading at any position between the mid-height and the top flange:

$$\omega_2^* = \omega_2 \left(1.4^{\frac{2y}{h_0}} \right) \tag{7-2}$$

where h_o is the distance between the flange centroids and y is the vertical coordinate of the load position about the mid-height that is positive for loading below the mid-height and negative for loading above.

Wong et al. (2015) proposed an effective length approach to determine the LTB capacity of girders loaded at their top flange. The effective length factor, which should be multiplied by the unbraced

length of the girder when computing the critical elastic moment M_u, is retrieved from a set of design curves that are a function of the torsional parameter R and consider various loading and restraint conditions. For the specimens of this study, the effective length factors found following the method of Wong et al. (2015) range between $1.1L$ to $1.17L$.

The load height adjustment factors are back-calculated for the test specimens by dividing the moment resistance of each specimen from the shear centre loading model by those of the top flange loading model and are given in Table 7-5. The load height adjustment factors are also compared to those obtained from Nethercot and Rockey (1971) and Helwig et al. (1997). Since the proposed adjustment factors are only applied to the elastic LTB capacity, the load height adjustment factors of G6-470-32-2-p, G6-430-32-1-p and G6-430-32-1-f, which approach their plastic cross-sectional capacity, are excluded from the comparison. The remaining girders that exhibit normalized moment resistances closer to the S16 elastic LTB cut-off point ($M/M_p = 0.67$) are compared. The comparison shows that the methods proposed by Nethercot and Rockey (1971) and Helwig et al. (1997) can estimate the load height factors of these specimens within 0.7% and 2.3%, respectively.

Table 7-5: Load height adjustment factors for top flange loading

Specimen ID	Current Study	Nethercot and Rockey (1971)	Helwig et al. (1997)
G6-470-32-2-p*	0.98	0.81	0.81
G6-430-32-1-p*	0.93	0.83	0.81
G6-430-32-1-f*	0.99	0.83	0.81
G6-300-32-1-p	0.84	0.88	0.81
G8-430-25-2-p	0.80	0.77	0.81
G8-390-32-2-p	0.79	0.80	0.81
G8-390-25-2-p	0.76	0.78	0.81
G9-360-32-3-p	0.79	0.79	0.81
G9-360-32-3-f	0.79	0.79	0.81
G9-360-25-3-f	0.76	0.78	0.81
G9-430-25-3-f	0.81	0.78	0.81

*Denotes girders with M/M_p ratios approaching 1.0

7.2.3 Evaluation of Load Height Methods for Top Flange Loading

The moment resistances for top flange loading are determined by the load height adjustment methods of CSA S16-19, Helwig et al. (1997), Nethercot and Rockey (1971) and Wong et al. (2015) and compared to the top flange moment resistance obtained from FEA. Figure 7-5 shows the normalized moment resistances predicted by each method over the range of studied cross-sectional geometries, while Table 7-6 gives the percent difference of moment resistances between the respective load height methods. In Table 7-6, a negative percent difference represents an under-prediction by the respective load height method, and a positive percent difference represents an over-prediction. It should be noted that the methods of Helwig et al. (1997), Nethercot and Rockey (1971) and Wong et al. (2015) only modify the elastic critical moment, M_u, which is then used to determine the moment resistance for top flange loading as per CSA S16-19 provisions for LTB.
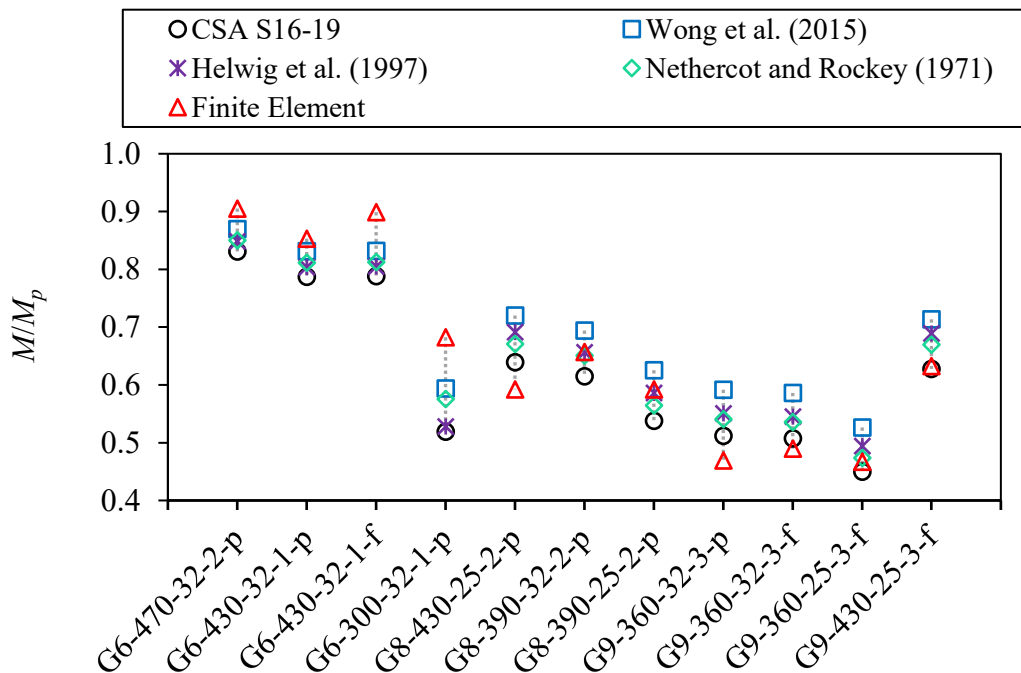
Figure 7-5: Normalized moment resistances for top flange loading

Referring to Figure 7-5 and Table 7-6, the moment resistances predicted by S16 are found to be lower than those predicted by Wong et al. (2015), Helwig et al. (1997) and Nethercot and Rockey (1971). Moreover, the S16 method results in a conservative estimation of the moment resistances in most of the cases, whereas Wong et al. (2015), Helwig et al. (1997) and Nethercot and Rockey

(1971) methods are often unconservative and overestimate the moment resistances on average by 7%, 1.3% and 0.3%, respectively. The method of Wong et al. (2015) is the least conservative of the load height methods studied here and over-predicts the moment resistances by a maximum of 26%. The methods by Helwig et al. (2015) and Nethercot and Rockey (1971) are relatively accurate; however, they can overestimate the moment resistances by a maximum of 17% and 15%, respectively.

The moment resistances predicted by the four load height adjustment methods studied become increasingly unconservative as the depth series and web slenderness ratios increase (i.e., the G9 series). Likely, the same phenomenon influencing the S16 shear centre loading provisions (see Section 7.1.2) to underperform when estimating the inelastic LTB capacity of specimens with slender webs influences the results shown in Figure 7-5 and Table 7-6.

Table 7-6: Comparison of moment resistances for top flange loading

Specimen ID	Finite Element Analysis, $M_{FE,TF}$ (kN-m)	Percent Difference in Moment Capacity (%)			
		CSA S16-19	Wong et al. (2015)	Helwig et al. (1997)	Nethercot and Rockey (1971)
G6-470-32-2-p	2923	-8.2	-3.9	-6.3	-6.1
G6-430-32-1-p	2556	-7.7	-2.6	-5.8	-4.9
G6-430-32-1-f	2693	-12.3	-7.4	-10.5	-9.6
G6-300-32-1-p	1470	-23.9	-12.9	-22.6	-15.7
G8-430-25-2-p	2138	+7.9	+21.6	+16.8	+13.3
G8-390-32-2-p	2566	-6.4	+5.6	-0.1	-0.9
G8-390-25-2-p	1984	-9.2	+5.6	-1.0	-4.7
G9-360-32-3-p	1863	+9.1	+26.1	+17.3	+15.2
G9-360-32-3-f	1946	+3.6	+19.6	+11.3	+9.3
G9-360-25-3-f	1594	-3.6	+12.8	+5.9	+1.4
G9-430-25-3-f	2521	-0.8	+12.9	+8.9	+5.9
Average		-4.7	+7.0	+1.3	+0.3
Standard Deviation		9.5	12.7	12.2	9.8

7.3 Discussion on the Adequacy of CSA S16-19 LTB Design Provisions

Using an amplitude of geometric imperfection and residual stress as measured in the experimental program of the current study to simulate LTB by FEA, the CSA S16-19 LTB design equation is shown to estimate the anticipated moment resistances of welded steel girders adequately and within 4% on average. For the same set of girders, AISC 360-16 and EC3 predict the anticipated moment resistances within 7% and -27%, respectively, on average. However, it should be noted that the prediction by CSA S16-19 can become poor as the web width-to-thickness ratio and initial geometric imperfection amplitude increase, to a maximum overestimation of 25%. These findings are solely based on the range of geometric and material properties considered in the test matrix of this study.

The effective length method prescribed by CSA S16-19 to determine the moment resistance of girders loaded at their top flange can suitably, and with implicit conservatism, estimate the anticipated moment resistance for the girders studied. However, it is expected that the CSA S16-19 moment resistance for top flange loading can become unconservative for the web slenderness ratios higher than those studied here.

8 CONCLUSIONS AND RECOMMENDATIONS

8.1 Summary

This research project sought to experimentally and numerically evaluate the lateral−torsional buckling (LTB) response of welded steel girders, expand the repository of modern experimental test data, evaluate the adequacy of the CSA S16-19 LTB design provisions for welded steel girders, and investigate the LTB response of welded steel girders damaged by LTB and repaired through heat-straightening.

The LTB experiments covered the testing of four welded steel girders of a larger experimental program (see Ji et al. 2019), totalling 11 welded steel girders of intermediate slenderness and nine unique cross-sections. The studied specimens were loaded by an approximate distributed load and feature a nominal unbraced length of 9.75 m, simple supports, and a restriction of the cross-section rotation at the end conditions. The test results were used to assess the inelastic LTB behaviour of welded steel girders, considering geometric and material properties, as well as fabrication methods, and included examining material inelasticity, initial geometric imperfections, residual stresses, web distortions, and plate cutting methods.

The heat-straightening component of this project included the experimental testing of five girders, which were repaired by heat-straightening and retested. The specimens that formed the heat-straightening experimental program exhibited out-of-tolerance lateral deviations from straightness after failing in the LTB mode and were repaired in consultation with Supreme Group. The heat-straightened girders were retested following identical procedures to those of the LTB experiments, and the test results were used to assess the stability response of heat-straightened girders through comparison to the original LTB experiments.

In the final phase of this project, a continuum finite element model was developed to evaluate the adequacy of the LTB equation prescribed by CSA S16-19 for welded steel girders. The model was first calibrated against the experimental test data of the LTB program and then used to simulate the experimental specimens for two loading conditions: top flange and shear centre. The S16 design provisions for welded steel girders were then assessed by comparing the code-predicted moment resistances with those obtained from the numerical analysis. Additionally, the requirements specified in S16 to account for top flange loading were evaluated through the

comparison between the moment resistances obtained from the finite element analysis and those calculated using the load height procedures proposed by Wong et al. (2015), Helwig et al. (1997) and Nethercot and Rockey (1971).

8.2   Conclusions

As this project included three phases, the conclusions drawn from each study are summarized separately. The following conclusions are made concerning the LTB experimental program:

- An analysis of the stresses present in the compression flange of the G9 series revealed that three of the four girders failed in the inelastic LTB mode, and one girder failed in the elastic LTB mode.

- The ratio $M/M_p = 0.67$ specified in CSA S16-19 to delineate elastic and inelastic LTB may not be an accurate parameter, as three of the four studied girders are found to fail by inelastic LTB despite exhibiting ratios of M/M_p within the CSA S16-19 specified elastic range.

- The moment resistances of girders with Class 1 or 2 cross-sections were observed to be sensitive to the torsional parameter R, where this sensitivity decreases by increasing the local web slenderness ratio.

- Girders exhibiting an initial compression flange sweep approaching the maximum amplitude of $L/1000$, which buckle in the direction of this geometric imperfection, exhibited lower moment resistances than those girders with initial compression flange sweeps near the mean value of measured initial compression flange sweep ($L/4500$).

- The influence of plasma cutting vs. flame cutting on the moment resistances of the studied girders was negligible.

- The G9 series of girders, which possess web width-to-thickness ratios near the Class 3 limit, experienced distortion in the web prior to global buckling and are found to have failed in the LDB mode.

- Initial compression flange sweep and initial cross-section twist were observed to promote higher magnitudes of lateral displacement and cross-section rotation at buckling, provided the buckling direction follows that of the initial geometric imperfection.

The key findings of the heat-straightening experimental program are as follows:

- Heat-straightening appears not to affect the LTB behaviour of welded steel girders, provided that the procedure is performed following specifications of governing design standards and the best practice requirements of the prevailing literature.

- Losses of moment resistance were observed when comparing the moment resistances obtained from the heat-straightened test program with those of as-built girders; however, this observation can be attributed to the magnitude of geometric imperfection present in the heat-straightened girders after the repair.

- A loss of initial lateral stiffness and increased displacements were observed when comparing the heat-straightened and as-built girder displacements at buckling; however, these observations can be attributed to the magnitude of geometric imperfection present in the heat-straightened girders after the repair.

The conclusions drawn from the finite element analyses are as follows:

- The maximum value of initial compression flange sweep of $L/1000$, commonly used in FEA to simulate LTB, may not be representative of modern fabrication practices, as the mean value of maximum initial compression flange sweep measured for the test specimens is $L/4500$.

- The LTB design provisions specified in the 2019 edition of CSA S16 can adequately estimate the flexural moment resistance of Class 1 and Class 2 welded steel girders that fail in the inelastic LTB mode.

- The moment resistances of welded steel girders with web width-to-thickness ratios near Class 3 limits (i.e., slender webs) can be overestimated by the S16 design provisions.

- The LTB design provisions of S16 were found to overestimate the moment resistances of welded steel girders exhibiting maximum initial geometric imperfections of $L/1000$.

- The S16 requirements to predict the moment resistance of flexural members loaded on their top flange were found to adequately and conservatively estimate the moment resistances of simply-supported welded steel girders under distributed loads.

- Transverse stiffeners required by steel design standards such as CSA S16 to increase the shear resistance of the web in welded steel girders should be explicitly simulated in FEA,

in particular, when the girder is sensitive to web distortion (e.g., girders with slender webs such as Class 3 sections in S16 or those with depth-to-width ratios greater than 2.0).

8.3 Recommendations for Future Work

The following recommendations are proposed to expand on the findings of this research:

- Perform a parametric FEA using a validated FE model representative of modern welded steel girders to expand the LTB database.
- Perform further experimental testing of welded steel girders to expand the available experimental dataset; consider larger web slenderness ratios and aspect ratios, and Class 3 cross-sections.
- Investigate the adequacy of the CSA S16-19 design provisions when predicting the moment resistance of welded steel girders with Class 3 webs.
- Perform further experimental testing of heat-straightened girders to expand the experimental database and verify if heat-straightened girders can meet the anticipated moment resistances predicted by CSA S16-19.
- Investigate the influence heat-straightening has on a steel girder's mechanical properties and quantify how a change of the mechanical properties can influence the LTB response.
- Investigate the residual stresses that develop due to heat-straightening and assess their influence on the LTB response of a straightened girder.

REFERENCES

Alpsten, G. A., and Tall, L. 1970. "Residual stresses in heavy welded shapes." *Welding Journal*, 49(3), 93-105.

AISC. 2010. *ANSI/AISC 360-10, Specification for Structural Steel Buildings*. American Institute of Steel Construction, Chicago, IL.

AISC. 2016. *ANSI/AISC 360-16, Specification for Structural Steel Buildings*. American Institute of Steel Construction, Chicago, IL.

ASTM International. 2018. *A370-18, Standard Test Methods and Definitions for Mechanical Testing of Steel Products*. American Society for Testing and Materials, West Conshohocken, PA.

Avent, R. R., Mukai, D. J., and Robinson, P. F. 2000. "Effect of heat straightening on material properties of steel." *Journal of Materials in Civil Engineering*, 12(3), 188-19. https://doi.org/10.1061/(ASCE)0899-1561(2000)12:3(188)

Avent, R. R., Mukai, D. J., and Robinson, P. F. 2001. "Residual stresses in heat-straightened steel members." *Journal of Materials in Civil Engineering*, 13(1), 18-25. https://doi.org/10.1061/(ASCE)0899-1561(2001)13:1(18)

AWS. 2010a. *AWS D1.1/D1.1M, Structural Welding Code–Steel*. American Welding Society. Miami, FL.

AWS 2010b. *AWS D1.7/D1.7M, Guide for Strengthening and Repairing Existing Structures*. American Welding Society. Miami, FL.

AWS. 2015. AASHTO/AWS D1.5M/D1.5, Bridge Welding Code. American Welding Society. Miami, FL.

AWS. 2020. *AWS D1.1/D1.1M, Structural Welding Code–Steel*. American Welding Society. Miami, FL.

Baker, K. A., and Laurie Kennedy, D. J. 1984. "Resistance factors for laterally unsupported steel beams and biaxially loaded steel beam column." *Canadian Journal of Civil Engineering*, 11(4), 1008-1019. https://doi.org/10.1139/l84-116

Bjorhovde, J., Brozzetti, J., Alpsten, G.A., and Tall, L. 1972. "Residual stresses in thick welded plates." *Welding Journal*, 51(8), 392-405.

Boissonnade, N., Somja, H. 2012. "Influence of imperfections in FEM modeling of lateral torsional buckling." In *Proc., Annual Stability Conference.*, Structural Stability Research Council. Grapevine, TX. 399-413.

Bradford, M.A., 1992. "Lateral distorsional-buckling of steel I-section members." *Journal of Constructional Steel Research*, 23(1-3), 97-116.

CEN. 1992. EN 1993-1-1:1992, *Eurocode 3: Design of steel structures – Part 1-1: General rules and rules for buildings*. European Committee for Standardization, Brussels, Belgium.

CEN. 2005. EN 1993-1-1:2005, *Eurocode 3: Design of steel structures – Part 1-1: General rules and rules for buildings*. European Committee for Standardization, Brussels, Belgium.

Chernenko, D. E., and Laurie Kennedy, D. J. 1991. "An analysis of the performance of welded wide flange columns." *Canadian Journal of Civil Engineering*, 18(4), 537-555. https://doi.org/10.1139/l91-067

Clark, J. W., and Hill, H. N. 1960. "Lateral buckling of beams." *Journal of the Structural Division*, 86(7), 175-196.

Crisfield, M. A., 1981. "A fast incremental/iterative solution procedure that handles Snap-Through." *Symposium on Computational Methods in Nonlinear Structural and Solid Mechanics*. Transport and Road Research Laboratory, Department of the Environment, Crowthorne, Berkshire, England, 55-62.

CSA. 2001. *CSA S16-01, Design of steel structures*. Canadian Standards Association, Mississauga, ON.

CSA. 2009. *CSA S16-09, Design of steel structures*. Canadian Standards Association, Mississauga, ON.

CSA. 2013. *CSA G40.20-13/G40.21-13, General requirements for rolled or welded structural quality steel/Structural quality steel*. Canadian Standards Association, Mississauga, ON.

CSA. 2014. *CSA S16-14, Design of steel structures*. Canadian Standards Association, Mississauga, ON.

CSA. 2018. *CSA W59-18. Welded steel construction*. Canadian Standards Association, Mississauga, ON.

CSA. 2019a. *CSA S16-19, Design of steel structures*. Canadian Standards Association, Mississauga, ON.

CSA. 2019b. *CSA S6-19, Canadian Highway Bridge Design Code*. Canadian Standards Association, Mississauga, ON.

Dassault Systèmes. 2016a. "Abaqus/CAE 2017." Dassault Systèmes Simulia Corp., Johnston, RI.

Dassault Systèmes. 2016b. *Abaqus Theory Guide (2017)*. Dassault Systèmes Simulia Corp., Johnston, RI.

Dibley, J. E. 1969. "Lateral torsional buckling of I-sections in grade 55 steel." *Instn Civ Engrs-Proc*, 43(4), 599-627.

Dong, J., and Sause, R. 2009. "Flexural strength of tubular flange girders." *Journal of Constructional Steel Research*, 65(3), 622-630.

Dux, P. F., and Kitipornchai, S. 1983. "Inelastic beam buckling experiments." *Journal of Constructional Steel Research*, 3(1), 3-9.

FHWA. 2008. FHWA-IF-08-999, Guide for Heat-Straightening of Damaged Steel Bridge Members. Federal Highway Administration. Washington, DC.

Fukumoto, Y. 1976. "Lateral buckling of welded beams and girders in HT 80 steel". *IABSE Congress Report*, 10(1976), 403-408.

Fukumoto, Y., and Itoh, Y. 1981. "Statistical study of experiments on welded beams." *Journal of the Structural Division,* 107(1), 89-103.

Fukumoto, Y., Itoh, Y., and Kubo, M. 1980. "Strength variation of laterally unsupported beams." *Journal of the Structural Division*, 106(1), 165-181.

Galambos, T. V., and Ketter, R. L. 1959. "Columns under combined bending and thrust." *Journal of the Engineering Mechanics Division*, 85(EM2), 135-152.

Gérard, L., Li, L., Kettler, M., and Boissonnade, N. 2019. "Recommendations on the geometrical imperfections definition for the resistance of I-sections" *Journal of Constructional Steel Research*, 162(2019): 105716. https://doi.org/10.1016/j.jcsr.2019.105716

Greiner, R., and Kaim, P. 2001. *Comparison of LT-buckling design curves with test results*, ECCS TC8 Report 23. European Convention for Constructional Steelwork, Brussels, Belgium.

Helwig, T. A., Frank, K. H., and Yura, J. A. 1997. "Lateral-torsional buckling of singly symmetric I-beams." *Journal of Structural Engineering*, 123(9), 1172-1179. https://doi.org/10.1061/(ASCE)0733-9445(1997)123:9(1172)

Ji, X. L., Driver, R. G., and Imanpour, A. 2019. *Large-scale lateral–torsional buckling tests of welded girders*, Steel Centre Engineering Report No. 015., University of Alberta, Edmonton, AB.

Kabir, I., and Bhowmick, A. K. 2018. "Applicability of North American standards for lateral torsional buckling of welded I-beams." *Journal of Constructional Steel Research,* 146(2018), 16-26. https://doi.org/10.1016/j.jcsr.2018.03.029

Kim, Y. D. 2010. "*Behavior and design of metal building frames using general prismatic and web-tapered steel I-section members.*" Ph.D. Dissertation, Georgia Institute of Technology.

MacPhedran, I., and Grondin, G. Y. 2011. "A simple steel beam design curve." *Canadian Journal of Civil Engineering*, 38(2), 141-153. https://doi.org/10.1139/L10-114

Nagaraja Rao, N., Estuar, F., and Tall, L. 1964. "Residual stresses in welded shapes." *Welding Journal*, 43(7), 295-306.

Nethercot, D. A. 1972. "Factors affecting the buckling stability of partially plastic beams." *Instn Civ Engrs-Proc*, 53(2), 285-304.

Nethercot, D. A., 1974. "Residual stresses and their influence upon the lateral buckling of rolled steel beams." *The Structural Engineer*, 52(3), 89-96.

Nethercot, D. A., and Rockey, K. C. 1971. "Unified approach to the elastic lateral buckling of beams." *Structural Engineer*, 49(8), 321-330.

Pekoz, T., Bjorhovde, R., Errera, S. J., Johnston, B. G., Sherman, D. R., and Tall, L. 1981. "Determination of residual stresses in structural shapes." *Experimental Techniques*, 5(3), 4-7.

Powel, G. and Simons, J., 1981. "Improved iteration strategy for nonlinear structures." *International Journal for Numerical Methods in Engineering*, 17(10), 1455-1467.

Ramm, E. 1981. "Strategies for tracing the nonlinear response near limit points." *Nonlinear Finite Element Analysis in Structural Mechanics*, Springer, Berlin, Heidelberg, Bochum, Germany, 63-89.

Roeder, C. W. 1986. "Experimental study of heat induced deformation." *Journal of Structural Engineering*, 112(10), 2247-2262. https://doi.org/10.1061/(ASCE)0733-9445(1986)112:10(2247)

Subramanian, L., and White, D. E. 2017. "Resolving the disconnects between lateral torsional buckling experimental tests, test simulations and design strength equations." *Journal of Constructional Steel Research*, 128(2017), 321-334. http://dx.doi.org/10.1016/j.jcsr.2016.08.009

Unsworth, D., Driver, R. G., and Li, L. 2019. *Characterization of residual stresses in modern welded girders,* Steel Centre Engineering Report No. 014., University of Alberta, Edmonton, AB.

Unsworth, D., Driver, R. G., and Li, L. 2020. "Measurement and prediction of residual stresses in welded girders." *Journal of Constructional Steel Research*, 169(2020). https://doi.org/10.1016/j.jcsr.2020.106007

White, D.W., and Jung, S.-K. 2007. "Effect of web distortion on the buckling strength of noncomposite discretely-braced steel I-section members." *Engineering Structures*, 29(8), 1872-1888.

Wong, E., Driver, R. G., and Heal, T. W. 2015. "Simplified approach to estimating the elastic lateral-torsional buckling capacity of steel beams with top-flange loading." *Canadian Journal of Civil Engineering*, 42(2), 130-138. https://doi.org/10.1139/cjce-2014-0265

Yarimci, E., Yura, J. A., and Lu, L. W. 1967. "Techniques for testing structures permitted to sway." *Experimental Mechanics*, 7(8), 321-331.

Ziemian, R. D. 2010. *Guide to Stability Design Criteria for Metal Structures*, 6th Ed., John Wiley and Sons, Inc., Hoboken, New Jersey.

Appendix A: Measured Initial Geometric Imperfections
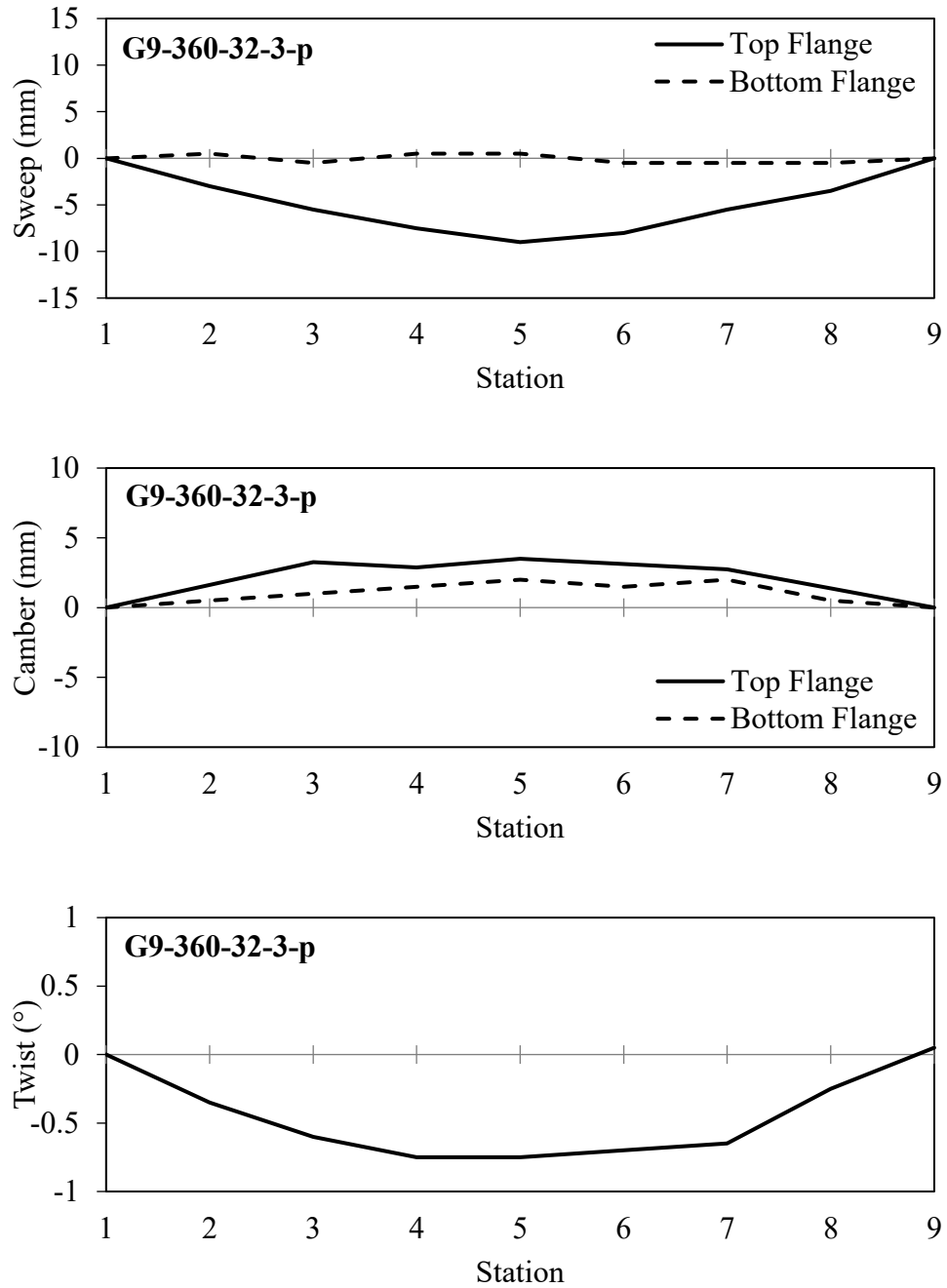
Figure A-1: Initial geometric imperfections of G9-360-32-3-p
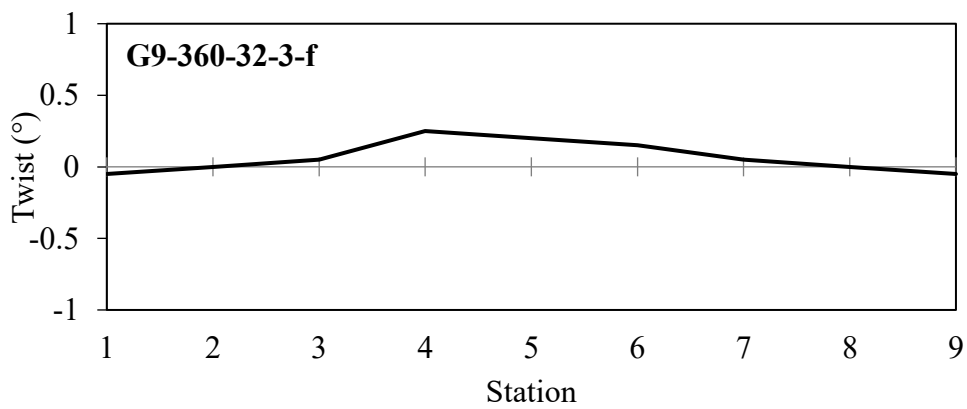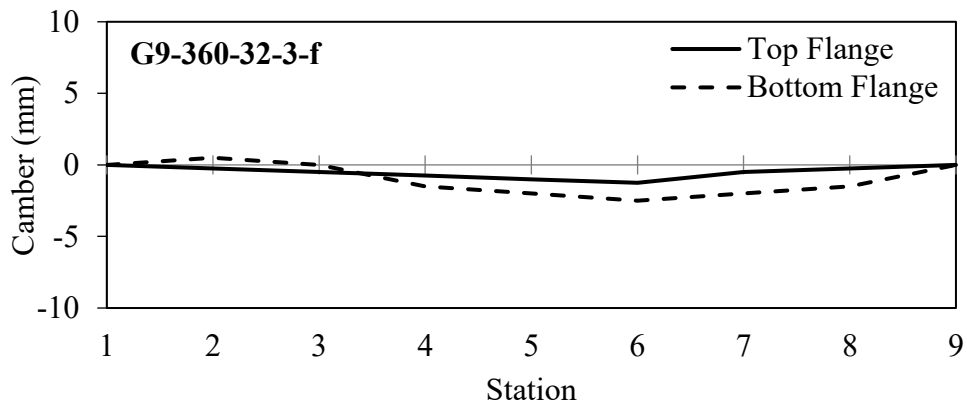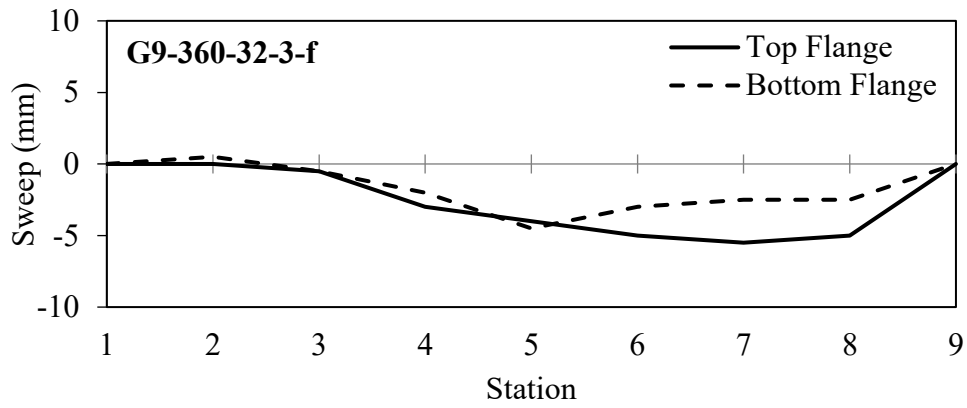
Figure A-2: Initial Geometric Imperfections of G9-360-32-3-f
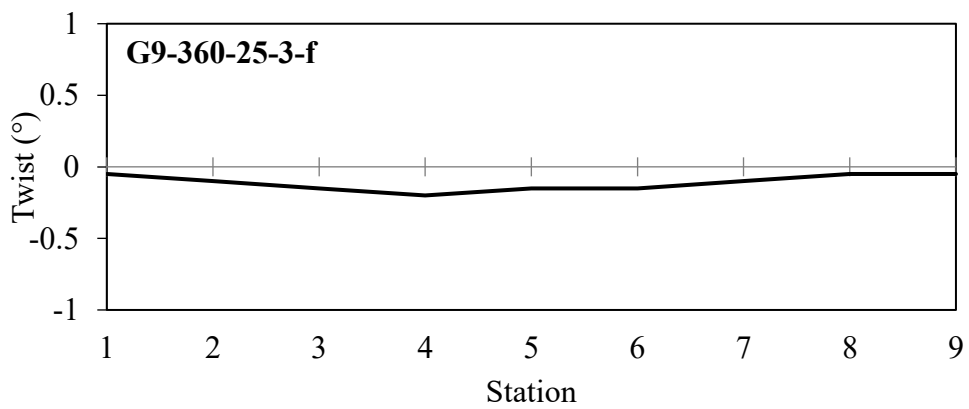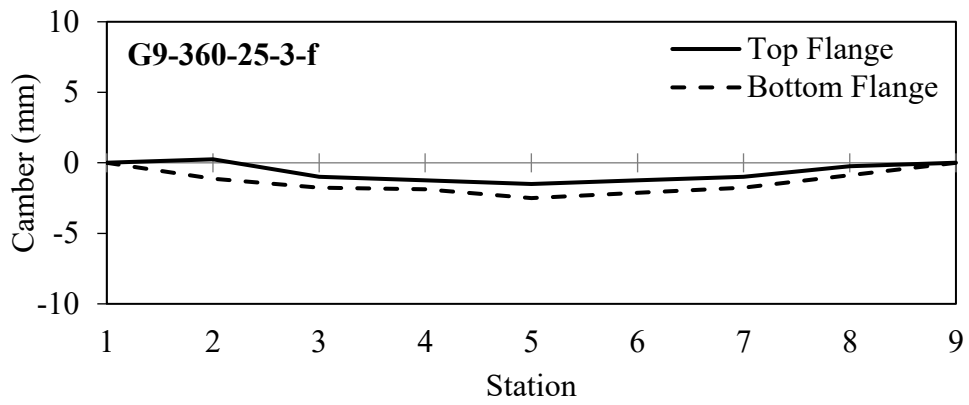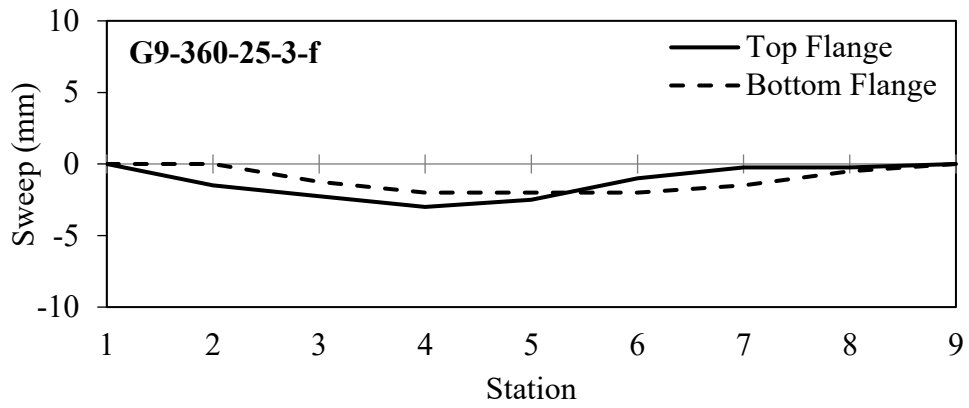
Figure A-3: Initial geometric imperfections of G9-360-25-3-f
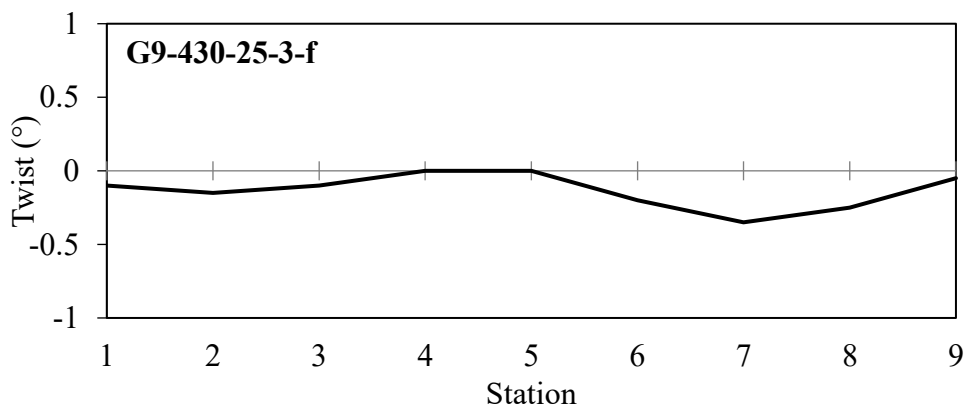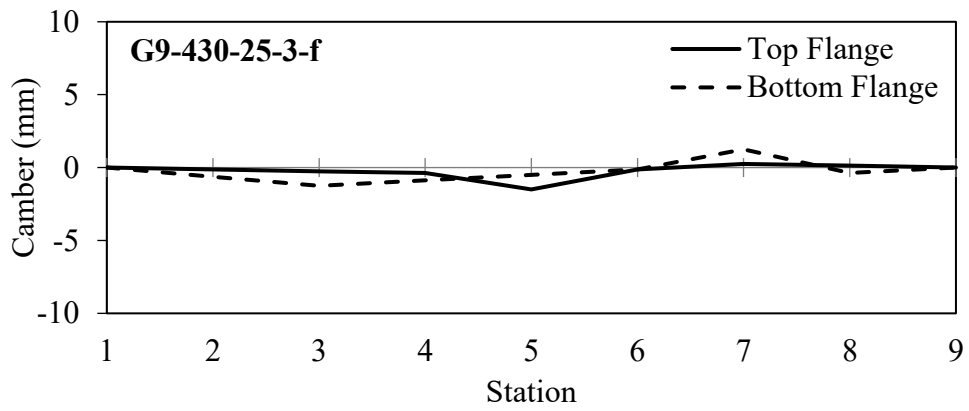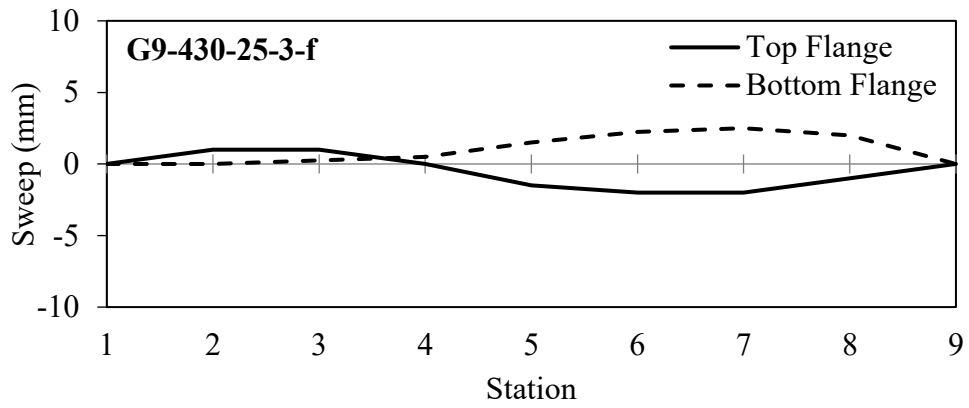
Figure A-4: Initial geometric imperfections of G9-430-25-3-f
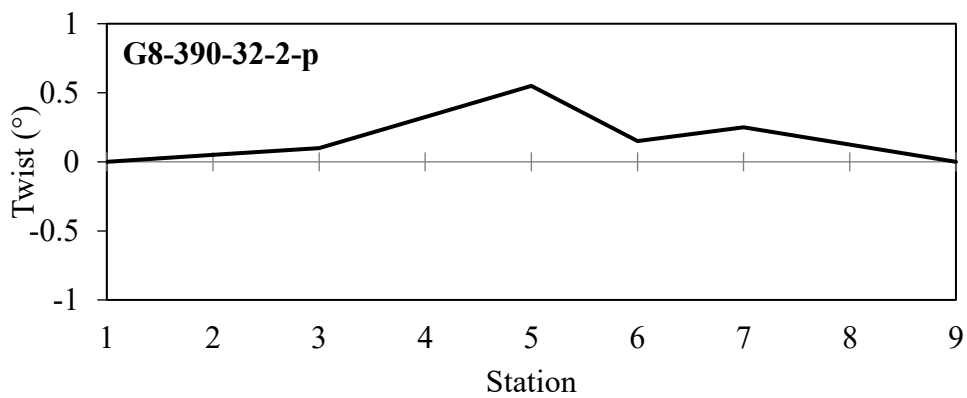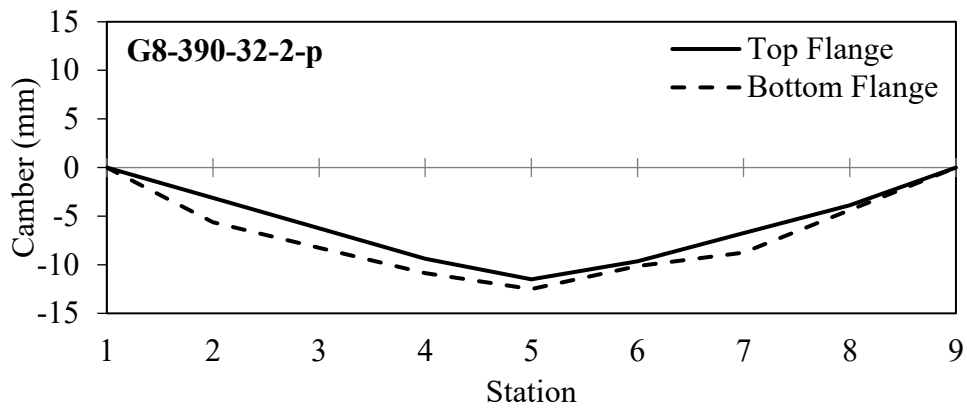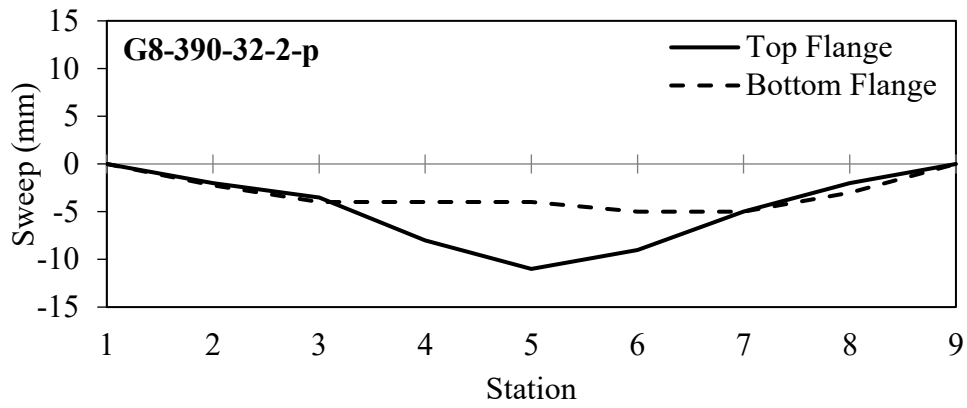
Figure A-5: Initial geometric imperfections of the heat-straightened G8-390-32-2-p
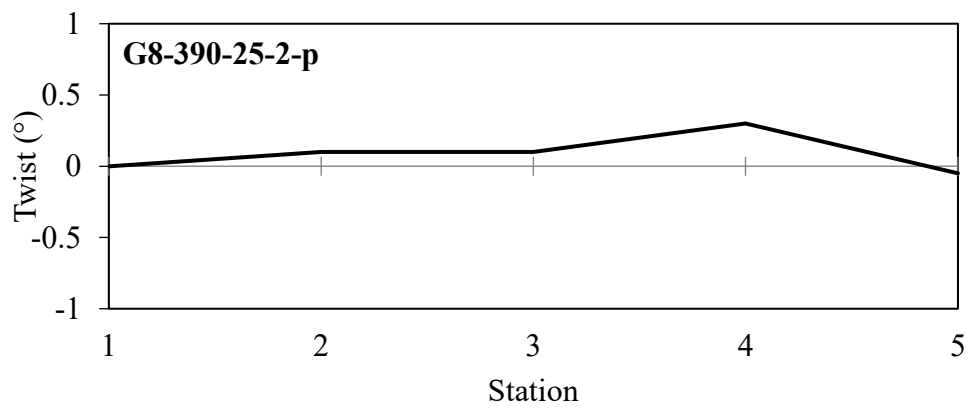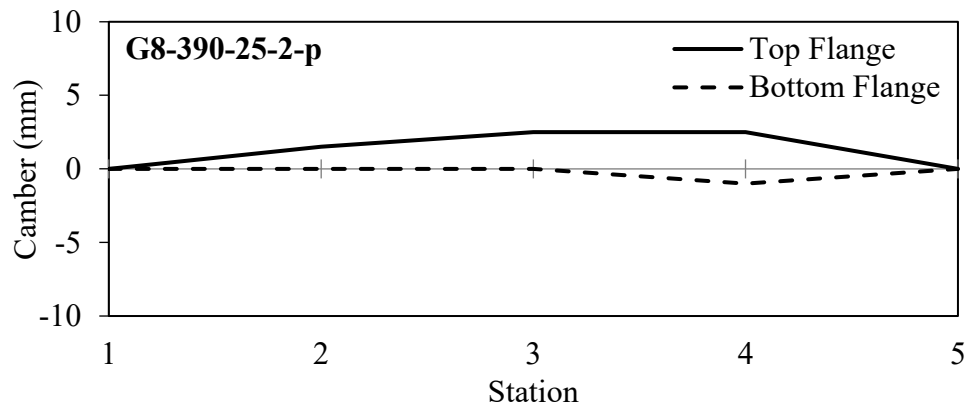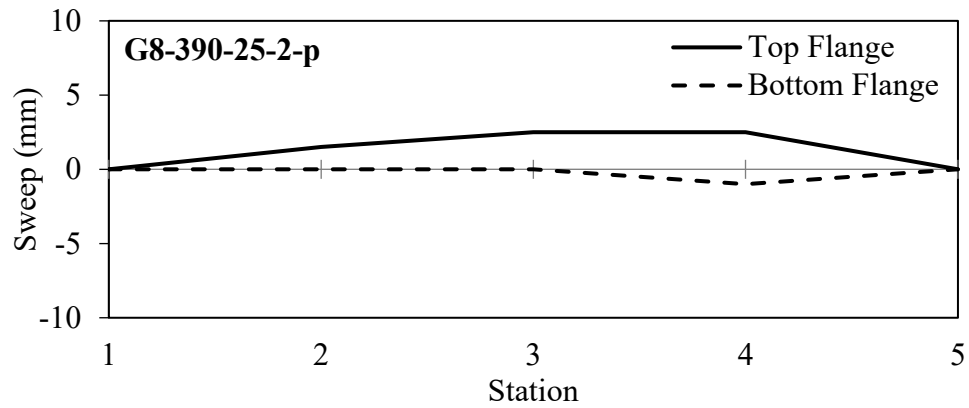
Figure A-6: Initial geometric imperfections of the heat-straightened G8-390-25-2-p
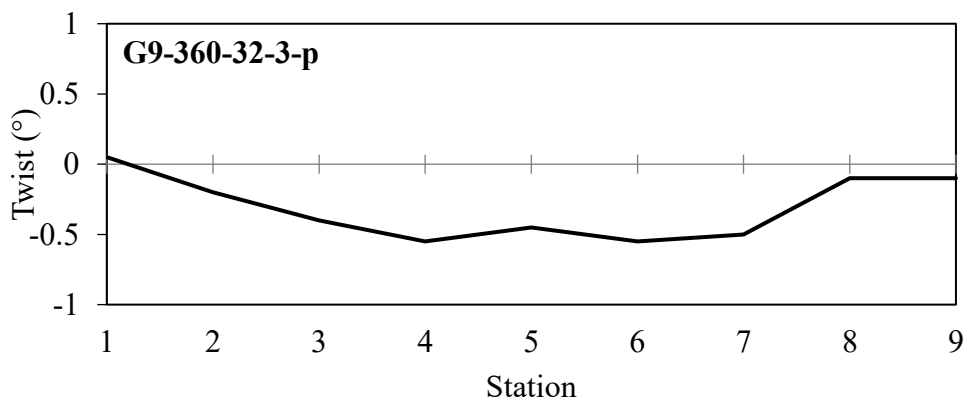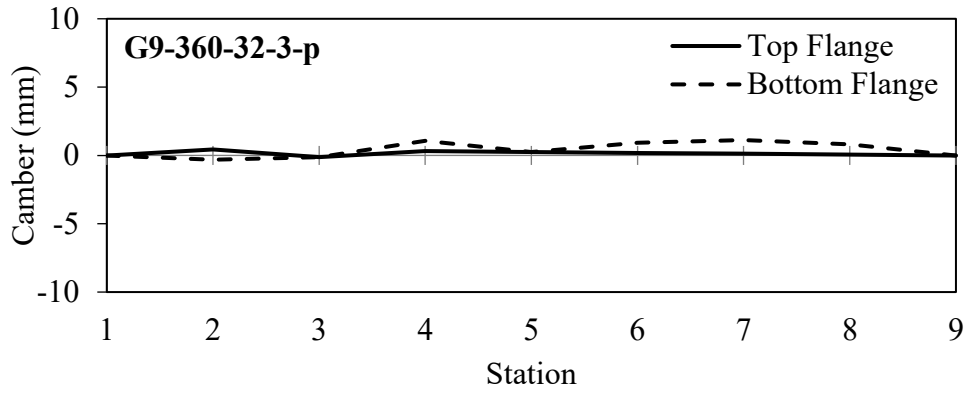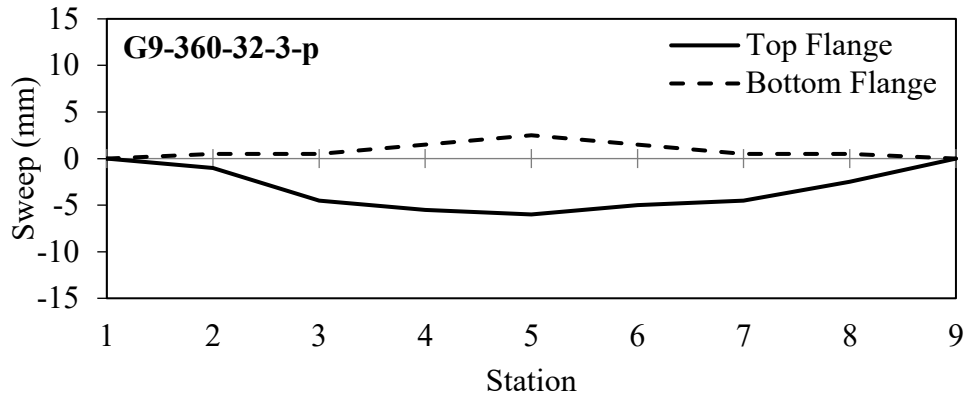
Figure A-7: Initial geometric imperfections of the heat-straightened G9-360-32-3-p
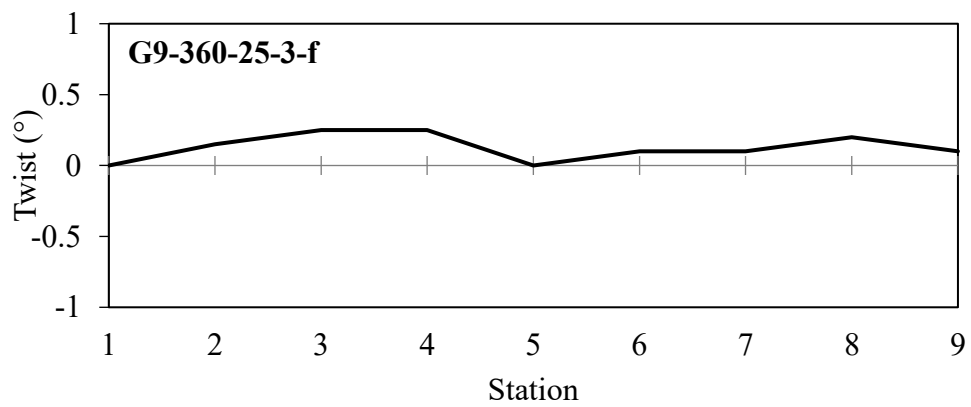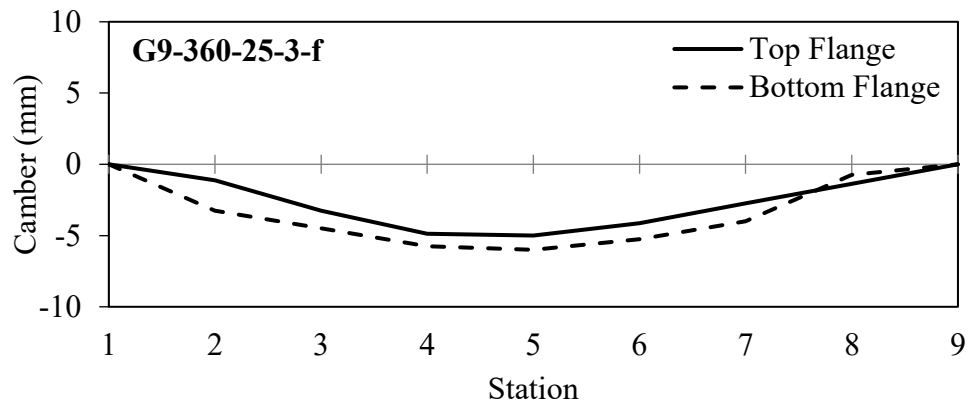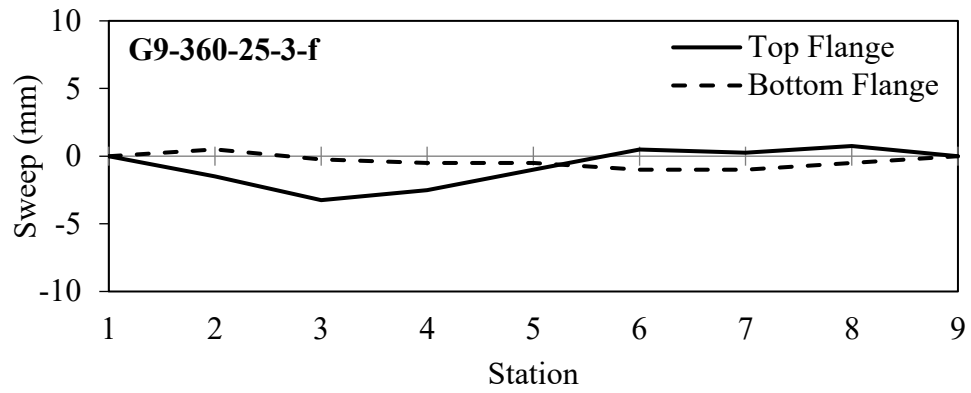
Figure A-8: Initial geometric imperfections of the heat-straightened G9-360-25-3-f
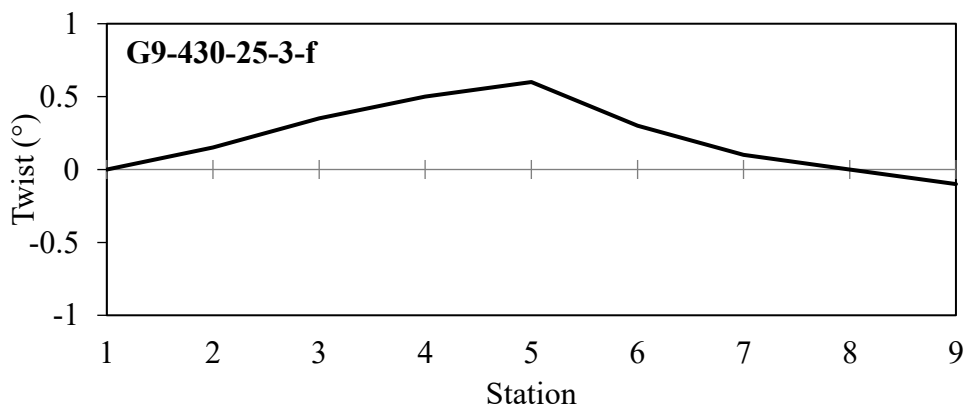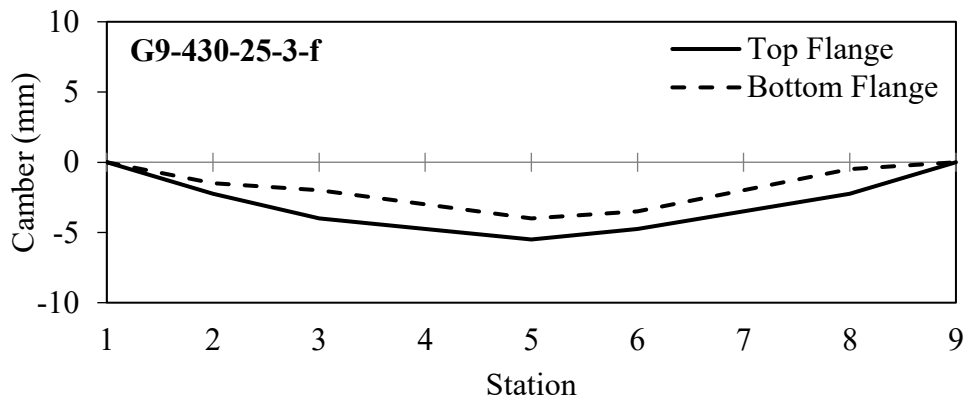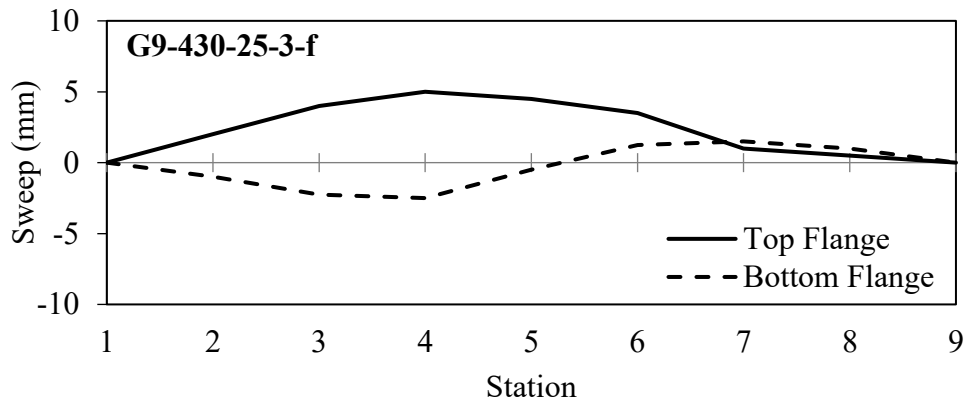
Figure A-9: Initial geometric imperfections of the heat-straightened G9-430-25-3-f
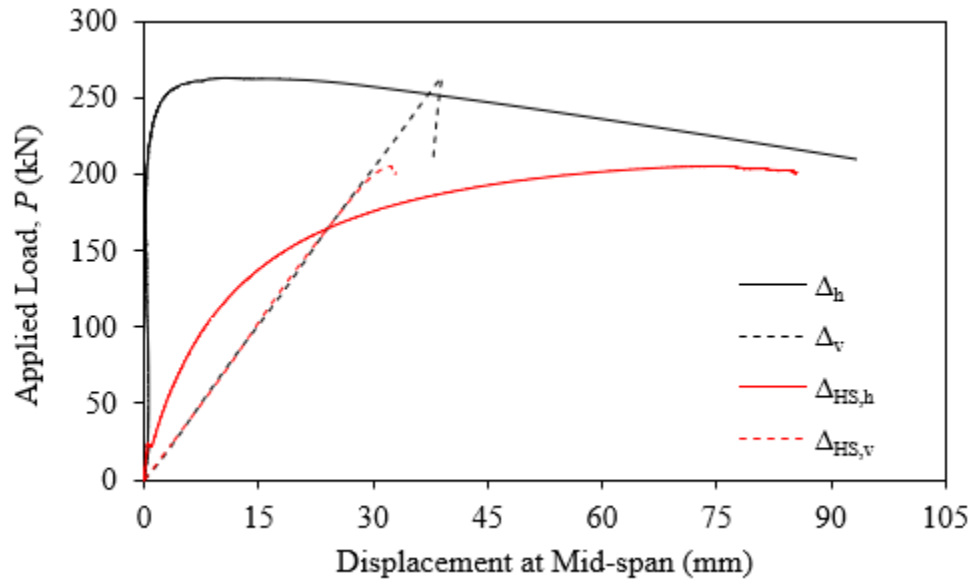
Figure B-1: Load-displacement responses of G8-390-32-2-p: Original and heat-straightened
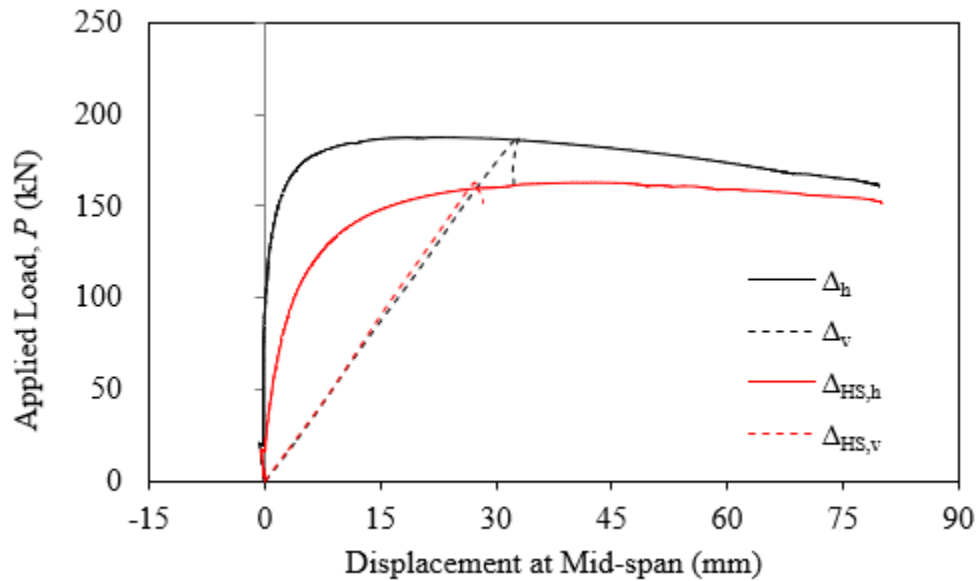
Figure B-2: Load-displacement responses of G8-390-25-2-p: Original and heat-straightened
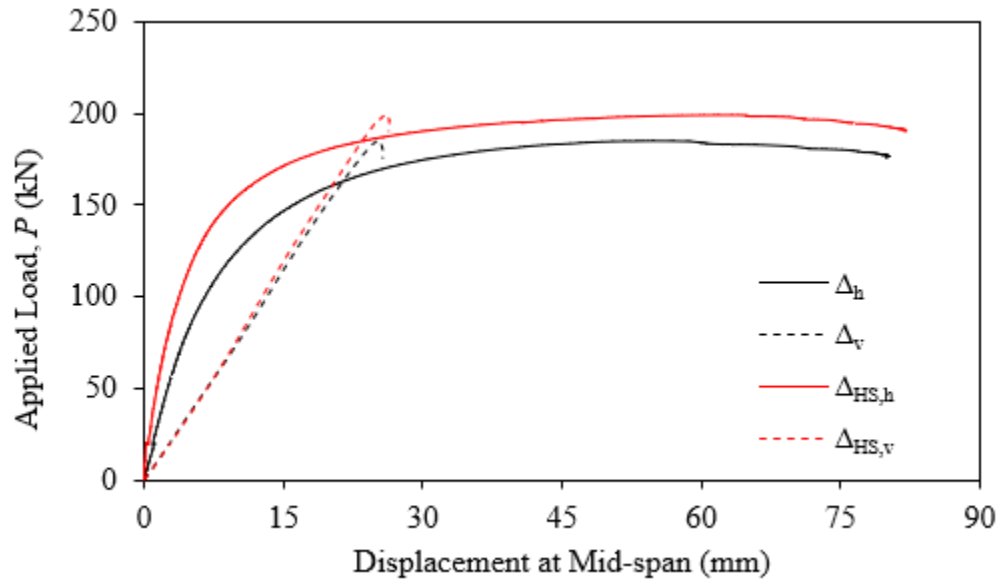
Figure B-3: Load-displacement responses of G9-360-32-3-p: Original and heat-straightened
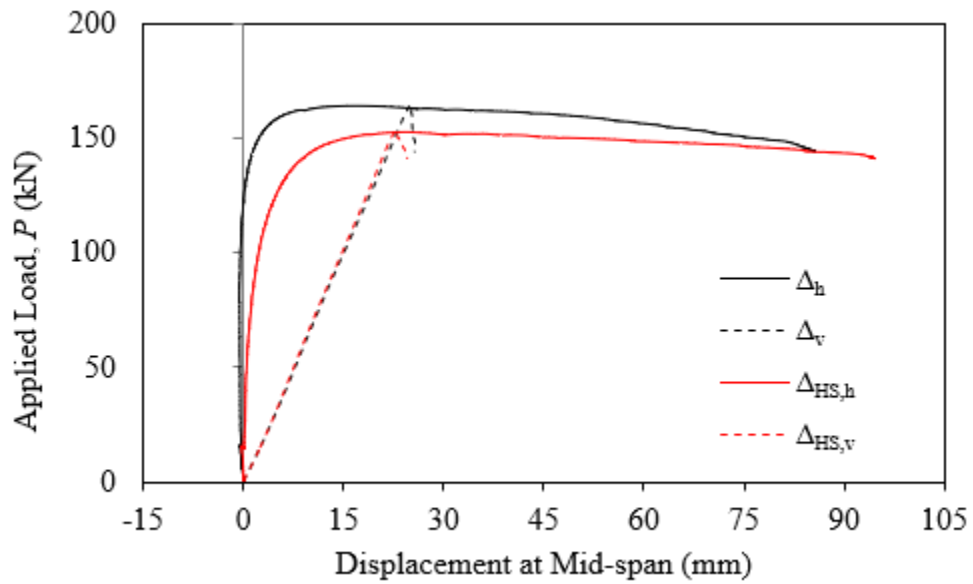
Figure B-4: Load-displacement responses of G9-360-25-3-f: Original and heat-straightened
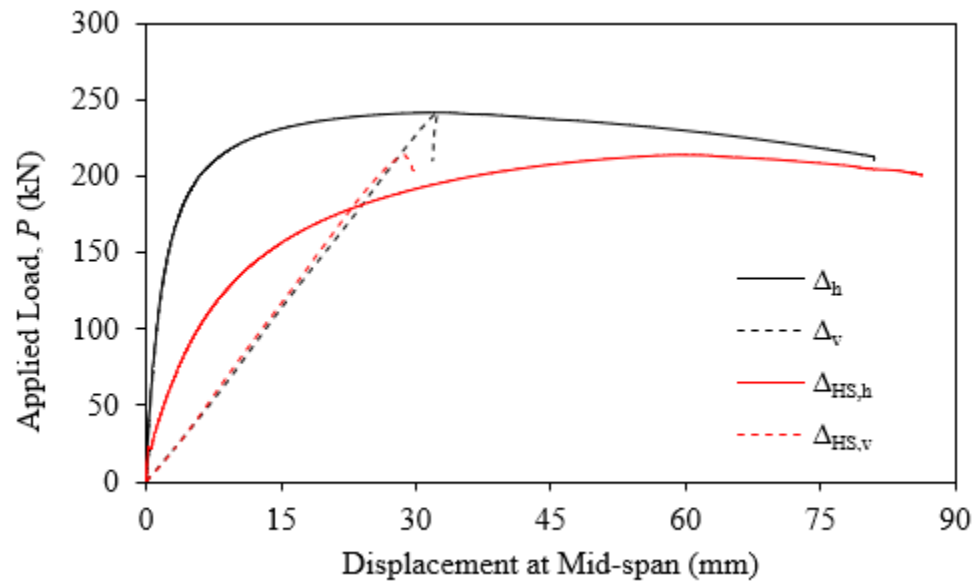
Figure B-5: Load-displacement responses of G9-430-25-3-f: Original and heat-straightened

Appendix C: FE Model Calibrations
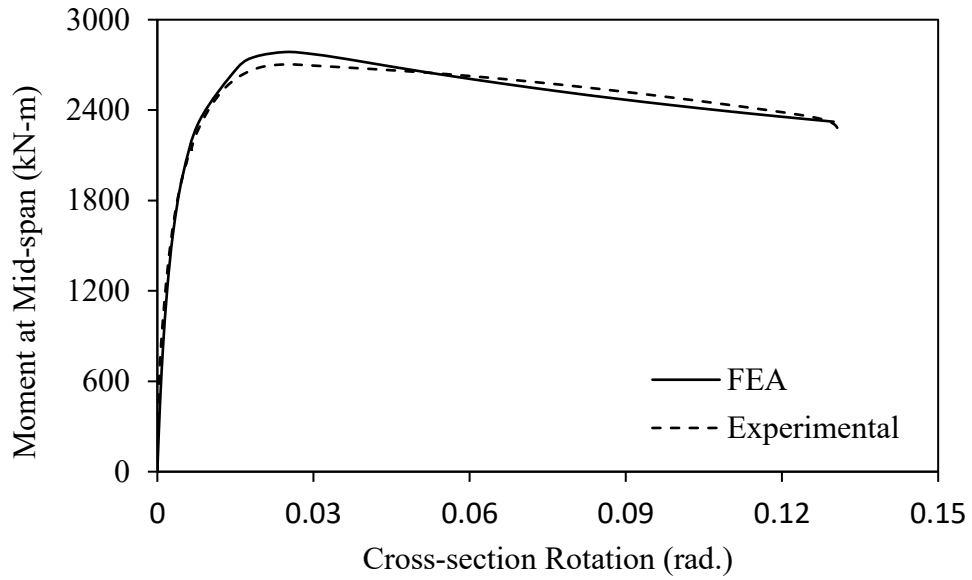
Figure C-1: Moment-Rotation Responses of G6-470-32-2-p: FEA and Experimental
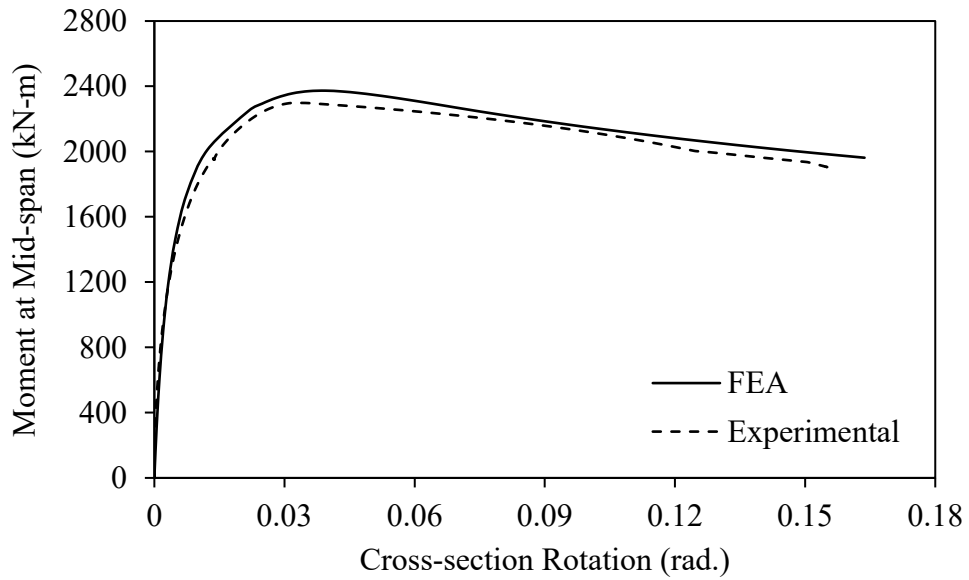
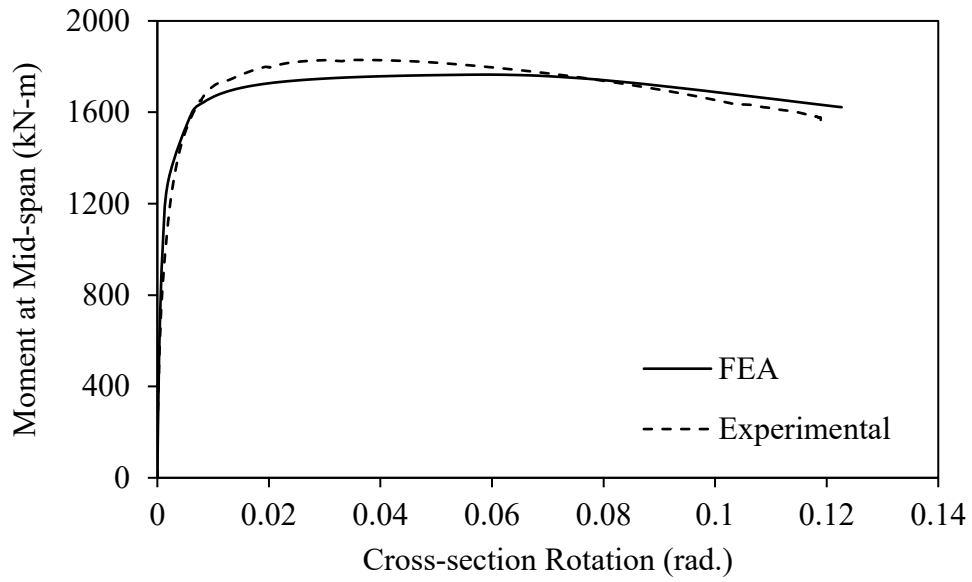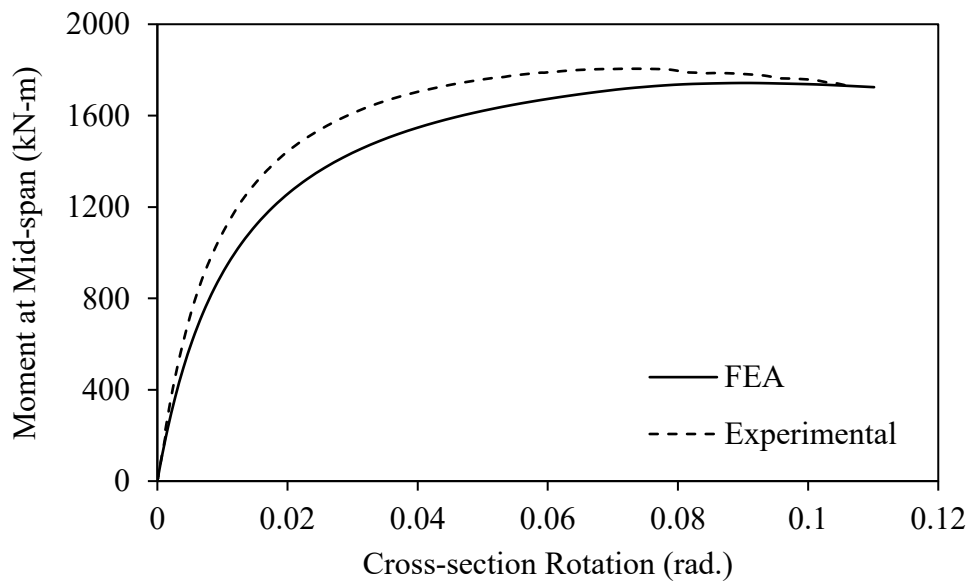Figure C-2: Moment-Rotation Responses of G6-430-32-1-p: FEA and Experimental
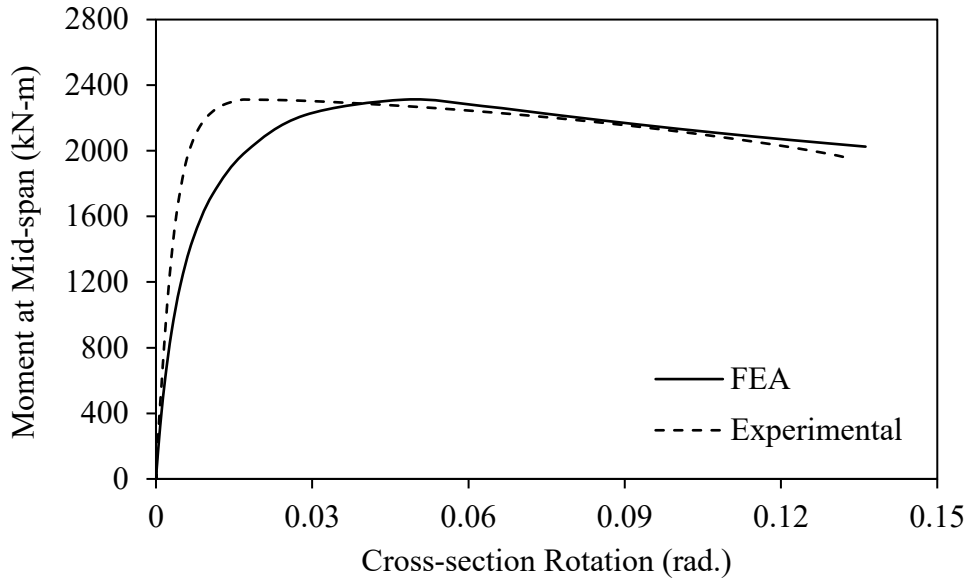
Figure C-3: Moment-Rotation Responses of G6-430-32-1-f: FEA and Experimental
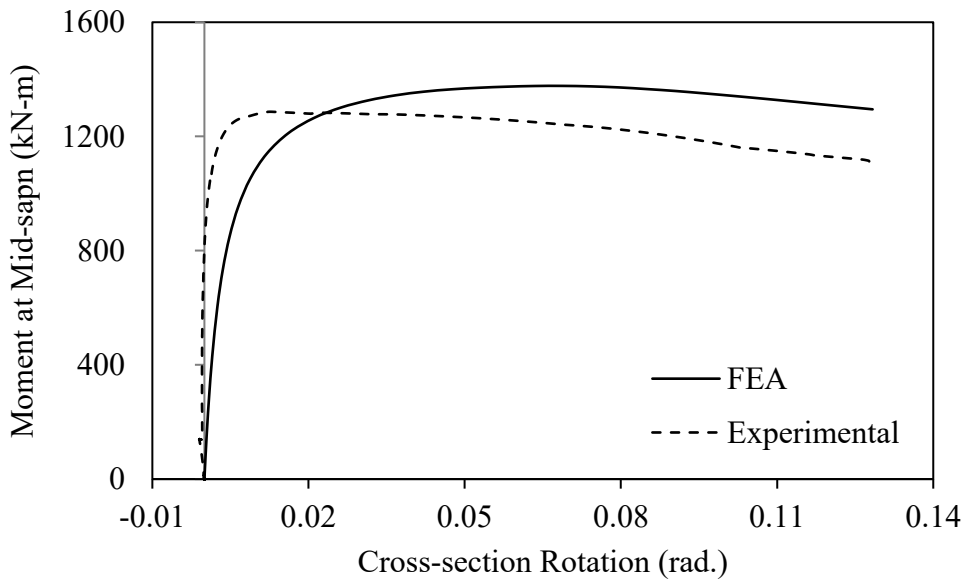
Figure C-4: Moment-Rotation Responses of G6-300-32-1-p: FEA and Experimental
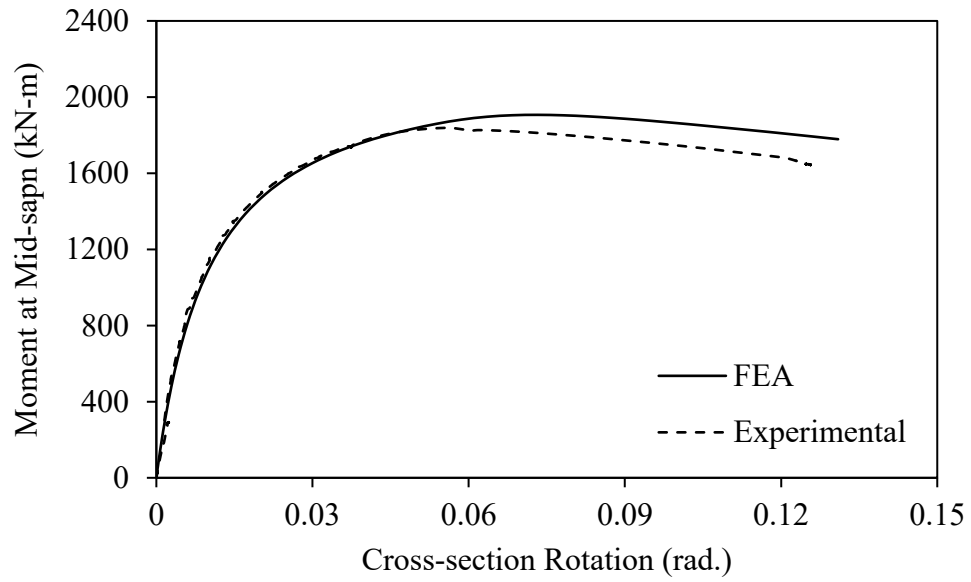
Figure C-5: Moment-Rotation Responses of G8-430-25-2-p: FEA and Experimental
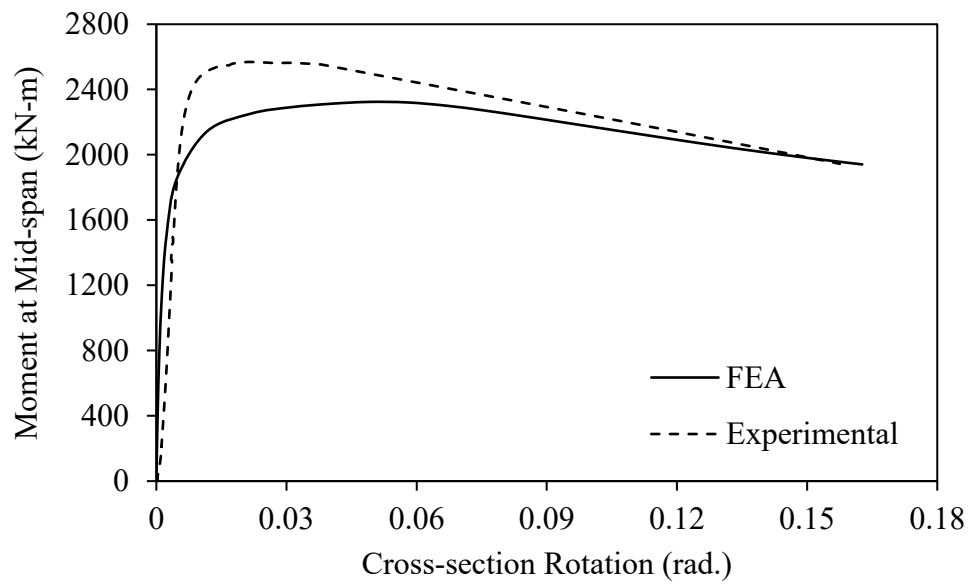
Figure C-6: Moment-Rotation Responses of G8-390-32-2-p: FEA and Experimental

Figure C-7: Moment-Rotation Responses of G8-390-25-2-p: FEA and Experimental

Figure C-8: Moment-Rotation Responses of G9-360-32-3-p: FEA and Experimental
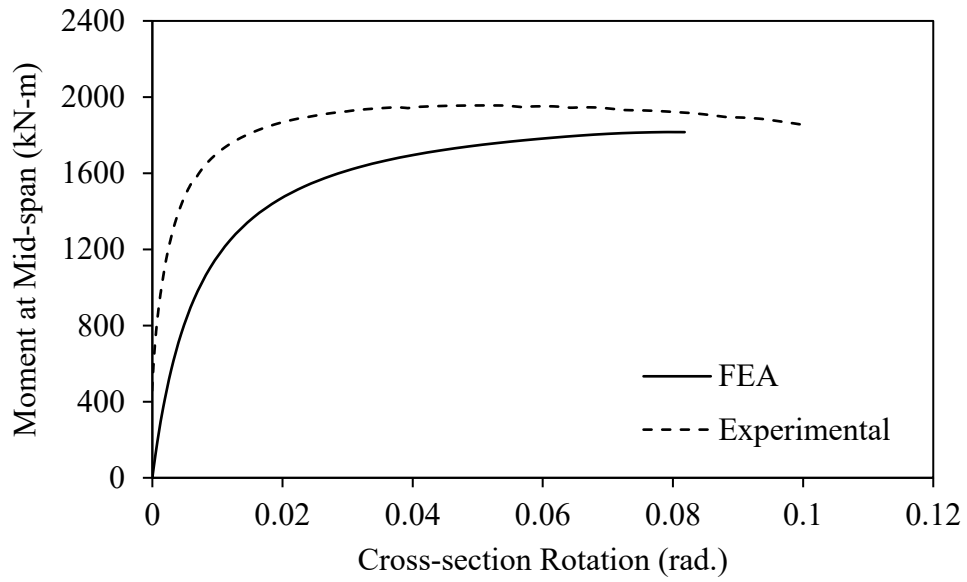
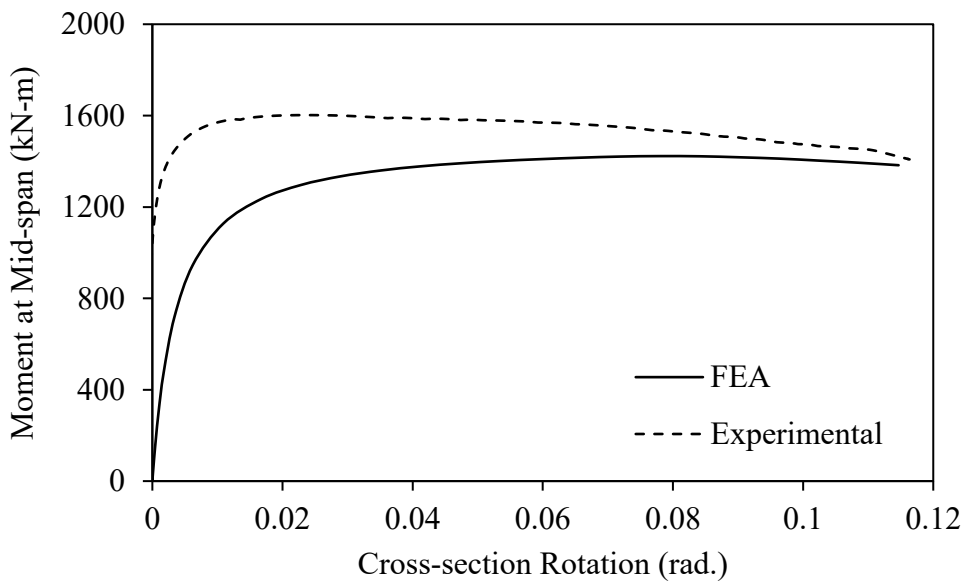Figure C-9: Moment-Rotation Responses of G9-360-32-3-f: FEA and Experimental

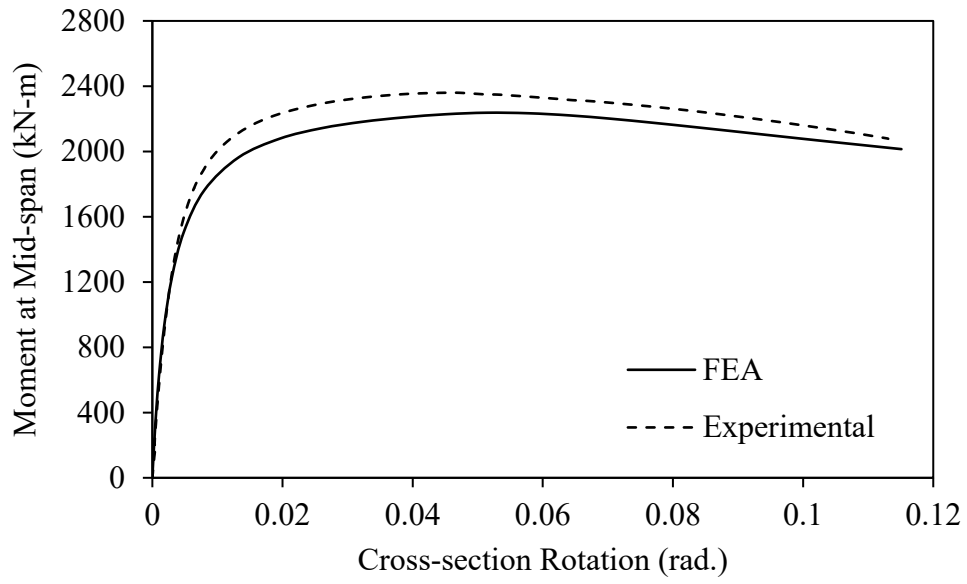Figure C-10: Moment-Rotation Responses of G9-360-25-3-f: FEA and Experimental

183

Figure C-11: Moment-Rotation Responses of G9-430-25-3-f: FEA and Experimental